Study of magnetic order in 3d transition metal substituted LPMO, and magnetic and transport properties of nanocrystalline LCMO manganite

A thesis submitted in partial fulfillment
of the award of the degree of
Doctor of Philosophy

By
Yugandhar Bitla

School of Physics
University of Hyderabad
Hyderabad - 500 046 India
June 2012

D E C L A R A T I O N

I hereby declare that the matter embodied in this thesis is the results of investigations carried out by me in School of Physics, University of Hyderabad, Hyderabad, under the supervision of Prof. S. N. Kaul.

Place: Hyderabad Yugandhar Bitla

Date:

C E R T I F I C A T E

This is to certify that the work contained in this thesis entitled, **"Study of magnetic order in 3d transition metal substituted LPMO, and magnetic and transport properties of nanocrystalline LCMO manganite"**, has been carried out by Mr. Yugandhar Bitla under my direct supervision and the same has not been submitted for the award of research degree of any university.

Place: Hyderabad (Thesis Supervisor)
Date:

Dean
School of Physics

To

My parents

Acknowledgements

It gives me an immense pleasure to express my gratitude to my mentor and thesis supervisor Prof. Sharika Nandan Kaul, for his constant encouragement and strong desire to share his knowledge. My long association with him was a rewarding experience, which I never wish to forget. I would also like to thank Mrs. Manjoo Kaul for the motherly care and affection during my stay on campus.

I wish to thank Dr. Srinath, my doctoral committee member, especially for allowing me to use his lab facilities during sample synthesis. I fondly cherish the company of my lab mate Dr. Shinto P. Mathew for all the good times we shared.

I thank all the teachers who taught us during the course work.

I would also like to thank the Dean, School of Physics, for making available all the necessary facilities for conducting the experiments. My thanks are also due to Prof. J. M. Barandiáran, Dr. Luis Fernández and other collaborators, for providing the LPMO samples used in this work and Dr. P. D. Babu, CSR, Mumbai for neutron diffraction measurements.

I am thankful to my seniors Dr. Sanjeev, Dr. Basheed and Dr. Ashutosh for being my support system and for the memorable outings. I extend my special thanks to my current lab mates Umasankar, Ravi and Pavan, Sendil and Suresh for their help and cooperation whenever sought.

I owe due thanks to all my batchmates - Anil, Arun, Balaji, Devaraju, Parthasarathy, Rambabu, Rangababu, Sadik, Shankaraiah, Sendil, Sita, Vasu, Venkaiah, Vijayan and Deepak, for the special moments we share. I would like to thank Devendra, Swaroop, Ravi, Ramu, Nivas, Kanth, Dileep and other research scholars in the School, for making my stay a really happy one.

I am thankful to the P. S. O. Dr. S. M. Ahmad, C. S. Murthy and the

members of technical staff of Central Instrumentation Laboratory, for their co-operation and help. I acknowledge the kind help rendered by Mr. Mantoo Kumar and Giri Bahadur in transferring Liquid Helium and Nitrogen.

I also want to thank to all non-teaching staff, particularly Mr. K. Srinivas, Mr. Abraham, Mr. Machandar and Mr. Chanderpal for their assistance throughout my Ph.D.

I express my sincere thanks to the Centre for Nanotechnology for the use of PPMS and SQUID systems. I am grateful to the UoH and CSIR for their financial support during my research work. A travel grant form the DST for presenting a paper at the MMM-2011 conference held at Scottsdale, Arizona is gratefully acknowledged.

I acknowledge with gratitude the unconditional love and support received from my parents, brother, sisters and other members of my family.

Finally, I thank all those who have, directly or indirectly, helped me all along.

Contents

Chapter 1

Introduction

The crucial concepts pertaining to the physics of ABO_3-type oxides are described briefly. A critical evaluation of the existing literature on the CMR manganites is followed by the aim and scope of the thesis.

1.1 Introduction

The understanding of the complex behaviour of transition-metal oxides (i.e., manganites, cobaltates, cuprates, nicklets, etc.) and related compounds has proved to be a daunting task due to degeneracy of the d-orbitals and the strong interactions between electrons. There has been enormous interest in the study of mixed-valence manganites and of strongly correlated electron systems, in general, because they show i) an unexpectedly large magneto-transport, ii) rich phase-diagram, and iii) intrinsic inhomogeneities (nanoscale phase separated states), which are thought to be the consequences of the coexistence and competition between different kinds of order involving charge, orbital, lattice and spin degrees of freedom. The

tunability of the properties can be achieved by varying ionic sizes, chemical composition, etc., i.e., small changes in them can bring about large changes in material properties. Magneto-resistance (MR) is defined as the relative change in the resistivity of material produced on the application of magnetic field.

$$MR = \Delta\rho/\rho(0) = (\rho(H) - \rho(0))/\rho(0) \tag{1.1}$$

where $\rho(H)$ and $\rho(0)$ are resistivities in the presence and absence of magnetic field at a given temperature, respectively. MR can be positive or negative. In non-magnetic pure metals and alloys, it is positive, showing quadratic dependence on H. MR can be negative in magnetic materials and highly resistive alloys due to the suppression of spin disorder and quantum mechanical interference by field, H. The large/giant magneto resistance (GMR) was first observed in magnetic superlattices [1] and magnetic semiconductors [2]. GMR is a result of reduction of extra resistance due to scattering of electrons by non-aligned ferromagnetic (FM) components in zero field. The negative colossal magneto resistance (CMR) [3–8] was discovered in rare earth manganates with pervoskite structure whose order of magnitude was many fold greater. The basic question-why CMR actually occurs has not yet been settled although basic ingredients (like double exchange, lattice distortion, magnetic localization, etc.,) leading to CMR have been identified.

1.2 Crystal Structure

The crystal structure of ideal $TMnO_3$ (ABO_3) is pervoskite structure as shown in figure 1.1. The mixed-valence manganites can be considered as

the solid solutions between the end members such as $TMnO_3$ and $DMnO_3$ where T stands for a trivalent rare earth (La, Pr, Nd, Sm, Eu, Gd, Ho, Tb, etc.,) element and D denotes the divalent alkaline earth (Sr, Ca, Ba, etc.,) element, with formal valence states, $T^{3+}Mn^{3+}O_3^{2-}$ and $D^{2+}Mn^{4+}O_3^{2-}$, resulting in $(T_{1-x}^{3+}D_x^{2+})(Mn_{1-x}^{3+}Mn_x^{4+})O_3^{2-}$. The nominal electronic configuration of Mn^{3+} and Mn^{4+} is $3d^4$ and $3d^3$, respectively. Each of the end member ($x = 0$ and $x = 1$) is an insulating antiferromagnet, but mostly a metallic ferromagnet for compositions around $x = 0.3$. Thus, depending on the values of x, the mixed valence manganites crystallize in various slightly distorted forms of ABO_3 pervoskite structure. Chemically, the system can be characterized by a wide range of cations occupying A site, which can be set as body center or cube corner. In general, the structure can be considered as a cubic closed packed array formed of O^{2-} anions, large A (T^{3+}, D^{2+}) cations and small B (Mn^{4+} or Mn^{3+}) cations. Manganese, smallest of the ions involved, is the one that is electrically and magnetically important while the other elements merely play a role in determining the precise crystal structure and charge density on the Mn site. The important

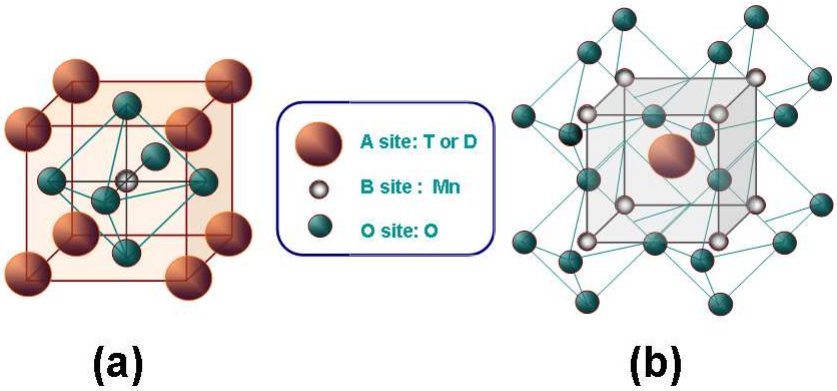

Figure 1.1: *Schematic view of the ABO_3 pervoskite structure*

geometrical quantity related to the ionic radius of the ion at A site, $< r >$, and thus to the crystal structure due to ion mismatch on A site, is the Goldschmidt tolerance factor Γ [9]:

$$\Gamma = \frac{r_A + r_O}{\sqrt{2}(r_B + r_O)} \tag{1.2}$$

where, r_i $(i = A, B, O)$ represents average ionic radius of each element. Γ is unity for ideally sized ions. However, for mixed-valence manganites, Γ is a density-weighted average of individual tolerance factors. If the A ions are too small to fill the space in the cube centers then oxygen tends to move towards center reducing the distance between A site and the nearest oxygen and also the $Mn{-}O{-}Mn$ bond angle ($< 180°$). As a consequence, tolerance factor ($\Gamma < 1$) decreases resulting in the increase of charge localization due to reduced carrier mobility. When $\Gamma \neq 1$, pervoskite structure adjusts the misfit in ionic sizes and electronically induced deformations by various kinds of distortions arising from cooperative rotation of BO_6 octahedra besides the Jahn-Teller effect, due to Mn^{3+} ion, which distorts MnO_6 octahedra in such a way that there are long and short $Mn - O$ bonds.

1.3 Electronic Structure

The electronic structure of transition-metal oxides is usually dictated by the competition between several interactions comparable in magnitude, all of the order of 1 eV.

i) The Mott-Hubbard interaction U_{dd}, which is cost of creating a $d^{n+1}d^{n-1}$ charge excitation in an array of d^n ions.

ii) The charge transfer interaction U_{pd}, which is the energy cost of transferring oxygen p electron to neighbouring d ion to create a p^5d^{n+1} charge

excitation from the p^6d^n, parent configuration.
iii) The transfer integral t resulting in the d-electron bandwidth $W = 2Zt$.
iv) The Hunds onsite exchange interaction U_{ex} ($\approx 2J_H$), the energy required to flip a d-electron spin.
v) The crystal field Δ_{cf} and Jahn-Teller δ_{JT} interactions.
Besides the classical Bloch-Wilson insulator, where Fermi-level falls within the gap in the one-electron density of states (DOS), transition-metal oxides may be Mott-Hubbard insulators ($U_{dd} > W$) or Charge-transfer insulators ($U_{pd} > W$) depending on the electron correlation [10,11]. Most of the oxides of early $3d$ metals are Mott-Hubbard insulators while many oxides of late $3d$ metals are Charge-transfer insulators. At the end of the $3d$ series, the charge-insulator gap goes to zero and oxides then become metallic. In the middle of series where $U_{dd} \approx U_{pd}$, the nature of the gap is not clear.

1.3.1 Crystalline Electric Field

Ionic model is employed to study the electronic structure of manganese ions occupying B site coordinated by an octahedron of oxygen neighbours, assuming that there is an integer number of d electrons per site. The inter-electronic correlations which give rise to Hund rules for the free ion are weakly perturbed by the crystalline electrostatic field (CEF). Crude calculations have been performed using the wavefunction $\Psi = R(r)_{(n=3,l=2)}Y_2^m(\theta,\phi)$ (for $m = \pm 2, \pm 1, 0$) with the assumption that wavefunctions of the active electrons (partially filled shells) are not dramatically distorted by the crystal environment and electrons are in fairly localized state centered at their ions even in a crystal. As a consequence of these calculations, the five d orbitals, each of which can accommodate one electron per spin, are split

into triplet t_{2g} (d_ϵ)- d_{xy}, d_{yz}, d_{zx} orbitals, which have their lobes oriented between the oxygen neighbours and doublet e_g (d_γ)-$d_{x^2-y^2}, d_{3z^2-r^2}$ orbitals, which are directed towards oxygen neighbours. The t_{2g} orbital has a lower energy because of electrostatic repulsion of electrons on neighbouring sites and the crystal field splitting, Δ_{cf}, is of the order of 1.5 eV. The divalent ion Mn^{2+} has a very stable $3d^5$ ($t_{2g}^{3\uparrow}e_g^{2\uparrow}$) configuration with $S = 5/2$ and a spherically symmetric electron density. Trivalent manganese ion has $3d^4$ ($t_{2g}^{3\uparrow}e_g^{\uparrow}$) electrons with $S = 2$, whereas quadravalent manganese ion has $3d^3(t_{2g}^{3\uparrow})$ electrons with $S = 3/2$. The spin-only magnetic moments of these ions are $5\mu_B$, $4\mu_B$ and $3\mu_B$, respectively.

1.3.2 Jahn-Teller Effect

As already mentioned, in cubic symmetry, the splitting due to CEF leads to an e_g doublet and a t_{2g} triplet. The remaining symmetry is usually broken by the lattice distortion. The ligand ions surrounding the transition metal ion under consideration (say, Oxygen around Manganese) slightly readjust their locations, creating an asymmetry between different directions that effectively removes the degeneracy. This lifting of degeneracy due to the orbital-lattice interaction is called Jahn-Teller effect (JTE). In other words, the distortion of Oxygen octahedron lowers the symmetry of the cubic crystal field in such a way that the centre of gravities of t_{2g} and e_g are unchanged and hence has no effect on Mn^{2+} and Mn^{4+} but Mn^{3+} tends to lower its energy in proportion to the distortion spontaneously because the energy penality of the lattice distortion grows as the square of that distortion. For example, the tetragonal elongation of octahedron stabilizes $d_{3z^2-r^2}$ orbital relative to $d_{x^2-y^2}$ as shown in figure 1.2. Δ_{cf} decreases with

increase in $Mn-O$ distance and has the values of 2.5 eV, 1.8 eV and 1.0 eV for Mn^{4+}, Mn^{3+} and Mn^{2+} in oxides, respectively. The Jahn-Teller splitting of e_g levels is in the range of $2\delta_{JT}$ =0.5 - 1.5 eV in various Mn^{3+} minerals [12]. The Jahn-Teller distortions can be static (for small x) or dynamic, namely a given ion is not frozen in one distorted configuration but evolves among several configurations as a function of time. The *static* JTE is the distortion of orbitally degenerate configuration to achieve a lower energy, observed in O' orhorhombic structure (e.g., low x in Fig.1.8), whereas the *dynamic* one is the hopping of the distortion from one orientation to the other. If there are large number of JTE cations, JTE can be cooperative and long-ranged and therefore can result in measurable changes in the crystalline symmetry. There are six normal modes of JT distortion (Q1, Q2, Q3, Q4, Q5 and Q6) of the oxygen atom cage containing the transition-metal (Mn) ion of which only Q2 and Q3 change $Mn-O$ distance, $Mn-O-Mn$ bond angle and lift the e_g orbital degeneracy as well. The Q2 mode is the *orthorhombic* distortion where opposing Mn-O bond lengths in the plane become longer and the other two become shorter so that $E(d_{x^2-y^2}) < E(d_{3z^2-r^2})$ while the Q3 mode is the *tetragonal* distortion, as displayed in figure 1.2, where the in-plane Mn-O bond lengths become shorter (or longer) and bond lengths for the apical oxygens become longer (or shorter) resulting in $E(d_{x^2-y^2}) > E(d_{3z^2-r^2})$.

1.3.3 Charge ordering

Charge Ordering (CO or Wigner crystallization), is driven by interatomic coulomb interactions. If the interelectronic coulomb interactions become comparable to conduction bandwidth, W, mobile d electrons get localized

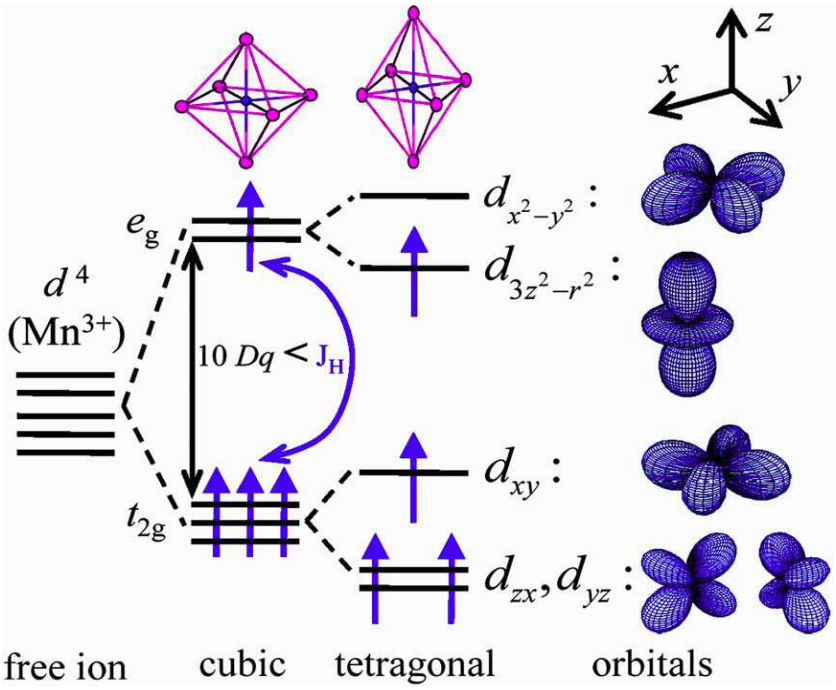

Figure 1.2: *Splitting of the energy levels of the d-orbitals of a Mn^{3+}-ion due to the cubic crystalline electric field and the Jahn-Teller effect.*

on certain manganese ions resulting in a regular lattice for particular occupancies of d band [13]. The effect is accentuated by small displacements of oxygen atoms to accommodate the ordered cation lattice. CO is most likely to occur when x is a fraction $(1/8, 1/2, 3/4$, etc.,) and the temperature is low. The extra fourth d electron may then be localized on alternate manganese sites in a plane, as shown in figure 1.3(a).

1.3.4 Orbital ordering

The carriers in mixed-valence manganites may strongly couple with local lattice distortions [14]. Orbital Ordering can occur at certain carrier con-

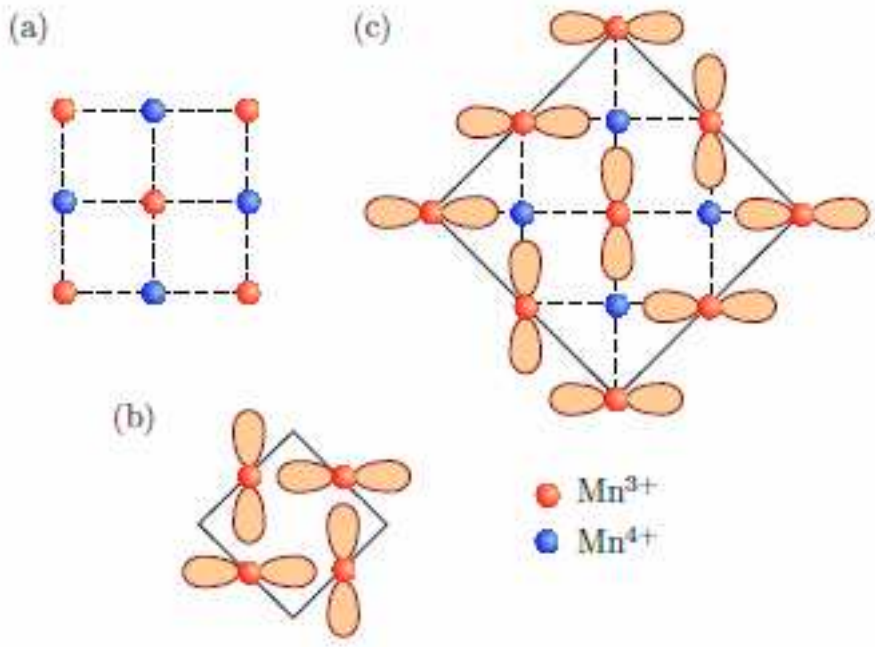

Figure 1.3: *(a) Charge ordering of Mn^{3+} and Mn^{4+} in a mixed crystal with $x = 0.5$. (b) Orbital ordering of the $d_{3z^2-r^2}$ orbitals of Mn^{3+} when $x = 0$. (c) Combined charge and orbital ordering when $x = 0.5$.*

centration x, when d electron occupies an asymmetric orbital, as shown in figure 1.3(b). The driving force is partly direct electrostatic repulsion of the charge clouds, but coupled Jahn-Teller distortions of adjacent octahedra stabilize the effect. The figure 1.3(c) shows coupled charge and orbital ordering for $x = 1/2$. The CO/OO phenomena tend to be most stabilized when the band filling coincides with a rational number for the periodicity of the crystal lattice.

1.4 Indirect exchange interactions

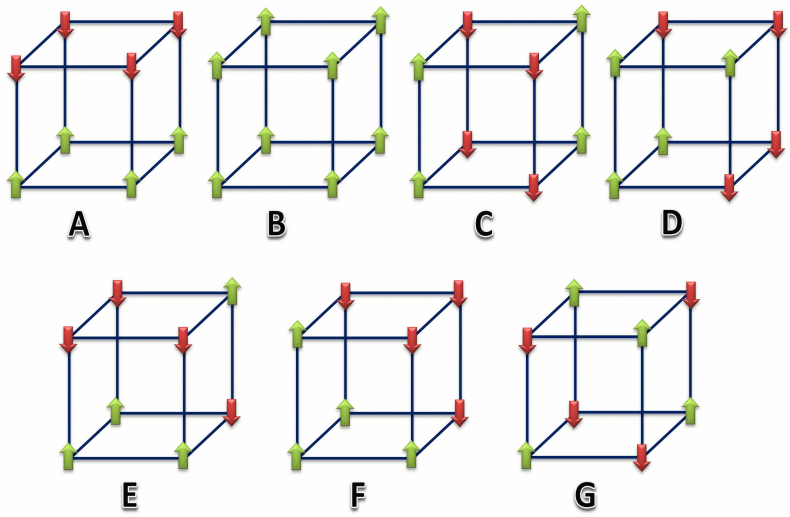

Figure 1.4: *Schematic magnetic unit cell configurations in manganites.*

First paper on pervoskite manganites was published in 1950 by Jonker and van Santen [15] where the results for polycrystalline $LaMnO_3$ with substitution on La by Ca, Sr, Ba were reported. In 1955, Wollan and Koehler [16] characterized the magnetic structure of $(La_{1-x}Ca_x)MnO_3$ in the entire range of composition using neutron diffraction technique and arrived at different possible magnetic structure configurations that are schematically depicted in Fig. 1.4. Interest in the study of mixed valence manganites dramatically accelerated in 1990 due to the large MR observed in $(Nd_{0.5}Pb_{0.5})MnO_3$ [17], in the films of $(La_{2/3}Ba_{1/3})MnO_3$ [3], $(La_{1-x}Ca_x)MnO_3$ [4] and $(La_{1-x}Sr_x)MnO_3$ [18]. Optimized films of $(La_{0.67}Ca_{0.33})MnO_3$, showed remarkable MR effects near T_c (which coincides with metal-insulator transition) termed 'colossal magneto-resistance by Jin et al [19]. Since then

the field of manganites is evolving at a rapid pace.

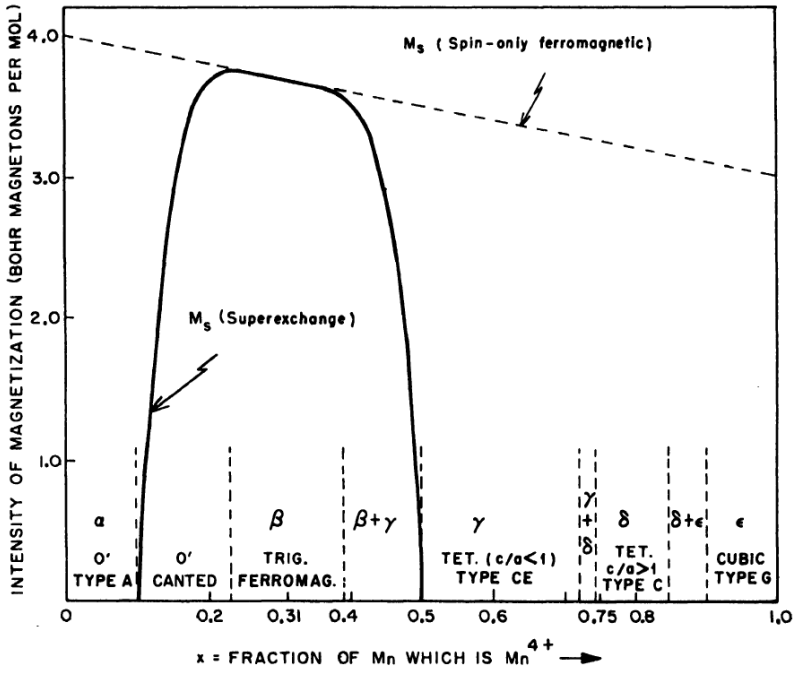

Figure 1.5: *Predicted saturation magnetization M_S, and semiempirical phase diagram for the system LCMO according to Goodenough [24] based on covalent bond and semicovalent-exchange model.*

Though study of $La_{1-x}Ca_xMnO_3$ manganites dates back to 1950s, only recently it has been systematically studied as a function of density and temperature. Figure 1.5 shows a semiempirical phase diagram for LCMO due to Goodenough and Wollan-Koehler. As the concentration of x is increased from zero to one, a sequence of structural (magnetic) transitions: $\alpha\ (A) \longrightarrow \beta\ (B) \longrightarrow \gamma\ (CE) \longrightarrow \delta\ (C) \longrightarrow \epsilon\ (G)$ occurs, where α, β, γ, δ and ϵ denote orthorhombic, cubic (with minimum resistivity), tetragonal ($c/a < 1$), tetragonal ($c/a > 1$) and cubic structures, respectively. The

system is ferromagnetic-metal in a narrow x range ($0.2 < x < 0.4$) and has a moment close to spin only value [15]. The double-exchange interaction adequately describes the ferromagnetic behaviour in this x range. The sub-lattice magnetizations of antiferromagnetic phases at $x = 0$ and $x = 1$ are also close to spin only values.

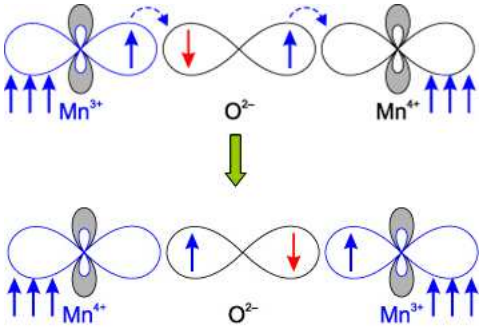

Figure 1.6: *Schematic representation of double exchange mechanism.*

1.4.1 Double exchange

In 1951, Zener [20] interpreted ferromagnetism as arising from indirect coupling between the unpaired d shells via conduction electrons. He considered that the intra-atomic Hund rule exchange was strong and the carriers do not change their spin orientation while hopping from one ion to the other, so that they can hop only if the spins of two ions are parallel. On minimizing the total free energy of the system, he found that ferromagnetic interactions are favoured when magnetic atoms are fairly well separated and conduction electrons are present. The theory was applied to manganese pervoskite [21] with the aim of explaining the strong correlation between ferromagnetism and conductivity and also the value of zero-temperature

magnetization which corresponds to the sum of all the unpaired electrons spins.

Starting from the insulating antiferromagnetic (AFM) $LaMnO_3$, where electrons are localized on the atomic orbitals, Zener showed that how system should gradually become more ferromagnetic upon hole doping (introduction of Mn^{4+} ions). He considered the problem of the interaction between the Mn^{3+} and Mn^{4+} ions through an oxygen ion and introduced the concept of simultaneous transfer of electron from Mn^{3+} to oxygen ion and from oxygen ion to the neighbouring Mn^{4+} ion, as shown in figure 1.6. Such a transfer was called the Double Exchange (DE). In the case of manganites, the configurations $Mn^{3+} - O^{2-} - Mn^{4+}$ and $Mn^{4+} - O^{2-} - Mn^{3+}$ are degenerate if the spins on d shells are parallel and the lowest energy of the system (ground state) corresponds to the parallel alignment of spins of two adjacent cations. DE always leads to a ferromagnetic metallic state while super-exchange, involving virtual electron transfer, frequently results in AFM insulating state.

Anderson and Hasegawa [22] generalized the DE mechanism by taking spin orientations of the t_{2g} electrons on the adjacent magnetic ions into account. They calculated the transfer integral t (hopping amplitude of the e_g electrons) as

$$t = t_{\circ} cos(\theta/2) \tag{1.3}$$

where $t_{\circ}$ is the normal transfer integral which depends on the spatial part of the wave functions and the term $cos(\theta/2)$ is due to the spin part of the wave functions, θ is the angle between the t_{2g} electron spin directions on the neighbouring Mn^{3+} and Mn^{4+} ions. By contrast, in $Mn^{3+}/Mn^{4+} - O^{2-} - Mn^{3+}/Mn^{4+}$ super-exchange, the coupling is proportional to $cos\theta$.

De Gennes [23] studied the case of low hole-doping of the end member $LaMnO_3$ and showed that mobile electrons in an antiferromagnetic lattice produce some canting of spin arrangements. Although this conclusion has been questioned recently, he successfully explained the values of saturation magnetization and the non-zero susceptibility at high fields and a canted structure, in accord with the neutron diffraction data. He also considered the case of mobile carriers localized in the vicinity of divalent A-site ion. The bound hole interacting with spins on the eight B sites neighbouring the impurity produces a local ferromagnetic distortion of spin system leading to the formation of bound magnetic (spin) polaron.

1.4.2 Super- and semicovalent exchange

Goodenough [24] rationalized the magnetic phase diagram of $(La_{1-x}Ca_x)MnO_3$ (mixed-valence manganite, in general), obtained by Wollan and Koehler, in terms of indirect exchange between manganese ions by invoking the semi-covalent and covalent bond/exchange based on the so-called Goodenough-Kanamori rules, schematically represented in figure 1.7. Mn^{3+} orbitals hybridize into dsp^2 orbital forming square coplanar bonds while Mn^{4+} hybridizes into d^2sp^3 orbital forming octahedral bonds to six near neighbours (oxygen). They can form bonds of different nature with surrounding oxygen through which magnetic interaction is mediated.

1) Covalent bonds are formed when two empty/half-filled Mn orbitals point towards an O^{2-} ion. This leads to an AFM super-exchange between two manganese ions (i.e., $Mn^{4+} - O^{2-} - Mn^{4+}$ and $Mn^{3+} - O^{2-} - Mn^{3+}$) forming strong short covalent bonds with a common oxygen atom, where each electron of bond has the same spin as its corresponding manganese due to

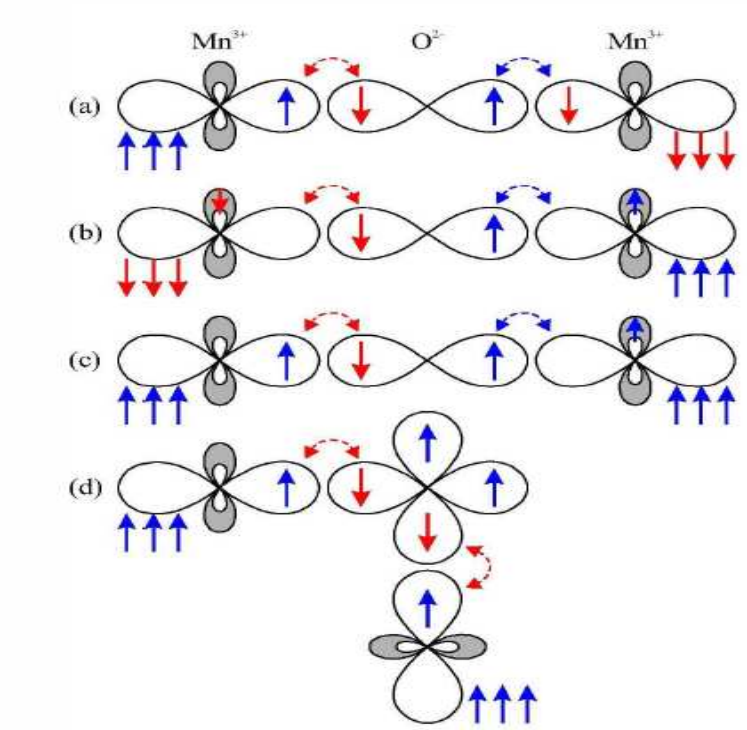

Figure 1.7: *A schematic representation of of Goodenough-Kanamori rules for the $d_{x^2-y^2}$(shadowed)-p_z- d_{z^2}-orbitals (to the left and right) forming a Mn-O-Mn bond. The small arrows in the orbitals describe the itinerant electrons, the three arrows outside the orbital denote the total core spin $S = 3/2$ of the three not shown t_{2g} orbitals. According to the realized occupation, either an antiferromagnetic (AF) (a,b) or a ferromagnetic (FM) (c,d) coupling will be established.*

Hund rule coupling and antiparallel spin of two electrons of common oxygen atom as they belong to same $2p$ orbital (the cases (a) and (b) of Fig. 1.7). 2) Semicovalence arises when only one out of the two manganese atoms surrounding an O^{2-} has a hybridized orbital available pointing towards oxygen. In such a case, full covalence is not possible because only one side of O^{2-} orbital can share electron with neighbouring manganese ion. The other bond

is ionic and the oxygen ion is displaced towards the first manganese, with which it forms a covalent bond. One of the electrons is then localized on the oxygen ion, whose spin is antiparallel to that of the covalent electron. Because of the Hunds rule, the manganese ion participating in the bond has its moment parallel to the electron shared with the oxygen. On this side of ionic bond, there is a direct (therefore AFM) exchange interaction between the magnetic moments of anion and that of the neighbouring manganese. The resulting configuration is FM arrangement (case (c) of Fig. 1.7) of spins on the manganese ions with an antiparallel spin on oxygen between them.
3) Ionic bonds are obtained when the empty Mn^{3+} (dsp^2) orbitals point away from the O^{2-} ions. This is a long bond appearing only between two Mn^{3+} ions. There is no indirect exchange in that case.
4) Double Exchange the last possibility involving the simultaneous transfer of an e_g-electron from Mn^{3+} to oxygen ion and an electron from oxygen ion to the neighbouring Mn^{4+}. Such hopping of e_g electrons is greatest only if the spins of the t_{2g} electrons on the two d shells are parallel, hence the lowest energy of the system at low temperature is obtained for ferromagnetic arrangement of spins on the two adjacent Mn^{3+} and Mn^{4+} manganese ions. In that case, the configurations $Mn^{3+}-O^{2-}-Mn^{4+}$ and $Mn^{4+}-O^{2-}-Mn^{3+}$ are degenerate.
The above interactions can account for the observed $Mn-Mn$ coupling [15,16]: AFM between two Mn^{4+} (covalent), FM between Mn^{4+} and Mn^{3+} (DE) and AFM (covalent) or FM (semicovalent) between two Mn^{3+}. Typical charge ordered arrangements were observed for the special ratio of Mn^{4+} to Mn^{3+} ions:
a) Pure $DMnO_3$, $D = Ca$ with 100% of Mn^{4+} ions, contains only Mn^{4+} ions which couple antiferromagnetically. The spin order is then nearest-

neighbour or three-dimensional antiferromagnetic (G-type) order (Fig.1.4) with no lattice distortion.

b) For 75% of Mn^{4+}, the arrangement is one of the planes of Mn^{4+} alternating with planes containing equal proportions of Mn^{3+} and Mn^{4+}. In the planes, the ordering is purely AFM but along the chains running in the c-direction (C-type in Fig.1.4), the coupling is on average FM (some $Mn^{4+} - Mn^{4+}$ bonds being mismatched).

c) For 50% of Mn^{4+}, case is more complex since three possible ordered bond arrangements are electrostatically equivalent. The minimum elastic energy, however, corresponds to a CE type ordering of semicovalent bonds.

d) For 30% of Mn^{4+}, the magnetic order is ferromagnetic with a moment almost equal to the spin only value. This is due to DE between Mn^{3+} and Mn^{4+} via conduction electrons. The DE is optimized for a disordered composition which has largest number of ions Mn^{3+} and only one Mn^{4+} near-neighbour. The corresponding content of $Mn^{4+} \simeq 31\%$. The transition temperature follows the relation $T_C \sim 2x(1-x) - x^2$. It is interesting to note that, for an ordered lattice, the optimum value would be 25% [24].

e) For 0% of Mn^{4+} (pure $TMnO_3$, $T = La$), the arrangement is A-type AFM (Fig.1.4) where all the bonds in c direction are covalent ($J_2 < 0$), while the in-plane orbital arrangement maximizes the number of FM semicovalent bonds ($J_1 > 0$), i.e., the structure has FM planes coupled antiferromagnetically with c axis shorter than a and b (the covalent bond is short). Goodenough predicted that semicovalent bonds would order in O' structure below a certain temperature, reducing elastic energy associated with different $Mn-Mn$ distance. This semicovalent-bond ordering (Orbital Ordering) is a cooperative effect that occurs well above Curie temperature, T_C.

Transitions between aforementioned magnetic phases are continuous. They

are realized either by inhomogeneous mixing in a two-phase region or by a homogeneous progressive magnetic transition involving canting, as in the low x region. It is observed that the MR resulting due to resistivity-magnetization ($\rho - M$) correlation cannot be explained solely by DE [20, 22, 23]. Both resistance and associated MR are thought to be related to hopping of lattice polarons in the paramagnetic state while below T_C, polarons breakup and the effect is due to individual electrons. The presence or absence of polarons is very sensitive to the ratio of electron-lattice coupling δ_{JT} and the hopping energy t (relative to kinetic energy gain for electrons to delocalize). The greater the distortion, the more localized are charge carriers. Results indicating the formation of small dielectric polarons [17,25–27], magnetic polarons [3, 17, 28–30], and elastic (Jahn-Teller) polarons [31–35] and the effect of isotope substitution on ESR [36] have been reported.
One can write the Hamiltonian for manganites based on known interactions as:

$$H = H_{KE} + H_H + H_{AF} + H_{el-ph} + H_{el-el} \tag{1.4}$$

Where H_{KE} corresponds to kinetic energy of e_g electrons, H_H for Hunds coupling between the spins of e_g and t_{2g} electrons, H_{AF} for inter-atomic Hunds coupling, H_{el-ph} for coupling between electrons and J-T distortion of MnO_6 and H_{el-el} for coulomb interactions among e_g electrons. The structural transitions of manganites depend on the temperature, doping, cation mismatch, pressure, size effects, etc.

1.4.3 Electronic phase separation

Electronic phase separation, in general, refers to the coexistence of two or more phases with distinctly different electronic properties, which does not

originate from chemical inhomogeneity or chemical phase separation. Many systematic studies of various manganites now indicate that the insulating nature above the Curie temperature is always associated with the presence of charge/orbital correlated nano-clusters, existing only in orthorhombic crystallographic structures. Thus, the nano-clusters will play a key role in producing CMR near the insulator-metal transition of the manganites. In other words, sensitive collapse of nano-scale charge/orbital ordering under a small magnetic field will essentially produce a huge drop in resistivity, inducing large negative magnetoresistance just above the Curie temperature.

1.5 Literature survey

It is widely accepted that colossal magnetoresistance (CMR) results from a magnetic-field-induced shift of the ferromagnetic Curie temperature, and the accompanying metal-insulator transition.

1.5.1 $La_{1-x}Pb_xMnO_3$

A detailed study of magnetic phase diagram in the $La_{1-x}Pb_xMnO_3$ (LPMO) ($0.25 \leq x \leq 0.45$) single crystals, due to Morrish and co-workers [39–44], dates back to 1969. In the composition range studied, all the compounds were found to be ferromagnetic with Curie temperatures ranging from 315 to 350 K and exhibit a sharp drop in resistivity at temperatures just below the Curie temperature. Ferromagnetism in these systems was understood in terms of the Zener double-exchange mechanism. Following the discovery of CMR in $Nd-Pb-Mn-O$, $La-Ba-Mn-O$ and $La-Ca-Mn-O$,

CMR in bulk polycrystalline $La_{1-x}Pb_xMnO_3$ ($0 \leq x \leq 1$) was investigated by Zhao et al., [45] with the main finding that MR goes through a maximum at $x \sim 0.4$. Subsequent studies were mainly confined to the compositions near the optimally hole-doped LPMO and as in the other manganites, several theories have been proposed for the CMR phenomenon in LPMO. The realization that a partial substitution of Mn by Fe, Co, Ni in the optimally hole-doped LPMO can provide a srtingent test for such theories by changing the charge and spin states of Mn in a controlled fashion led to a flurry of scientific activity [46–55] in $La_{0.7}Pb_{0.3}Mn_{1-y}TM_yO_3$ ($TM = Fe, Co, Ni$). However, the charge and spin states of Co and Ni and the nature of magnetic order in Fe-doped LPMO near the critical concentration for ferromagnetism remained obscure.

1.5.2 $La_{1-x}Ca_xMnO_3$

$La_{1-x}Ca_xMnO_3$ (LCMO) manganites, main subject matter of the current thesis, presents some characteristics of large bandwidth manganites like the presence of a robust ferromagnetic metallic phase and also the features that indicate strong deviations from double-exchange behavior, including the existence of charge/orbital-ordered phases. For this reason, the it is often regarded as 'intermediate-bandwidth manganite'. This compound is particularly interesting because it has one stable structure for the whole range of substitution, due to the high tolerance factor (the ionic radii of La^{3+} and Ca^{2+} being similar). The $T - x$ phase diagram in figure 1.8 [56–58] presents an intriguing combination of structural, magnetic and electronic transitions. An important observation is that the phase diagram presents the electron-hole asymmetry. At very high temperature, the compound ex-

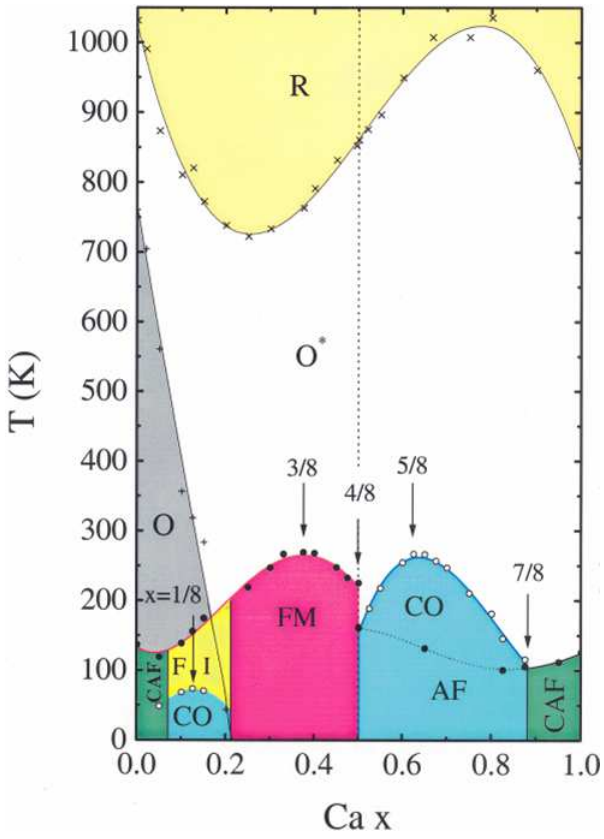

Figure 1.8: *Phase diagram for the LCMO manganite based on magnetization and resistivity measurements [58].*

hibits paramagnetic-insulating (PI) behaviour with rhombohedral structure which transforms to the orthorhombic one below $700K$ while at low temperatures, three different regimes can be discerned: 1) for $0 < x < 0.10$, the material is ferromagnetic-insulator (FMI); 2) for $0.20 < x < 0.45$, the material is a ferromagnetic-metal (FMM) and displays the CMR effect; 3) for $0.45 < x < 1$, the compound is AFM insulator (AFI). The end member parent compounds $LaMnO_3$ and $CaMnO_3$ are AFIs characterised by cubic structures. However, due to the mismatch of the cation radii, tilting

of the oxygen octahedra occurs which together with local J-T type distortions produces the orthorhombic symmetry characteristic of the entire doping range. $LaMnO_3$ becomes an insulator below the Jahn-Teller distortion temperature 758 K, because Mn^{3+} is a good Jahn-Teller ion, and the doubly degenerate e_g bands split due to the Jahn-Teller distortion. In this special O'-orthorhombic structure, $LaMnO_3$ is known to become an A-type antiferromagnet below 140 K, wherein ferromagnetic coupling exists in the orthorhombic basal plane and antiferromagnetic coupling perpendicular to the basal plane. For $x = 1$, antiferromagnetic superexchange interaction between Mn^{4+} ions via an intervening oxygen makes $CaMnO_3$ a normal G-type antiferromagnet. Therefore, the initial Ca substitution in $LaMnO_3$ produces hole carriers in the Jahn-Teller split e_g band, and the low doping of La in $CaMnO_3$ induces electrons in the empty e_g band. For $0.08 < x < 0.2$, the system is still insulating but with ferromagnetic or canted antiferromagnetic (CAF) coupling. Similarly, the samples with high Ca doping ($x > 0.875$), i.e., low La doping into $CaMnO_3$, also exhibits CAFI behaviour. In samples with $0.2 \leq x \leq 0.5$, where the CMR has been observed, a PMI-FMM transition occurs and can be adequately described by the DE mechanism. For the higher doping range with $x > 0.5$, doped charge carriers localize and order with stripe modulations at a charge ordering temperature T_{CO} and an antiferromagnetic ordering occurs at lower temperatures (at the Néel temperature T_N). The charge ordering is accompanied by a sharp increase of resistivity for doping ranges $0.5 \leq x \leq 0.875$. The striped ordering of charge carriers reflects a generic tendency toward microscopic (nano-scale) electronic phase separation in the system, due to strong electron-lattice and electron-electron interactions.

N/8 anomalies

As is evident from the phase diagram, there are well-defined features at the commensurate carrier concentrations of $x = N/8$ ($N = 1, 3, 5, 7$) in $La_{1-x}Ca_xMnO_3$. $x = 1/8$ shows a T_{CO} maximum below the PMI-FMI transition temperature, T_C. The CO that is seen in this composition is more of JT distorted Mn^{3+} ion dominated one while the one seen at $x = 5/8$ is Mn^{4+} dominated with higher resistivity. T_C becomes maximum at $x = 3/8$ while T_{CO} peaks at $x = 5/8$ with similar values of ordering temperatures. For $x = 3/8$, the electron hopping/transfer intergral attains its maximum value within the framework of the DE mechanism. Therefore, in the context of existing strong electron-lattice coupling in the manganites, it can be inferred that the maximum electron hopping at $x = 3/8$ is closely associated with the minimized local lattice distortions and maximized ferromagnetic correlation. It is also observed that lattice parameters at this concentration are isotropic [56]. For $x = 3/8$ the dominant interaction is FM DE that leads to metallic behaviour while in $x = 5/8$ the dominant interaction is super-exchange leading to an insulating nature. It is noteworthy that the transition temperatures from O-orthorhombic ($Pbnm$) to rhombohedral ($R\overline{3}c$) structure display an interesting electron-hole symmetry as a function of carrier concentration. In other words, a minimum temperature for the structural transition occurs near $x = 2/8$ (hole doping), while a maximum exists near $x = 6/8$ (2/8 electron doping). Those temperatures become lower below $x = 0.50$ and higher above $x = 0.50$, forming an asymmetric phase line centered at $x = 0.50$. It is an interesting question to be answered how the evolution of high temperature structural transition is linked to the ground state properties of the system. Interestingly, the compound

$x = 4/8$ is located at the x -dependent first-order phase-transition line between FMM ($x < 0.5$) and COI ($x > 0.5$) at low temperature. The $x = 0.5$ sample exhibits both ferromagnetic and charge ordering at 220 K and 180 K, respectively. It turns out that the FM metallic and CO insulating phases coexist even at the lowest temperature.

1.6 Aim and objectives

Following the realization that the critical behavior of a spin system in the vicinity of a magnetic order-disorder phase transition is solely governed by the nature of the magnetic ordering present, critical phenomena have been investigated in a large number of manganite systems. However, conflicting reports about the critical exponents, that characterize the ferromagnetic - paramagnetic (PM) phase transition, have rendered such studies inconclusive. The nature of interactions that sustain FM order below T_C remains obscure. Consequently, the basic issue of whether or not the percolation picture or the two-fluid model forms a correct description of (a) the ferromagnetic metallic (FMM) and paramagnetic insulating (PMI) states, (b) the transition between these states, and (c) the associated metal-insulator transition, cannot be unambiguously resolved.

A partial substitution of Mn by TM ($TM = Fe, Co, Ni$) ions in an optimally hole-doped $La_{0.7}Pb_{0.3}Mn_{1-y}TM_yO_3$ manganite alters the magnetic and transport properties of the host $La_{0.7}Pb_{0.3}MnO_3$ (LPMO) in a specific fashion depending on the charge and spin states of the TM solute ions, and thereby provides a fertile testing ground for the theoretical models proposed hitherto. Though $La_{1-x}Ca_xMnO_{3+\delta}$ (LCMO) [57–59] is one of the most ex-

haustively studied manganite systems, even in this system, many aspects of physics are still poorly understood. For instance, no general consensus has emerged so far on how the ferromagnetic insulating (FMI) state at low doping levels $x \approx 1/8$ evolves from the AFM insulating state at $x = 0$? or why the FMM-PMI phase transition temperature, T_c, and the charge ordering temperature, T_{CO}, peak at $x = 3/8$ and $x = 5/8$, respectively, in LCMO, as opposed to $x = 1/3$ and $x = 1/2$ in other manganites? These gaps in understanding the physics of manganites prompted us to undertake extensive investigations with the following objectives in mind.

- To investigate the charge and spin states of 3d transition metals, Co and Ni, substituting Mn in optimally hole-doped manganite, LPMO, and the influence of these states on the magnetic and transport properties.

- To unravel the nature of magnetic order in random Fe-substitued LPMO.

- To exploit the extreme sensitivity of non-linear magnetic susceptibility to local magnetic inhomogeneities in the study of the phenomenon of phase separation.

- To unambiguously identify the type of interactions that stabilize FM order in the insulating state in LCMO at very low hole-doping levels.

- To ascertain whether or not magnetic order-disorder and electronic transitions have a common origin. If so, what is the underlying mechanism?

- How does the reduction in the crystallite size to nanometre regime affect the magnetically-ordered, charge-ordered and orbitally-ordered states, the metal-insulator and insulator-insulator transitions at different hole doping levels in LCMO?

- Attempt a thorough understanding of the magnetization processes: irreversibility in magnetization, magnetization reversal, magnetic relaxation and approach-to-saturation, as well as of low-lying magnetic excitations in nanocrystalline LCMO.

1.7 Organization of the thesis

In the current chapter, a critical evaluation of the existing literature on the CMR manganites is followed by the aim and scope of the thesis.
Chapter 2 gives a brief description of the synthesis and characterization of nanomanganites and the physical property measurement techniques used in this work.
The experimental signatures of the FM-PM phase transition in nonlinear magnetic susceptibilities are established in chapter 3 from the mean-field calculation of nonlinear susceptibilities for ferromagnets of arbitrary spin.
Chapter 4 deals with the changes in the magnetic order in a conventional double-exchange ferromagnet, $La_{0.7}Pb_{0.3}MnO_3$ (LPMO), brought about by a partial substitution of Mn atoms by 3d transition metal atoms. It is observed that the Co and Ni doped samples show a crossover from 3d isotropic dipolar to 3d isotropic Heisenberg behaviour in the asymptotic critical region.
Extreme sensitivity of nonlinear magnetic susceptibility to the nature of

magnetic order (FM, AFM, SG, etc.,) and magnetic inhomogeneities has been fully exploited in chapter 4 to determine the nature of magnetic order present Fe doped LPMO. That these samples behave as a cluster spin glass is unambiguously established.

The results of a comparative study of nanocrystalline $La_{0.875}Ca_{0.125}MnO_3$, $La_{0.875}Ca_{0.125}MnO_{3+\delta}$, $La_{0.625}Ca_{0.375}MnO_3$ and $La_{0.375}Ca_{0.625}MnO_{3-\delta}$, while treating their bulk counterparts as reference systems, are summarized in chapters 6-8. A detailed study of the FM/AF-PM phase transition occuring in the insulating state reveals that these systems behave as a three-dimensional ($d = 3$) *uniaxial dipolar* (UD) ferromagnet in the asymptotic critical region (ACR) and exhibit a *crossover* to the $d = 3$ *isotropic dipolar* (ID) critical behaviour outside ACR. The width of the ACR *narrows* down with increasing Ca concentration indicating weakening of the uniaxial anisotropy. Irrespective of the Ca concentration, the dipolar interactions operate between localized e_g-electron spins.

Chapter 9 summarizes the results obtained on Mn-site doped LPMO and on the under, optimal and over hole-doped LCMO and outlines the future scope for work in this area.

References

1. P. M. Levy, *Giant Magnetoresistance in Magnetic Layered and Granular Materials*, Solid State Phys. **47**, 367 (1994); P. M. Levy and S. Zang, *Our current understanding of giant magnetoresistance in transition-metal multilayers*, J. Magn. Magn. Mater. **151**, 315 (1995).

2. N. B. Brandt and V. V. Moshchalkov, *Semimagnetic semiconductors.*, Adv. Phys. **33**, 193 (1984).

3. R. von Helmot, J. Wecker, B. Holzapfel, L. Schultz and K. Samwer, *Giant negative magnetoresistance in perovskite like* $La_{2/3}Ba_{1/3}MnO_x$ *ferromag- netic films*, Phys. Rev. Lett. **71**, 2331 (1993).

4. K. -I. Chahara, T. Ohno, M. Kasai and Y. Kozono, *Magnetoresistance in magnetic manganese oxide with intrinsic antiferromagnetic spin structure*, Appl. Phys. Lett. **63**, 1990 (1993).

5. M. Mc. Cormack, S. Jin, T. H. Tiefel, R. M. Fleming, J. M. Phillips and R. Ramesh, *Very large magnetoresistance in perovskite-like* $La - Ca - Mn - O$ *thin films*, Appl. Phys. Lett. **64**, 3045 (1994).

6. R. Mahesh, R. Mahendiran, A. K. Raychaudhuri and C. N. R. Rao, *Giant Magnetoresistance in Bulk Samples of* $La_{1-x}A_xMnO_3(A = SrorCa)$, J. Solid state Chem. **114**, 297 (1995).

7. C. N. R. Rao, A. K. Cheetham and R. Mahesh, *Giant magnetoresistance and related properties of rare-earth manganates and other oxide systems*, Chem. Mater. **8**, 2421 (1996).

8. A. Urushibara, Y. Moritomo, T. Arima, A. Asamitsu, G. Kido and Y. Tokura, *Insulator-metal transition and giant magnetoresistance in* $La_{1-x}Sr_xMnO_3$, Phys. Rev. B **51**, 14103 (1995).

9. V. Goldschmidt, *Geochemistry* (Oxford University press 1958).

10. J. Zaanen, G. A. Sawatzky and J. W. Allen, *Band gaps and electronic structure of transition-metal compounds*, Phys. Rev. Lett. **55**, 418 (1985).

11. J. Zaanen and G. A. Sawatzky, *Systematics in band gaps and optical spectra of 3D transition metal compounds*, J. Solid-st. Chem. **88**, 8 (1990).

12. R. G. Burns, *Mineralogical Application of Crystal field theory*, second ed, (London: Cambridge University Press, 1992).

13. J. R. Cullen and E. R. Callen, *Multiple ordering in magnetite*, Phys. Rev. **7**, 397 (1973).

14. J. Kanamori, *Superexchange interaction and symmetry properties of electron orbitals* , J. Phys. Chem. Solids **10**, 87 (1959).

15. G. H. Jonker and J. H. Van Santen, *Ferromagnetic compounds of manganese with perovskite structure* , Physica (Utrecht) **16**, 337 (1950) and *Electrical conductivity of ferromagnetic compounds of manganese with perovskite structure* **16**, 599 (1950).

16. E. O. Wollan and W. C. Koehler, *Neutron diffraction study of the magnetic properties of the series of perovskite-type compounds* $[(1-x)La, xCa]MnO3$, Phys. Rev. **100**, 545 (1955).

17. R. M. Kusters, J. Singleton, D. A. Keen, R. McGreevy and W. Hayes, *Magnetoresistance measurements on the magnetic semiconductor* $Nd_{0.5}Pb_{0.5}MnO_3$, Physica B **155**, 362 (1989).

18. H. L. Ju, C. Kwon, Qi Li, R. L. Greene, and T. Venkatesan, *Giant magnetoresistance in* $La_{1-x}Sr_xMnO_z$ *films near room temperature* , Appl. Phys. Lett. **65**, 2108 (1994).

19. S. Jin, T. H. Tiefel, M. McCormack, R. A. Fastnacht, R. Ramesh and J. H. Chen, *Thousandfold change in resistivity in magnetoresistive La-Ca-Mn-O films*, Science **264**, 413 (1994).

20. C. Zener, *Interaction between d shells in the transition metals*, Phys. Rev. **81**, 440 (1951).

21. C. Zener, *Interaction between d shells in the transition metals. II. Ferro- magnetic compounds of manganese with perovskite structure*, Phys. Rev. **82**, 403 (1951).

22. P. W. Anderson and H. Hasewaga, *Considerations on Double Exchange*, Phys. Rev. **100**, 675 (1955).

23. P. -G. de Gennes, *Effects of double exchange in magnetic crystals*, Phys. Rev. **118**, 141 (1960).

24. J. B. Goodenough, *Theory of the Role of covalency in the perovskite-tyoe manganites [La, M(II)]MnO3*, Phys. Rev. **100**, 564 (1955).

25. P. Gerthsen and K. H. Hardtl, Z.Natur f (a) **17**, 514 (1962).

26. R. R. Heikes, R. C. Miller and R. Mazelsky, *Magnetic and electrical anomalies in* $LaCoO_3$, Physica **30**, 1600 (1962).

27. S. J. L. Billinge, R. G. Difrancesco, G. H. Kwei, J. J. Neumeier and J. D. Thompson, *Direct observation of lattice polaron formation in the local structure of* $La_{1-x}Ca_xMnO_3$ Phys. Rev. Lett. **77**, 715 (1996).

28. J. Fontcuberta, B. Martínez, A. Seffar, S. Piñol, J. L. García-Muñoz and X. Obradors, *Chemical tuning of the colossal magnetoresistance of ferromagnetic perovskites* Europhys. Lett. **34**, 379 (1996).

29. J. M. De Teresa, M. R. Ibarra, J. Blasco, J. García, C. Marquina, P. A. Algarabel, Z. Arnold, K. Kamenev, C. Ritter and R. von Helmolt, *Spontaneous behavior and magnetic field and pressure effects on* $La_{2/3}Ca_{1/3}MnO_3$ *perovskite*, Phys. Rev. B **54**, 1187 (1996).

30. J. M. De Teresa, M. R. Ibarra, P. A. Algarabel, C. Ritter, C. Marqina, J. Blasco, C. Garcia, A. Del Moral, and Z. Arnold, *Evidence for magnetic polarons in the magnetoresistive perovskites*, Nature **386**, 256 (1992).

31. A. J. Millis, B. I. Shraiman and R. Mueller, *Dynamic Jahn-Teller effect and colossal magnetoresistance in* $La_{1-x}Sr_xMnO_3$, Phys. Rev. Lett. **77**, 175 (1996).

32. V. Caignaert, E. Suard, A. Maignan, Ch. Simon and B. Raveau, *Neutron diffraction evidence for an antiferromagnetic ordering in the CMR manganites* $Pr_{0.7}Ca_{0.3-x}Sr_xMnO_3$, J. Magn. Magn. Mater. **153**, L260 (1996).

33. J. L. García-Muñoz, J. Fontcuberta, B. Martínez, A. Seffar, S. Piñol,and X. Obradors, *Magnetic frustration in mixed valence manganites*, Phys. Rev. B **55**, R668 (1997).

34. P. G. Radaelli, M. Marezio, H. Y. Hwang, S. W. Cheong and B. Batlogg, *Charge localization by static and dynamic distortions of the MnO_6 octahedra in perovskite manganites*, Phys. Rev. B **54**, 8992 (1996).

35. D. N. Argyriou, J. F. Mitchell, C. D. Potter, D. G. Hinks, J. D. Jorgensen and S. D. Bader, *Lattice Effects and Magnetic Order in the Canted Ferromagnetic Insulator $La_{0.875}Sr_{0.125}MnO_{3+d}$*, Phys. Rev. Lett. **76**, 3826 (1996).

36. G. Zhao, K. Conder, H. Keller and K. A. Müller, *Giant oxygen isotope shift in the magnetoresistive perovskite $La_{1x}Ca_xMnO_{3+y}$*, Nature **381**, 676 (1996).

37. J. M. D. Coey, M. Viret and S. von Molnar, *Mixed-valence manganites*, Adv. Phys. **48**, 167 (1999).

38. J. B. Goodenough and J.-S. Zhou, *Localized to Itinerant Electronic Transition in Perovskite Oxides*, Structure and Bonding Vol. 98, edited by J. B. Goodenough (Springer, Berlin, 2001).

39. A. H. Morrish, B. J. Evans, J. A. Eaton and L. K. leung, *Studies of the ionic ferromagnet $(LaPb)MnO_3$. I. Growth and characteristics of single crystals*, Can. J. Phys. **47**, 2691 (1969).

40. L. K. Leung, A. H. Morrish and C. W. Searle, *Studies of the ionic ferromagnet $(LaPb)MnO_3$. II. Static magnetization properties from 0 to 800 °K*, Can. J. Phys. **47**, 2697 (1969).

41. C. W. Searle and S. T. Wang, *Studies of the ionic ferromagnet $(LaPb)MnO_3$. III. Ferromagnetic resonance studies*, Can. J. Phys. **47**, 2703 (1969).

42. M. J. Oretzki and P. Gaunt, *Studies of the ionic ferromagnet* $(LaPb)MnO_3$. *IV. Lattic distortion and ferromagnetism*, Can. J. Phys. **48**, 346 (1970).

43. C. W. Searle and S. T. Wang, *Studies of the ionic ferromagnet* $(LaPb)MnO_3$. *V. Electric transport and ferromagnetic properties*, Can. J. Phys. **48**, 2023 (1970).

44. C. W. Searle and S. T. Wang, *Studies of the ionic ferromagnet* $(LaPb)MnO_3$. *VI. Antiresonance and the Ferromagnetic Resonance Line Shape* , Can. J. Phys. **49**, 387 (1971).

45. T. Y. Zhao, M. Li, Zhao Xue-gen, Wang Fang-wei, Li Yun-fei, Shen Bao-gen and Zhao Jian-gao, *Negative magnetoresistance effect in La-Pb-Mn-O bulk manganese oxides* , Chin. Phys. Lett. **13**, 129 (1996).

46. J. Gutiérrez, A. Peña, J. M. Barandiarán, J. L. Pizarro, T. Hernandez, L. Lezama, M. Insausti and T. Rojo, *Structural and magnetic properties of* $La_{0.7}Pb_{0.3}(Mn_{1-x}Fe_x)O_3$ $(0 \leq x \leq 0.3)$ *giant magnetoresistance perovskites*, Phys. Rev. B **61**, 9028 (2000).

47. J. Gutiérrez, F. J. Bermejo, J. M. Barandiarán, S. P. Cottrell, P. P. Romano, C. Mondelli, J. R. Stewart, L. Fernández Barquín, and A. Peña, *Role of disorder and competing ferromagnetic and antiferromagnetic interactions in the magnetic, electrical, and dynamic properties of* $La_{0.7}Pb_{0.3}(Mn_{1-x}Fe_x)O_3$, $0 \leq x \leq 0.2$ *manganites*, Phys. Rev. B **73**, 054433 (2006).

48. J. Gutiérrez, F. J. Bermejo, N. Veglio, J. M. Barandiarán, P. Romano, C. Mondelli, M. A. González and A. P. Murani, *Structural cor-*

relations in $La_{0.7}Pb_{0.3}(Mn_{1-x}Fe_x)O_3$ manganites as probed by small-angle and polarized neutron diffraction, J.Phys.: Condens. Matter **18**, 9951 (2006).

49. J. Gutiérrez, J. M. Barandiarán, F. J. Bermejo, C. Mondelli, P. Romano, P. Fouquet and M. Monkenbusch, *Evidence for two disparate spin dynamic regimes within Fe-substituted $La_{0.7}Pb_{0.3}(Mn_{1-x}Fe_x)O_3$ ($0 \leq x \leq 0.2$) colossal magnetoresistive manganites: Neutron spin-echo measurements*, Phys. Rev. B **76**, 184401 (2007).

50. J. M. Barandiarán, F. J. Bermejo, J. Gutiérrez and L. Fernández Barquín, *Spin disorder in Fe-doped manganites*, J. Non-Cryst. Solids **353**, 757 (2007).

51. J. Gutiérrez, J. M. Barandiarán, A. Peña, L. Lezama, M. Insausti, T. Rojo and J.L. Pizarro, *Structural, magnetic and magnetotransport properties of $La_{0.7}Pb_{0.3}Mn_{0.9}TM_{0.1}O_3$ (TM = Fe, Co, Ni) CMR perovskites*, J. Phys.: Condens. Matter **12**, 10523 (2000).

52. A. Peña, J. Gutiérrez, J. M. Barandiarán, J. L. Pizarro, T. Rojo, L. Lezama and M. Insausti, *Magnetism in $La_{0.7}Pb_{0.3}(Mn_{0.9}TM_{0.1})O_3$ (TM = Fe, Co, Ni) CMR perovskites*, J. Magn. Magn. Mater. **226 – 230**, 831 (2001).

53. A. Peña, J. Gutiérrez, J. M. Barandiarán and T. Rojo, *Magneto-transport properties of Co- and Ni-doped manganites: from conductive to insulating behavior*, J. Magn. Magn. Mater. **272 – 276**, e1425 (2004).

54. A. Peña, J. Gutiérrez, I. Gil de Muro, J. Campo, J. M. Barandiarán and T. Rojo, *Correlation between structure and magnetic and magnetotransport properties of* $La_{0.7}Pb_{0.3}(Mn_{1-x}Co_x)O_3$ $(0.1 \leq x \leq 0.3)$ *CMR manganites*, Eur. J. Inorg. Chem. **16**, 3227 (2006) and references cited therein.

55. A. Peña, J. Gutiérrez, J. Campo, J. M. Barandiarán, L. Lezama, I. Gil de Muro and T. Rojo, *Structural, magnetic and magnetotransport properties of* $La_{0.7}Pb_{0.3}(Mn_{1-x}Ni_x)O_3$ $(0.1 \leq x \leq 0.3)$ *CMR manganites*, Eur. J. Inorg. Chem. **18**, 2569 (2008) and references cited therein.

56. S. -W. Cheong and H. Y. Hwang, Chap. 7 in *Colossal Magnetoresistive Oxides* Edited by Y. Tokura (Gordon and Breach Science Publisher, 2000).

57. E. Dagotto, *Nanoscale phase separation and colossal magnetoresistance*, (Springer, Berlin, 2003).

58. P. Schiffer, A. P. Ramirez, W. Bao and S. -W. Cheong Phys. Rev. Lett. **75**, 3336 (1995).

59. Y. Tokura, *Critical features of colossal magnetoresistive manganites*, Rep. Prog. Phys. **69**, 797 (2006) and references cited therein.

Chapter 2

Experimental Techniques

This chapter gives a brief description of the synthesis and characterization of nanomanganites and the physical property measurement techniques used in this work.

2.1 Synthesis

The structure and physical properties of mixed-valence manganites are very sensitive to the synthesis conditions. The main emphasis in the present work was not to investigate the synthesis-property correlations in detail but to maintain the same synthesis conditions as far as possible so as to ensure that the genuine composition-dependent hole-doping effects are not masked by the alterations in the process parameters.

2.1.1 Sol gel method

The sol-gel process is a wet-chemical technique for the preparation of materials starting either from a chemical solution or colloidal particles (sol is abbreviation for solution for particles usually in the nm size range) to produce an integrated network (gel). The gel may be processed to form a powder or a film. The samples were prepared using the easiest and elegant variation of sol-gel route, Pechini method [1], wherein polymeric precursors, made from metal salts, ethylene glycol and citric acid, result in the stoichiometric compositions by low-temperature heat-treatment. This method allows the metal cations to be mixed at a molecular level and offers several advantages like including low cost, homogeneous compositions, high purity, and low heat-treatment temperatures. When compared with the majority of the hydrocarboxylic acids, citric acid is more widely used in Pechinis processing [2] because of its high stability and the typical metal complexes with citric ligands tend to be fairly stable due to the strong coordination of the citric ion to the metal cation involving two carboxyl groups and one hydroxyl group. The addition of a glycol such as ethylene glycol leads to the formation of an organic ester. Condensation reaction occurs with the formation of a water molecule. The hydroxide ions arise from the carboxylic acid and the protons from the alcohol, generating water molecules. Citric acid (CA) is well soluble in ethylene glycol (EG), which provides a wide range of CA:EG ratios for the Pechini method, and makes it possible to tune the conditions of synthesis for each particular system. From practical viewpoint, high viscosity of the concentrated CA solution slows down the dissolution of metal salts and, in addition, the precipitation of citric acid might occur while pH, temperature or metal salt

concentration (ionic strength) change during the processing. Another reason to use excess of EG is connected with a need to remove water from the reaction mixture. In this case, the vapour contains ethylene glycol as a major fraction that can be progressively removed from the reaction. In the typical synthesis of ($La_{1-x}Ca_xMnO_3$, $x = 0.125, 0.375, 0.625$) materials by Pechini-type process, soluble metal nitrates of the high purity metal precursors La_2O_3, $Ca(NO_3)_2.4H_2O$, $(CH_3COO)_2Mn.4H_2O$, $Co(NO_3)_2.6H_2O$, $Ni(NO_3)_2.6H_2O$ and $Fe(NO_3)_3.9H_2O$ of Sigma-Aldrich make are dissolved in water along with citric acid. The pH of the solution was adjusted to 7 by adding ammonia (NH_4) solution. The solution was constantly stirred by a magnetic stirrer with constant heating for 12 hours. The gelling agent was added and temperature was raised further with the result that a viscous gel is formed after a few hours. The temperature of the hot plate was monitored regularly till gel dries up and forms a solid resin, which on further heating to $673K$, resulted in the combustion of this mass yielding powder sample. The collected powder was sintered at temperatures in 100 K steps from $673K$ to $1073K$ for at least 2 hours at each sintering temperature with intermediate grinding. The XRD patterns corresponding to the selected sintering temperatures were recorded and the change monitered so as to keep a check on the formation of single phase. The powder was pelletized under a pressure of 11 ton /cm^2 and sintered at 1173 K for 5 hours. The pellets were cut in desired dimensions for use in the magnetic and transport property measurements.

2.2 Characterization

2.2.1 X-ray diffraction (XRD)

X-ray diffraction (XRD) patterns of all the samples referred to in this thesis were obtained from a small mass ($\simeq$ 20 mg) of the sample, fixed with silcone paste onto a glass slide that was subsequently placed into a slot in the chamber of the diffractometer where they are exposed to CuK_α X-ray ($\lambda = 0.154nm$) radiation. The X-ray detector could be scanned through the scattering angle, 2θ, between $20^\circ - 120^\circ$ with a step of 0.02° at a counting time of $2s$ per step which can be controlled with a software package.

One of the more frequent applications of XRD analysis is to determine the crystallite size and lattice strain in nanocrystalline materials. The peak broadening in x-ray powder diffraction patterns for nanomaterials is the result of the finite size effect. For a finite size nanocrystal, the x-ray radiation reflected from successive lattice planes interfere constructively or destructively to produce the observed x-ray diffraction pattern. Additionally, the factors such as inhomogeneous lattice strains and structural faults lead to the broadening of diffraction peaks. Figure 2.1 displays the XRD pattern at room temperature for the nanocrystalline sample $x1$ with composition $La_{0.875}Ca_{0.125}MnO_3$.

2.2.2 Neutron diffraction (ND)

Neutron beam coming out of a nuclear reactor (which is in thermal equilibrium with the moderator) have their kinetic energies distributed according to the Maxwell distribution law. The largest fraction of these so-called ther-

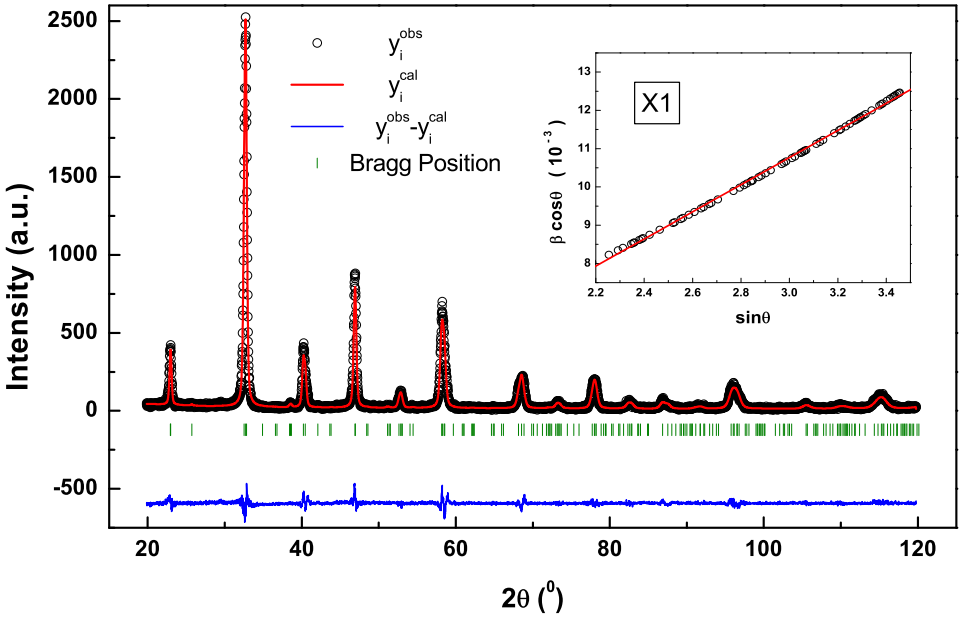

Figure 2.1: *Room temperature XRD pattern for* $x1$.

mal neutrons has kinetic energy equal to k_BT. A monochromatic beam of neutrons is obtained when the thermal neutrons get Bragg-reflected from a single crystal. The thermal wavelength of such neutrons is obtained by the relation

$$\lambda = \frac{h}{\sqrt{2mk_BT}} \tag{2.1}$$

At T = 300 K to 400 K, λ ranges from 2 $\mathring{A}$ to 1 $\mathring{A}$ and is of the same order as the interatomic spacing in crystalline solids and hence the diffraction of neutrons from the atoms forming a crystalline lattice can be used for the determination of crystallographic structure. In neutron diffraction experiments, the intensity of the diffracted neutron beam from the sample

is measured with a proportional counter filled with BF_3 gas. The neutron diffraction has following advantages over electron or x- ray diffraction technique [3]. A neutron beam is highly penetrating and thus gives details about

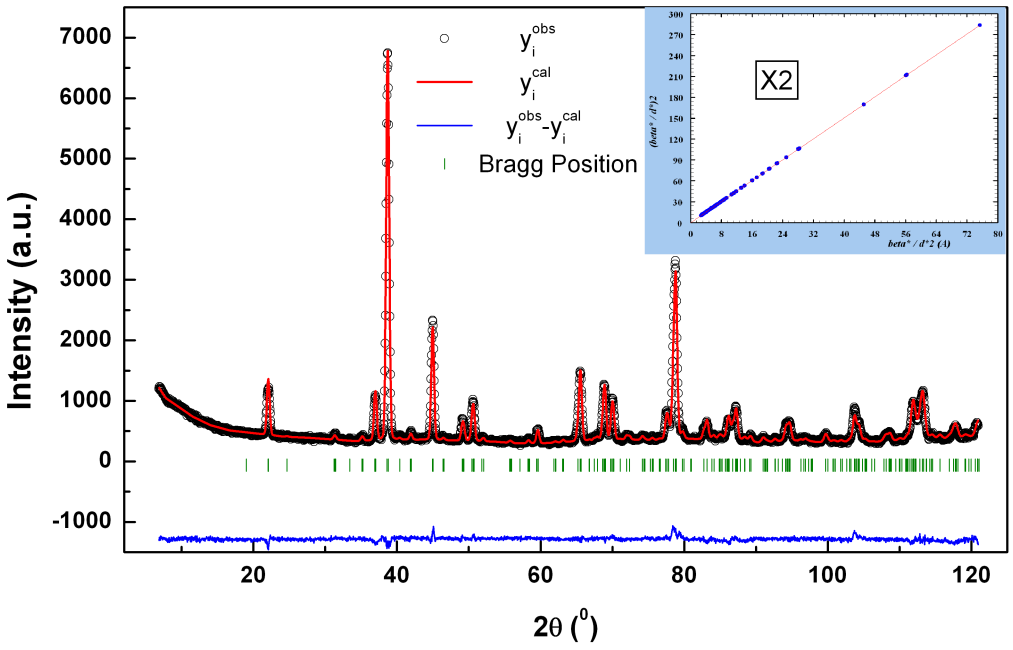

Figure 2.2: *Room temperature ND pattern for $x2$.*

not only the surface but also about the bulk of the sample. The intensity of neutron scattering varies quite irregularly with the atomic number, Z, of the scattering atom. Thus, neutrons can also distinguish in many cases elements differing by just one atomic number. Moreover, some light elements like hydrogen and carbon scatter neutrons more intensely than x-rays. Neutrons have a small magnetic moment. If the scattering atom also has a net

magnetic moment, the two interact and modify total scattering. In the case of magnetic materials (antiferromagnetic, ferrimagnetic and ferromagnetic) neutron diffraction can reveal both the magnitude and direction of the moments. Only neutron diffraction can furnish such information that is crucial to the studies of magnetic structures. Figures 2.2 - 2.4 depict the room temperature neutron diffraction patterns for the samples $x2$, $x3$ and $x5$ with the composition $La_{0.875}Ca_{0.125}MnO_{3.06}$, $La_{0.625}Ca_{0.375}MnO_{2.99}$ and $La_{0.375}Ca_{0.625}MnO_{2.94}$, respectively, recorded on powder diffractometer at Consortium for Scientific Research (CSR), Mumbai.

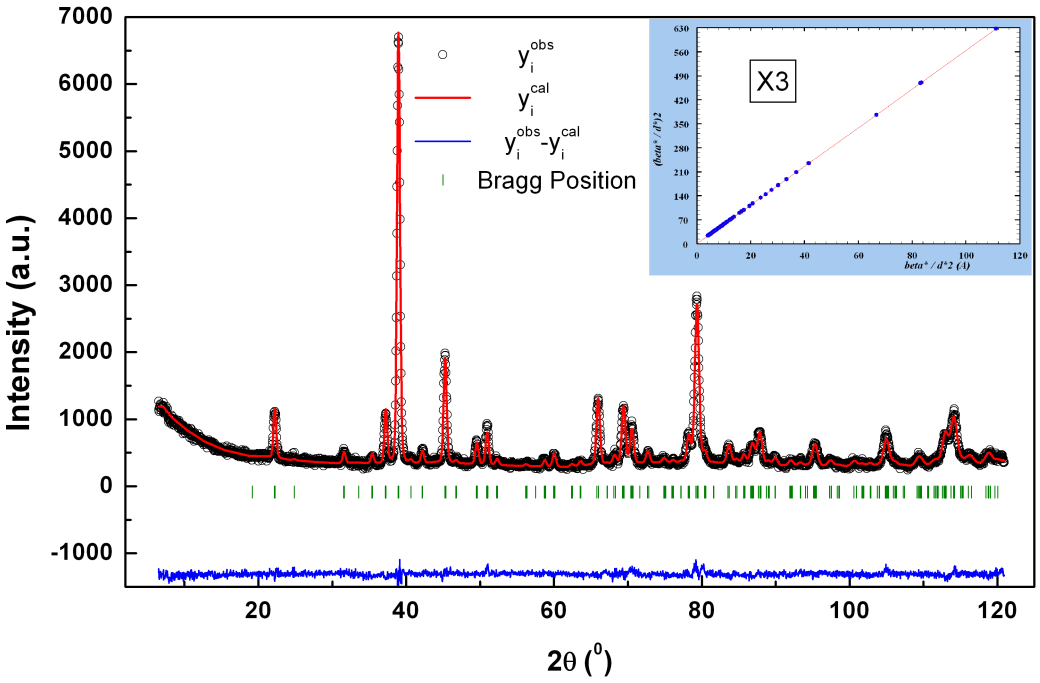

Figure 2.3: *Room temperature ND pattern for $x3$.*

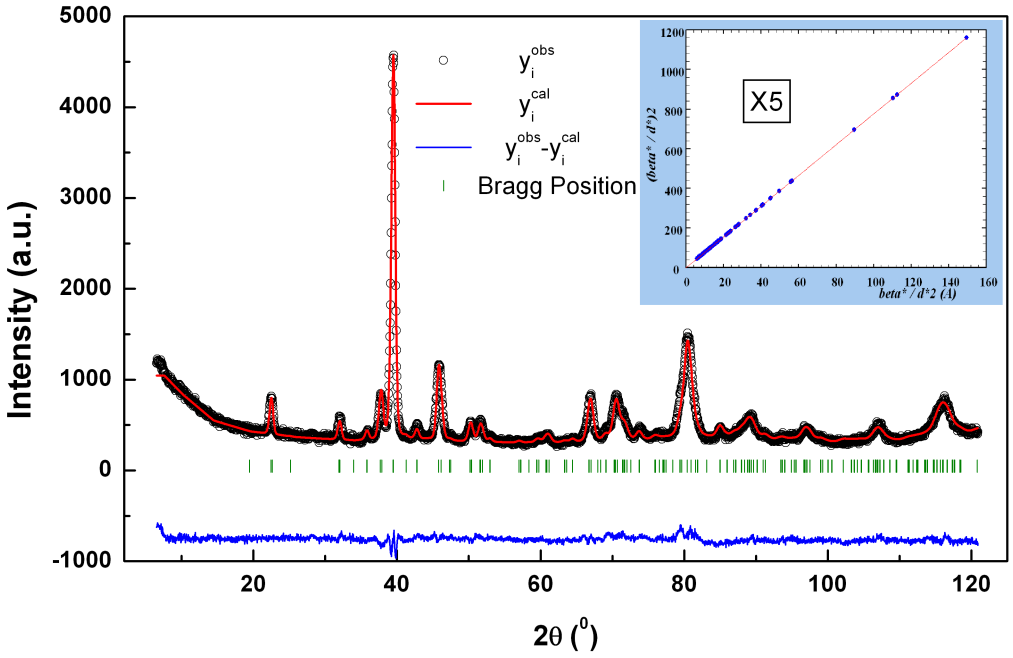

Figure 2.4: *Room temperature ND pattern for* $x5$.

The Rietveld method

The Rietveld method [4, 5] is a technique used to refine crystal structures from x-ray and neutron powder diffraction data. Due to the random orientation of crystallites in a polycrystalline sample, a large amount of overlap of independent Bragg peaks occur and information is lost, particularly in low symmetry materials. In a Rietveld refinement the individual reflections are not analysed. Instead, a curve fitting procedure is used over the entire pattern, where the observed intensity is described as:

$y_i = y_{i\ back} + \sum_i y_{i\ Bragg}^{(i)}$ where y_i and $y_{i\ back}$ is the observed and background intensity, respectively and $\sum_i y_{i\ Bragg}^{(i)}$ is the sum of the contributions of reflections close to the powder pattern step i. A mathematical expression that includes factors relating to both the crystal structure and other non-diffraction terms is used to calculate the contribution from reflections.

The difference between the observed and calculated profiles is minimised by least squares refinement and it is therefore very important to have a good structural starting model including space group, lattice parameters and atomic co-ordinates. The powder diffraction data must be in digitised form so that a numerical intensity value, y_i, is recorded at each of several thousand equal steps, i, in the pattern. In the least-squares refinement, a best fit to all of the y_i is sought simultaneously and the quantity minimised is the residual, S_y: $S_y = \sum w_i(y_i^{obs} - y_i^{calc})^2$ where $w_i = 1/y_i^{obs}$, y_i^{obs} is the observed intensity at the i^{th} step and y_i^{calc} is the calculated intensity of the i^{th} step.

At any randomly chosen point, i, in the pattern, there is generally a contribution from many Bragg peaks to the intensity, y_i^{obs}. The calculated intensity, y_i^{calc}, at the point i is therefore determined by summing the contributions from all the Bragg reflections, K, close to the step and it also includes a background intensity [6].

$y_i^{calc} = s \sum_K L_K |F_K|^2 \phi(2\theta_i - 2\theta_K) P_K A + y_i^{back})$

where s is the scale factor,

K stands for the Miller indices, $h\ k\ l$, for a Bragg reflection,

L_K contains the Lorentz, polarization and multiplicity factors,

ϕ is the reflection profile function,

P_K is the preferred orientation factor,

A is the absorption factor,

F_K is the structure factor for the Bragg reflection with Miller indices $h\ k\ l$,

y_i^{back} is the background intensity at the i^{th} step

The background intensity at the i^{th} step can be modelled by a linear interpolation between two background points, with the aid of a specified background function such a Chebychev polynomial [7] or by manually inserting a table of background intensities.

In Rietveld refinement, it is important to have accurate peak shape fitting as both the instrument and sample affects the shape and position of the Bragg peaks. For constant wavelength experiments the instrumental broadening is almost fully Gaussian and the Full Width at Half Maximum (FWHM) is given by:

$$\tau_K = Utan^2\theta_K + Vtan\theta_K + W$$

Where U, V and W are refinable parameters. A pseudo-Voight [8] function was used in the refinements of the x-ray diffraction data in this work. It takes into account both the instrumental (Gaussian, G) and sample (Lorentzian, L) broadening which is essential as high-resolution x-ray and neutron diffractometers have a narrow instrument profile and broadening due to sample defects becomes significant.

$$\phi(2\theta_i - 2\theta_K) = \eta L + (1-\eta)G$$

where η is a complex function which depends on the Full Width at Half Maximum for the Gaussian (Γ_{GK})and Lorentzian (Γ_{LK}) broadening of the K^{th} Bragg reflection:

$$\tau_{GK} = (Utan^2\theta_K + Vtan\theta_K + W + \frac{Z}{cos^2\theta_K})^{1/2}$$

$$\tau_{LK} = Xtan\theta_K + \frac{Y}{cos\theta_K}$$

Z is the Scherrer coefficient for Gaussian particle size broadening whilst X and Y model the Lorentizian strain and the Scherrer broadening respectively. The parameters that can be refined by the Rietveld method, in addition to those already mentioned include the cell parameters, the atomic coordinates, the temperature factors, site occupancies and intensity corrections. In the refinement process, the parameters are adjusted until S_y is minimised, i.e., when the best fit between the calculated and observed pattern is obtained. Having a starting model close to the correct one will prevent the system from diverging or reaching a false minimum. The goodness of fit of the least-square refinement and whether a true minimum has been achieved can be evaluated from the residual R-values.

$R_f = \frac{\sum\|(I_K^{obs})^{1/2} - (I_K^{calc})^{1/2}\|}{\sum(I_K^{obs})^{1/2}}$	R-Structure factor
$R_B = \frac{\sum\|(I_K^{obs}) - (I_K^{calc})\|}{\sum(I_K^{obs})}$	R-Bragg factor
$R_p = \frac{\sum(y_i^{obs} - y_i^{calc})^2}{\sum(y_i^{obs})}$	R-pattern
$R_{wp} = \| \frac{\sum w_i(y_i^{obs} - y_i^{calc})^2}{\sum w_i(y_i^{obs})^2} \|$	R-weighted pattern
$\chi^2 = \sum_i \frac{w_i(y_i^{obs} - y_i^{calc})^2}{N - p + C}$	Goodness of fit parameter

Where I_K^{obs} and I_K^{calc} are the observed and calculated intensities assigned

to the K^{th} Bragg reflection at the end of the refinement cycle and N, p and C are the number of observations, refined parameters and constraints, respectively. It should be noted that, besides having low residual R factors from the refinement, the refined model has to make sense both chemically and physically. Structural refinements were performed on LCMO series with the Fullprof program suite using *pnma* space group and fits are shown in Figs. 2.1-2.4. The relevant parameter valences are similar to those reported in the bulk [9–12] and are tabulated in table 2.1.

The average crystallite sizes were determined using Williamson-Hall plots [13], shown in the insets of the figures 2.1 - 2.4, which relate the mean coherent diffraction domains $[L(\mathring{A})]$ and the distribution of d spacings $[\Delta d/d]$ for a selected class of reflections through the equation:

$$\beta cos\theta = (K\lambda/L) + 4(\Delta d/d)\ sin\theta, \tag{2.2}$$

where β (FWHM) is expressed in radians, K is a shape factor close to unity, λ is the wavelength of the radiation used ($\lambda(ND) = 0.148\ nm$ and $\lambda(XRD) = 0.154\ nm$), L is the mean coherent diffraction domain size, and $\Delta d/d$ is the sample broadening factor due to the microstrains. This last term includes the effects of structural defects such as dislocations, stacking faults, microtwinings, and intergrowths. Isotropic apparent strains and size can also be estimated from a $(\beta*/d*)^2 = f(\beta*/(d*)^2)$ plot rather than from a Williamson-Hall plot ($beta* = f(d*)$) using fullprof package [14] as shown in insets of figures 2.2-2.4. The instrumental full width at half-maximum (FWHM) in the operating conditions was determined by recording a pattern for $Na_2Al_2Ca_3F_{14}$ (NAC) [15] which show the narrowest diffraction peaks with FWHM values approaching those theoretically calculated for this ultrahigh-resolution diffractometer [16]. The NAC FWHM values have

Table 2.1: *Structurral parameters for $x1$, $x2$, $x3$ and $x5$.*

Parameters	$x1$	$x2$	$x3$	$x5$
a ($\AA$)	5.4495(2)	5.4596(4)	5.4346(2)	5.3786(2)
b ($\AA$)	7.7430(1)	7.7273(5)	7.6763(4)	7.5501(1)
b ($\AA$)	5.4979(3)	5.4947(3)	5.4489(3)	5.3827(1)
(La/Ca)				
x	-0.0060(1)	-0.01420(1)	-0.018450(2)	-0.01410(2)
y	0.2500	0.25000	0.25000	0.25000
z	0.0022(6)	0.0017(2)	0.0027(3)	0.0013(3)
Mn				
(0,0,0)				
O1				
x	0.4781(2)	0.5067(5)	0.5102(1)	0.5084(1)
y	0.25000	0.25000	0.25000	0.25000
z	0.9580(3)	0.9360(4)	0.9356(1)	0.9405(4)
O2				
x	0.7499(3)	0.7312(3)	0.7267(3)	0.7303(1)
y	0.0375(1)	0.0321(2)	0.0309(4)	0.0330(5)
z	0.2287(3)	0.2674(4)	0.2762(2)	0.2772(1)
Mn-O(1) ($\AA$)	1.953(2)	1.9639(3)	1.9567(4)	1.9150(3)
Mn-O(2) ($\AA$)	2.0410(1)	1.9616(2)	1.9596(3)	1.9552(2)
Mn-O(2) ($\AA$)	1.8764	1.9530	1.9362	1.8986
Mn-O(1)-Mn (°)	162.25(1)	159.27(2)	159.03(2)	160.59(3)
Mn-O(2)-Mn (°)	164.71(2)	163.27(1)	162.03(3)	161.69(2)
χ^2	1.81	1.86	2.27	1.84
R_p	13.3	4.37	5.33	4.99
R_{wp}	17.8	5.98	6.87	6.27
R_B	5.66	9.69	6.69	11.4

been used to correct the measured peak widths of ND pattern yielding the sample FWHM data to be used in Eq.(2.2) resulting in average crystallite sizes of 27(5) nm, 18(3) nm and 13(5) nm for $x1/x2$, $x3$ and $x5$, respectively.

2.2.3 Scanning Electron Microscopy (SEM)

The primary limitations of SEM, as a general imaging and analytical technique, are the restrictions imposed on the samples by requiring a high vacuum sample environment. Samples have to be clean, dry, and electrically conductive. The Environmental SEM (ESEM) [17] permits one to vary the sample environment through a range of pressures, temperatures and gas compositions. It retains all the features of a conventional SEM, but removes the high vacuum constraint on the sample environment. Wet, oily, dirty, non-conductive samples may be examined in their natural state without modification or preparation. The ESEM offers a high resolution secondary electron imaging in a gaseous environment of practically any composition, at pressures as high as 50 $Torr$ and temperature as high as 1500^o C.

Description and working principle

A SEM consists of an electron column, that creates a beam of electrons; a sample chamber, where the electron beam interacts with the sample; detectors, that monitor a variety of signals emanating from the beam-sample interaction; and a viewing system that constructs images from the signal, as shown in Fig. 2.5.

An electron gun at the top of the column generates the electron beam. In the gun, an electrostatic field directs the electrons, emitted from a very small region on the surface of an electrode, through a small spot called crossover. The gun then accelerates the electrons down the column towards the sample with energies typically ranging from a few hundred to ten thousand volts and the generated electron beam has stable and sufficient current and the

smallest possible size. The electrons emerge from the gun as a divergent beam. A series of magnetic lenses and apertures in the column focus the beam into a demagnified image of the crossover. Bottom of the column has a set of scan coils which deflects the beam in a scanning pattern over the sample surface. The final lens focuses the beam into the smallest possible spot on the sample surface. The beam exits from the column into the sample chamber. The chamber incorporates a stage for manipulating the sample, a door or airlock for interacting and removing the sample. As the beam of electrons penetrates the sample, it gives up energy, which is emitted from the sample in a variety of ways. Each emission mode is potentially in a signal form which creates an image.

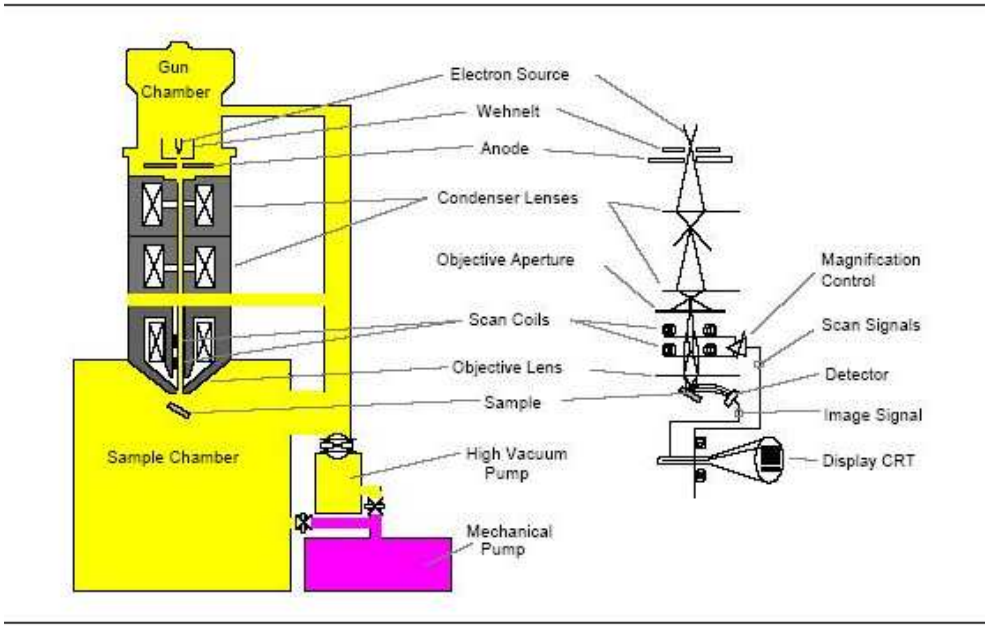

Figure 2.5: *Schematic of the scanning electron microscope*

Imaging principle

SEM uses a simple imaging device based on a Cathode Ray Tube (CRT). A CRT consists of a vacuum tube covered at one end (the viewing surface) with light emitting phosphor, and at the other end, an electron gun and a set of deflection coils. The CRT gun forms a beam of electrons and accelerates it towards the phosphor screen. The deflection scans the beam in a raster pattern over the display surface. The phosphor converts the energy of the incident electrons into visible light. The intensity of the light depends on the current in the CRT electron beam. By synchronizing the CRT scan in the SEM with the scan modulating the CRT beam current with the imaging signal, the system maps the signal point onto the viewing surface of the CRT, thus creating the image.

Indeed, not all specimens can be analyzed by SEM directly. One typical example is an insulating material. For specimen with poor electrical conductivity, a negative charge builds up gradually from bombardment by the high-energy electron beam. An abnormal contrast and splitting of the image result from the uneven distribution of the negative charge on the sample. A simple solution is to coat a very thin (generally 10 - 20 nm thick) gold layer on the sample's surface. It can enhance the emission of secondary and backscattered electron, reduction of thermal damages as well as the elimination of charge accumulating effect.

The grain size and surface morphology of the LCMO series were investigated by scanning electron microscopy (SEM). The SEM micrographs were recorded at room temperature on the same pellet pieces of $x1$, $x2$, $x3$ and $x5$ samples that were used for the physical property measurement. The

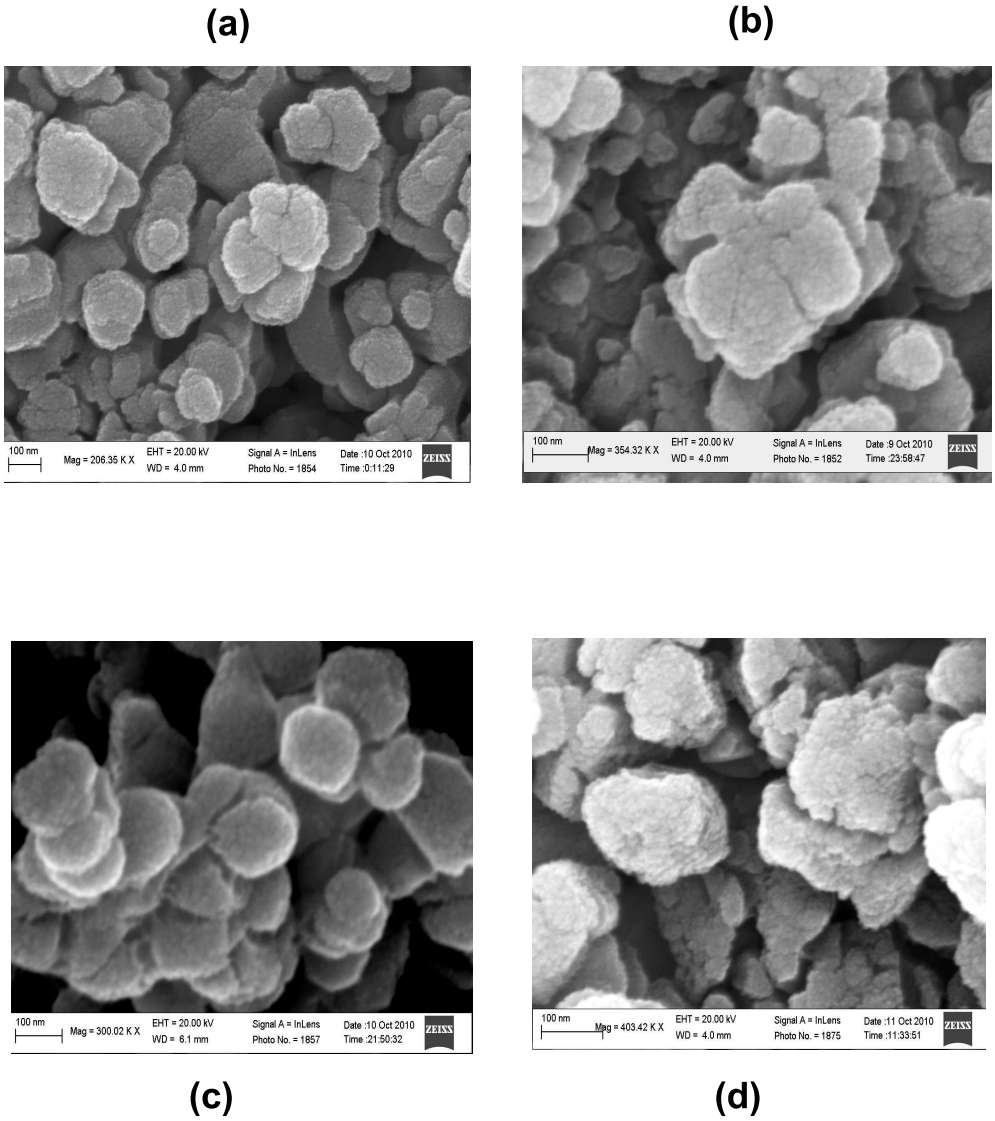

Figure 2.6: *The room temperature SEM micrograph for (a) $x1$, (b) $x2$, (c) $x3$ and (d) $x5$.*

variation in composition causes significant orphological changes. The SEM micrographs for the LCMO samples, shown in Fig.2.6, consist of closely packed aggregated grains of typical sizes $100 - 150\ nm$, which are composed of finer crystallites. When the Ca content is increased, the grain size decreases.

2.3 Compositional analysis

2.3.1 Energy Dispersive Absorption of x-rays (EDAX)

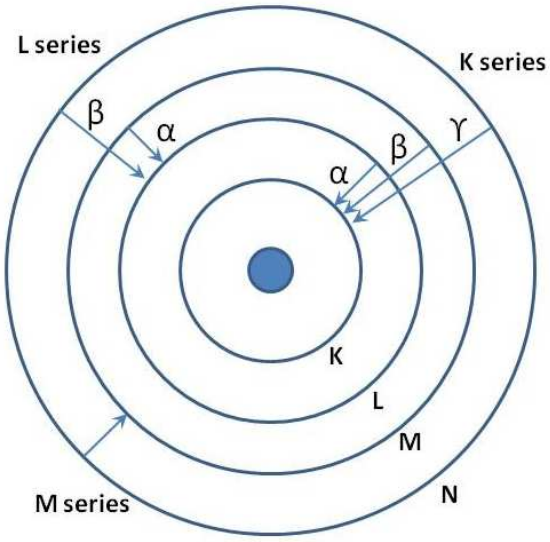

Figure 2.7: *Elements in an EDX spectrum are identified based on the energy content of the x-rays emitted by their electrons as they (electrons) make transitions from a higher-energy shell to a lower-energy one*

Energy Dispersive Absorption of x-rays (EDAX) or Energy Dispersive x-ray analysis (EDX) is a method used to determine the energy spectrum of

x-ray radiation emitted by a sample. It is a technique used for identifying the elemental composition of the specimen in an area of interest thereof. The EDAX attachment works as an integrated feature of a scanning electron microscope (SEM), and cannot operate, on its own, without the SEM.

During EDAX analysis, the specimen is bombarded with an electron beam inside the scanning electron microscope. The bombarding electrons collide with the electrons of the atoms constituting the specimen, knocking some of them off in the process. A position vacated by an ejected inner shell electron is eventually occupied by a higher-energy electron from an outer shell. To be able to do so, however, the transferring outer electron must give up some of its energy by emitting x-rays of energy equal to the energy difference between the outer and inner shells. The amount of energy released by the transferring electron thus depends on which shell it is transferring from, as well as on which shell it is transferring to. Furthermore, the atom of every element releases x-rays with unique amounts of energy during the transferring process. Thus, by measuring the x-ray energy spectrum emitted by a specimen during electron beam bombardment, the identity of the atoms from which the x-rays are emitted can be established. Therefore, the output of an EDAX analysis is an EDAX spectrum. The EDAX spectrum is just a plot of how frequently x-rays of some given energy are received by the detector. An EDAX spectrum normally displays peaks corresponding to the energy levels from which the most x-rays had been received. Each of these peaks is unique to an atom, and therefore, corresponds to a single element. The higher the intensity of a peak in a spectrum, the more the concentration of the element in the specimen.

An EDAX spectrum plot not only identifies the element corresponding

to each of its peaks, but the type of x-rays to which it corresponds as well. For example, a peak corresponding to the amount of energy possessed by x-rays emitted by an electron in the L-shell when it makes a transition to the K-shell is identified as a K_α peak. The peak corresponding to x-rays emitted by M-shell electrons when it falls into the K-shell is identified as a K_β peak, as shown in figure 2.7. The EDAX measurements were carried out using *Carl Zeiss Smarts SEM* Field Emission SEM up to 20 KV bias voltage over a $\sim 30 \times 30$ μm area at a number of regions. The EDAX spectra measured over many areas like the ones shown in figure 2.6 confirms the presence of La, Ca, Mn and O as main elements and no undesired composition/element was detected. The spatial homogeneity of these elements was found to be reasonably good across different locations in the sample.

2.3.2 Estimation of oxygen off-stoichiometry, δ

Titrimetric analysis, a quantitative (volumetric) chemical analysis in which one measures the volume of the titrant (standard solution) required to react with a measured volume of the titrand (unknown). The concentration of titrand is then determined using the principles of equivalence (Conc. A $\times$Vol. A = Conc. B $\times$Vol. B) and this method is capable of high precision (1 part in 1000) [18]. In *iodometric* titration, titrations involving iodine, the iodine liberated in a chemical reaction is titrated with sodium thiosulfate ($Na_2S_2O_3$) solution. $Na_2S_2O_3$ solution is not stable for long period of time and hence, it is standardized with an oxidizing agent like Potassium dichromate, $Kr_2Cr_2O_7$, solution of known normality, prior to the titration experiment.

A weighed amount of $La_{1-x}Ca_xMnO_{3\pm\delta}$ powders was dissolved in a stirred mixture of 10 ml of a 10 mass % KI aqueous solution and 2.5 ml 2 M HCl [19]. Chlorine is produced by the reactions

$$2Mn^{III} + 2Cl^- \rightarrow Cl_2 + 2Mn^{II} \tag{2.3}$$

$$Mn^{IV} + 2Cl^- \rightarrow Cl_2 + Mn^{II} \tag{2.4}$$

The *in situ* generated chlorine reacts with the iodide and iodine is formed:

$$Cl_2 + 2I^- \rightarrow 2Cl^- + I_2 \tag{2.5}$$

This iodine is titrated with a standard volumetric solution of sodium thiosulfate (0.0202 N) until a clear and colorless solution is obtained. When the end-point is approached, few drops of 1 mass % starch solution (indicator) are added in order to observe the colour change better.

$$2S_2O_3^{2-} + I_2 \rightarrow 2I^- + S_4O_6^{2-} \tag{2.6}$$

The lanthanum calcium manganite, with $Mn(III/IV)$, $La^{III}_{1-x}Ca^{II}_x Mn^{III}_{1-\alpha}Mn^{IV}_\alpha O_{3\pm\delta}$, yields Mn^{IV} concentration, α, from the titration results as:

$$\alpha = \frac{m - (M - 8x)NV}{8NV - m} \tag{2.7}$$

where m and M are the mass and molecular weight of the LCMO sample while N, V are the normality, added volume of the $S_2O_3^{2-}$ standard volumetric solution and x is the *nominal* concentration of Mn^{IV}. Thus, the oxygen off-stoichiometry is estimated using the relation $\delta = (\alpha - x)/2$. The oxygen off-stoichiometry, δ, assuming the compound formula $La_{1-x}Ca_xMnO_{3+\delta}$, estimated using iodometry titration, for 5 trials, was 0.003(2), 0.06(2), -0.01(1) and -0.06(3) for the samples $x1$, $x2$ with $x = 0.125$, $x3$ with $x = 0.375$ and $x5$ with $x = 0.625$, respectively.

2.4 Physical Property Measurement

2.4.1 Magnetic Property Measurement System SQUID VSM

MPMS SQUID VSM is a SQUID magnetometer based on the 2ω detection technique that makes use of the SQUID and VSM techniques in combination. It can measure DC and ac magnetization (down to $\sim 10^{-9}$ emu) in the temperature range 1.8 K to 400 K with a maximum temperature sweep rate of 50 K/min and fields up to ± 7 T with a maximum field ramp rate of 700 Oe/sec. Superconducting Quantum Interference Device (SQUID) is

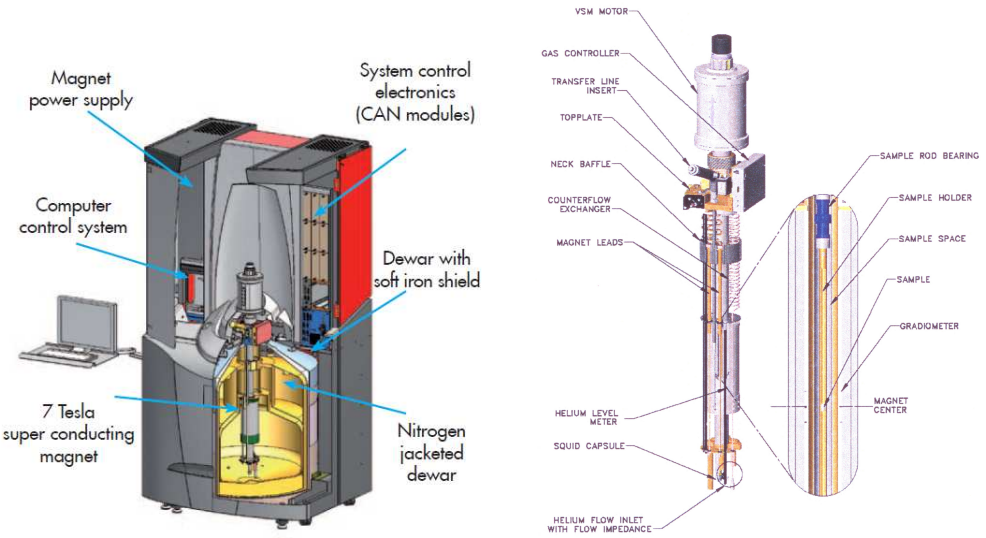

Figure 2.8: *Cross-sectional view of MPMS VSM SQUID along with (right panel) magnified view of VSM head, magnet and Sample rod assembly.*

an extremely sensitive flux-to-voltage transducer that converts a change in magnetic flux to change in voltage, which is readily detectable with conventional electronics. It is a device which makes use of flux quantization and

Josephson tunneling and can operate at temperatures as low as few Kelvin. The sensitivity of a Josephson junction to applied magnetic field increases with the area of the junction, which justifies making the devices large so that the control currents can be reduced to a minimum. The switching speed of the junction, however, decreases as the area increases. In recent devices, the conflicting demands of speed and sensitivity are met by replacing a single junction with two or more junctions connected by a continuous superconducting loop. Such a multi-junction device is called a Josephson interferometer or a Superconducting Quantum Interference Device (SQUID). In the case of two Josephson junctions connected in parallel, as the magnetic flux Φ threading a superconducting loop is changed, the critical current of two junctions oscillates with a period equal to the flux quantum Φ_0. These oscillations arise due to the interference of macroscopic wave functions at two junctions. This phenomenon of superconductiing quantum interference forms the basis of a SQUID. The superconducting detection coils are configured as a second-order gradiometer, with counterwound outer loops which make the set of coils non-responsive to uniform magnetic fields and linear magnetic field gradients. The detection coils only generate a current in response to local magnetic field disturbances. The current in the detection coils is a function of sample position (see Fig. 2.9) and it is inductively coupled to the instrument's SQUID. The SQUID feedback nulls the current in the detection coils and this nulling current yields the actual SQUID voltage for analysis. The sample is set to vibrate at a frequency, ω, about the center of the detection coils, where the signal peaks as a function of sample position, z. $V(z) = Az^2$ for small vibration amplitude, B and $z(t) = Bsin(\omega t)$,

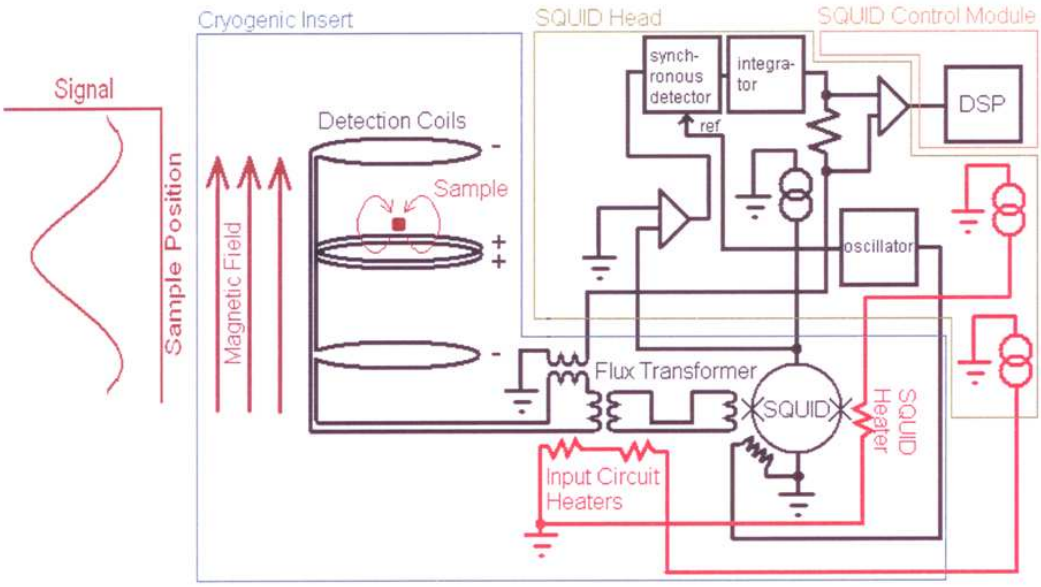

Figure 2.9: *SQUID detection system in a simplified diagram.*

it generates a SQUID signal, V, as a function of time, t

$$V(t) = \frac{AB^2}{2}(1 - cos(2\omega t)) \tag{2.8}$$

where A is a scaling factor related to the magnetic moment of the sample. The lock-in technique is used to isolate and quantify the signal occurring at frequency 2ω, which is caused extensively by the sample. Briefly, this is achieved by multiplying the measured signal with a phase corrected reference signal at 2ω and then extracting the DC component, which is proportional to the 2ω component of the measured signal. This technique quickly and precisely isolates the sample signal from other noise sources, including drifting SQUID signal and mechanical noise sources synchronized to the sample. To locate the sample position in the detection coil, sample signal for various vertical sample positions are obtained and compared with the

response of a point dipole in a uniform magnetic field.

2.4.2 Physical Property Measurement System (PPMS)

The Physical Property Measurement System (PPMS) [20] provides a flexible, automated workstation that can perform a variety of experiments requiring precise thermal control. PPMS can be used to perform magnetomerty (AC susceptibility and DC magnetization), heat capacity, electrotransport (ac and dc resistivity, magnetoresistance, Hall effect and I-V characteristics) and thermal transport (Thermal conductivity, Seebeck coefficient and Thermoelectric figure of merit) measurements, or can be modified to perform the user-select experiment.

The PPMS has extremely good temperature control over the entire range of 1.8 $K \leq T \leq 350$ K. This system possesses a superconducting magnet which can generate fields up to ± 9 Tesla, with a high field-homogeneity (0.01%) within the measuring region. The MultiVu software also provides options for sweeping the magnetic field in several modes, the most important of which are *linear* and *no-overshoot*. In the linear mode, the field is ramped linearly to the set-point, while in the *no-overshoot* mode, the field is quickly ramped to $\sim$ 70 % of the desired value, then slowly increased to avoid overshooting the set-point. The PPMS platform can apply a constant field during both AC and DC measurements.

AC Measurements System (ACMS) Option

ACMS option is a versatile DC magnetometer and AC susceptometer. The ACMS [21] insert houses the drive and detection coils, thermometer and

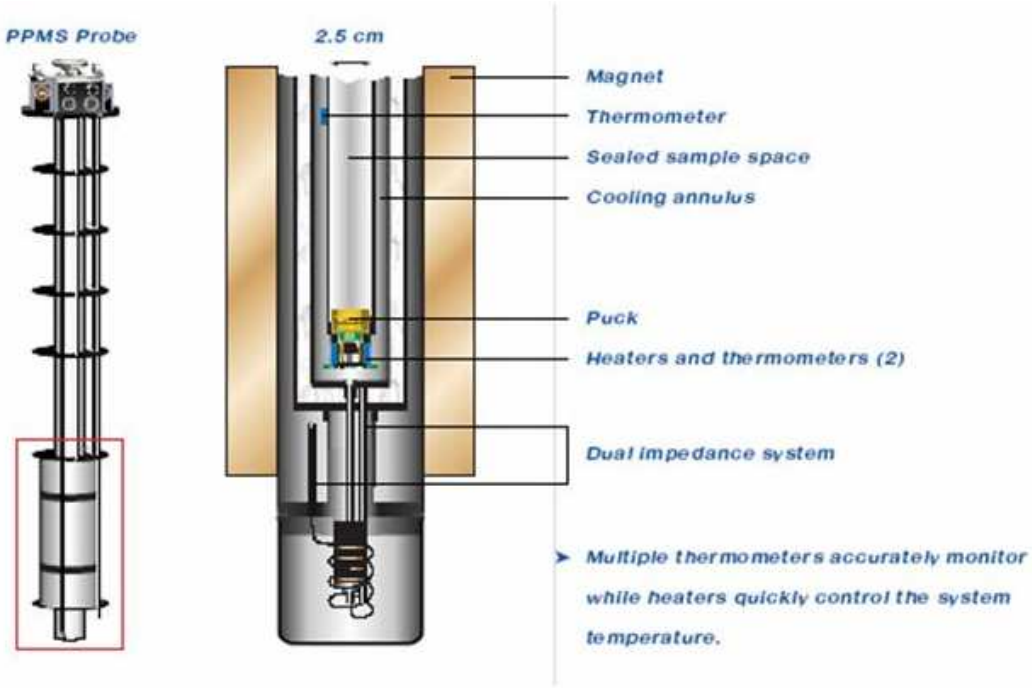

Figure 2.10: *Sample rod assemble for PPMS.*

electrical connections for the ACMS system. The insert fits directly in the PPMS sample chamber and contains a sample space that lies within the uniform magnetic field region of the host PPMS, so DC field and temperature control can be performed with conventional PPMS methods. The sample is held with the insert's coil-set on the end of a thin rigid sample rod. The sample holder is translated longitudinally by a DC servo-motor located in the ACMS sample transport assembly which provides rapid and very smooth longitudinal sample motion. The ACMS sample transport mounts on top of the PPMS probe.

AC susceptibility

The ACMS contains an AC-drive coil set that provides an alternating excitation field and a detection coil-set that inductively responds to the combined sample moment and excitation field. The copper drive and detection coils are situated within the ACMS inserts, concentric with the superconducting DC magnet of the PPMS (Fig. 2.10). The drive coil is wound longitudinally around the detection coil set. The detection coils are arranged in a first-order gradiometer configuration so as to isolate the sample signal from uniform background sources. This configuration utilizes two sets of counter wound copper coils connected in series and separated by several centimeters. A compensation coil is situated outside the AC drive coil. The drive coil and compensation coil are counterwound and connected in series so that they receive same excitation signal. A net field remains within the measurement region, but outside the measurement region the fields from the two coils tend to cancel. Each detection coil also contains a low-inductance calibration coil. The two single-turn calibration coils are connected in series and are situated at the center of each detection coil. During an ac susceptibility measurement, an alternating magnetic field (up to ± 10 Oe in a frequency range of 10 Hz to 10 kHz) is applied to the measurement region by exciting the drive and compensation coils. The sample undergoes a five-point measurement process that utilizes the calibration coil to increase measurement accuracy. The first three readings are made with sample positioned in the center of the bottom, then in the top and again in the bottom detection coils. The signal from the detection coil array amplified, low-pass filtered, digitized and stored as waveform blocks in the data buffer. The points are fitted and compared to the driving signal to determine the real and imag-

inary components of the response. Two more readings are taken with the sample placed at the center of the detection coil array by switching the calibration coil into the detection circuit with opposing polarities. The real and imaginary components of each response waveform are obtained and it is subtracted to obtain the sample signal as ac susceptibility in real and imaginary components.

DC magnetometry

During DC measurements, a constant field is applied to the measurement region and the sample is moved quickly through both sets of coils, inducing a signal in them according to Faraday's Law. This measurement method is commonly called the *extraction* method. The amplitude of the detection signal depends on both the extraction speed and the sample magnetic moment. The DC servo-motor used by the ACMS extracts samples at speeds of approximately 100 cm/sec., thus increasing the signal strength over conventional DC extraction systems and reducing the contribution of time-dependent errors such as drift and 1/f noise. The short scan time also allows the averaging of several scans for each measurement, further reducing the contributions of random error. These advantages result in a greater accuracy and sensitivity compared to systems with slower sample extraction speeds. A Digital Signal Processor (DSP) is used to analyze the signal and determine the sample magnetic moment.

Centering the sample

Knowing the sample location with respect to the detection coil assembly is important to determine the proper range of motion for DC magnetization measurements and the correct sample position relative to the detection coils for AC susceptibility measurements. As long as the sample is mounted relative to the detection coils (approximately 10.5 ± 0.8 cm from the end of the long sample rod on the ACMS sample holder), the ACMS determines the position of the sample within the detection coil by obtaining the sample signal as a function of Z and automatically center it by adjusting the sample position relative to servo motor zero. There is about $8-mm$ window within which the magnetic center of the sample must lie in order to allow automatic centering. If the sample is not properly centered, it is difficult for the ACMS to determine its true magnetic moment.

VSM option

VSM option for PPMS is a fast and sensitive DC magnetometer consisting of a VSM linear motor transport head. To locate the sample and for vibrating it, a compact gradiometer pickup coil for detection and the electronics for driving the linear motor transport and detecting the response from the pick up coils are used. With relatively large oscillation amplitude (1-3 mm peak) and a frequency of 40 Hz, the system can resolve magnetization changes less than 10^{-6} emu at a data sampling rate of 1 Hz. When the sample is set to vibrate sinusoidally, the changing magnetic flux induces a time-dependent

voltage in the pickup coil,

$$V_{coil} = \frac{d\Phi}{dt} = \left(\frac{d\Phi}{dz}\right)\left(\frac{dz}{dt}\right)$$

$$= 2\pi f C m A \; sin(2\pi f t) \tag{2.9}$$

where Φ is the flux enclosed by the pickup coil, z is the vertical position of the sample with respect to the coil, t is time, C is the coupling constant, m is the DC magnetic moment of the sample, A is the amplitude and f is the frequency of oscillation. The response from the pickup coil is calibrated with a standard sample. After obtaining the signal profile in the pickup coil, the system identifies the sample position with respect to the pickup coil and locates the sample at the center of the coil after the touch-down process. If the measurement is a temperature dependent one, the sample position may change due to the thermal expansion/contraction of the sample rod. Hence the sample position in the pickup coil has to be monitored by touching the sample rod down and relocate it to the actual position, if it has changed.

Resistivity option

Resistivity option is a configurable resistance bridge board. It can simultaneously measure resistance/resistivity of 3 samples using four probe method with current reversal option. A resistivity puck with three samples mounted for four probe measurement is shown in figure 2.11. The user bridge board automatically adjusts the excitation current of its active channels, but the maximum allowable current, power and voltage can be specified. The current, power and voltage limits are $\pm 0.01 - 5 \; mA$, $0.001 - 1 \; mW$ and $1 - 95 \; mV$, respectively. The nominal resolution in the most sensitive

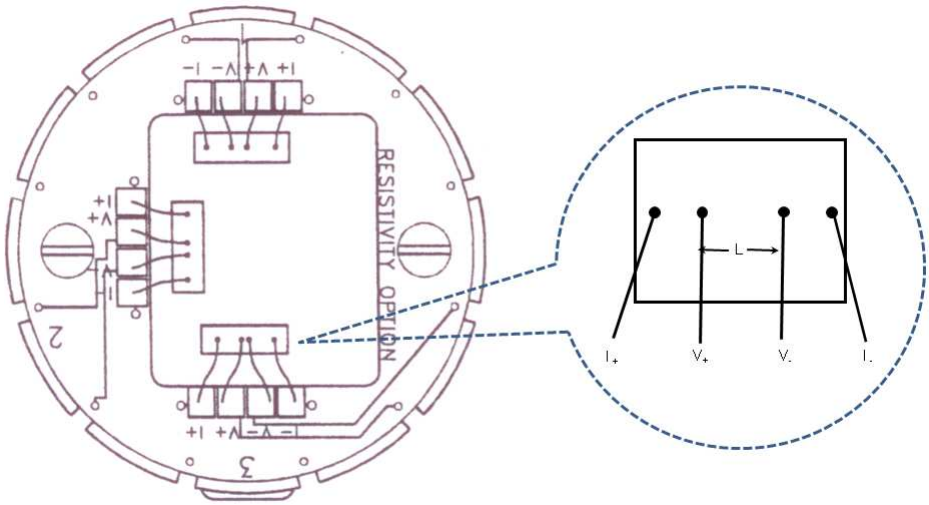

Figure 2.11: *The resistivity sample puck with three samples mounted for four-wire resistance measurements.*

range is 3.8 $nV/5\ mA = 0.76\ \mu\Omega$.

2.4.3 Field correction

The superconducting magnet used in SQUID (PPMS) VSM [22, 23] is capable of generating fields up to 70 (90) kOe with the value determined to a very high degree of accuracy over most of this range. The magnetic field value reported in the system is based only on the current flowing through the superconducting magnet coil supplied by the magnet power supply. At low fields (less than 10 kOe), the magnetic field experienced by the sample can deviate significantly from the reported magnetic field. The magnitude of this field error can be as large as 50 G in SQUID VSM magnets. The two important factors that lead to discrepancy in actual and reported fields in low field region are: (a) Magnet remanence: At sufficiently large magnetic

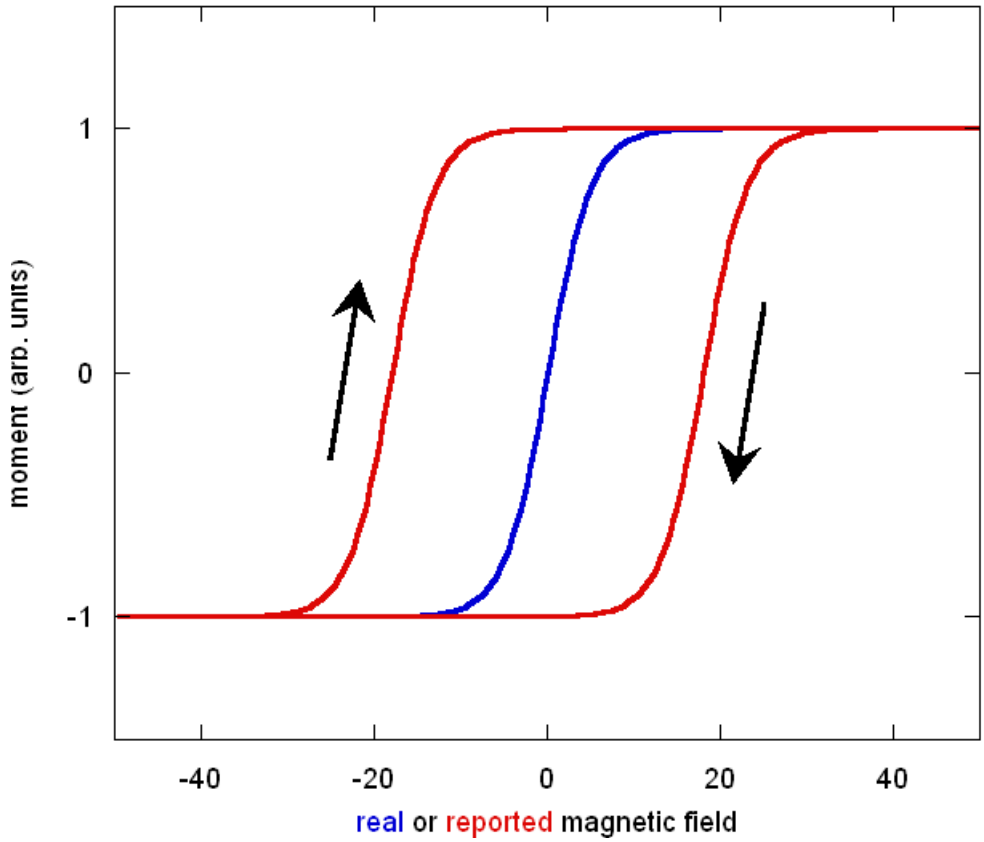

Figure 2.12: *The magnetic hysteresis loop expected (blue) and measured (red) for a paramagnetic sample due to remanence of superconducting magnet.*

fields $\gtrsim$ 10 kOe, alloys used in the windings of superconducting magnets permit the magnet field to enter the superconducting material as threads of quantized magnetic flux and these flux lines get pinned at defects in the material. When the magnetic field is removed (i.e., when the magnet current is set back to zero from a high value), some of these pinned flux lines remain behind resulting in a small trapped magnetic field at the sample location. (b) Flux creep and escape: over a period of time, some of these pinned magnetic flux lines redistribute and may even leave the wire material

altogether. The term flux creep describes the diffusion of flux lines inside a superconductor. At a stable magnetic field, escape of flux from the interior of the wire can lead to induced currents in the magnet due to the topology of the superconducting magnet.

The effect of magnet remanence at low fields is an offset error in the reported magnetic field. This offset is dependent on the magnet history and is always opposite to applied field giving rise to inverted hysteresis, as is evident in figure 2.12. This behaviour is expected when the sample, under the measurement protocol, has coercive field less than field error value. The field error, ΔH, is computed as

$$\Delta H = H_a - H_{Rep} \tag{2.10}$$

where H_a is the actual magnetic field experienced by the sample and H_{Rep} is the field reported by the system (set by user in the measurement sequence). The field error at various fields and temperatures was computed using the magnetic standards like Pd, Dy_2O_3 and $Er : YAG$ provided by the Quantum design and this field error variation is temperature-independent. A typical field error variation computed for Pd standard at room temperature for both PPMS-VSM and SQUID-VSM is shown in figure 2.13. The field error is more in SQUID than in PPMS because SQUID uses hybrid superconducting magnets.

The remanence properties of the superconducting magnet are history dependent and is unique to the system. They are very reproducible as long as the same field charging/discharging protocol is followed each time and once the field error table is determined by using a standard sample, one can run the same field sequence on samples of interest and apply this field

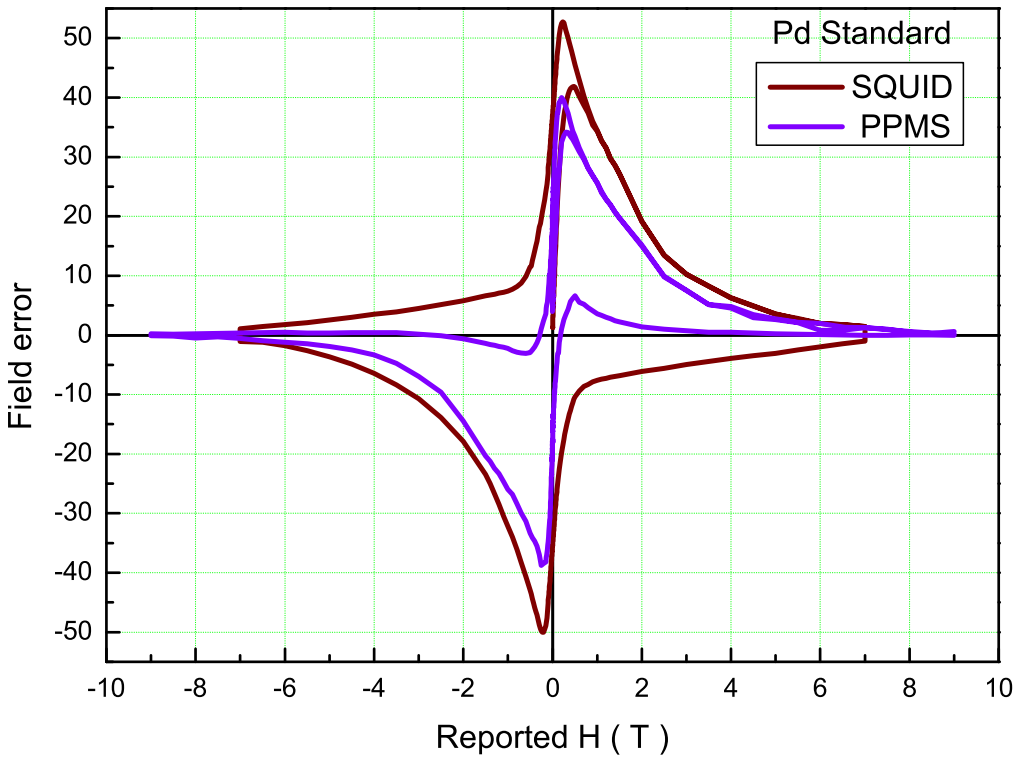

Figure 2.13: *The estimated field error on the PPMS and SQUID systems used for measuring $M-H$ loops using Pd standard at room temperature.*

correction.

The magnitude of the remanence in the magnet can typically be reduced down to $1-2$ G by setting the field to zero (from an initial field above 10 kOe) in the oscillate mode. This mode also attentuates the flux creep effects. Remanence can be further reduced down to < 0.05 gauss by using the Ultra Low Field option which employs a fluxgate magnetometer and the modulation coil in the magnet to compensate trapped flux from the magnet.

References

1. M.P. Pechini, *Method of preparing lead and alkaline earth titanates and niobates and coating method using the same to form a capacitor.* US Patent 3330697 (1967)

2. *Sol-Gel Processing*, Volume 1, Ed. Hiromitsu Kozuka of *Handbook of Sol-Gel Science and Technology: Processing, Characterization and Applications* edited by Sumio Sakka, Kluwer Academic Publishers.

3. B. D. Cullity, *Elements of X-ray diffraction*, second edi. Addsion-Wesely company, (1978).

4. H.M. Rietveld, *Line Profiles of Neutron Powder-diffraction Peaks for Structure Refinement*, Acta Cryst., **22**, 151 (1967).

5. H.M. Rietveld, *A Profile Refinement Method for Nuclear and Magnetic Structures*, J. Appl. Cryst., **2**, 65 (1969).

6. R.A. Young, *The Rietveld Method*; Oxford University Press: Oxford, 1995.

7. A.C. Larson and R.B.V. Dreele, General Structureal Analysis System (GSAS); Los Alamos National Laboratory: Los Alamos, 1990.

8. P. Thompson, D.E. Cox and J.B. Hastings, *Rietveld refinement of Debye-Scherrer synchrotron X-ray data from* Al_2O_3, J. Appl. Cryst., **20**, 79 (1987).

9. E. Bose, S. Karmakar, B. K. Chaudhuri, S. Pal, C. Martin, S. Hébert and A. Maignan, *Correlation of structural, magnetic and transport*

properties with the tolerance factor in a low-doped $La_{0.875}Ca_{0.125-x}Sr_xMnO_3$, *(*$0 \leq x \leq 0.125$*) system: cross-over from Mott to Shklovskii-Efros variable range hopping conduction*, J. Phys.: Condens. Matter **19**, 266218 (2007).

10. J. A. Collado, C. Frontera, J. L. García-Muñoz, C. Ritter, M. Brunelli and M. A. G. Aranda, *Room Temperature Structural and Microstructural Study for the Magneto-Conducting* $La_{5/8-x}Pr_xM_{3/8}MnO_3$ *(*$0 \leq x \leq 5/8$*) series*, Chem. Mater. **15**, 167 (2003).

11. P. R. Sagdeo, Shahid Anwar and N. P. Lalla, *Powder X-ray diffraction and Rietveld analysis of* $La_{1-x}Ca_xMnO_3$ *(*$0 < X < 1$*)*, Powder Diffr. **21**, 40 (2006).

12. M. Pissas and G. Kallias, *Phase diagram of the* $La_{1-x}Ca_xMnO_3$ *compound (* $0.5 \leq x \leq 0.9$*)*, Phys. Rev. B **68**, 134414 (2003).

13. G. K. Williamson and W. H. Hall, *X-ray line broadening from filed Aluminium and Wolfram*, Acta Metall. **1**, 22 (1953).

14. J. Rodriguez-Carvajal: FULLPROF, Ver. 3.1 d-LLB-JRC, ILL, France (1998) and can be downloaded from http://www.ill.eu/sites/fullprof/.

15. G. Courbion and G. J. Ferey, $Na_2Ca_3Al_2F_{14}$*: A new example of a structure with "independent* F^-*"A new method of comparison between fluorides and oxides of different formula*, Solid State Chem. **76**, 426 (1988).

16. O. Masson, E. Dooryhee, R. W. Cheary and A. N. Fitch, *Instrumental resolution function of the ESRF powder diffraction beamline BM16*, Mater. Sci. Forum **378-381**, 300 (2001).

17. *Environmental Scanning Electron Microscopy*, second ed. Philips Electron Optics, Eindhoven, The Netherlands (1996).

18. A. I. Vogel, *A textbook of Quantitaive Inorganic Analysis including Elementary Instrumental Analysis*, Longman, London, 4^{th} Ed., 1978.

19. C. Vázquez-Vázquez, M. C. Blanco, M. A. López-Quintela, R. D. Sánchez, J. Rivas and S. B. Oseroff, *Characterization of* $La_{0.67}Ca_{0.33}MnO_{3\pm\delta}$ *particles prepared by the solgel route*, J. Mater. Chem., **8**, 991 (1994).

20. Physical Property Measurements System (PPMS), User's Manual, Quantum Design, San Diego, CA, USA, **1084-100A**, (2009).

21. Magnetic Property Measurements System (MPMS XL), User's Manual, Quantum Design, San Diego, CA, USA, **1014-110A**, (2010).

22. *Using SQUID VSM Superconducting Magnets at Low Fields, Quantum Design Application Note* ***1500-011****, 1 (2010).*

23. Using PPMS VSM Superconducting Magnets at Low Fields, Quantum Design Application Note ***1070-207****, 1 (2010).*

Chapter 3

Nonlinear susceptibilities for a ferromagnet of arbitrary spin

The experimental signatures of the nonlinear magnetic susceptibilities across the ferromagnetic (FM)-paramagnetic (PM) phase transition are established in this chapter from the mean-field calculation of nonlinear susceptibilities for a ferromagnet of arbitrary spin. The intrinsic linear and nonlinear magnetic susceptibilities, χ_n, are shown to diverge in the asymptotic critical region (ACR) with the exponent $\gamma_n = n\gamma + (n-1)\beta$ and $n = 1, 2, \cdots$. This behaviour of χ_n in the ACR is consistent with the magnetic scaling equation of state. With increasing spin, the divergence in $\chi_n(T)$, as the FM-PM phase transition temperature, T_C, is approached from below or above, progressively slows down with the result that the width of the ACR increases. For a given spin, higher the order of nonlinear susceptibility, narrower the ACR. These results are in qualitative agreement with the critical behaviour of $\chi_n(T)$ observed in an archetypal ferromagnet.

3.1 Introduction

Over the years, nonlinear magnetic susceptibility, χ_n $(n = 2, 3, ...)$, has emerged as a powerful experimental tool to unambiguously distinguish between different types of magnetic order. This is so because the theory [1–3] predicts distinctly different behaviour of χ_n in the critical region for spin glasses, ferromagnets and antiferromagnets, and these predictions have been clearly borne out by experiments [4–19]. These characteristic features of χ_3, which serve as unambiguous experimental signatures for different kinds of magnetic order, are as follows. In spin glasses, χ_3 is *negative* at all temperatures and diverges on both sides of the spin-glass freezing temperature. By contrast, in ferromagnets, χ_3 is *positive* for temperatures below the Curie temperature T_C, *changes sign* at $T = T_C$ and diverges on both sides of T_C. On the other hand, in antiferromagnets, χ_3 is positive for temperatures below the Néel temperature T_N, has a discontinuity at $T = T_N$ and drops to positive (negative) values for $T \geq T_N$ when the coordination number $z \leq 6$ $(z \geq 7)$. Most of these theoretical models use the mean-field approximation.

So far as the ferromagnets are concerned, only the nonlinear susceptibilities up to second order (i.e., χ_3) have been addressed theoretically and such calculations are confined to $S = 1/2$ ferromagnets [2, 3, 7, 11] alone. It is well known that $S = 1/2$ ferromagnets are rarely encountered in practice. Thus, it is imperative to extend the mean-field (MF) calculations to nonlinear susceptibilities beyond the second order and ascertain the critical behaviour of the linear and nonlinear susceptibilities in ferromagnets with spin other than $S = 1/2$. To this end, the analytical expressions for linear and nonlinear magnetic susceptibilities in the critical region for a fer-

romagnet with arbitrary spin, based on the MF theory, are derived by the derivative as well as expansion methods and their behaviour across the ferromagnetic (FM) - paramagnetic (PM) phase transition is examined. Owing to its mathematical simplicity, MF theory represents the first step towards predicting the phase diagrams and certain properties observed in systems exhibiting a continuous phase transition. This approximation, treats the order parameter as spatially invariable and becomes exact only when the range of interactions is infinite. Though MF approach neglects the critical fluctuations of the order parameter (crucial in most of the systems) and is valid in systems with spatial dimensionality ≥ 4, it makes qualitatively correct predictions in real systems.

The nonlinearity in magnetization of a ferromagnet becomes more pronounced as the T_C is approached from either side. The magnetization m in a weak external magnetic field of amplitude, h, can be expanded in powers of h as

$$m = \begin{cases} m_0 + \chi_1 h + \chi_2 h^2 + \chi_3 h^3 + \cdots & (T < T_C) \\ \chi_1 h + \chi_3 h^3 + \chi_5 h^5 + \cdots & (T > T_C) \end{cases} \tag{3.1}$$

where m_0 is the spontaneous magnetization, χ_1 is the linear susceptibility and $\chi_2,\ \chi_3, \cdots$ (smaller compared to χ_1) are the nonlinear susceptibilities. In the paramagnetic state, $m_0 = 0$ and m has an inversion symmetry with respect to a change in the sign of h and hence only odd powers of h appear in the expression for m. The above expression holds for both real (dispersion) and imaginary (absorption) parts of complex susceptibility $\chi = \chi' + i\chi''$, hence, $m = \sum_{n=1}^{N} (\chi'_n + i\chi''_n)\ h^n,\ (n = 1, 2, ...)$. In this work, the in-phase components alone are calculated since $\chi_n \cong \chi'_n$ as $\chi'_n \gg \chi''_n$. χ_n, in general, is a function of temperature, h_{dc} and the rms amplitude, h_{ac}, as well as the frequency, ν, of the ac driving field. Theoretically, the

spin-fluctuation-spin-fluctuation correlation length diverges at the critical point and hence, all the quantities related to it exhibit singularity at T_C. Experimentally, it is difficult to observe the true critical behaviour below T_C as it is masked by the formation of FM domains and the susceptibility is usually demagnetization-limited. Moreover, due to the finite size of the sample, inherent non-zero field (e.g. Earth's field, rest field of the superconducting magnet), the temperature instability, etc., the expected singularity manifests itself in a maximum/crossover/minimum at T_C. The nonlinear susceptibility, though small compared to the linear counterpart, is sensitive to the local magnetic order arising due to spin-reorientation, magnetic inhomogeneities, domain wall pinning, etc.,. However, the effective contribution from demagnetization factor becomes increasingly dominant while the critical regime, where power laws are expected to be valid, narrows down in higher harmonics of susceptibility. An accurate estimate of T_C can be obtained from the characteristic peak/crossover temperature of the higher harmonics measured at low fields and frequencies.

Within the mean-field framework, the magnetization of a ferromagnetic system is given by

$$\begin{aligned} m(h,T) &= Ng\mu_B J \;\; B_J(x) \\ &= N\mu \;\; B_J(x) \end{aligned} \tag{3.2}$$

where

$$x = \frac{\mu}{k_B T}(h + \lambda m), \tag{3.3}$$

$$B_J(x) = \frac{2J+1}{2J}\coth(\frac{2J+1}{2J}x) - \frac{1}{2J}\coth(\frac{1}{2J}x), \tag{3.4}$$

N, g, μ_B, k_B, J and λ $(= \frac{k_B T_C}{N\mu^2}\frac{3J}{J+1})$ are the number of atoms per unit

volume, Landé g-factor, Bohr magneton, Boltzmann constant, total angular momentum and the molecular-field constant, respectively.

3.2 Expansion Method

In the asymptotic critical region (ACR), i.e., $T \to T_C$, x is small for weak fields and hence, the Brillouin function for the case $J \cong S$, $B_S(x)$ can be expanded in powers of x as

$$B_S(x) = \alpha_S x - \beta_S x^3 + \gamma_S x^5 + \cdots \tag{3.5}$$

where

$$\begin{aligned} \alpha_S &= \frac{1}{3}\frac{S+1}{S} \equiv \frac{1}{u} \\ \beta_S &= \frac{1}{45}\frac{S+1}{S}\frac{2S^2+2S+1}{2S^2} \\ \gamma_S &= \frac{2}{945}\frac{S+1}{S}\frac{16S^4+32S^3+28S^2+12S+3}{16S^4} \end{aligned} \tag{3.6}$$

Combining Eqs.(3.2) and (3.5) and equating the coefficients of h^n (n = 0 - 5) in the resulting expression with those in Eq.(3.1), one obtains:

$$m_0 \equiv m(h=0) = \begin{cases} N\mu\ B_S(x_0) & \text{t} < 1 \\ 0 & \text{t} > 1 \end{cases} \tag{3.7}$$

where $t = T/T_C$

$$\chi_1 = \begin{cases} \frac{N\mu^2}{k_B T_C}\frac{A}{[t-uA]} & \text{t} < 1 \\ \frac{N\mu^2}{k_B T_C}\frac{\alpha_S}{[t-1]} & \text{t} > 1 \end{cases} \tag{3.8}$$

$$\chi_2 = \begin{cases} \frac{N\mu^3}{(k_B T_C)^2}\ t\ x_0 \frac{B}{[t-uA]^3} & \text{t} < 1 \\ 0 & \text{t} > 1 \end{cases} \tag{3.9}$$

$$\chi_3 = \begin{cases} \frac{N\mu^4}{(k_B T_C)^3}\frac{t}{[t-uA]^4}\{2ux_0^2\frac{B^2}{[t-uA]} + C\} & \text{t} < 1 \\ \frac{N\mu^4}{(k_B T_C)^3}\frac{t}{[t-1]^4}(-\beta_S) & \text{t} > 1 \end{cases} \tag{3.10}$$

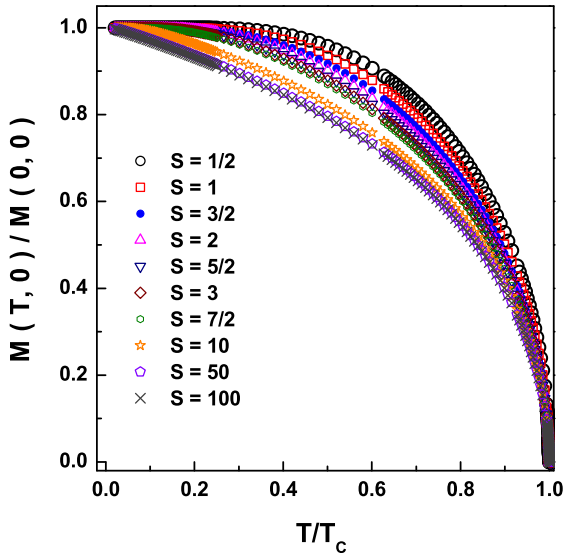

Figure 3.1: *Normalized spontaneous magnetization for various spin values as a function of reduced temperature.*

$$\chi_4 = \begin{cases} \frac{N\mu^5}{(k_B T_C)^4} \frac{t}{[t-uA]^5} x_0 \{4u^2 x_0^2 \frac{B^3}{[t-uA]^2} + 5u \frac{BC}{[t-uA]} + 5\gamma_S\} & \text{t} < 1 \\ 0 & \text{t} > 1 \end{cases} \tag{3.11}$$

$$\chi_5 = \begin{cases} \frac{N\mu^6}{(k_B T_C)^5} \frac{t}{[t-uA]^6} \{12u^3 x_0^4 \frac{B^4}{[t-uA]^3} + 21u^2 x_0^2 \frac{B^2 C}{[t-uA]^2} \\ \quad +3u \frac{C+10\gamma_S x_0^2 B}{[t-uA]} + \gamma_S\} & \text{t} < 1 \\ \frac{N\mu^6}{(k_B T_C)^5} \frac{t}{[t-1]^6} \{3u \frac{\beta_S^2}{[t-1]} + \gamma_S\} & \text{t} > 1 \end{cases} \tag{3.12}$$

with $x_0 = x(h=0) = \frac{1}{t}\frac{m_0}{N\mu}u$, $A = \alpha_S - 3\beta_S x_0^2 + 5\gamma_S x_0^4$, $B = -3\beta_S + 10\gamma_S x_0^2$ and $C = -\beta_S + 10\gamma_S x_0^2$. For $S = 1/2$, the above expressions for χ_1, χ_2 and χ_3 reduce to those reported in [7, 11].

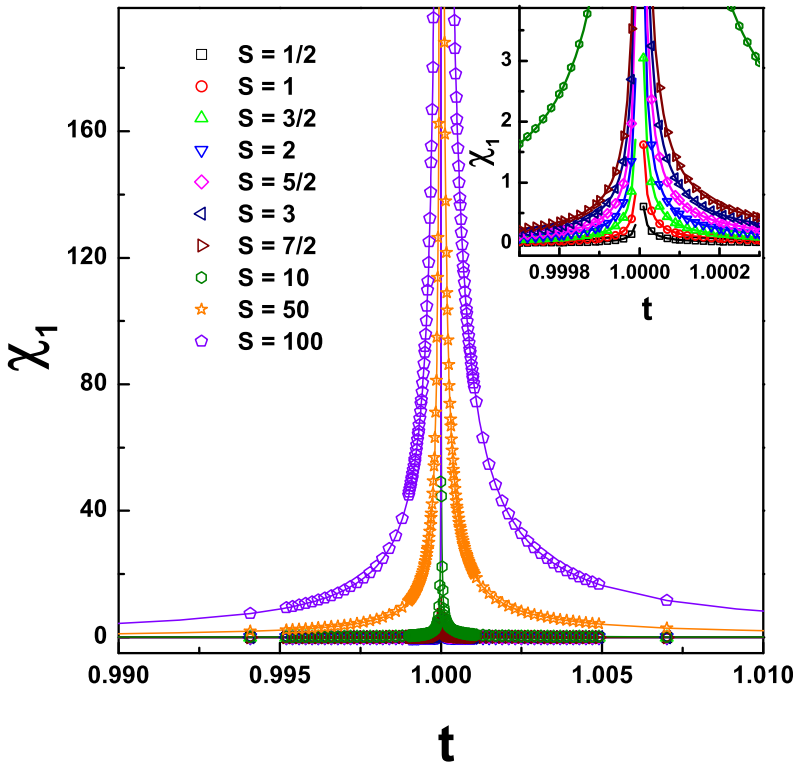

Figure 3.2: *The linear susceptibility χ_1 for various spin values as a function of reduced temperature t, obtained by the expansion (derivative) method and represented by symbols (continuous curves). The inset shows the expanded view of the divergence in the asymptotic critical region.*

3.2.1 Critical behaviour

Eq.(3.7), when solved for spontaneous magnetization, yields

$$\left(\frac{m_0}{N\mu}\right)^2 = \begin{cases} \frac{10}{3}\frac{(S+1)^2}{S^2+(S+1)^2}\, t^2\,(1-t) & \mathrm{t} < 1 \\ 0 & \mathrm{t} > 1 \end{cases} \tag{3.13}$$

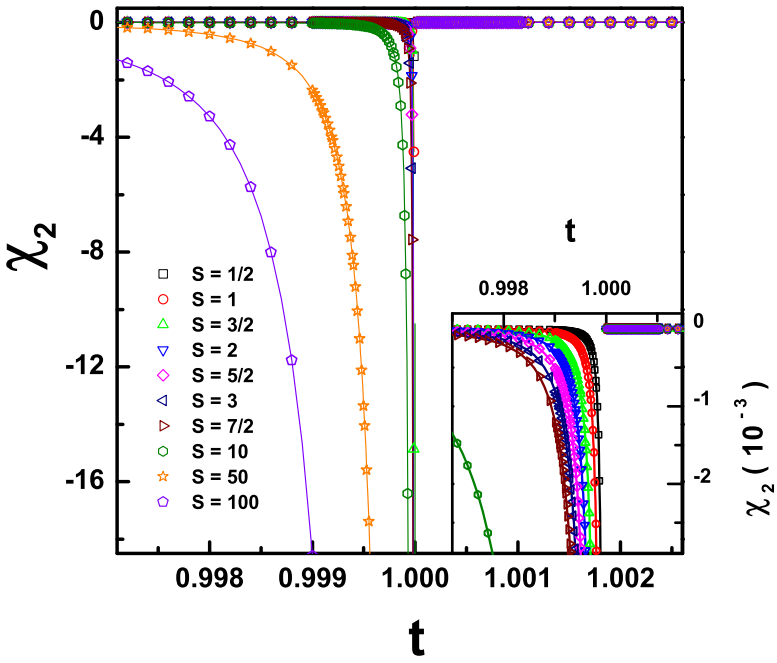

Figure 3.3: *The first-order nonlinear susceptibility χ_2 for various spin values as a function of reduced temperature t, obtained by the expansion (derivative) method and represented by symbols (continuous curves). The inset shows the expanded view of the divergence in the asymptotic critical region below T_C.*

with the critical exponent for spontaneous magnetization (order parameter), $\beta = 0.5$. Using this value of $(m_0/N\mu)^2$ in x_0 and simplifying Eq.(3.8) gives

$$\chi_1 = \begin{cases} \frac{N\mu^2}{2(k_B T_C)}\ \alpha_S\ (1-t)^{-1} & \text{t} < 1 \\ \frac{N\mu^2}{k_B T_C}\ \alpha_S\ (t-1)^{-1} & \text{t} > 1. \end{cases} \tag{3.14}$$

Thus, the linear susceptibility, χ_1, is positive for temperatures below and above T_C and diverges with the critical exponent, $\gamma = 1.0$. As T_C is approached from either side, χ_1 has the characteristic Curie-Weiss form. From Eq.(3.9), it is clear that χ_2 $(\sim m_0\chi_1^3)$ is non-zero as long as m_0 is finite.

Simplifying Eq.(3.9), one obtains

$$\chi_2 = \begin{cases} -\frac{3}{8}(\alpha_S\beta_S)^{1/2}\frac{N\mu^3}{(k_BT_C)^2}\ t\ (1-t)^{-5/2} & \mathrm{t} < 1 \\ 0 & \mathrm{t} > 1 \end{cases} \tag{3.15}$$

$\chi_2 < 0$ and diverges with the exponent $\gamma_2 = 2.5 = 2\gamma + \beta$ as $T \to T_C^-$ from below and $\chi_2 = 0$ at and above T_C. Eq.(3.10) can be recast into the form

$$\chi_3 = \begin{cases} (\frac{\beta_S}{2})\frac{N\mu^4}{(k_BT_C)^3}\ t\ (1-t)^{-4} & \mathrm{t} < 1 \\ -\beta_S\frac{N\mu^4}{(k_BT_C)^3}\ t\ (t-1)^{-4} & \mathrm{t} > 1 \end{cases} \tag{3.16}$$

It follows that χ_3 ($\sim \chi_1^4$) is *positive* in the FM phase and *negative* in the PM phase but as $T \to T_C^-$ or T_C^+, χ_3 diverges with the exponent $\gamma_3 = 4.0 = 3\gamma + 2\beta$. In its alternative form, Eq.(3.11) can be written as

$$\chi_4 = \begin{cases} -\frac{105}{128}(\frac{\beta_S^3}{\alpha_S})^{1/2}\frac{N\mu^5}{(k_BT_C)^4}\ t\ (1-t)^{-11/2} & \mathrm{t} < 1 \\ 0 & \mathrm{t} > 1 \end{cases} \tag{3.17}$$

χ_4 ($\propto \chi_2\chi_1^3$) exhibits a behaviour similar to that of χ_2 but the critical exponent $\gamma_4 = 5.5 = 4\gamma + 3\beta$. In general, the nonlinear susceptibilities χ_2 and χ_4 reflect the presence of a symmetry-breaking field and are observed only in materials with spontaneous magnetization or in the presence of a dc field. Similarly, Eq.(3.12), simplifies into

$$\chi_5 = \begin{cases} \frac{3}{2}\frac{\beta_S^2}{\alpha_S}\frac{N\mu^6}{(k_BT_C)^5}\ t\ (1-t)^{-7} & \mathrm{t} < 1 \\ 3\frac{\beta_S^2}{\alpha_S}\frac{N\mu^6}{(k_BT_C)^5}\ t\ (t-1)^{-7} & \mathrm{t} > 1 \end{cases} \tag{3.18}$$

Evidently, χ_5 ($\propto |\chi_3|\chi_1^3$) is positive both below and above T_C and diverges as T_C is approached on either side. The corresponding exponent, $\gamma_5 = 7.0 = 5\gamma + 4\beta$. The critical exponents $\gamma_1 - \gamma_5$ characterize the divergence of the linear and nonlinear susceptibilities in accordance with the relation $\chi_n \sim| t-1 |^{-\gamma_n}$ with $\gamma_n = n\,\gamma + (n-1)\,\beta$, where $\gamma = 1.0$, $\beta = 0.5$ and $n = 1, 2, \cdots$.

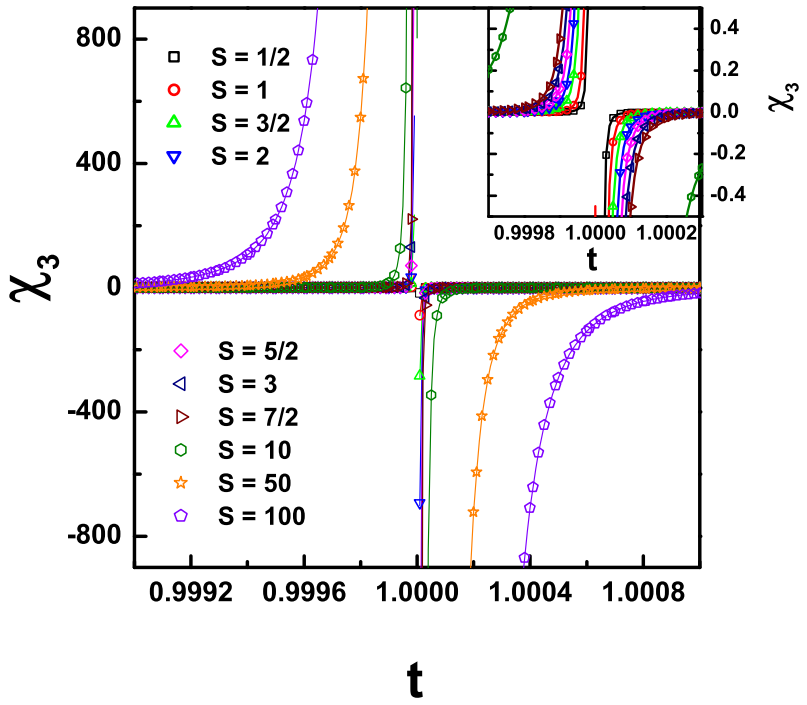

Figure 3.4: *The second-order nonlinear susceptibility χ_3 for various spin values as a function of reduced temperature t, obtained by the expansion (derivative) method and represented by symbols (continuous curves). The inset shows the expanded view of the divergence in the asymptotic critical region.*

However, it should be emphasized that the nonlinear susceptibilities χ_2 and χ_4 are zero in the PM state where $m_0 = 0$ for $h \simeq 0$. The above expressions for $\chi_1 - \chi_5$ can be derived, in a more general form, from the magnetic scaling equation of state, $m = |\epsilon|^{\beta} f_{\pm}\left(h/|\epsilon|^{\beta+\gamma}\right)$, as $\chi_n = |\epsilon|^{-\gamma_n} f_{\pm}^{(n)}\left(h/|\epsilon|^{\beta+\gamma}\right)$ where $\epsilon = (T - T_C)/T_C = t - 1$, $f_{+}^{(n)}$ and $f_{-}^{(n)}$ represent the n^{th} order field derivative of the scaling function $f_{\pm}$, $\frac{\partial^n f_{\pm}}{\partial h^n}$, at $T > T_C$ and $T < T_C$, respectively. In

addition, the above scaling approach asserts that

$$(\chi_3/\chi_1) = |\epsilon|^{-2\Delta}\, g_{\pm}^{31}\left(\frac{h}{|\epsilon|^{\Delta}}\right) \tag{3.19}$$

$$(\chi_4/\chi_2) = |\epsilon|^{-2\Delta}\, g_{\pm}^{42}\left(\frac{h}{|\epsilon|^{\Delta}}\right) \tag{3.20}$$

$$(\chi_5/\chi_1) = |\epsilon|^{-4\Delta}\, g_{\pm}^{51}\left(\frac{h}{|\epsilon|^{\Delta}}\right) \tag{3.21}$$

where $\Delta = \beta + \gamma$ is the gap exponent and $g_{\pm}^{ij} \equiv f_{\pm}^{(i)}/f_{\pm}^{(j)}$ are the scaling functions.

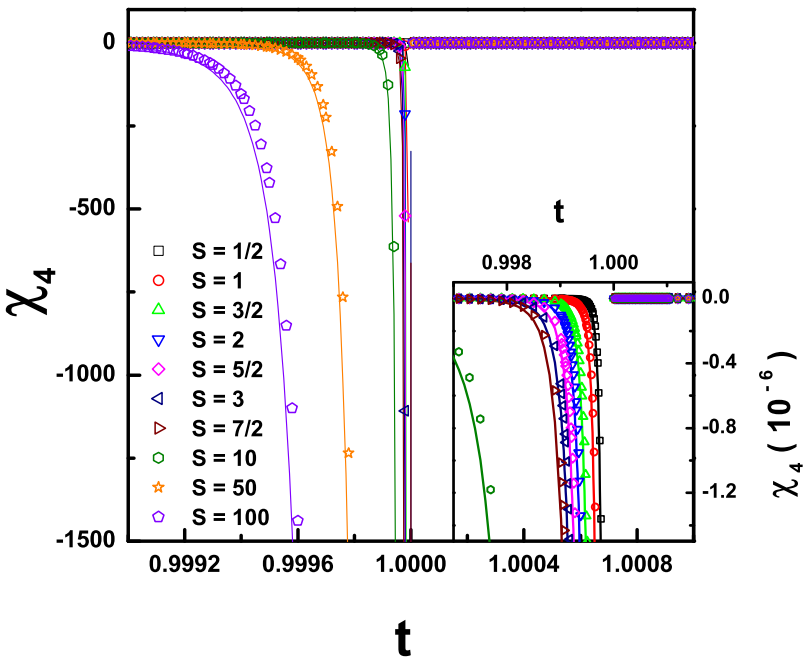

Figure 3.5: *The third-order nonlinear susceptibility χ_4 for various spin values as a function of reduced temperature t, obtained by the expansion (derivative) method and represented by symbols (continuous curves). The inset shows the expanded view of the divergence in the asymptotic critical region below T_C.*

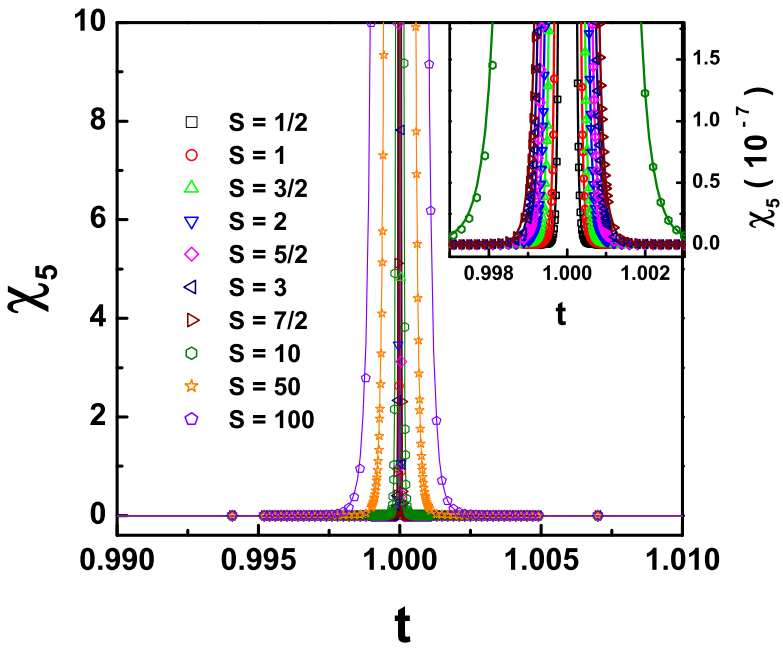

Figure 3.6: *The fourth-order nonlinear susceptibility χ_5 for various spin values as a function of reduced temperature t, obtained by the expansion (derivative) method and represented by symbols (continuous curves). The inset shows the expanded view of the divergence in the asymptotic critical region.*

3.3 Differentiation Method

At low fields, magnetization m, given by Eq.(3.2), can be expanded around m_0 using Maclaurins expansion, i.e., Eq.(3.1) with

$$\chi_n = \frac{1}{n!}\left(\frac{\partial^n m}{\partial h^n}\right)_{h=0}, \qquad (n = 1, 2, 3, \cdots) \tag{3.22}$$

Differentiating Eq.(3.2) with respect to h successively and using Eq.(3.22) yields

$$\chi_1 = \frac{N\mu^2}{k_B T_C}\,\frac{B'}{[t - uB']} \tag{3.23}$$

$$\chi_2 = \frac{1}{2}\ \frac{N\mu^3}{(k_B T_C)^2}\ t\ \frac{B''}{[t-uB']^3} \tag{3.24}$$

$$\chi_3 = \frac{1}{6}\frac{N\mu^4}{(k_B T_C)^3}\ t\ \{\frac{B'''}{[t-uB']^4} + 3u\frac{(B'')^2}{[t-uB']^5}\} \tag{3.25}$$

$$\chi_4 = \frac{1}{24}\frac{N\mu^5}{(k_B T_C)^4}\ t\ \{\frac{B'^v}{[t-uB']^5} + 10u\frac{B''B'''}{[t-uB']^6} + 15u^2\frac{(B'')^3}{[t-uB']^7}\} \tag{3.26}$$

$$\chi_5 = \frac{1}{120}\frac{N\mu^6}{(k_B T_C)^5}\ t\ \{\frac{B^v}{[t-uB']^6} + 5u\frac{2(B''')^2 + 3B''B'^v}{[t-uB']^7} + 15u^2\frac{7(B'')^2B'''}{[t-uB']^8} + 105u^3\frac{(B'')^4}{[t-uB']^9}\} \tag{3.27}$$

where

$$\begin{aligned} B' &= q^2(\phi^2-1) - p^2(\Gamma^2-1) \\ -B'' &= 2q^3(\phi^3-\phi) - 2p^3(\Gamma^3-\Gamma) \\ B''' &= 2q^4(3\phi^4-4\phi^2+1) - 2p^4(3\Gamma^4-4\Gamma^2+1) \\ -B'^v &= 8q^5(3\phi^5-5\phi^3+2\phi) - 8p^5(3\Gamma^5-5\Gamma^3+2\Gamma) \\ B^v &= 8q^6(15\phi^6-30\phi^4+17\phi^2-2) \\ &\quad -8p^6(15\Gamma^6-30\Gamma^4+17\Gamma^2-2) \end{aligned} \tag{3.28}$$

are the successive derivatives of the Brillouin function with respect to its argument with $q = 1/2S$, $p = 1+q$, $\Gamma = coth(px_0)$ and $\phi = coth(qx_0)$.

The spontaneous magnetization, presented in figure 3.1, for various spin values was obtained by solving the transcendental equation (3.7) by the Newton-Raphson method. The thermal variations of linear/nonlinear susceptibilities, calculated using the analytical expressions (3.8)-(3.12) and

(3.23)-(3.27), are presented in figures 3.2 - 3.6. An excellent agreement between the results of the expansion and derivative methods, in the ACR, is evident from these figures. The expressions for nonlinear susceptibilities calculated by the differentiation method, valid even for temperatures away from T_C, reduce to those obtained by the expansion method for temperatures in the close vicinity of T_C. The main observations are as follows. With increasing S, the divergences in the linear and nonlinear susceptibilities on both sides of T_C become less sharp with the result that the ACR widens. Large values of S are applicable to molecular magnets or to the systems in which the range of interactions tends to be infinite. For a given value of S, higher the order of nonlinear susceptibility, lower its magnitude, sharper the divergence and consequently, narrower the ACR.

3.4 Experimental detection

In this section, the expressions that relate the intrinsic linear and nonlinear susceptibilities to those experimentally measured (harmonics of susceptibility) are obtained.

For a field $h = h_{ac} + h_{dc}$, where $h_{ac} = h_0 sin\omega t$ is driving ac field and h_{dc} is superimposed dc field, the induced signal proportional to AC-susceptibility in the secondary coil due to the magnetic sample is given by

$$E = -nAf\frac{dm}{dt} \tag{3.29}$$

Here, n is the number of turns per unit length of the secondary coil, A is the cross-sectional area of the pickup coil and f is the filling factor.

3.4.1 $T < T_C$

The magnetization of a ferromagnet in presence of a field h is given by first part of Eq. (3.1). Differentiating first part Eq.(3.1) with respect to 't', we get

$$\frac{dm}{dt} = h_0\omega(\chi_1 + 2\chi_2 h + 3\chi_3 h^2 + 4\chi_4 h^3 + 5\chi_5 h^4 + \cdots)cos\omega t \tag{3.30}$$

and

$$E = -nAfh_0\omega[\chi_1^t cos\omega t + \chi_2^t h_0 sin2\omega t - \frac{3}{4}\chi_3^t h_0^2 cos3\omega t - \frac{1}{2}\chi_4^t h_0^3 sin4\omega t + \frac{5}{16}\chi_5^t h_0^4 cos5\omega t + \frac{3}{16}\chi_6^t h_0^5 sin6\omega t - \frac{7}{64}\chi_7^t h_0^6 cos7\omega t + \cdots] \tag{3.31}$$

with

$$\chi_1^t = \chi_1 + 2h_{dc}\chi_2 + (3h_{dc}^2 + \frac{3}{4}h_0^2)\chi_3 + h_{dc}(4h_{dc}^2 + 3h_0^2)\chi_4 + (5h_{dc}^4 + \frac{15}{2}h_{dc}^2 h_0^2 + \frac{5}{8}h_0^4)\chi_5 h_{dc}(6h_{dc}^4 + 15h_{dc}^2 h_0^2 + \frac{15}{4}h_0^4)\chi_6 + (7h_{dc}^6 + \frac{105}{4}h_{dc}^4 h_0^2 + \frac{105}{8}h_{dc}^2 h_0^4 + \frac{77}{64}h_0^6)\chi_7 + \cdots \tag{3.32}$$

$$\chi_2^t = \chi_2 + 3h_{dc}\chi_3 + (6h_{dc}^2 + h_0^2)\chi_4 + h_{dc}(10h_{dc}^2 + 5h_0^2)\chi_5 + (15h_{dc}^4 + 15h_{dc}^2 h_0^2 + \frac{15}{16}h_0^4)\chi_6 + h_{dc}(21h_{dc}^4 + 35h_{dc}^2 h_0^2 + \frac{105}{16}h_0^4)\chi_7 + \cdots \tag{3.33}$$

$$\chi_3^t = \chi_3 + 4h_{dc}\chi_4 + (10h_{dc}^2 + \frac{5}{4}h_0^2)\chi_5 + h_{dc}(20h_{dc}^2 + \frac{15}{2}h_0^2)\chi_6 + (35h_{dc}^4 + \frac{105}{4}h_{dc}^2 h_0^2 + \frac{7}{16}h_0^4)\chi_7 + \cdots \tag{3.34}$$

$$\chi_4^t = \chi_4 + 5h_{dc}\chi_5 + (15h_{dc}^2 + \frac{3}{2}h_0^2)\chi_6 + h_{dc}(35h_{dc}^2 + \frac{21}{2}h_0^2)\chi_7 + \cdots \tag{3.35}$$

$$\chi_5^t = \chi_5 + 6h_{dc}\chi_6 + (21h_{dc}^2 + \frac{7}{4}h_0^2)\chi_7 + \cdots \tag{3.36}$$

and so on. For small fields, neglecting the higher powers of h, the above equations reduce to $\chi_n^t \approx \chi_n + (n+1)h_{dc}\chi_{n+1}, \quad (n = 1, 2, \cdots)$. Thus, for

small field values of h_{ac} and h_{dc}, the harmonics of susceptibility measured corresponds to the intrinsic counterpart with an additonal term involving a product of h_{dc} and higher order susceptibility. This term gives rise to asymmetry in χ_n^t.

In the absence of the static field ($h_{dc} = 0$), the above equations reduce to the following form:

$$\chi_1^t = \chi_1 + \frac{3}{4}\chi_3 h_0^2 + \frac{5}{8}\chi_5 h_0^4 + \frac{77}{64}\chi_7 h_0^6 + \cdots \tag{3.37}$$

$$\chi_2^t = \chi_2 + \chi_4 h_0^2 + \frac{15}{16}\chi_6 h_0^4 + \cdots \tag{3.38}$$

$$\chi_3^t = \chi_3 + \frac{5}{4}\chi_5 h_0^2 + \frac{7}{16}\chi_7 h_0^4 + \cdots \tag{3.39}$$

$$\chi_4^t = \chi_4 + \frac{3}{2}\chi_6 h_0^2 + \cdots \tag{3.40}$$

$$\chi_5^t = \chi_5 + \frac{7}{4}\chi_7 h_0^2 + \cdots \tag{3.41}$$

and so on. For small fields, neglecting the higher powers of h, the above equations reduce to $\chi_n^t \approx \chi_n$, $(n = 1, 2, \cdots)$. Hence, the harmonics of susceptibility are the same as their intrinsic counterparts in the absence of static field.

3.4.2 $T > T_C$

The magnetization in the presence of a magnetic field h is given by the second part of Eq.(3.1) with only odd powers of h. and hence,

$$E = -nAfh_0\omega[\chi_1^t cos\omega t + 3\chi_2^t h_0 sin2\omega t - \frac{3}{4}\chi_3^t h_0^2 cos3\omega t - \frac{5}{2}\chi_4^t h_0^3 sin4\omega t + \frac{5}{16}\chi_5^t h_0^4 cos5\omega t + \frac{21}{8}\chi_6^t h_0^5 sin6\omega t - \frac{7}{64}\chi_7^t h_0^6 cos7\omega t + \cdots] \tag{3.42}$$

with

$$\chi_1^t = \chi_1 + (3h_{dc}^2 + \frac{3}{4}h_0^2)\chi_3 + (5h_{dc}^4 + \frac{15}{2}h_{dc}^2h_0^2 + \frac{5}{8}h_0^4)\chi_5 + (7h_{dc}^6 + \frac{105}{4}h_{dc}^4h_0^2 + \frac{105}{8}h_{dc}^2h_0^4 + \frac{77}{64}h_0^6)\chi_7 + \cdots \quad (3.43)$$

$$\chi_2^t = h_{dc}\chi_3 + \frac{1}{3}h_{dc}(10h_{dc}^2 + 5h_0^2)\chi_5 + h_{dc}(7h_{dc}^4 + \frac{35}{3}h_{dc}^2h_0^2 + \frac{35}{16}h_0^4)\chi_7 + \cdots \quad (3.44)$$

$$\chi_3^t = \chi_3 + (10h_{dc}^2 + \frac{5}{4}h_0^2)\chi_5 + (35h_{dc}^4 + \frac{105}{4}h_{dc}^2h_0^2 + \frac{7}{16}h_0^4)\chi_7 + \cdots \quad (3.45)$$

$$\chi_4^t = h_{dc}\chi_5 + h_{dc}(7h_{dc}^2 + \frac{21}{10}h_0^2)\chi_7 + \cdots \quad (3.46)$$

$$\chi_5^t = \chi_5 + (21h_{dc}^2 + \frac{7}{4}h_0^2)\chi_7 + \cdots \quad (3.47)$$

and so on. In absence of the static field, the above expressions for odd harmonics reduce to Eqs. (3.37), (3.39) and (3.41), respectively, while even harmonics become zero. For weak fields, neglecting the higher non-linear powers of field, the equations above reduce to $\chi_n^t \approx \chi_n$, $(n = 1, 3, 5, \cdots)$ and $\chi_n^t \approx h_{dc}\chi_{n+1}$, $(n = 2, 4, 6, \cdots)$. In the presence of the DC field, h_{dc}, the coefficients of the 2ω, 4ω, etc, terms (χ_2^t, χ_4^t, etc.,) are also finite. The temperature dependence of odd harmonics are not affected by the presence of h_{dc} at low fields. Note that the even harmonics are dictated by spontaneous magnetization in the FM phase like h_{dc} in the PM phase. Thus, non-zero even harmonic susceptibility is taken as an indication of existence of long-range order in the system. However, in the PM state, as shown in above expressions, they are odd functions of h_{dc} while even functions of h_0 and their temperature variations are solely governed by those of odd-order susceptibilities. The temperature dependence of the odd harmonics are unaffected in presence of static field. Experimentally, one minimises the even harmonics at a temperature where maxima in odd harmonics are expected

by applying a static field, to compensate the remanent of the superconducting magnet. Another interesting aspect is that observation of any feature in PM phase will also directly point out to the presence of local magnetic order (arising due to magnetic inhomogeneities, etc.,) whose transition point is higher than the global T_C. Using an AC susceptometer (QUANTUM DESIGN PPMS Model 6000), one, in fact, measures the temperature dependence of the coefficients of the ωt, $2\omega t$, $3\omega t$, etc., terms in Eqs.(3.31) and (3.42) which essentially reflects the thermal variations of χ_1^t, χ_2^t, χ_3^t, etc., [5]. The number of harmonics to be detected depends on the sensitivity of the instrument.

3.5 A case study

Figure 3.7 compares the critical behaviour of linear and nonlinear susceptibilities, observed [20] in the $La_{0.7}Pb_{0.3}Mn_{0.8}Co_{0.2}O_3$ manganite at the ac driving field of rms amplitude of 5 Oe and frequency 100 Hz, with that predicted by the present MF calculations. ac field was applied along the length of a polycrystalline sample of cylindrical shape: diameter $\simeq 3mm$ and length $\simeq 2mm$. To make a correct comparison between theory and experiment, due consideration has to be given to the following. (i) The present theoretical treatment does not account for the magneto-crystalline and shape anisotropies present in a (*real*) ferromagnetic sample but calculates the *intrinsic* linear and nonlinear susceptibilities in the presence of an internal/molecular field and an extremely weak external magnetic field. By contrast, the shape anisotropy (as the magneto-crystalline anisotropy is averaged out to a large extent in a polycrystalline sample) has a domi-

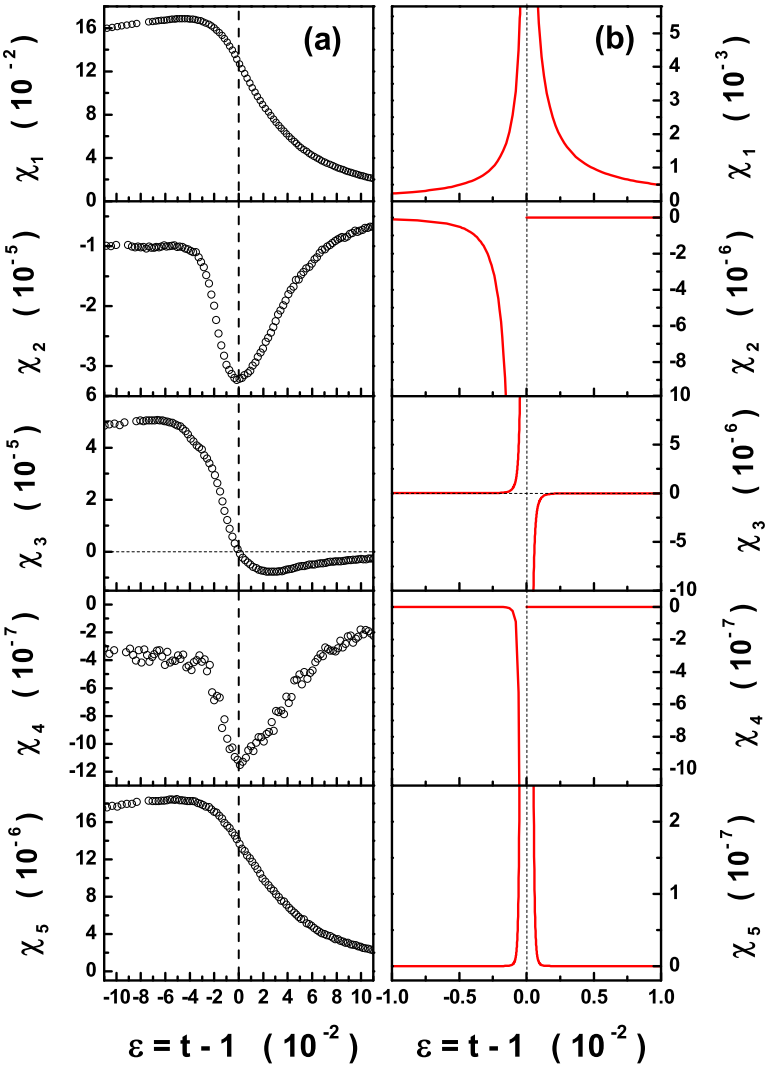

Figure 3.7: *(a) The linear and nonlinear susceptibilities as functions of the reduced temperature, $\epsilon = (T - T_C)/T_C = t - 1$, at $h_{dc} = 0$, $h_{ac} = 5Oe$ and $\nu = 100Hz$ for $La_{0.7}Pb_{0.3}Mn_{0.8}Co_{0.2}O_3$. (b) The corresponding mean-field predictions for a ferromagnet with $S = 2$ (appropriate for the manganite system in question).*

nant influence on the measured susceptibilities particularly for $T \leq T_C$ in that it prevents χ_1, χ_3, χ_5 from diverging as $T \rightarrow T_C^-$ and instead these susceptibilities get demagnetization-limited for $T < T_C$. Shape anisotropy also limits the divergence of χ_2 and χ_4 at $T = T_C$. To ascertain the effect of shape anisotropy, the expressions for the measured linear and nonlinear susceptibilities, χ_n^{meas} with $n = 1, 2, ...5$, can be obtained by repeating the present MF calculations with the field h in Eqs.(3.1) and (3.3) replaced by $h - 4\pi D\ m$, where D is the demagnetizing factor; $\simeq 0.5$ for the present sample. The expressions for χ_n^{meas}, so obtained, when compared with those, Eqs.(3.8) - (3.12), for their intrinsic counterparts, χ_n^{int}, bring out clearly the role of shape anisotropy in limiting the divergences at $T = T_C$ in χ_n^{meas}. It is relatively easy to demonstrate this for the measured linear susceptibility since only a couple of algebraic steps suffice to yield the well-known relation, $(\chi_1^{meas})^{-1} = (\chi_1^{int})^{-1} + 4\pi D$, between the measured and intrinsic linear susceptibility, from which it follows that $(\chi_1^{meas})^{-1} = 4\pi D$ at $T = T_C$ where χ_1^{int} diverges. (ii) Even a weak superposed dc magnetic field, h_{dc} (e.g., the earth's magnetic field or the rest field of the superconducting magnet) smears out the divergences further and makes χ_2 and χ_4 *finite* at $T \geq T_C$ as it respectively adds a term proportional to $h_{dc}\ \chi_3$ and $h_{dc}\ \chi_5$ [5] to the expressions, Eqs.(3.9) and (3.11) or Eqs.(3.24) and (3.26), for χ_2 and χ_4. (iii) The theory deals with a conventional pure ferromagnet with a *uniform* spin-spin exchange coupling as against $La_{0.7}Pb_{0.3}Mn_{0.8}Co_{0.2}O_3$, whose magnetic behaviour is governed by the interplay between the dipole-dipole interactions [21], $Mn^{3+} - O - Mn^{4+}$ ferromagnetic double exchange and the $Mn^{3+}/Mn^{4+} - O - Mn^{3+}/Mn^{4+}$ antiferromagnetic superexchange interactions, besides the $Co - O - Mn$ and $Co - O - Co$ interactions.

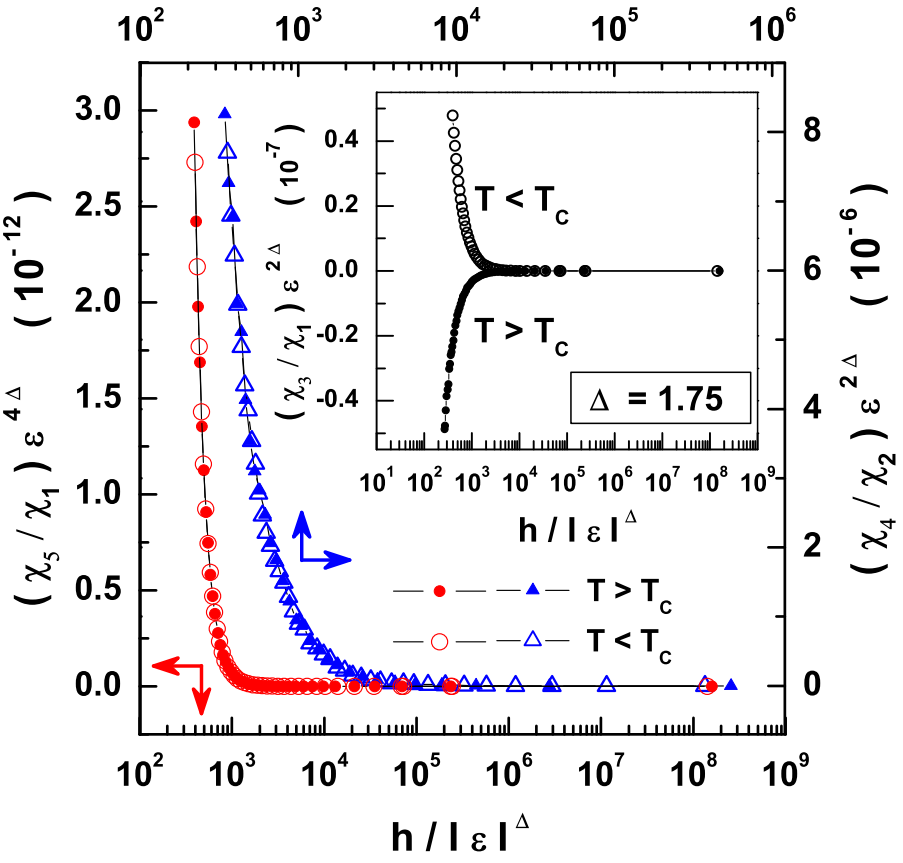

Figure 3.8: *Scaled nonlinear susceptibilities,* $(\chi_3/\chi_1)\epsilon^{2\Delta}$, $(\chi_4/\chi_2)\epsilon^{2\Delta}$ *and* $(\chi_5/\chi_1)\epsilon^{4\Delta}$, *plotted against the scaled field,* $h/|\epsilon|^{\Delta}$, *obey the equations of state, Eqs.(3.19) - (3.21), of the text.*

Notwithstanding the above remarks (i) - (iii), the present MF treatment yields the correct sign and order of magnitude of the linear and nonlinear susceptibilities and provides an adequate qualitative description of the critical behaviour of χ_1, χ_3 and χ_5 (χ_2 and χ_4) for $T \geq T_C$ ($T \leq T_C$). As expected from the observation (iii), the theoretical predictions are in much better agreement with the $\chi_1(T)$ and $\chi_3(T)$ data reported [8] previously on

pure Ni in the critical region.

Recognizing that the scaling functions $f_{\pm}^{(n)}\left(h/|\epsilon|^{\beta+\gamma}\right)$ represent a generalized form of the corresponding field derivatives of the Brillouin function, Eq.(3.28), the ratios χ_3/χ_1, χ_4/χ_2 and χ_5/χ_1 are far less sensitive to the material parameters than the individual linear or nonlinear susceptibilities. Hence, instead of a direct comparison between theory and experiment of the type attempted in Fig.3.7, a better approach is to exploit the scaling equations of state, Eqs.(3.19) - (3.21), that relate the reduced nonlinear susceptibilities $(\chi_3/\chi_1)\epsilon^{2\Delta}$, $(\chi_4/\chi_2)\epsilon^{2\Delta}$ and $(\chi_5/\chi_1)\epsilon^{4\Delta}$ with the reduced conjugate field $h/|\epsilon|^{\Delta}$, to arrive at a reliable estimate for the gap exponent Δ, as illustrated in figure 3.8. We find that the quality of data collapse onto two universal curves, g_{-}^{ij} for $T < T_C$ and g_{+}^{ij} for $T > T_C$, over a wide temperature range, is optimum for the choice $\Delta = \beta + \gamma = 1.75(5)$, which is consistent with the value $\gamma = 1.390(1)$, previously determined [21] from the linear susceptibility data, and $\beta = 0.37$, theoretically predicted [22] for a three-dimensional isotropic dipolar ferromagnet.

References

1. M. Suzuki, *Phenomenological Theory of Spin-Glasses and Some Rigorous Results*, Prog. Theor. Phys. **58**, 1151 (1977).

2. K. Wada and H. Takayama, *Nonlinear Susceptibilities of the Sherrington-Kirkpatrick Model and the Spherical Model*, Prog. Theor. Phys. **64**, 327 (1980).

3. S. Fujiki and S. Katsura, *Nonlinear Susceptibility in the Spin Glass*, Prog. Theor. Phys. **65**, 1130 (1981).

4. T. Bitoh, K. Ohba, M. Takamatsu, T. Shirane and S. Chikazawa, *Comparative study of linear and nonlinear susceptibilities of fine-particle and spin-glass systems: Quantitative analysis based on the superparamagnetic blocking model*, J. Magn. Magn. Mater. **154**, 59 (1996).

5. S. C. Bhargava, A. H. Morrish, H. Kunkel and Z. W. Li, *Spin-glass ordering in a spinel ferrite,* $Mg(Al,Fe)_2O_4$, J. Phys.: Condens. Matter **12**, 9667 (2000).

6. A. Gencer, I. Ercan and B. Özcelik, *Harmonic susceptibilities of an alloy of* $Ni_{77}Mn_{23}$, J. Phys.: Condens. Matter **10**, 191 (1998).

7. T. Sato and Y. Miyako, *Nonlinear susceptibility and specific heat of* $(Pd_{0.9966}\ Fe_{0.0034})_{0.95}Mn_{0.05}$, J. Phys. Soc. Jpn. **51**, 1394 (1981).

8. T. Shirane, T. Moriya, T. Bitoh, A. Sawada, H. Aida and S. Chikazawa, *Nonlinear susceptibility of Ni near the curie temperature*, J. Phys. Soc. Jpn. **64**, 951 (1995).

9. S. Chikazawa, H. Arisawa, T. Bitoh, T. Kikuchi, N. Hasegawa and S. Taniguchi, *Linear and nonlinear susceptibilities of amorphous* $Fe_{10}Ni_{70}B_{19}Si_1$ *alloy*, J. Magn. Magn. Mater. **90-91**, 343 (1990).

10. T. Taniyama and I. Nakatani, *Nonlinear susceptibility of ferromagnetic* $Ga_{0.6}Mo_2S_4$*spinel*, J. Magn. Magn. Mater. **177-181**, 263 (1998).

11. S. Nair and A. Banerjee, *Probing a ferromagnetic critical regime using nonlinear susceptibility*, Phys. Rev. B **68**, 094408 (2003).

12. V. A. Ryzhov, A. V. Lazuta, V. P. Khavronin, I. I. Larionov, I. O. Troaynchuk and D. D. Khalyavin, *Linear and nonlinear critical magnetic properties and transport in* $Nd_{0.75}Ba_{0.25}MnO_3$ *single crystal: Evidence for its anomalous critical behavior near* T_C, Solid State Commun. **130**, 803 (2004).

13. V. A. Ryzhov, A. V. Lazuta, I. A. Kiselev, V. P. Khavronin, P. L. Molkanov, I. O. Troaynchuk and S. V. Trukhanov, *Unusual peculiarities of paramagnet to ferromagnet phase transition in* $La_{0.88}MnO_{2.91}$, J. Magn. Magn. Mater. **300**, e159 (2006).

14. F. Canepa, S. Cirafici, M. Napoletano and R. Masini, *Nonlinear effects in the ac magnetic susceptibility of selected magnetic materials*, J. Alloys Compd. **442**, 142 (2007).

15. A. P. Ramirez, P. Coleman, P. Chandra, E. Brück, A. A. Menovsky, Z. Fisk and E. Bucher, *Nonlinear susceptibility as a probe of tensor spin order in* URu_2Si_2, Phys. Rev. Lett. **68**, 2680 (1992).

16. N. Narita and I. Yamada, *Nonlinear Magnetic-Susceptibility of Two-Dimensional Magnets* $(C_nH_{2n+1}NH_3)_2CuCl_4$ *with n = 1, 2 and 3* , J. Phys. Soc. Jpn. **65**, 4054 (1996).

17. V. Tsurkan, J. Hemberger, M. Klimm, A. Loidl, S. Horn and R. Tidecks, *Ac susceptibility studies of ferrimagnetic* $FeCr_2S_4$ *single crystals*, J. Appl. Phys. **90**, 4639 (2001).

18. S. Nair and A. K. Nigam, *A re-entrant canted antiferromagnetic state in the Mn site substituted manganite* $La_{0.46}Sr_{0.54}Mn_{0.98}Cr_{0.02}O_3$, Europhys. Lett. **84**, 37008 (2008).

19. I. Zivkovic, V. P. S. Awana and H. Berger, *Nonlinear magnetic response in ruthenocuprates*, Eur. Phys. J. B **62**, 423 (2008).

20. Yugandhar Bitla et al., unpublished data.

21. Yugandhar Bitla, S. N. Kaul, L. Fernández Barquín, J. Gutiérrez, J. M. Barandiarán and A. Peña, *Observation of isotropic-dipolar to isotropic-Heisenberg crossover in Co-and Ni-substituted manganites*, New J. Phys. **12**, 093039 (2010).

22. A. D. Bruce and A. Aharony, *Critical exponents of ferromagnets with dipolar interactions: Second-order* ε *expansion*, Phys. Rev. B **10**, 2078 (1974).

Chapter 4

Charge and spin states of Co and Ni ions in TM doped LPMO manganites

An elaborate ac magnetic susceptibility data analysis presented in this chapter (i) enables the first observation of a crossover from a three-dimensional ($d = 3$) *isotropic long-range dipolar behaviour in the asymptotic critical region to* ($d = 3$) *isotropic Heisenberg behaviour outside in the manganite system* $La_{0.7}Pb_{0.3}Mn_{1-y}(Co, Ni)_yO_3$*, and (ii) brings out clearly the importance of dipole-dipole interactions in establishing long-range ferromagnetic order in the insulating state. The final charge and spin states of Co and Ni ions, substituting for the* Mn^{3+} *and/or* Mn^{4+} *ions, are arrived at using a scenario of substitution that is consistent with not only the present results but also with the previously published structural, thermo-gravimetric, bulk magnetization, dc magnetic susceptibility and electrical resistivity data on the same system. A marked similarity between the magnetic behaviour of the manganite system in question and the quenched random-exchange*

ferromagnets, within and outside the critical region, suggests that the percolation model forms an adequate description of the ferromagnetic-metal to paramagnetic-insulator transition.

4.1 Introduction

A rich diversity and complex nature of the physical phenomena occurring in hole-doped manganite perovskites $R^{3+}_{1-x}A^{2+}_{x}Mn^{3+}_{1-x}Mn^{4+}_{x}O^{2-}_{3}$ (R = La, Sm, Pr, Nd ; A = Ca, Sr, Ba, Pb, Cd) has generated an overwhelming interest in the study of such systems (for comprehensive reviews, see Refs: [1-7]). A quantitative, or in some cases even qualitative, understanding of these physical phenomena necessitated a theoretical approach that goes beyond the double exchange (DE) mechanism, initially proposed for metallic ferromagnetism, in recognizing the importance of (i) the superexchange between the nearest-neighbor localized t_{2g} spins, which can be antiferromagnetic (AF), or even ferromagnetic (FM), depending on the relevant e_g orbital configurations, (ii) the strong coupling of the two-fold degenerate e_g orbitals to the octahedral symmetry-breaking Jahn-Teller (JT) lattice modes, and (iii) the strong on-site Mott-Hubbard Coulomb repulsion between two e_g electrons in different orbitals. By contrast, the DE formalism relies on a large Hund coupling between the e_g-electron spin and the localized t_{2g}-spin on the same site to optimize the kinetic energy, or the inter-site hopping amplitude, of the e_g-electrons. However, no single theoretical model is able to adequately handle the interplay between the charge, spin, orbital and lattice degrees of freedom and thereby account for the existence of a variety of phases in the magnetic phase diagram of manganites.

A partial substitution of Mn by TM (TM = Fe, Co, Ni) ions in hole-doped $La_{1-x}A_xMn_{1-y}TM_yO_3$ manganites alters the magnetic and transport properties of the host (LAMO) in a specific fashion depending on the charge and spin states of the TM solute ions, and thereby provides a fertile testing ground for the theoretical models proposed hitherto. Bulk of such studies have been carried out on the $La_{0.7}Pb_{0.3}Mn_{1-y}(Fe, Co, Ni)_yO_3$ manganite system [8-14] rather than on the A = Ca or Sr counterparts [15-18]. While there seems to be a broad consensus [8,9,11,15-18] that the Fe ion exists in the Fe^{3+} high-spin (HS) $t_{2g}^3e_g^2$ S = 5/2 state, the opinions about the charge and spin states of Co and Ni ions are sharply divided. The configurations such as Co^{3+} low-spin (LS) [11,13] $t_{2g}^6e_g^0$ S = 0, Co^{3+} covalent intermediate-spin (IS) [13, 19, 20] $t_{2g}^5e_g^1$ S = 1, Co^{3+} HS [9] $t_{2g}^4e_g^2$ S = 2, Co^{4+} HS [13] $t_{2g}^3e_g^2$ S = 5/2, and Ni^{2+} HS [10] $t_{2g}^6e_g^2$ S = 1, Ni^{3+} LS [14] $t_{2g}^6e_g^1$ S = 1/2, Ni^{3+} HS [9] $t_{2g}^5e_g^2$ S = 3/2 have been invoked in the case of Co and Ni ions. In all the cases, the solute Fe, Co, Ni ions are supposed to partially substitute the Mn^{3+} HS $t_{2g}^3e_g^1$ S = 2 ion. Following the realization that the critical behavior of a spin system in the vicinity of a magnetic order-disorder phase transition is solely governed by the nature of the magnetic ordering present, critical phenomena have been investigated in a large number of manganite systems. However, conflicting reports about the critical exponents, that characterize the ferromagnetic (FM)- paramagnetic (PM) phase transition, have rendered such studies inconclusive. In this context, a compilation of the susceptibility critical exponent γ values (reported in the literature [21–24, 26–29, 29–39]), presented in Table 4.1, serves to highlight a wide disparity between the values of γ for the same system and the erratic variation of γ within a given compositional series. Since the reported exponent values either range between the values theoretically predicted for

Table 4.1: *Reported values of the susceptibility critical exponent for manganites (a-single crystal and b-polycrystalline system).*

System	Method	T_C (K)	γ	ϵ range (10^{-3})	Refs.
$La_{0.8}Ca_{0.2}MnO_3^a$	BM	174	1.45		[21]
$La_{0.8}Ca_{0.2}MnO_3^a$	ACS	179.5(5)	1.33(1)	25 - 65	[22]
$La_{0.79}Ca_{0.21}MnO_3^a$	ACS	182(1)	1.65(1)	30 - 120	[22]
$La_{0.7}Ca_{0.3}MnO_3^b$	BM	248	1.2		[23]
$La_{0.67}Ca_{0.33}(Mn_{0.9}Ga_{0.1})O_3^b$	BM	115.88(6)	1.362(2)		[24]
$La_{0.6}Ca_{0.4}MnO_3^b$	BM	265.5(5)	1.03(5)	2 - 40	[29]
$La_{0.73}Ba_{0.27}MnO_3^a$	ACS	245.0(5)	1.392(5)	2 - 30	[26]
$La_{0.7}Ba_{0.3}MnO_3^a$	ACS	310.0(5)	1.41(2)		[27]
$La_{0.67}Ba_{0.33}MnO_3^b$	BM	338.1(2)	1.29(2)		[28]
$La_{0.67}(Ba_{0.5}Ca_{0.5})_{0.33}MnO_3^b$	BM	306.1(2)	1.12(2)		[28]
$La_{0.67}(Ba_{0.25}Ca_{0.75})_{0.33}MnO_3^b$	BM	276.7(2)	1.12(3)		[28]
$La_{0.67}Ba_{0.33}Mn_{0.99}Sn_{0.01}O_3^b$	BM	327.6(4)	1.17(2)		[29]
$La_{0.67}Ba_{0.33}Mn_{0.98}Sn_{0.02}O_3^b$	BM	315.7(2)	1.07(2)		[29]
$La_{0.60}Ba_{0.40}Mn_{0.99}Sn_{0.01}O_3^b$	BM	330.5(2)	1.28(3)		[29]
$La_{0.60}Ba_{0.40}Mn_{0.98}Sn_{0.02}O_3^b$	BM	310.2(3)	1.10(2)		[29]
$La_{0.875}Sr_{0.125}MnO_3^a$	BM	186	1.38(3)		[30]
$La_{0.8}Sr_{0.2}MnO_3^b$	BM	315.71	1.08(3)	- 6.2 - 5.6	[31]
$La_{0.75}Sr_{0.25}MnO_3^a$	ACS	345.6	1.27(6)	0.6 - 6	[32]
$La_{0.7}Sr_{0.3}MnO_3^a$	BM	354.0(2)	1.22(3)	2 - 30	[33]
$La_{0.7}Sr_{0.3}MnO_3^b$	BM	362.9	1.083		[34]
$La_{0.7}Sr_{0.3}Mn_{0.95}Al_{0.05}O_3^b$	BM	336.24	1.001		[34]
$La_{0.7}Sr_{0.3}Mn_{0.95}Ti_{0.05}O_3^b$	BM	303.7	1.149		[34]
$La_{0.7}Sr_{0.3}Mn_{0.8}Ti_{0.2}O_3^b$	BM	150.1	1.002		[35]
$La_{0.67}Sr_{0.33}MnO_3^b$	BM	369.2	1.13(1)		[36]
$La_{0.67}Sr_{0.33}Mn_{0.99}Mo_{0.01}O_3^b$	BM	367.9	1.17(1)		[36]
$La_{0.67}Sr_{0.33}Mn_{0.98}Mo_{0.02}O_3^b$	BM	366.7	1.15(1)		[36]
$La_{0.67}Sr_{0.33}Mn_{0.97}Mo_{0.03}O_3^b$	BM	365.8	1.25(1)		[36]
$La_{0.67}Sr_{0.33}Mn_{0.96}Mo_{0.04}O_3^b$	BM	364.6	1.13(1)		[36]
$La_{0.67}Sr_{0.33}Mn_{0.94}Mo_{0.06}O_3^b$	BM	360.8	1.17(1)		[36]
$La_{0.67}Sr_{0.33}Mn_{0.99}Sn_{0.01}O_3^b$	BM	365.4(6)	1.10(1)		[29]
$La_{0.67}Sr_{0.33}Mn_{0.98}Sn_{0.02}O_3^b$	BM	352.6(1)	1.26(2)		[29]
$La_{0.60}Sr_{0.40}Mn_{0.99}Sn_{0.01}O_3^b$	BM	360.5(1)	1.19(1)		[29]
$La_{0.60}Sr_{0.40}Mn_{0.98}Sn_{0.02}O_3^b$	BM	354.5(2)	1.38(2)		[29]
$La_{0.9}Pb_{0.1}MnO_3^b$	ACS	162	1.456		[37]
$La_{0.7}Pb_{0.3}MnO_3^a$ $(H \geq 1T)$	BM	334.4	1.27(2)	- 40 - 40	[38]
$La_{0.7}Pb_{0.3}MnO_3^a$ $(H \leq 1T)$	BM	336.5	1.0(1)		[38]
$La_{0.67}Pb_{0.33}MnO_3^b$	ACS	340.5(5)	1.39(6)		[39]

different universality classes (e.g., three-dimensional (3D) isotropic short-range Heisenberg $d = 3, n = 3$ with [40] $\gamma = 1.386(4)$, three-dimensional isotropic short-range Ising $d = 3, n = 1$ with [40] $\gamma = 1.241(2)$, mean-field (MF) with $\gamma = 1.0$, where d and n are the space/lattice dimensionality and spin dimensionality, respectively) or are completely anomalous, the nature of interactions that sustain FM order below T_C remains obscure. Consequently, the basic issue of whether the percolation picture or the two-fluid model forms a correct description of both FM-PM and the associated metal-insulator transition, cannot be unambiguously resolved.

The unresolved issues mentioned-above and the possibility that non-asymptotic data could be responsible for the chaotic dispersion in the γ values, prompted us to undertake an exhaustive study of the critical behavior near the FM-PM phase transition in the $La_{0.7}Pb_{0.3}Mn_{1-y}(Co, Ni)_yO_3$ ($y = 0, 0.1, 0.2, 0.3$) system. The critical behavior of $y = 0$ (the LPMO host) turns out to be markedly different from that of the Co- and Ni-doped (i.e., $y \neq 0$) samples. Barring a systematic trend with y, the compositions $y = 0.1, 0.2, 0.3$ exhibit essentially the same behavior in the critical region. Therefore, only the representative results (obtained on the compositions $y = 0$ and $y = 0.2$) are presented and the observed trend with y is highlighted as and when required.

4.2 Experimental details

Extensive ac magnetic susceptibility measurements have been carried out on polycrystalline samples of nominal composition $La_{0.7}Pb_{0.3}Mn_{1-y}(Co, Ni)_yO_3$

($y = 0, 0.1, 0.2, 0.3$) at an ac driving field of rms amplitude, ranging from 0.1 Oe to 10 Oe, and frequency, from 100 Hz to 10 kHz, over a wide temperature range $4K \leq T \leq 355K$ that embraces the critical region. These samples were prepared by the sol-gel method [8], thoroughly characterized by scanning electron microscopy, energy dispersive absorption of x-rays and neutron diffraction [13, 14], and are the same as those used for bulk magnetization, dc magnetic susceptibility and electrical resistivity measurements [12-14]. In the Ni and Co containing compounds, the presence of Ni^{2+}, Ni^{3+}, Ni^{4+} and Co^{2+}, Co^{3+}, Co^{4+} at different temperatures [13, 14] was revealed by the thermo-gravimetric analysis. The redox titration yielded the Mn^{3+}/Mn^{4+} ratio as 0.35/0.65, 0.28/0.62, 0.20/0.60 and 0.10/0.60 for the compositions y =0, 0.1, 0.2 and 0.3, respectively. Note that the ratio $Mn^{3+}/Mn^{4+} = 0.35/0.65$ in the parent LPMO compound differs radically from that (0.70/0.30) expected for the stoichiometric LPMO compound. This departure from the expected Mn^{3+}/Mn^{4+} ratio is caused by the oxygen non-stoichiometry $\delta = 0.17$ which gives rise to vacancies ($\Box$) at the cation sites in accordance with the formula $La^{3+}_{[0.7\times\frac{3}{(3+\delta)}]}\Box_{[\frac{\delta}{(3+\delta)}]}Pb^{2+}_{[0.3\times\frac{3}{(3+\delta)}]}Mn^{3+}_{[\frac{3(0.7-2\delta)}{(3+\delta)}]}Mn^{4+}_{[\frac{3(0.3+2\delta)}{(3+\delta)}]}\Box_{[\frac{\delta}{(3+\delta)}]}O_3^{2-}$. Detailed structural characterization by neutron diffraction confirmed that all the samples are *single phase* and belong to the trigonal space group ($R\overline{3}c$). The Ni or Co substitution causes a slight reduction in the unit-cell volume (average volume change, $< \Delta v/v >= 9 \times 10^{-4}$ per at. % Ni and 7.9×10^{-4} per at. % Co) but leaves the remaining structural parameters such as the tolerance factor, $Mn - O$ bond lengths as well as $Mn - O - Mn$, $O - Mn - O$ bond angles essentially unaltered. The compositions $La_{0.7}Pb_{0.3}MnO_3$, $La_{0.7}Pb_{0.3}Mn_{0.8}Ni_{0.2}O_3$ and $La_{0.7}Pb_{0.3}Mn_{0.8}Co_{0.2}O_3$ are henceforth referred to as LPMO, $Ni_{0.2}$ and $Co_{0.2}$, respectively.

4.3 Data analysis, results and discussion

4.3.1 Linear magnetic susceptibility

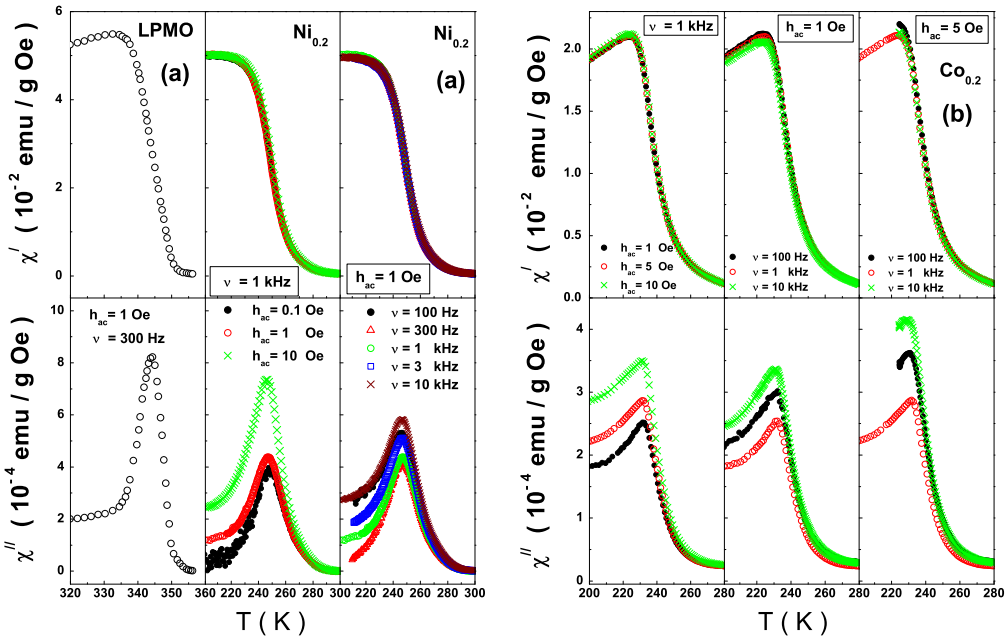

Figure 4.1: *The real, χ', and imaginary, χ'', components of ac susceptibility as a function of temperature at a fixed rms field amplitude, $h_{ac} = 1Oe$, and variable frequency (ν) or at fixed ν and varying h_{ac} for (a) LPMO $\equiv La_{0.7}Pb_{0.3}MnO_3$ and $Ni_{0.2} \equiv La_{0.7}Pb_{0.3}(Mn_{0.8}Ni_{0.2})O_3$ and (b) $Co_{0.2} \equiv La_{0.7}Pb_{0.3}(Mn_{0.8}Co_{0.2})O_3$.*

Figure 4.1 displays the temperature dependence of the real (reactive/dispersion), $\chi'(\nu)$, and imaginary (dissipative/absorption), $\chi''(\nu)$, components of ac susceptibility (ACS) for LPMO measured at an ac driving magnetic field of rms amplitude $h_{ac} = 1Oe$ and frequency, $\nu = 300Hz$, and for $Ni_{0.2}$ and $Co_{0.2}$ measured either at fixed frequency $\nu = 1kHz$ and rms am-

plitudes $h_{ac} = 0.1, 1, 5, 10Oe$ or at $h_{ac} = 1Oe$ in the frequency range $100Hz \leq \nu \leq 10kHz$ over a wide temperature range (that embraces the critical region near the FM-PM phase transition). Recognizing that the critical fluctuations of the order parameter (spontaneous magnetization) have *maximum amplitude* as well as *range* (divergent spin fluctuation-spin fluctuation correlation length) at the critical point, T_C, and that the fluctuations are directly related to dissipation (the fluctuation-dissipation theorem), the temperature T_p at which a sharp peak in $\chi''(T)$ occurs provides a reasonably accurate estimate of T_C. No discernible shift in T_p, or equivalently in the Curie temperature T_C, over a frequency range spanning two decades testifies to a *true thermodynamic* phase transition at T_C. Since χ'' is at least two orders of magnitude smaller (Fig. 4.1) than χ' at any temperature, χ' decides the magnitude of ACS. In the PM state ($T \gtrsim T_C$), the inverse *intrinsic* susceptibility, $\chi^{-1}(T)$, varies with temperature as

$$\chi^{-1}(T) = A_{eff}(T) \ \ \epsilon^{\ \gamma_{eff}(T)} \qquad (\epsilon > 0) \tag{4.1}$$

where $\epsilon = (T - T_C)/T_C$ and γ_{eff} (A_{eff}) is the effective critical exponent (amplitude). $\chi^{-1}(T)$ is related to the *measured* $\chi'^{\ -1}(T)$ via the demagnetizing factor, N, as

$$\chi'^{\ -1}(T) = \chi^{-1}(T) + 4\pi N \tag{4.2}$$

According to Eq.(4.1), as $T \to T_C$, $\chi^{-1}(T) \to 0$, and $\gamma_{eff}(T) \to \gamma$ (the asymptotic critical exponent) with the result that $\chi'^{\ -1}(T) \to 4\pi N$ from Eq.(4.2).

Estimation of T_C

The 'range-of-fit' (ROF) analysis [41-44] of the $\chi'^{-1}(T)$ data, based on Eqs.(4.1) and (4.2), permits an accurate determination of T_C and N, and hence of $A_{eff}(T)$ and $\gamma_{eff}(T)$, as elucidated below. Since $T_p \cong T_C$, T_C is *held constant* at *one* of the temperatures ($\approx 80\ mK$ apart), in the range $T_p - 10K \leq T_C \leq T_p + 10K$, at which χ' has been measured. The parameters N, A_{eff} and γ_{eff} are varied to optimize agreement between the experimentally observed and theoretically predicted (by Eqs.(4.1) and (4.2)) $\chi'^{-1}(T)$ over the temperature range $\epsilon_{min} \leq \epsilon \leq \epsilon_{max}$, where ϵ_{min} corresponds to the first data point above T_C. In the ROF analysis, the temperature range $\epsilon_{min} \leq \epsilon \leq \epsilon_{max}$ of the fit is varied by keeping ϵ_{min} fixed and progressively raising $\epsilon \equiv \epsilon_{max}$ (by including one more data point above T_C for successive fits) and the variations of N, A_{eff} and γ_{eff} with ϵ are monitored. The correct choice of T_C (and hence of N, A and γ) is the one that yields constant values for N, A_{eff} and γ_{eff} in the asymptotic critical region, i.e., $N(\epsilon) \rightarrow \chi'^{-1}(T_C)/4\pi$, $A_{eff}(\epsilon) \rightarrow A$ and $\gamma_{eff}(\epsilon) \rightarrow \gamma$ as $\epsilon \rightarrow 0$. Figure 4.2 illustrates this behavior of $N(\epsilon)$, $A_{eff}(\epsilon)$ and $\gamma_{eff}(\epsilon)$, as an outcome of the ROF analysis, by treating the $\chi'^{-1}(T)$ data taken at $h_{ac} = 1Oe$ and $\nu = 1kHz$ on $Ni_{0.2}$ as an example. Out of the temperature variations of N, A_{eff} and γ_{eff} yielded by the ROF analysis for the three specified choices of T_C, the criterion that $N(\epsilon)$, $A_{eff}(\epsilon)$ and $\gamma_{eff}(\epsilon)$ should attain their limiting but *constant* values as $\epsilon \rightarrow 0$ is satisfied only for the (*correct*) choice $T_C = 247.43K$. The values of T_C determined in this way are displayed in tables 4.2 and 4.3. Figure 5.3 demonstrates that the value for T_C, so obtained, exactly coincides with the temperature corresponding to the inflection point (where $d\chi'/dT$ goes through a *sharp well-defined minimum*) in the $\chi'(T)$

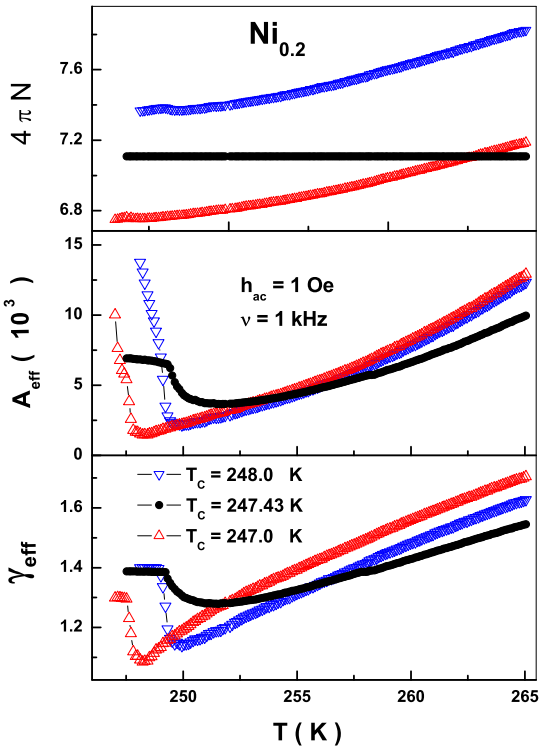

Figure 4.2: *Temperature variations of the parameters $4\pi N$, A_{eff} and γ_{eff} corresponding to three different choices of T_C yielded by the 'range-of-fit' analysis (see text for details).*

curve (compare the T_C values given in Fig. 4.2, Fig. 4.3 and tables 4.2-4.3) but lies just above (within 1 K) T_p, the temperature at which χ'' peaks. Another important observation is that the T_C of the parent compound gets depressed progressively as the Ni or Co concentration increases but the Co substitution depresses T_C (of the host) at a much faster rate (see also, [12-14]). The values of T_C, so determined, are in much closer agreement with the numerical estimates directly obtained earlier from the 'zero-field' neutron diffraction data [13, 14] than with those (less reliable values), deduced

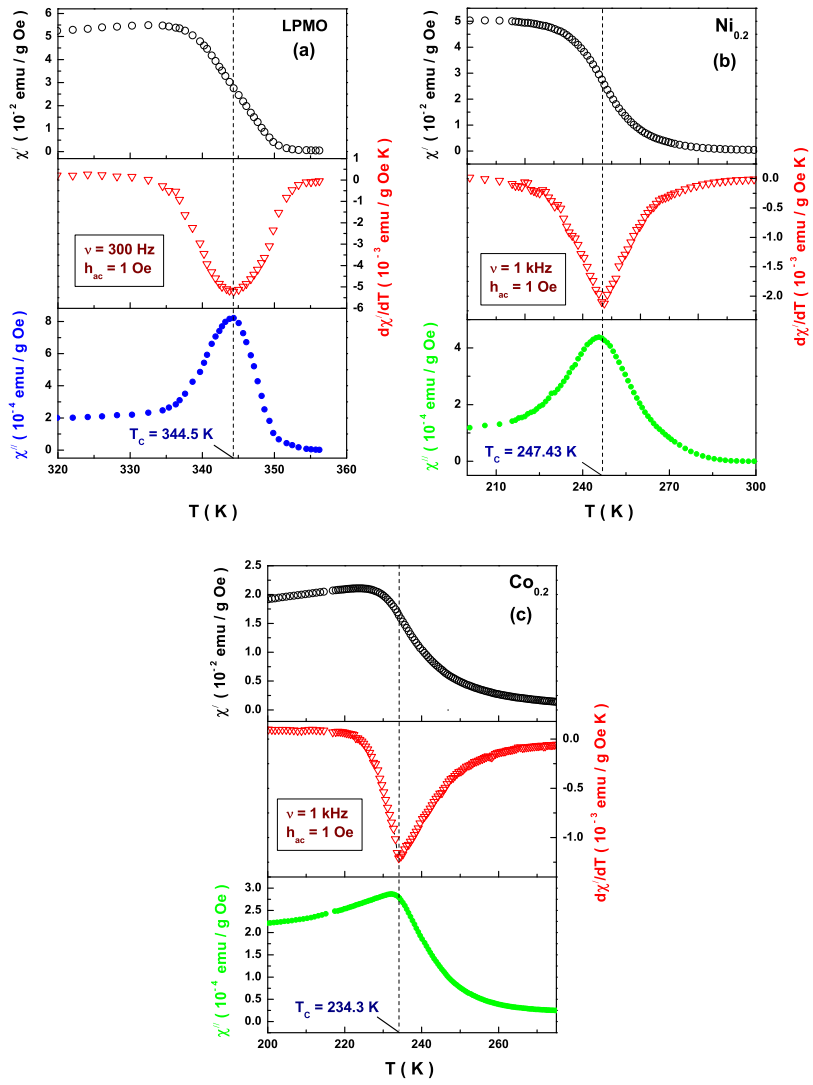

Figure 4.3: *Real part, χ', its temperature-derivative, $d\chi'/dT$, and imaginary part, χ'', of ac susceptibility as functions of temperature for (a) LPMO at $h_{ac} = 1Oe$, $\nu = 300Hz$, (b) $Ni_{0.2}$ at $h_{ac} = 1Oe$, $\nu = 1kHz$, and (c) $Co_{0.2}$ at $h_{ac} = 1Oe$, $\nu = 1kHz$.*

from the 'in-field' bulk magnetization data through an extrapolation to zero magnetic field.

Having determined the T_C correctly, the inverse intrinsic susceptibility, $\chi^{-1}(\epsilon)$, is obtained by subtracting $4\pi N(\epsilon = 0)$ from $\chi'^{-1}(\epsilon)$. The behavior of $\chi^{-1}(\epsilon)$ over a wide temperature range above T_C is shown in the insets of figure 4.4. $\chi^{-1}(\epsilon)$, in the critical region, is depicted in the upper panels of Fig. 4.4 and compared with the theoretical fits that use the 3D Heisenberg value of $\gamma_H = 1.386$ for the asymptotic critical exponent γ in Eq.(4.1). The bottom panels display the corresponding percentage deviation of the observed $\chi^{-1}(\epsilon)$ data from the theoretical fits plotted against the reduced temperature ϵ. These deviation plots demonstrate that the 3D Heisenberg value of γ adequately describes $\chi^{-1}(\epsilon)$ in the asymptotic critical region, more so in the LPMO compound.

The physical significance of such deviations, particularly at intermediate temperatures $\epsilon \approx 0.03$ within the critical region, for $Ni_{0.2}$ and $Co_{0.2}$, will become clear at a later stage when a theoretical explanation is provided for the γ_{eff} versus ϵ plots shown in figure 4.5. The salient features of $\gamma_{eff}(\epsilon)$ (Fig. 4.5) are as follows. (I) γ_{eff} in LPMO assumes the 3D isotropic Heisenberg value of $\gamma_H = 1.386(4)$ at $\epsilon < \epsilon^H$ and goes through a peak at $\epsilon_p \cong 0.01$ with $\gamma^p_{eff} \cong 2.45$ before approaching the mean-field value of $\gamma = 1$ at $\epsilon > 0.06$. (II) By contrast, *irrespective* of the Co or Ni concentration in the range $0.1 \leq y \leq 0.3$, a dip in $\gamma_{eff}(\epsilon)$ occurs at ϵ_{dip}, a peak at ϵ_p and γ_{eff} attains the values $\gamma_D \cong 1.39$, $\gamma_{dip} = 1.280(4)$ and $\gamma_H = 1.386(4)$ at $\epsilon \lesssim \epsilon^*$, ϵ_{dip} and ϵ^{**}, respectively. Note that the values of ϵ_{dip}, γ_{dip}, $\gamma_H(\epsilon = \epsilon^{**})$ and ϵ^{**} for different data sets taken on $Co_{0.2}$ and $Ni_{0.2}$ are listed in Tables 4.2 and 4.3. (IIIa) As y increases, ϵ^*, ϵ_{dip}, ϵ^{**} and ϵ_p shift to higher temperatures

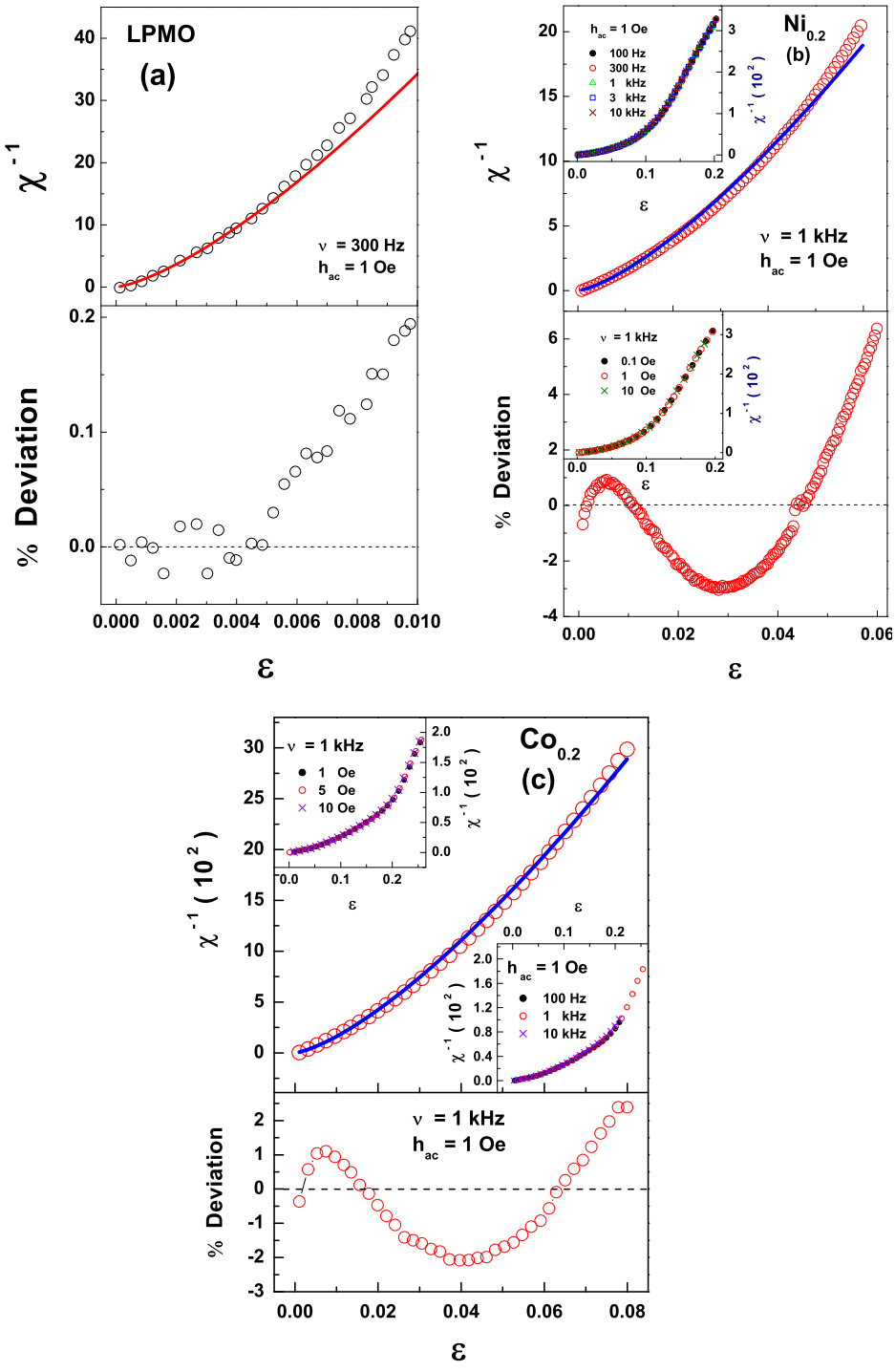

Figure 4.4: *Top panel compares the inverse intrinsic susceptibility, χ^{-1}, as a function of reduced temperature, $\epsilon = (T - T_C)/T_C$, measured (open cicles) in the critical region with the theoretical fit (continuous curve) based on Eq.(4.1) of the text with $\gamma = \gamma_{eff} = 1.386$ while the bottom panel depicts the corresponding percentage deviations of the experimental data from the fit for (a) LPMO, (b) $Ni_{0.2}$ and (c) $Co_{0.2}$. The insets in (b) and (c) show the $\chi^{-1}(\epsilon)$ over a very wide temperature range above T_C.*

while the peak value γ^p_{eff} increases. (IIIb) For a given y, e.g., $Co_{0.2}$ and $Ni_{0.2}$, ϵ^*, ϵ_{dip}, ϵ^{**} and ϵ_p are higher while γ^p_{eff} is lower in the case of Co. $\gamma_{eff}(\epsilon)$ of the type (I) has been observed [32, 45] previously in several spin systems with quenched random-exchange disorder, which behave as normal ferromagnets down to the lowest temperature. In sharp contrast, $\gamma_{eff}(\epsilon)$

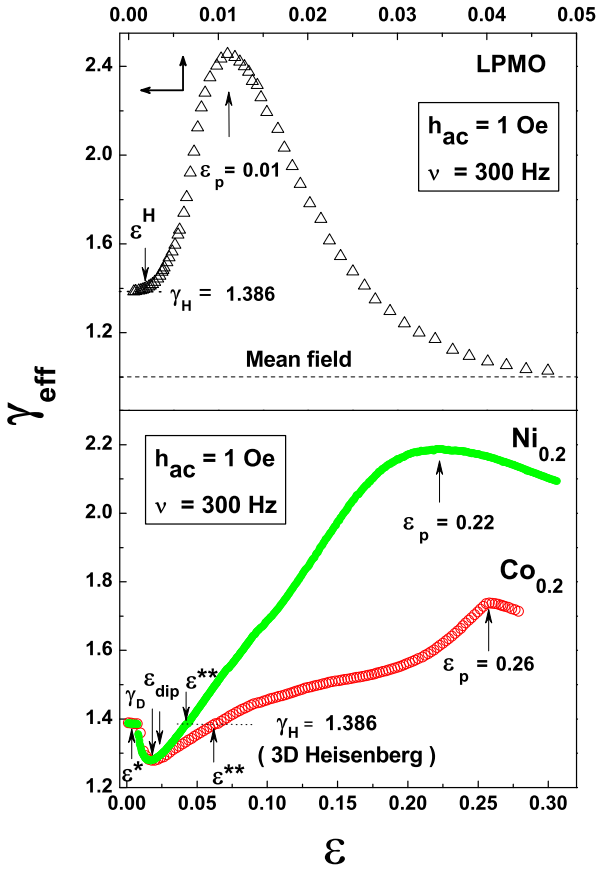

Figure 4.5: *The effective critical exponent for suceptibility, γ_{eff}, as a function of reduced temperature, $\epsilon = (T - T_C)/T_C$, for LPMO, $Ni_{0.2}$ and $Co_{0.2}$.*

of the type (II) + (III) occurs [32] in amorphous ferromagnets (a-FMs)

that have composition close to, but above, the percolation threshold for the appearance of long-range FM order and exhibit re-entrant behavior at low temperatures. Consistent with these observations, the composition $La_{0.7}Pb_{0.3}MnO_3$, corresponding to a Mn^{3+}/Mn^{4+} ratio that maximizes the DE interaction (and hence T_C), has a collinear FM ground state whereas in the composition range $0.1 \leq y \leq 0.3$, the Co- or Ni-substituted LPMO undergoes a transition to the re-entrant-like state (where long-range FM order coexists with cluster spin-glass-like order) at $T \ll T_C$ [8-14]. In a-FMs, the type (I) $\gamma_{eff}(\epsilon)$ has found the following interpretation in terms of the percolation model [45] in which finite FM clusters coexist with an infinite FM network for $T \leq T_C$. The spin-spin correlation length, $\xi(T)$, of the $d = 3$ Heisenberg-like FM network diverges at $T = T_C$ so that the presence of the spin clusters is not felt in the asymptotic critical region (ACR), $\epsilon \leq \epsilon^H$, where the $d = 3$ Heisenberg-like critical behavior is observed. With temperature increasing above T_C, $\xi(T)$ declines rapidly and infinite FM network breaks up into finite FM clusters so that at $T > T_C$, finite FM clusters are embedded in a paramagnetic (PM) matrix. At $\epsilon = \epsilon^H$, $\xi(\epsilon)$ equals the caliper dimension of the largest spin cluster, $(d_c)_{max}$, with the result that the magnetic inhomogeneity in the spin system is now no longer averaged out and γ_{eff} begins to increase as ϵ exceeds ϵ^H till it attains a maximum value γ^p_{eff} at $\epsilon = \epsilon_{max}$ when $\xi(\epsilon) \cong (d_c)_{min}$= smallest cluster size. It follows that *smaller* the average cluster size and *narrower* the cluster size distribution, *higher* the values of ϵ^H and ϵ_p, *narrower* the peak in $\gamma_{eff}(\epsilon)$ and *lower* the peak value γ^p_{eff} (for details, see [45]).

Analogy with the percolation picture

In the case of manganites, *a percolation picture* (strikingly similar to that described above), in which *metallic FM clusters* of various sizes coexist with the *insulating PM matrix* at $T > T_C$, has gained wide acceptance [3,5] over the years. As the temperature is lowered towards T_C, the localized nearest-neighbor t_{2g}-spins (coupled by Heisenberg-like interactions) in the insulating PM phase order better progressively due to the growing spin-spin correlations between them. Ordering of t_{2g}-spins, in turn, facilitates hopping of e_g-electrons and hence the metallic FM clusters grow in size. For $\epsilon \leq \epsilon^H$, $\xi(T)$ is much larger than the size of the largest FM cluster and a $d = 3$ Heisenberg-like critical behavior is expected, as observed in Fig. 4.5 for LPMO. However, at $T = T_C$ and for temperatures below T_C, metallic FM clusters coalesce to form an infinite percolating network, in which the finite insulating AF clusters are embedded, and a transition from the insulating ($T > T_C$) to metallic ($T < T_C$) state occurs. Generally, at constant hole density, the transition between the electronic phase-separated metallic FM and insulating AF/CO (charge ordered) phases in manganites is of the *first order*. However, the disorder introduced by a partial but random replacement of R^{3+} ions by A^{2+} ions of larger/smaller ionic radius, and in the present case by the substitution at the Mn site, results in randomly distributed coexisting insulating and metallic percolative clusters. The temperature induced growth of clusters and the percolation of such clusters renders the insulating PM to metallic FM transition *continuous* (second order).

Although the mechanisms responsible for the formation of finite FM

clusters and FM network/matrix are radically different in the percolation pictures for a-FMs and manganites, the type of interplay between $\xi(T)$ and the temperature-dependent length scale introduced by the finite FM spin clusters at $T > T_C$ [45] permits the conclusion that with respect to the parent compound $y = 0$, the average FM cluster size reduces while the cluster size distribution narrows down as one goes from Ni to Co for a given y. Monte Carlo (MC) simulations [3] on hole-doped manganites have shown that weaker the disorder, larger the cluster size. In view of this MC result, the above inference about the cluster size and cluster size distribution asserts that the disorder increases in the sequence LPMO $\rightarrow$ Ni- $\rightarrow$ Co-substituted LPMO.

Figure 4.6 shows an enlarged view of the steep minimum (dip) in $\gamma_{eff}(\epsilon)$, witnessed in the case of $Ni_{0.2}$ and $Co_{0.2}$ at temperatures close to T_C in Fig. 4.5, for the $\chi'(T)$ data taken at $h_{ac} = 1Oe$ for different frequencies (ν) and at $\nu = 1kHz$ for different values of h_{ac}. With a view to bring out clearly the physical significance of the dip in $\gamma_{eff}(\epsilon)$, and hence of the type (II)+(III) behavior of $\gamma_{eff}(\epsilon)$, a brief account of the relevant theoretical results is given below. Motivated by the fact that long-range dipole-dipole interaction between spins (magnetic dipole moments) is invariably present in all *real* magnetic materials, the renormalization group (RG) calculations [46] on an *isotropic* spin system with $d = 3$ and $n = 3$ revealed that dipolar perturbations render the isotropic short-range Heisenberg (IH) fixed point of RG unstable and give rise to a new *stable* 'isotropic dipolar' (ID) fixed point. However, the critical exponents, characterizing the ID fixed point, calculated to two-loop order, are very close [47] to (within 0.5%) those associated with $d = 3$ *pure* IH ferromagnet. Subsequent theoretical in-

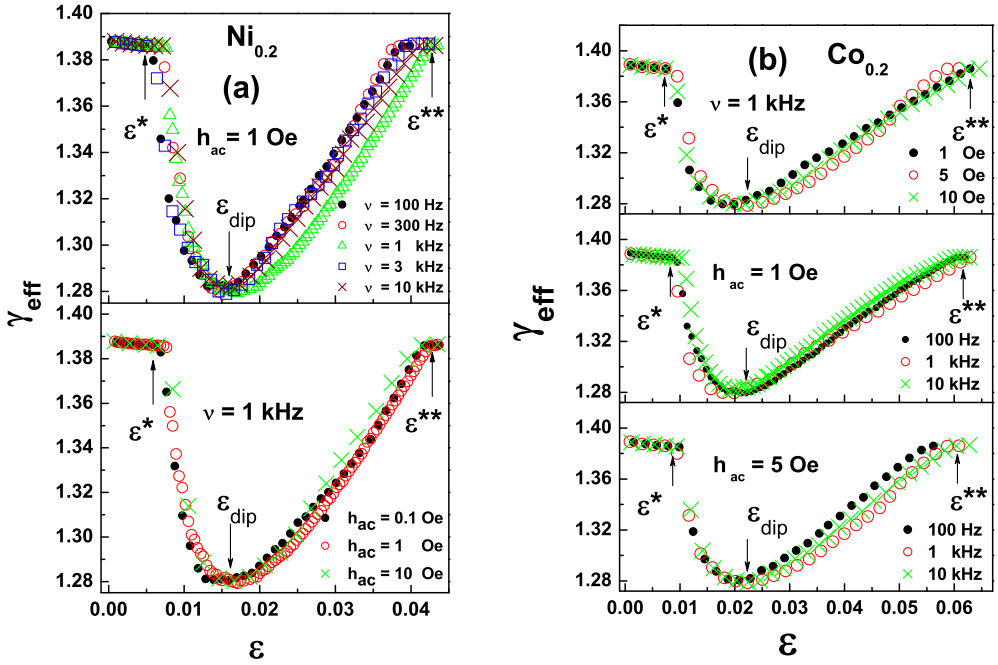

Figure 4.6: *The effective critical exponent for suceptibility, γ_{eff}, as a function of reduced temperature, $\epsilon = (T - T_C)/T_C$, in the critical regime (that embraces the crossover region) for (a) $Ni_{0.2}$ and (b) $Co_{0.2}$.*

vestigations, using different RG methods [48-51], dealt exclusively with the thermally-induced crossover from a critical behavior at $T > T_C$, governed by the short-range isotropic exchange (Heisenberg) interaction, to the asymptotic ($\epsilon \to 0$) critical behavior dictated by the long-range dipolar interaction. Irrespective of the RG method used, the most remarkable outcome of these theoretical approaches is the occurrence of a deep minimum in $\gamma_{eff}(\epsilon)$ in the crossover region ($\epsilon > 0$) which turns out to be a *universal* feature of the isotropic $d = 3$, $n = 3$ spin systems with *weak* dipolar interactions (com-

pared to the Heisenberg exchange interactions). The numerical results of these RG calculations are summarized in table 4.4.

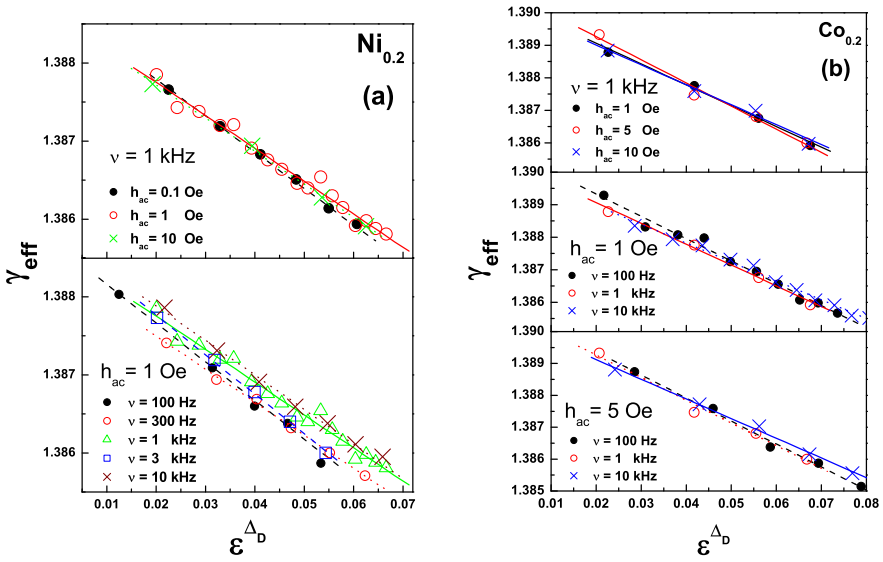

Figure 4.7: *γ_{eff} versus ϵ^{Δ_D} data (symbols) taken in the asymptotic critical region $0 \lesssim \epsilon \leq \epsilon^*$ and the linear fits (straight lines through the data points) based on Eq.(6.17) for (a) $Ni_{0.2}$ and (b) $Co_{0.2}$.*

Comparison with theory

The prediction of a dip in $\gamma_{eff}(\epsilon)$ prompted us to attempt a quantitative comparison between the theory and experiment. These RG calculations [48-51] yield the final expressions for susceptibility and its effective critical exponent, defined as [52] $\gamma_{eff}(\epsilon) = \partial[ln\chi^{-1}(\epsilon)]/\partial(ln\epsilon)$, as

$$\chi(\tau) = \Gamma \;\; \tau^{\gamma_H/\phi} \;\; (1-\tau)^{-\gamma_D} \;\; p(\tau) \tag{4.3}$$

Table 4.2: *Critical-point parameters for* $Ni_{0.2}$.

Parameters	$\nu = 100Hz$	$\nu = 300Hz$	$\nu = 1kHz$			$\nu = 3kHz$	$\nu = 10kHz$
	$h_{ac} = 1Oe$	$h_{ac} = 1Oe$	$h_{ac} = 0.1Oe$	$1Oe$	$10Oe$	$h_{ac} = 1Oe$	$h_{ac} = 1Oe$
Fit range							
ϵ (10^{-4})	4 - 49	5 - 64	5 - 69	4 - 77	4 - 65	5 - 50	5 - 71
T_C (K)	247.50(2)	247.42(3)	247.40(3)	247.43(3)	247.49(2)	247.43(2)	247.46(3)
γ_D	1.389(2)	1.389(3)	1.389(4)	1.389(3)	1.389(2)	1.389(4)	1.389(2)
a_χ	0.090(8)	0.077(2)	0.085(4)	0.077(3)	0.077(2)	0.092(2)	0.080(6)
ϵ_{dip}	0.015(3)	0.014(3)	0.014(3)	0.017(3)	0.017(2)	0.016(2)	0.014(3)
γ_{dip}	1.282(3)	1.279(3)	1.281(3)	1.280(2)	1.280(2)	1.279(2)	1.283(4)
$\gamma_H(\epsilon = \epsilon^{**})$	1.386(3)	1.386(2)	1.386(3)	1.386(2)	1.386(5)	1.386(3)	1.386(5)
ϵ^{**}	0.039(2)	0.038(2)	0.041(2)	0.041(2)	0.040(3)	0.039(3)	0.041(2)

Table 4.3: *Critical-point parameters for* $Co_{0.2}$.

Parameters	$\nu = 100Hz$		$\nu = 1kHz$			$\nu = 10kHz$	
	$h_{ac} = 1Oe$	$5Oe$	$1Oe$	$5Oe$	$10Oe$	$h_{ac} = 1Oe$	$5Oe$
Fit range ϵ (10^{-4})	4 - 87	7 - 99	5 - 75	5 - 73	5 - 74	3 - 94	6 - 94
T_C (K)	234.40(3)	234.45(2)	234.35(3)	234.38(3)	234.45(2)	234.40(4)	234.40(3)
γ_D	1.391(3)	1.391(2)	1.390(2)	1.391(4)	1.390(2)	1.390(2)	1.390(2)
a_χ	0.125(6)	0.131(6)	0.116(8)	0.129(7)	0.111(5)	0.105(2)	0.112(4)
ϵ_{dip}	0.021(2)	0.021(2)	0.019(4)	0.022(3)	0.022(5)	0.019(3)	0.022(4)
γ_{dip}	1.280(3)	1.281(5)	1.280(5)	1.279(2)	1.280(2)	1.281(2)	1.279(2)
$\gamma_H(\epsilon = \epsilon^{**})$	1.386(2)	1.386(2)	1.386(2)	1.386(4)	1.386(3)	1.386(6)	1.386(3)
ϵ^{**}	0.060(2)	0.056(3)	0.063(2)	0.059(3)	0.062(2)	0.060(2)	0.060(2)

$$\gamma_{eff}(\tau) = (1 - \tau^{1/\phi})[\gamma_H + \phi\ \gamma_D(\frac{\tau}{1-\tau}) + \phi\ (\frac{\tau\ p\ '(\tau)}{p(\tau)})] \qquad (4.4)$$

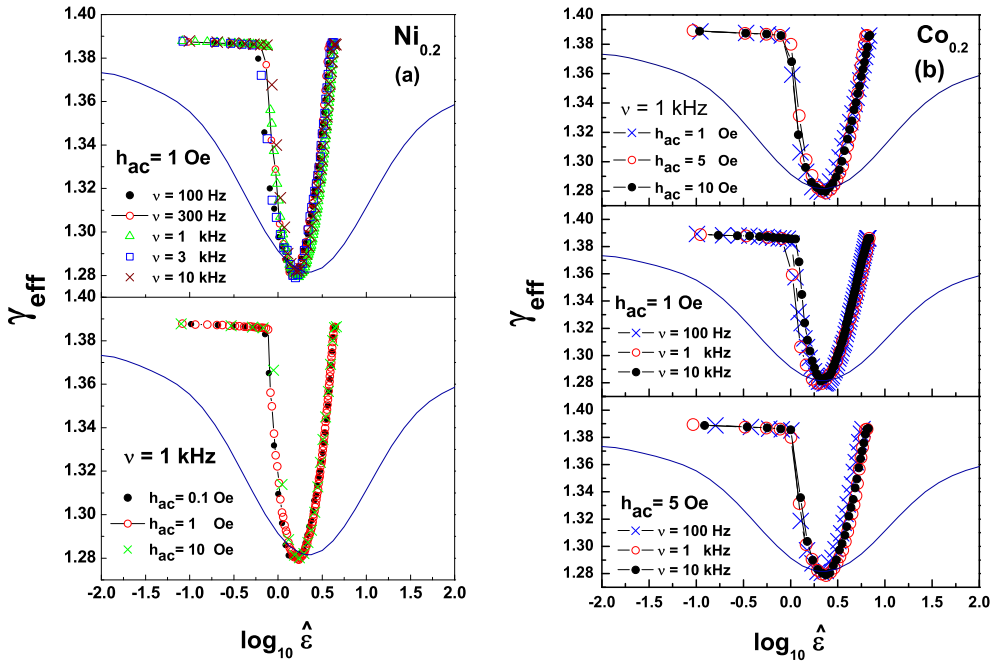

Figure 4.8: *A direct quantitative comparison between theory (solid curve) and experiment (symbols) for (a) $Ni_{0.2}$ and (b) $Co_{0.2}$.*

where Γ is a non-universal critical amplitude, $\tau = (\epsilon_g/\epsilon_H)^\phi$, $\epsilon_H = [T - T_C(0)]/T_C(0)$, $T_C(0) \equiv T_C(g = 0)$ is the transition temperature and γ_H the susceptibility critical exponent of the pure ($g = 0$) IH $d = 3, n = 3$ spin system, $\epsilon_g = [T_C(g) - T_C(0)]/T_C(0)$ is the shift in T_C caused by ID interactions of relative strength (i.e., the ratio of the ID energy to isotropic exchange energy), g, γ_D is the susceptibility critical exponent of the $d = 3$ ID fixed point, $\phi = \gamma_H$ is the crossover exponent, $p(\tau)$ is the 'correction-to-

scaling' function, $\tau^{-1/\phi} - 1 = \widehat{\epsilon} = [(1+\epsilon_g)/\epsilon_g]\epsilon$ and $\epsilon = (T - T_C(g))/T_C(g)$. The explicit forms of $p(\tau)$ and its derivative with respect to τ, $p\,'(\tau)$, are given in [50]. Equations (4.3) and (4.4) assert the following. (a) The ID interactions become important below a crossover temperature $\epsilon_{co} \approx \epsilon_{dip} \equiv g^{1/\phi}$ such that for $\epsilon \ll \epsilon_{co}$, the asymptotic critical behavior is that of a $d = 3$ ID ferromagnet whereas for $\epsilon \gg \epsilon_{co}$ the spin system behaves as a *pure* $d = 3, n = 3$ system. (b) $\gamma_{eff}(\epsilon)$ goes through a minimum in the crossover region such that at $\epsilon = \epsilon_{dip}$, γ_{eff} has the universal (*independent* of the RG coupling parameter [51]) value [50] $\gamma_{dip} = 1.28(1)$, for weak dipolar system with $g \leq 10^{-4}$. (c) $\gamma_{eff} \to \gamma_D$ and γ_H in the ID ($\tau \to 1$) and IH ($\tau \ll 1$) limits. The results for $Ni_{0.2}$ and $Co_{0.2}$, presented in Fig. 4.6, testify to the validity of the predictions (a) - (c). Considering that the dipolar interactions between the localized t_{2g}-electron spins are extremely weak compared to the Heisenberg-like superexchange interactions (which, in turn, are swamped by double exchange interactions) in hole-doped manganites such as LAMO (A = Ca, Sr, Ba, Pb, Cd), a crossover to the isotropic dipolar critical behavior is expected to occur at temperatures, $\epsilon < \epsilon_{co} \approx 10^{-6}$, which are inaccessible to experiments. Thus, it is not surprising that a dip in $\gamma_{eff}(\epsilon)$ is completely absent in LPMO. In the ACR ($0 < \epsilon \leq \epsilon^* \ll \epsilon_{co}$), the expansion of the scaling function $p(\tau)$ in Eqs.(4.3) and (4.4) yields the result [42, 53]

$$\chi(\epsilon) = A_\chi\ \epsilon^{-\gamma_D}[1 + a_\chi\ \epsilon^{\Delta_D}] \tag{4.5}$$

$$\gamma_{eff}(\epsilon) = \gamma_D - a_\chi\ \Delta_D\ \epsilon^{\Delta_D} \tag{4.6}$$

$$a_\chi \simeq 0.099\ \epsilon_g^{-\Delta_D} \tag{4.7}$$

and

$$\epsilon_g \cong 0.349\ \dot{\epsilon}, \tag{4.8}$$

where a_χ and Δ_D are the leading 'correction-to-scaling' amplitude and exponent, and $\dot{\epsilon}$ is the reduced temperature ϵ at which $\chi^{-1} = 4\pi$. The $\gamma_{eff}(\epsilon^{\Delta_D})$ data (symbols) and the best least-squares linear fits (straight lines), based on Eq.(4.6), are shown in figure 4.7 (while the corresponding critical-point parameters are displayed in tables 4.2 and 4.3 for different sets of data taken on $Ni_{0.2}$ and $Co_{0.2}$). It is evident from Fig. 4.7 that Eq.(4.6) with $\Delta_D = 0.55$ [32] is valid in the asymptotic critical region ($\epsilon \leq \epsilon^*$) and yields the true asymptotic susceptibility critical exponent $\gamma_D = 1.390(1)$, *irrespective* of Co or Ni concentration (and hence γ_D is *universal*, as expected), and (non-universal) *composition-dependent* a_χ. Like a_χ, the width of the ACR *increases with* y and is larger for Co, e.g., $a_\chi = 0.08(1)$, ACR width: $5.0 \times 10^{-4} \leq \epsilon \leq \epsilon^* = 7.0 \times 10^{-3}$ for $Ni_{0.2}$ and $a_\chi = 0.12(1)$; $5.0 \times 10^{-4} \leq \epsilon \leq \epsilon^* = 9.0 \times 10^{-3}$ for $Co_{0.2}$ (Tables 4.2 and 4.3). This finding implies that among Ni and Co doped systems, the dipolar interactions are *stronger* in Co and grow in strength as y increases in both Ni and Co containing samples. Inserting the experimental value of $\dot{\epsilon}$ in Eqs.(4.7) and (4.8) with $\Delta_D = 0.55$ yield $a_\chi = 0.973(6)$ for $Ni_{0.2}$ and $a_\chi = 0.966(3)$ for $Co_{0.2}$. Compared to the observed values displayed in Tables 4.2 and 4.3, these estimates are an order of magnitude higher. In order to make a direct comparison with the predictions of the RG calculations [50], γ_{eff} is plotted against $log_{10}\widehat{\epsilon}$ in figure 4.8. These γ_{eff} - $log_{10}\widehat{\epsilon}$ plots make use of the $\widehat{\epsilon}$ values, estimated from the relation $\widehat{\epsilon} = [(1 + \epsilon_g)/\epsilon_g]\epsilon$ and Eq.(4.8) using the observed values of $\dot{\epsilon}$. A glance at Fig. 4.8 reveals that the theory overestimates the width of the crossover region, underestimates γ_D and γ_H but estimates ϵ_{dip} with reasonable accuracy and yields the same value $\gamma_{dip} = 1.28$ as observed for γ_{eff} at $\epsilon = \epsilon_{dip}$. Considering that the most accurate theoretical value [40] $\gamma_H = 1.386(4)$ is in perfect agreement with

the presently determined value of γ_H, more refined RG calculations for the IH-ID crossover are needed to reproduce the experimental values of γ_D and γ_H. That ϵ_{dip} is higher in Co than in Ni basically reflects that the strength of the dipolar interactions, g, is greater in Co.

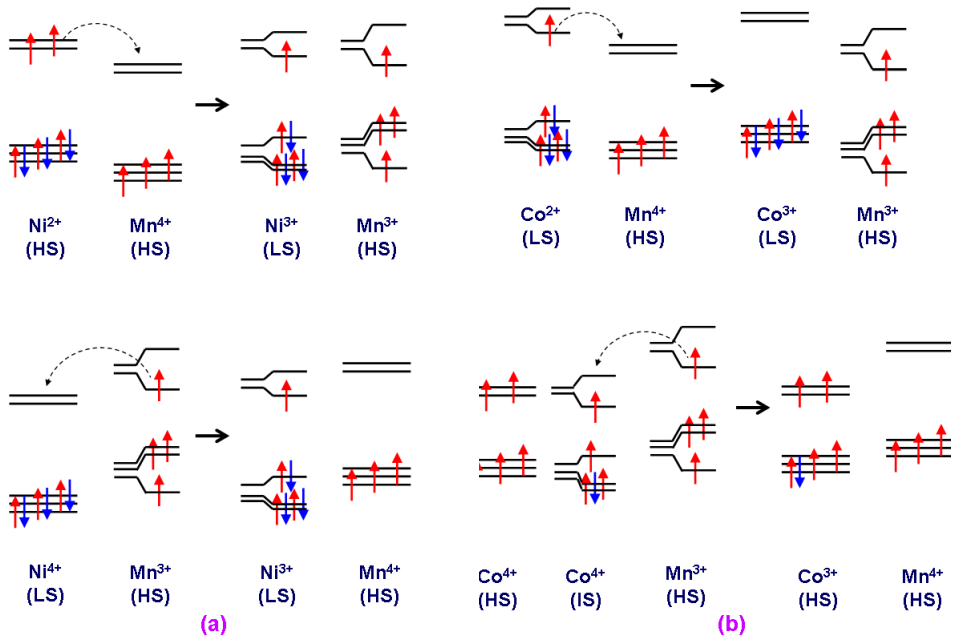

Figure 4.9: *Schematic representation of the charge and spin states of (a) Ni and (b) Co ions in the Ni- and Co-doped LPMO as they evolve from their initial to final configurations through charge transfer.*

A comparison between the deviation plots, shown in the lower panels of Fig. 4.4(b), 4.4(c), and the $\gamma_{eff}(\epsilon)$ plots, displayed in Fig. 4.6(a), 4.6(b), reveals the following. First, the inferences drawn from a direct fit to the $\chi^{-1}(T)$ data, based on Eq.(4.1) and using the 3D Heisenberg value $\gamma_H =$

1.386 for γ_{eff}, are consistent with the results of the ROF data analysis in that $\gamma_{eff} \cong \gamma_H$ for $\epsilon \leq \epsilon^* \simeq 0.01$ and at $\epsilon^{**} \simeq 0.04$ for $Ni_{0.2}$ ($\epsilon^{**} \simeq 0.06$ for $Co_{0.2}$). Second, the significantly large deviations of the $\chi^{-1}(T)$ data from the fit, yielded by Eq.(4.1) when $\gamma_{eff} = \gamma_H$, at intermediate temperatures (Fig. 4.4(b), 4.4(c)) basically reflect the reduced magnitude (Fig. 4.6(a), 4.6(b)) of γ_{eff}, compared to $\gamma_H = 1.386$, in the crossover region. Third, a wide dispersion in the values of the critical exponent γ reported in the literature for a given series of the hole-doped manganites with or without substitution at the Mn site can be attributed to one or more of the following factors [45]. (a) T_C not fixed to an accuracy demanded by a precise determination of the critical exponents. (b) The determinations are based on data that either fall completely within the crossover region or well outside the crossover region or partly overlap the asymptotic critical region. (c) Uncertainities associated with the extrapolation of the magnetization data, taken in finite magnetic fields, to zero field to arrive at the 'zero-field' quantities such as spontaneous magnetization and initial susceptibility.

Charge and spin states of Ni and Co

Recognizing that the resolution of the controversy surrounding the charge and spin states of Co and Ni in Co- or Ni-substituted hole-doped manganites is crucial to understanding the origin of dipolar interactions and the process of electron localization/charge ordering, an attempt is made to arrive at the most probable scenario of substitution at Mn^{3+} and/or Mn^{4+} sites that is consistent with the following main observations. (i) Reduction in the unit-cell volume (v)/lattice parameters (a and c), the critical temperature T_C and the magnetic moment per 3d transition metal atom (μ)

in the FM and PM states, with the Ni or Co concentration, y. (ii) Robustness of the tolerance factor against substitution. (iii) Localization of the conduction electrons as y increases, as inferred from the increase in the electrical resistivity with y irrespective of temperature [12-14]. The substitution of Mn^{3+} HS ion (with $S = 2$ and ionic radius $r_{ion} = 0.645\mathring{A}$) by : (a) Ni^{3+} LS ($S = 1/2, r_{ion} = 0.56\mathring{A}$) or Co^{3+} LS ($S = 0, r_{ion} = 0.545\mathring{A}$) reduces both v and μ at a rate that is much faster than the observed one; (b) Ni^{2+} HS ($S = 1, r_{ion} = 0.69\mathring{A}$) increases v but decreases μ; (c) Co^{3+} HS ($S = 2, r_{ion} = 0.61\mathring{A}$) reduces v but keeps μ constant; (d) Co^{4+} HS ($S = 5/2, r_{ion} = 0.53\mathring{A}$) reduces v drastically but increases μ. Thus, the above possibilities (a)-(d) invoked in the literature [9-14,19,20], are in direct conflict with the consistency conditions (i) and (ii); the latter due to an appreciable change in the tolerance factor. After exhausting other possibilities involving substitution of Mn^{4+} HS ($S = 3/2, r_{ion} = 0.53\mathring{A}$) by Ni or Co ions of different charge and spin states, we propose the substitution scheme, sketched in figure 4.9, that is compatible with the observations (i) - (iii). In this scheme, Ni^{2+} HS ($t_{2g}^6 e_g^2, S = 1, r_{ion} = 0.69\mathring{A}$) [$Co^{2+}$ LS ($t_{2g}^6 e_g^1, S = 1/2, r_{ion} = 0.65\mathring{A}$)] and Ni^{4+} LS ($t_{2g}^6 e_g^0, S = 0, r_{ion} = 0.48\mathring{A}$) [$Co^{4+}$ HS ($t_{2g}^3 e_g^2, S = 5/2, r_{ion} = 0.53\mathring{A}$)] substitute for Mn^{3+} HS ($t_{2g}^3 e_g^1, S = 2, r_{ion} = 0.645\mathring{A}$) and Mn^{4+} HS ($t_{2g}^3 e_g^0, S = 3/2, r_{ion} = 0.53\mathring{A}$) ions, respectively. Such a substitution introduces the least mismatch between the ionic radii of the solute and the substituted host ions with the result that only a minute reduction in v and essentially no change in the tolerance factor and the bond lengths Mn-O occurs, in accordance with the experimental observation. By virtue of the substitution at the Mn^{3+} and Mn^{4+} sites, Ni^{2+} HS /Co^{2+} LS and Ni^{4+} LS /Co^{4+} HS ions find themselves respectively in the neighborhood of Mn^{4+} and Mn^{3+} ions. In order to minimize the to-

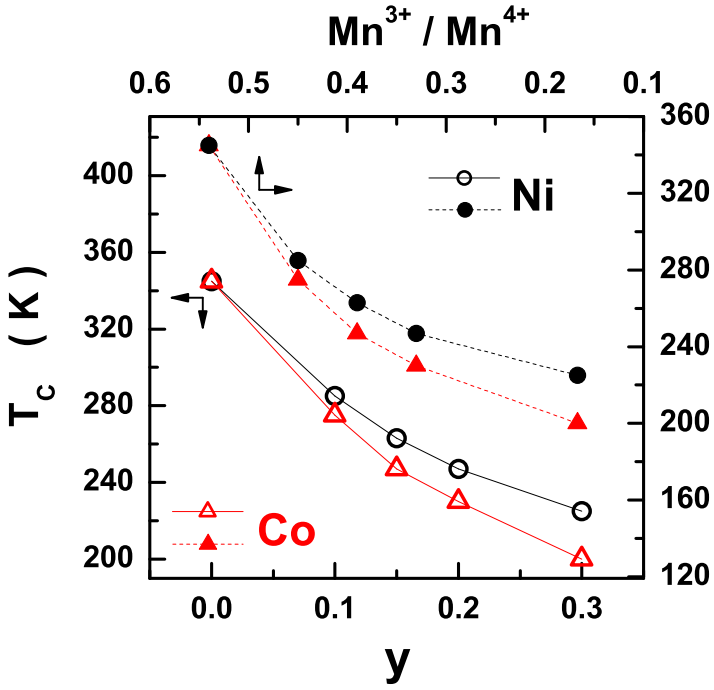

Figure 4.10: *The variation of ferromagnetic to paramagnetic transition temperature (T_C) as a function of Co/Ni dopant concentration, y (open symbols) or the Mn^{3+}/Mn^{4+} ratio (filled symbols). The continuous and dashed curves through data points serve as a guide to the eye.*

tal energy of the system, Ni^{2+} HS and Co^{2+} LS ions assume their stable configurations, Ni^{3+} LS and Co^{3+} HS ions, by donating one e_g electron per ion to Mn^{4+} ions (via the intervening oxygen 2p orbitals) and converting them into Mn^{3+} ions. By contrast, Ni^{4+} LS and Co^{4+} HS ions achieve the same goal (energy minimization) by accepting one e_g electron per ion from the Mn^{3+} HS neighbor (Co^{4+} HS state lowers its energy through the Jahn-Teller distortion and changes over to the Co^{4+} *intermediate spin* configuration before accepting the e_g electron) and transform themselves into

the stable Ni^{3+} LS and Co^{3+} HS ions (Mn^{3+} HS ions get converted to Mn^{4+} HS ions, in the process), as depicted in Fig. 4.9. Since the energy considerations do not permit the electron transfer to be reversible, the final configurations Ni^{3+} LS - O^{2-} - Mn^{3+} HS (Ni^{3+} LS - O^{2-} - Mn^{4+} HS) and Co^{3+} LS - O^{2-} - Mn^{3+} HS (Co^{3+} HS - O^{2-} - Mn^{4+} HS) do not revert back to the initial configurations Ni^{2+} HS - O^{2-} - Mn^{4+} HS (Ni^{4+} LS - O^{2-} - Mn^{3+} HS) and Co^{2+} LS - O^{2-} - Mn^{4+} HS (Co^{4+} HS - O^{2-} - Mn^{3+} HS). Consequently, in the final configurations, the e_g and/or t_{2g} electrons on Ni^{3+} LS, Co^{3+} LS/HS, Mn^{3+} HS and Mn^{4+} HS sites get localized and the dipolar interactions couple their spins ferromagnetically. The most remarkable feature of this approach is that one naturally ends up with the most probable charge and spin states for Ni, Co ions as Ni^{3+} LS, Co^{3+} LS and Co^{3+} HS, respectively. In sharp contrast with the Ni- or Co-doped LPMO, in the parent LPMO compound, the double exchange interactions dominate over the antiferromagnetic Mn^{3+} - O^{2-} - Mn^{3+} and Mn^{4+} - O^{2-} - Mn^{4+} superexchange interactions and the localization mechanism, brought about by the Ni or Co substitution, is absent and hence the ID interactions do not show up.

Relevance of dipolar interactions

Within the framework of the above picture (Fig. 4.9), Co^{3+} HS ion has two localized e_g electrons as against one per Ni^{3+} LS ion. It immediately follows that the Co-substitution should be *more effective* in weakening double exchange (and hence in reducing T_C), as corroborated by experiments (figure 4.10). Had the role of such e_g-electron localization been merely to reduce the double exchange, T_C would have dropped in proportion to the

Ni/Co concentration or Mn^{3+}/Mn^{4+} ratio (with a faster drop in the Co case); superexchange interactions, favoring antiferromagnetic coupling between the t_{2g}-electron spins of the ion pairs $Ni^{3+}/Co^{3+} - O^{2-} - Ni^{3+}/Co^{3+}$ or $Mn^{3+}/Mn^{4+} - O^{2-} - Mn^{3+}/Mn^{4+}$, would make the decline of T_C with increasing Ni/Co concentration (or decreasing Mn^{3+}/Mn^{4+} ratio) even faster. As noticed from Fig. 4.10, this expectation is in direct conflict with the ob-

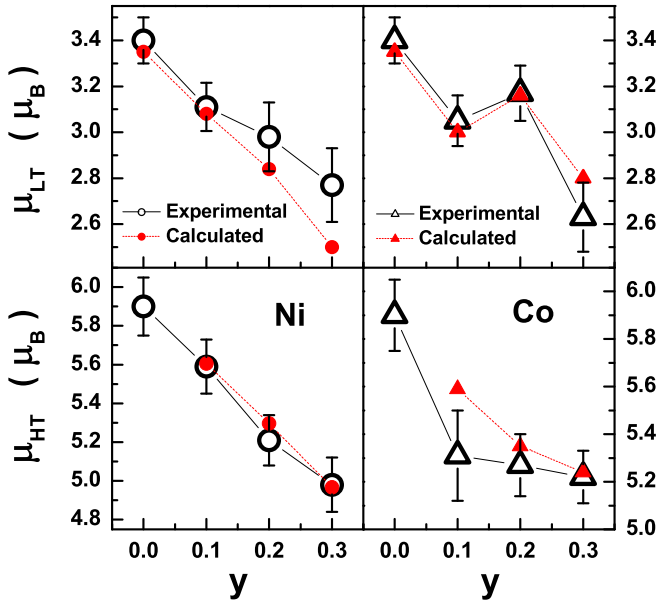

Figure 4.11: *Comparison of the calculated low- and high-temperature magnetic moments with those obtained experimentally for both Ni and Co doped LPMO. The continuous and dotted lines joining the data points or the calculated values serve as a guide to the eye.*

served slowing down of the rate of decrease of T_C in both the cases as the concentration of Ni/Co solute ions increases or the Mn^{3+}/Mn^{4+} ratio decreases. We propose that the *dipolar interactions*, that couple the $e_g - e_g$ ($e_g - t_{2g}$) spins on the Ni^{3+} LS - O^{2-} - Ni^{3+} LS, Ni^{3+} LS - O^{2-} - Mn^{3+}

HS, Co^{3+} HS - O^{2-} - Co^{3+} HS (Ni^{3+} LS - O^{2-} - Mn^{4+} HS, Co^{3+} HS - O^{2-} - Mn^{4+} HS) nearest-neighbor ion pairs ferromagnetically, slow down the rate of decline of T_C caused by the reduced double exchange and/or enhanced superexchange. This is so because the dipolar interactions, though *extremely weak* compared to the double exchange (DE) and superexchange (SE) interactions, tilt the balance in favour of FM order when the *competing* DE FM interactions between e_g-electron spins and SE AF interactions between t_{2g}-electron spins are both *large but* of *similar magnitude*. The dipolar interactions are stronger in Co-substituted LPMO because of the greater number of localized e_g electrons and larger magnetic moments on the Co^{3+} HS ion and this also explains higher electrical resistivity [12–14] for the Co-containing manganites. Assuming that the substitution of Mn^{3+} HS and Mn^{4+} HS ions by Ni or Co solute ions is completely biased by the 35/65::Mn^{3+}/Mn^{4+} ratio prevalent in the LPMO host, we arrive at the values for the low-temperature (saturation) magnetic moment, μ_{LT}, and high-temperature (in the PM state) magnetic moment, μ_{HT}, for all the compositions in the Ni- and Co-substituted series that are in very good agreement (figure 4.11) with the corresponding experimental values [13,14]. In the case of Co substituted LPMO, the agreement between the calculated and observed values of μ_{LT} and μ_{HT} can be improved further by considering that at low (high) temperatures, almost all the Co^{3+} ions are in the LS (HS) state, as the energy difference between the two spin states is as low as [54] ≈ 0.03 eV.

Before assessing the impact of the present findings on the current understanding of the underlying physics of the novel physical phenomena exhibited by manganites, the salient features of this work are summarized below.

Table 4.4: *Theoretically predicted susceptibility critical exponent γ for isotropic $d = 3, n = 3$ spin system with or without long-range dipolar interactions.*

RG method	Ref.	Isotropic Dipolar fixed point (γ_D)	Minimun γ in crossover region (γ_{dip})	Isotropic Heisenberg fixed point (γ_H)	Remarks
$\epsilon(= 4 - d)$-expansion to $O(\epsilon)$; recursion relations	[46]	1.265		1.25	quantitatively less accurate estimates
ϵ-expansion to $O(\epsilon^2)$; recursion relations	[47]	1.372		1.365	more refined values
Parquet-graph analysis to $O(\epsilon)$	[48]	1.32	1.24	1.29	less accurate estimates
Scaling function analysis to $O(\epsilon)$; recursion relations	[49]	1.265	1.21	1.25	less accurate estimates
Scaling function analysis to $O(\epsilon^2)$; Feynman graph approach	[50]	1.372	1.28(1)	1.365	more refined values; RG calculations to two-loop order.
Field theory; generalized minimal subtraction calculations to $O(\epsilon)$	[51]	1.265	1.22	1.25	less accurate estimates; RG calculations to one-loop order only.
ϕ^4-Field theory; Borel transformation and conformal mapping	[40]			1.386(4)	most accurate value

(A) In the optimally hole-doped parent LPMO compound, the SE AF interactions between the localized t_{2g}-electron spins are *completely dominated* by the DE FM interactions between e_g-electron spins and the dipolar interactions between the localized t_{2g}-electron spins are *extremely weak* compared to the SE interactions. Thus, dipolar interactions have essentially no role to play in establishing the FM state in LPMO. (B) A strong evidence for the presence of *finite metallic* FM clusters within the *insulating* PM matrix for $T > T_C$, and hence for the phase separation, is provided by the

peak in $\gamma_{eff}(\epsilon)$ at ϵ_p in the parent LPMO compound as well as in the Ni- or Co-substituted LPMO. (C) In LPMO and weakly Ni- or Co-doped ($y < 0.1$) LPMO, finite metallic FM clusters grow in size as the temperature is decreased towards T_C so much so that at $T \lesssim T_C$, metallic FM clusters coalesce to form an *infinite* FMM percolating network in which *finite* antiferromagnetic (AF) *insulating* clusters are embedded, and thus a percolative transition from the insulating ($T > T_C$) to metallic ($T < T_C$) state occurs. (D) As more and more of the Mn ions in LPMO are replaced by Ni or Co ions (i.e., as y increases), increased number of e_g electrons get localized via the mechanism illustrated in Fig.4.9. Consequently, the DE FM interactions get rapidly suppressed and become similar in magnitude to the SE AF interactions, so that even *weak dipolar interactions* between the localized e_g-electron spins and/or between $e_g - t_{2g}$ electron spins are able to establish the FM insulating (FI) phase, which grows at the expense of the FMM phase with increasing y. Thus, a transition from PI phase ($T > T_C$) to the FI phase ($T < T_C$) occurs at $T = T_C$ when the Ni or Co solute concentration exceeds a certain threshold value ($y > 0.2$ in the present case). That the dipolar interactions play a decisive role in establishing FM order in the vicinity of T_C when the fraction of localized e_g electrons becomes substantial ($y \geq 0.2$) is clearly borne out by the increase in the isotropic dipolar-to-isotropic Heisenberg crossover temperature with y. Since the presently studied manganite system shares the same underlying physics with other optimally-doped manganites, e.g., $La_{0.7}A_{0.3}Mn_{1-y}TM_yO_3$ where A = Ca, Sr, Ba, Cd and TM = Fe, Co, Ni, the above observations (A)-(D) should be applicable to these systems as well and provide a means to resolve the controversy surrounding the nature of FM - PM phase transition as well as the spin and charge states of Co and Ni in $La_{0.7}A_{0.3}Mn_{1-y}TM_yO_3$ manganites

too.

In the recent years, substantial progress in understanding the pronounced 'electron-hole asymmetry' as well as the occurrence of a variety of phases in the phase diagram of $La_{1-x}A_xMnO_3$ manganites has been made by recognizing the importance of the competition between DE interactions, Hund coupling between e_g-electron spin and localized t_{2g}-electron spin, Jahn-Teller (JT) electron-phonon coupling between e_g electrons and the local distortions of the MnO_6 octahedron, the Coulomb interactions among the e_g electrons and AF Heisenberg coupling between nearest-neighbor t_{2g} spins. However, many aspects of the physics of manganites are still poorly understood. For instance, no general consensus on how the FI state at low doping levels $x \approx 1/8$ evolves from the AF insulating state at $x = 0$ has emerged so far. Taking cognizance of the inference (D), we suggest that the dipole-dipole interaction (completely ignored in the previous considerations) between the *localized e_g-electron spins* (regardless of the actual localization mechanism) may hold the key to the formation of the FI phase at low doping levels as elucidated below. As the hole concentration (x) increases from zero, the double exchange interaction grows at the expense of the superexchange interaction so that at a certain value of x, the double exchange FM interactions between mobile e_g-electron spins become similar in magnitude to, and compete with, the superexchange AF interactions between localized t_{2g}-electron spins with the result that even extremely weak dipolar interactions suffice to tilt the balance in favour of FM order.

4.3.2 Nonlinear magnetic susceptibility

In the critical region near T_C, the temperature and field dependence of magnetization is characterized by the scaling equation of state (SES) of the form

$$m = |\epsilon|^{\beta} f_{\pm}\left(\frac{h}{|\epsilon|^{\beta+\gamma}}\right) \tag{4.9}$$

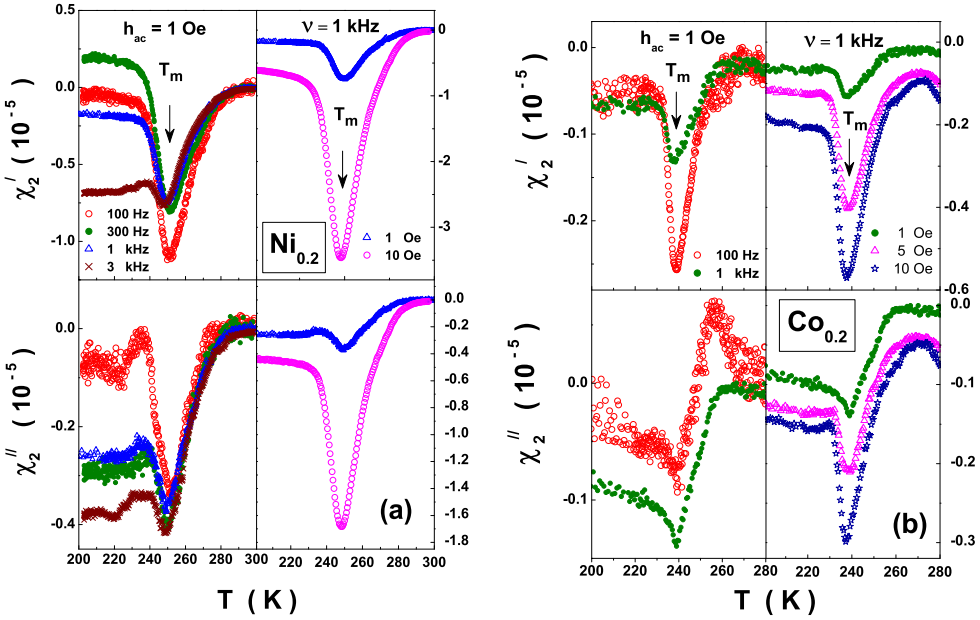

Figure 4.12: *In-phase and out-phase components of first order nonlinear susceptibility, χ_2, for (a) $Ni_{0.2}$ and (b) $Co_{0.2}$ as a function of temperature at a driving field of amplitude, $h_{ac} = 1\ Oe$ and variable frequency, ν, and at $\nu = 1\ kHz$ and variable h_{ac}.*

Successive derivatives of Eq.(4.9) with respect to h yields

$$\chi_n = |\epsilon|^{-\gamma_n} f_{\pm}^{(n)}\left(\frac{h}{|\epsilon|^{\beta+\gamma}}\right), \tag{4.10}$$

where $\gamma_n = n\gamma+(n-1)\beta$ $(n = 1, 2, \cdots)$ is the critical exponent for nonlinear susceptibility, χ_n and $f_{\pm}^{(n)}(x)$ represent the n^{th} field derivative of $f_{\pm}(x)$.

Figure 4.12 presents $\chi_2(T)$ data for $Co_{0.2}$ and $Ni_{0.2}$ at different fields and frequencies. The existence of a nonzero χ_2 for $T < T_C$ is a clear indication that the system exhibits long-range magnetic order as it is related to the spontaneous magnetization. In accordance with theoretical prediction that negative χ_2 should diverge below, and vanish above the transition point (see chapter 3), χ_2 is negative with a dip at T_m (which is slightly higher than T_C). The $\chi_2^{-1}(T)$ data are analyzed in terms of the expression

$$\chi_2^{-1}(T) = -A_2(T) \ \ (-\epsilon)^{\ \gamma_2(T)} \ + N_2 \quad (\epsilon < 0) \tag{4.11}$$

(where $\epsilon = (T-T_m)/T_m$, A_2, γ_2 and N_2 are the reduced temperature, critical amplitude, critical exponent and demagnetization factor, respectively) using a 'range-of-fit' analysis. Figure 4.13(a) displays the fits to the normalized inverse nonlinear susceptibility, $\chi_2^{-1}(\epsilon)/\chi_2^{-1}(\epsilon = 0)$, in the asymptotic critical region based on Eq.(4.11). The theoretical fits are noticed to describe the $\chi_2^{-1}(\epsilon)$ data quite well. The 'range-of-fit' analysis yields the temperature variations of the corresponding critical exponent γ_2 as shown in figure 4.13(b). The main features of the data presented in Fig.4.13 are as follows. (i) At low frequencies (100 and 300 Hz), γ_2 assumes the value 3.15(3) as $\epsilon \to 0$ and reaches a similar value below the dip. The value $\gamma_2 = 2\gamma + \beta$ $= 2 \times 1.39 + 0.37 = 3.15$ is theoretically expected for a three-dimensional $(d = 3)$ isotropic dipolar ferromagnet. This observation and the dip in $\gamma_2(\epsilon)$, characteristic of $d = 3$ isotropic dipolar to $d = 3$ isotropic Heisenberg crossover, are consistent with our findings in the section 4.3.1 based on the linear susceptibility, $\chi_1(\epsilon)$, on these systems. (ii) At $h_{ac} = 1Oe$, as the frequency of the driving field increases, T_m falls rapidly (not shown),

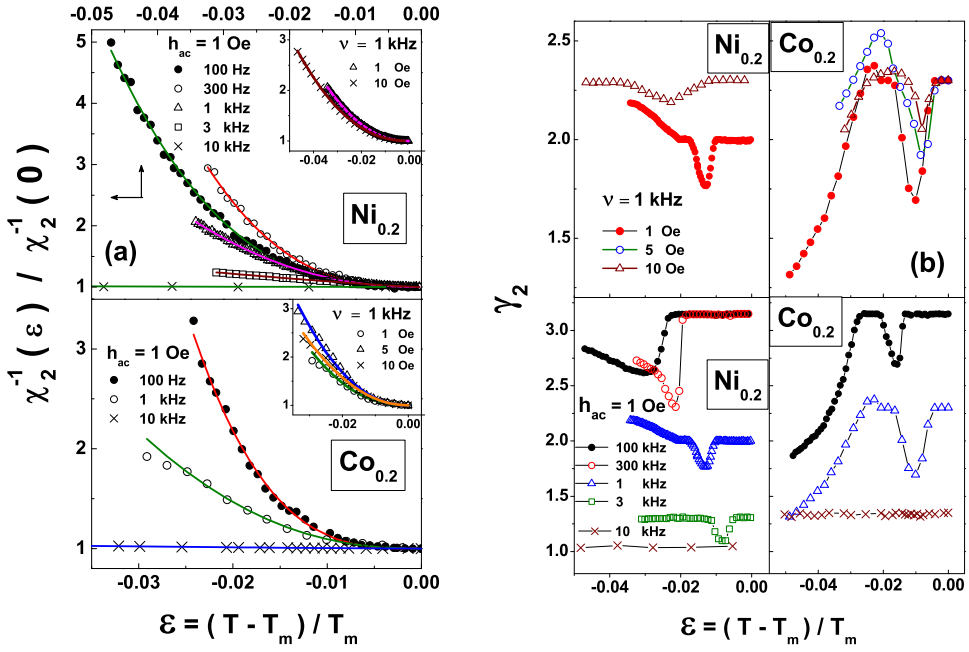

Figure 4.13: *(a) Normalized inverse first order nonlinear susceptibility and (b) corresponding effective critical exponent as a function of reduced temperature.*

the asymptotic value of γ_2 reduces drastically and the dip in $\gamma_2(\epsilon)$ shifts towards $\epsilon = 0$ so much so that at $\nu = 10\ kHz$, γ_2 approaches the mean-field value of $\gamma = 1$. This observation implies that, as T_m falls well below T_C with increasing frequency, the divergence of χ_2 is suppressed progressively. The suppression of the divergence and the fall of T_m is a direct indication of the finite size of the clusters that are probed at a given frequency (or time window); higher the frequency, smaller the size of the magnetic clusters probed. These results thus suggest the phase segregation of the conducting and insulating magnetic phases within the ferromagnetic regime. Fig.4.14 depicts the thermal variation of third harmonic of susceptibility at various

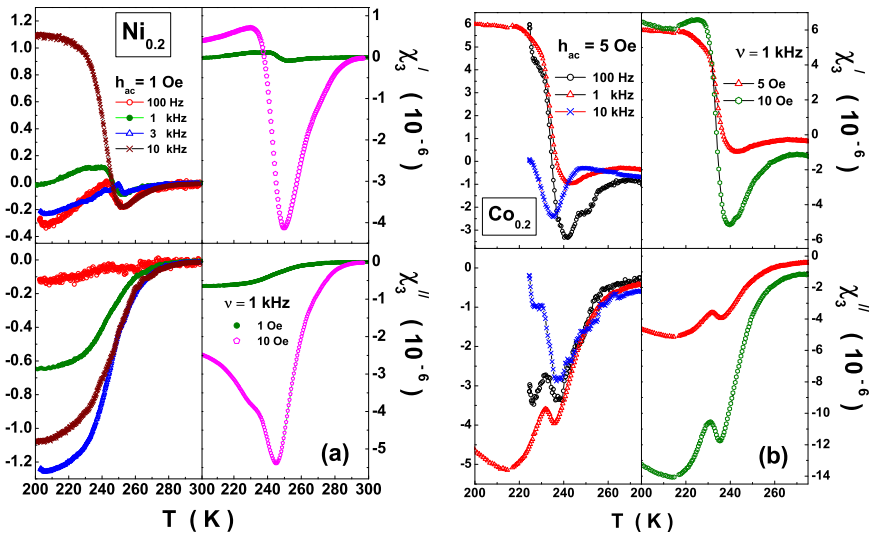

Figure 4.14: *Temperature variation of the in-phase and out-phase components of first order nonlinear susceptibility, χ_3, for (a) $Ni_{0.2}$ and (b) $Co_{0.2}$ at a driving field of amplitude, $h_{ac} = 1$ Oe and variable frequency, ν, and at $\nu = 1$ kHz and variable h_{ac}.*

driving field amplitudes and frequencies. $\chi_3(T)$ has a positive maximum in FM phase and changes over to a negative dip ($T_m > T_C$) in PM phase as predicted by theory. The $\chi_3(T)$ data are analysed in the PM phase using

$$\chi_3^{-1}(T) = -A_3(T) \ \ (\epsilon)^{\ \gamma_3(T)} \ + N_3 \quad (\epsilon > 0) \tag{4.12}$$

with A_3, γ_3 and N_3 as critical amplitude, critical exponent and demagnetization factor, respectively. The fits obtained using Eq.(4.12) represents data excellently in the ACR as shown in Fig.4.15(a). The thermal of the corresponding critical exponent, $\gamma_3(\epsilon)$, presented in figure 4.15(b) has a value of $\gamma_3 \sim 2.3$ in ACR at low field and frequency instead of $\gamma_3 = 4.91$ ($=3\gamma + 2\beta$) predicted by theory and its value decreases with field and frequency. However, $\gamma_3(\epsilon)$ exhibits a dip similar to the one seen in $\gamma_1(\epsilon)$ whose magnitude

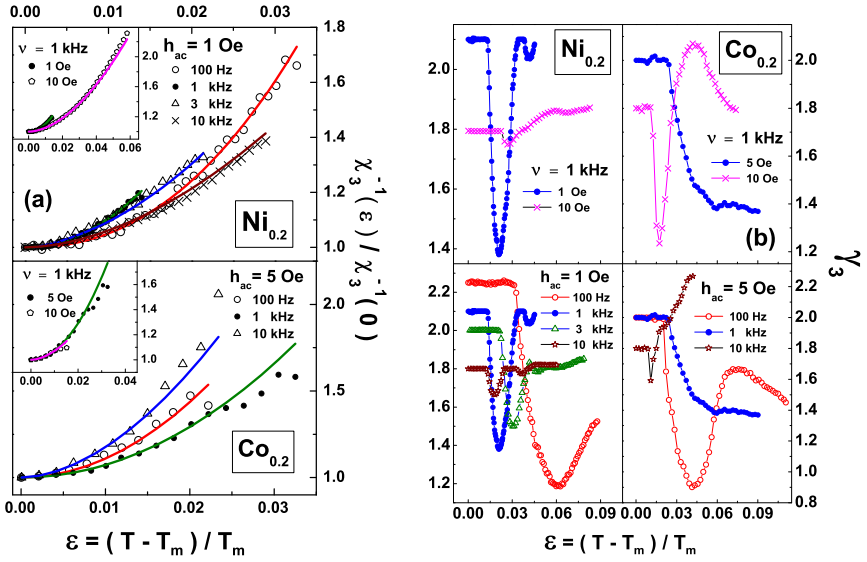

Figure 4.15: *(a) Normalized inverse second order nonlinear susceptibility and (b) corresponding effective critical exponent as a function of reduced temperature.*

gets suppressed and position shifts to lower temperature with frequency. This observation directly points to the presence of FMM clusters of various sizes in PMI state.

4.4 Summary and Conclusion

An extensive investigation of the magnetic behavior of $La_{0.7}Pb_{0.3}Mn_{1-y}(Co,Ni)_yO_3$ $(y = 0, 0.1, 0.2, 0.3)$ hole-doped manganite system over a wide range of temperatures, that covers the critical region near the ferromagnetic (FM)- paramagnetic (PM) phase transition and the PM region, has been carried out by measuring ac susceptibility (ACS) at the ac driving field whose rms amplitudes (frequencies) ranged from 0.1 Oe to 10

Oe (100 Hz to 10 kHz). A detailed 'range-of-fit' analysis of the ACS data enabled a precise determination of the Curie temperature, T_C and hence of the effective critical exponent, γ_{eff}, for susceptibility as a function of reduced temperature, $\epsilon = (T - T_C)/T_C$. The main observations are as follows. In the parent LPMO compound, (I) $\gamma_{eff}(\epsilon) \rightarrow \gamma_H = 1.386$ (the 3D isotropic Heisenberg value) in the asymptotic critical region (ACR), and goes through a peak before approaching the mean field value of $\gamma = 1$ at $T \gg T_C$. (II) By contrast, regardless of the Ni or Co concentration in the range $0.1 \leq y \leq 0.3$, as the temperature is raised from T_C, γ_{eff} starts with the value $\gamma_D = 1.390(1)$ in the ACR ($\epsilon \lesssim \epsilon^*$), goes through a steep minimum (dip) at ϵ_{dip} with $\gamma_{dip}(\epsilon = \epsilon_{dip}) = 1.280(4)$, rises to the value $\gamma_H = 1.386(4)$ at ϵ^{**} and then peaks at ϵ_p assuming a value $\gamma_{eff}(\epsilon = \epsilon_p)$, which depends on y. (III) As y increases, ϵ^*, ϵ_{dip}, ϵ^{**} and ϵ_p shift to higher temperatures while γ^p_{eff} increases. (IV) For a given y, ϵ^*, ϵ_{dip}, ϵ^{**} and ϵ_p are higher while γ^p_{eff} is lower in the case of Co. (V) A progressive drop in T_C (from its value in the LPMO host) occurs as the Ni or Co concentration increases but the Co-substitution depresses T_C at a much faster rate. However, the rate of decline of T_C slows down with increasing y, i.e., $T_C(y)$ is concave upwards. The renormalization group (RG) calculations predict that (a) a 3D isotropic spin system, in which short-range Heisenberg interactions coexist with *weak* long-range dipolar interactions, exhibits a thermally-induced crossover from the 3D isotropic Heisenberg (IH) critical behavior to the 3D isotropic dipolar (ID) asymptotic critical behavior when the temperature is lowered towards T_C from high temperatures, and (b) the *characteristic feature* of this IH to ID crossover is a *dip* in $\gamma_{eff}(\epsilon)$ in the crossover region with γ_{eff} attaining the values γ_D in the ACR, $\gamma_{dip} = 1.28(1)$ at ϵ_{dip} and γ_H at ϵ^{**}, respectively. In view of these RG predictions, the observations (II)-(IV) permit us to

conclude that an ID to IH crossover occurs in the Ni- and Co-substituted LPMO, and the ID interactions, not discernable in the parent LPMO compound, grow in strength with y and among Ni and Co solutes, are stronger in the Co-substituted LPMO.

Within the framework of a percolation model, the peak in $\gamma_{eff}(\epsilon)$ at ϵ_p in the LPMO host and the Ni- or Co-substituted LPMO is shown to result from an interplay between the diverging spin-spin correlation length of the *insulating* PM matrix as $\epsilon \to 0$ and the temperature-dependent length scale due to the *finite metallic* FM clusters while the observed upward shift in ϵ_p and the decrease in γ^p_{eff} as one follows the sequence $y = 0 \to Ni \to Co$ (for a given Ni or Co concentration, e.g., $y = 0.2$ in Fig.4.5 imply that the average FM cluster size reduces and the cluster size distribution narrows down. The peak in γ_{eff} for $\epsilon > 0$ thus constitutes a new experimental signature for the phenomenon of phase separation in hole-doped manganites. To address the issues connected with the localization of e_g electrons (and hence weakening of double exchange) and the origin of dipolar interactions, we have proposed the charge and spin states for Ni and Co ions in the Ni- and Co-substituted LPMO that are consistent with not only the present results but also with the previously published structural (neutron diffraction), thermo-gravimetric, bulk magnetization, dc magnetic susceptibility and electrical resistivity data on the same system. Finally, the physical implications of our results, so far as the physics of manganites is concerned, are discussed in the preceding section.

The results of the above nonlinear susceptibility analyses is summarised as follows. In the asymptotic critical region, both $Ni_{0.2}$ and $Co_{0.2}$ systems behave as a 3D isotropic dipolar ferromagnet (FM) and as the temperature is raised above the critical point (T_C), crossover from 3D isotropic long-range

dipolar (ID) to 3D isotropic short-range Heisenberg (IH) fixed point occurs. This inference is drawn based on the analyses of χ_1 and χ_2 as functions of frequency, field amplitude and temperature. Clear-cut signatures for the existence of segregated ferromagnetic metallic (FMM) phase in the paramagnetic insulating (PMI) matrix above T_C and ferromagnetic insulating (FMI) phase in the FMM matrix below T_C are exhibited by $\gamma_{eff}(\epsilon)$ plots based on $\chi_3(T)$ and $\chi_2(T)$. As the frequency of the driving ac field increases, the contributions from the FMM clusters (phase) at $T > T_C$ and FMI clusters (phase) at $T < T_C$, to the nonlinear magnetic response become increasingly dominant. A minimum in $\gamma_{eff}(\epsilon)$, a characteristic of a crossover from ID ($\beta = 0.37$, $\gamma = 1.39$) to IH ($\beta = 0.365$, $\gamma = 1.386$) spin system, present in $\gamma_2(\epsilon)$ and $\gamma_3(\epsilon)$ plots, reflects the importance of dipolar interactions in giving rise to the insulating FM/PM phase. By contrast, a constant decrease in the magnitude of γ_2 and γ_3 with increasing frequency is a manifestation of the increasingly dominant contribution from finite FMM/FMI clusters. Hence, nonlinear susceptibility can be used an effective tool in the study of phase separation phenomena in manganites.

References

1. J. M. D. Coey, M. Viret and S. von Molnar, *Mixed-valence manganites*, Adv. Phys. **48**, 167 (1999).

2. M. B. Salamon and M. Jaime, *The physics of manganites: Structure and transport*, Rev. Mod. Phys. **73**, 583 (2001).

3. E. Dagotto, T. Hotta and A. Moreo, *Colossal magnetoresistant materials: The key role of phase separation* , Phys. Rep. **344**, 1 (2001).

4. J. B. Goodenough, *Electronic and ionic transport properties and other physical aspects of perovskites*, Rep. Prog. Phys. **67**, 1915 (2004).

5. E. Dagotto, *Open questions in CMR manganites, relevance of clustered states and analogies with other compounds including the cuprates*, New J. Phys. **7**, 67 (2005).

6. Y. Tokura, *Critical features of colossal magnetoresistive manganites*, Rep. Prog. Phys. **69**, 797 (2006).

7. T. V. Ramakrishnan, *Modelling colossal magnetoresistance manganites*, J. Phys.:Condens. Matter **19**, 125211 (2007).

8. J. Gutiérrez, J. M. Barandiarán, A. Peña, L. Lezama, M. Insausti, T. Rojo and J.L. Pizarro, *Structural, magnetic and magnetotransport properties of* $La_{0.7}Pb_{0.3}Mn_{0.9}TM_{0.1}O_3$ *(TM = Fe, Co, Ni) CMR perovskites*, J. Phys.: Condens. Matter **12**, 10523 (2000);
   J. Gutiérrez, A. Peña, J. M. Barandiarán, J. L. Pizarro, T. Hernandez, L. Lezama, M. Insausti and T. Rojo, *Structural and magnetic*

properties of $La_{0.7}Pb_{0.3}(Mn_{1-x}Fe_x)O_3$ $(0 < x < 0.3)$ *giant magnetoresistance perovskites*, Phys. Rev. B **61**, 9028 (2000).

9. S. L. Young, Y. C. Chen, L. Horng, T. C. Wu, H. Z. Chen and J. B. Shi, *Structural and magnetic properties in* $La_{0.7}Pb_{0.3}Mn_{1-x}Co_xO_3$ *systems*, J. Magn. Magn. Mater. **289**, 145 (2000);
S. L. Young, Y. C. Chen, H. Z. Chen, L. Horng and J. F. Hsueh, *Effect of the substitutions of* Ni^{3+}, Co^{3+}, *and* Fe^{3+} *for* Mn^{3+} *on the ferromagnetic states of the* $La_{0.7}Pb_{0.3}MnO_3$ *manganite*, J. Appl. Phys. **91**, 8915 (2002).

10. S. Pal, E. Bose, B. K. Chaudhuri, H. D. Yang, S. Neeleshwar and Y. Y. Chen, *Effect of Ni doping in rare-earth manganite* $La_{0.7}Pb_{0.3}Mn_{1-x}Ni_xO_3$ *(x = 0.0-0.5)*, J. Magn. Magn. Mater. **293**, 872 (2005).

11. G. Gritzner, M. Koppe, K. Kellner, J. Przewoznik, J. Chmist, A. Kolodziejczyk and K. Krop, *Preparation and properties of* $La_{0.67}Pb_{0.33}(Mn_{1-x}Fe_x)O_3$ *compounds*, Appl. Phys. A **81**, 1491 (2005);
G. Gritzner, J. Ammer, K. Kellner, V. Kavečanský, M. Mihalik, S. Maťaš and M. Zentková, *Preparation, structure and properties of* $La_{0.67}Pb_{0.33}(Mn_{1-x}Co_x)O_{3-\delta}$, Appl. Phys. A **90**, 359 (2008).

12. A. Peña, J. Gutiérrez, J. M. Barandiarán, J. L. Pizarro, T. Rojo, L. Lezama and M. Insausti, *Magnetism in* $La_{0.7}Pb_{0.3}(Mn_{0.9}TM_{0.1})O_3$ *(TM = Fe, Co, Ni) CMR perovskites*, J. Magn. Magn. Mater. **226 – 230**, 831 (2001);
A. Peña, J. Gutiérrez, J. M. Barandiarán and T. Rojo, *Magneto-transport properties of Co- and Ni-doped manganites: from conduc-*

tive to insulating behavior, J. Magn. Magn. Mater. **272 − 276**, e1425 (2004).

13. A. Peña, J. Gutiérrez, I. Gil de Muro, J. Campo, J. M. Barandiarán and T. Rojo, *Correlation between structure and magnetic and magnetotransport properties of* $La_{0.7}Pb_{0.3}(Mn_{1-x}Co_x)O_3$ $(0.1 \leq x \leq 0.3)$ *CMR manganites*, Eur. J. Inorg. Chem. **16**, 3227 (2006) and references cited therein.

14. A. Peña, J. Gutiérrez, J. Campo, J. M. Barandiarán, L. Lezama, I. Gil de Muro and T. Rojo, *Structural, magnetic and magnetotransport properties of* $La_{0.7}Pb_{0.3}(Mn_{1-x}Ni_x)O_3$ $(0.1 \leq x \leq 0.3)$ *CMR manganites*, Eur. J. Inorg. Chem. **18**, 2569 (2008) and references cited therein.

15. K. H. Ahn, X. W. Wu, K. Liu and C. L. Chien, *Magnetic properties and colossal magnetoresistance of* $La(Ca)MnO_3$ *materials doped with Fe*, Phys. Rev. B **54**, 15299 (1996).

16. L. Righi, P. Gorria, M. Insausti, J. Gutiérrez and J. M. Barandiarán, *Influence of Fe in giant magnetoresistance ratio and magnetic properties of* $La_{0.7}Ca_{0.3}Mn_{1-x}Fe_xO_3$ *perovskite type compounds*, J. Appl. Phys. **81**, 5767 (1997);
M. Pissas, G. Kallias, E. Devlin, A. Simopoulos and D. Niarchos, *Mssbauer study of* $La_{0.75}Ca_{0.25}Mn_{0.98}Fe_{0.02}O_3$ *compound*, *ibid* **81**, 5770 (1997).

17. J. Gutiérrez, J. M. Barandiarán, M. Insausti, L. Lezama, A. Peña, J. J. Blanco and T. Rojo, *Magnetic and transport properties of Pb*

perovskites and Fe containing giant magnetoresistance perovskites, J. Appl. Phys. **83**, 7171 (1998).

18. K. Ghosh, S. B. Ogale, R. Ramesh, R. L. Greene, T. Venkatesan, K. M. Gapchup, R. Bathe and S. I. Patil, *Transition-element doping effects in* $La_{0.7}Ca_{0.3}MnO_3$, Phys. Rev. B **59**, 533 (1999).

19. M. A. Korotin, S. Yu. Ezhov, I. V. Solovyev, V. I. Anisimov, D. I. Khomskii and G. A. Sawatzky, *Intermediate-spin state and properties of* $LaCoO_3$, Phys. Rev. B **54**, 5309 (1996).

20. P. Ravindran, H. Fjellvåg, A. Kjekshus, P. Blaha, K. Schwarz and J. Luitz, *Itinerant metamagnetism and possible spin transition in* $LaCoO_3$ *by temperature/hole doping*, J. Appl. Phys. **91**, 291 (2002).

21. C. S. Hong, W. S. Kim and N. H. Hur, *Transport and magnetic properties in the ferromagnetic regime of* $La_{1-x}Ca_xMnO_3$, Phys. Rev. B **63**, 92504 (2001).

22. Wanjun Jiang, X. Z. Zhou, Gwyn Williams, Y. Mukovskii and K. Glazyrin, *Is a Griffiths Phase a Prerequisite for Colossal Magnetoresistance?*, Phys. Rev. Lett. **99**, 177203 (2007).

23. Subhrangsu Taran, B. K. Chaudhuri, S. Chatterjee, H. D. Yang, S. Neeleshwar and Y. Y. Chen, *Critical exponents of the* $La_{0.7}Sr_{0.3}MnO_3$, $La_{0.7}Ca_{0.3}MnO_3$, *and* $Pr_{0.7}Ca_{0.3}MnO_3$ *systems showing correlation between transport and magnetic properties*, J. Appl. Phys. **98**, 103903 (2005).

24. S. Rößler, U. K. Rößler, K. Nenkov, D. Eckert, S. M. Yusuf, K. Dörr

and K.-H. Müller, *Rounding of a first-order magnetic phase transition in Ga-doped* $La_{0.67}Ca_{0.33}MnO_3$, Phys. Rev. B **70**, 104417 (2004).

25. D. Kim, B. Revaz, B. L. Zink, F. Hellman, J. J. Rhyne and J. F. Mitchell, *Tricritical Point and the Doping Dependence of the Order of the Ferromagnetic Phase Transition of* $La_{1-x}Ca_xMnO_3$, Phys. Rev. Lett. **89**, 227202 (2002).

26. Wei Li, H. P. Kunkel, X. Z. Zhou, Gwyn Williams Y. Mukovskii and D. Shulyatev, *Estimates of the critical exponents of single-crystal* $La_{0.73}Ba_{0.27}MnO_3$, Phys. Rev. B **70**, 214413 (2004).

27. Wanjun Jiang, X. Z. Zhou, Gwyn Williams, Y. Mukovskii and K. Glazyrin, *Griffiths phase and critical behavior in single-crystal* $La_{0.7}Ba_{0.3}MnO_3$*: Phase diagram for* $La_{1-x}Ba_xMnO_3$ $(x \leq 0.33)$, Phys. Rev. B **77**, 064424 (2008).

28. N. Moutis, I. Panagiotopoulos, M. Pissas and D. Niarchos, *Structural and magnetic properties of* $La_{0.67}(Ba_xCa_{1-x})_{0.33}MnO_3$ *perovskites* $(0 < x < 1)$, Phys. Rev. B **59**, 1129 (1999).

29. H. Assaridis, I. Panagiotopoulos, A. Moukarika, V. Papaefthymiou and T. Bakas, *Structural and magnetic properties of* $La_{0.67-y}(Sr, Ba, Ca)_{0.33+y}Mn_{1-x}Sn_xO_3$ $(x = 0.01, 0.02,\ y = 0, 0.07)$ *perovskites*, Solid State Commun. **139**, 473 (2006).

30. Sunil Nair, A. Banerjee, A. V. Narlikar, D. Prabhakaran and A. T. Boothroyd, *Observation of three-dimensional Heisenberg-like ferromagnetism in single crystal* $La_{0.875}Sr_{0.125}MnO_3$, Phys. Rev. B **68**, 132404 (2003).

31. Ch. V. Mohan, M. Seeger, H. Kronmüller and P. Murugaraj, *Critical behaviour near the ferromagneticparamagnetic phase transition in* $La_{0.8}Sr_{0.2}MnO_3$, J. Magn. Magn. Mater. **183**, 348 (1998).

32. D. Kim, B. L. Zink, F. Hellman and J. M. D. Coey, *Critical behavior of* $La_{0.75}Sr_{0.25}MnO_3$, Phys. Rev. B **65**, 214424 (2002).

33. K. Ghosh, C.J. Lobb, R.L. Greene, S.G. Karabashev, D.A. Shulyatev, A.A. Arsenov and Y. Mukovskii, *Critical Phenomena in the Double-Exchange Ferromagnet* $La_{0.7}Sr_{0.3}MnO_3$, Phys. Rev. Lett. **81**, 4740 (1998).

34. N. V. Khiem, P. T. Phong, L. V. Bau, D. N. H. Nam, L. V. Hong and N. X. Phuc, *Critical parameters near the ferromagneticparamagnetic phase transition in* $La_{0.7}A_{0.3}(Mn_{1-x}B_x)O_3$ *(A = Sr; B = Ti and Al; x = 0.0 and 0.05) compounds*, J. Magn. Magn. Mater. **321**, 2027 (2009).

35. N. V. Khiem, L. V. Bau, P. T. Phong, L. V. Hong, N. V. Dai, D. N. H. Nam and N. X. Phuc, *Critical Exponents for the Ferromagnetic-Paramagnetic Transition in* $La_{0.7}Sr_{0.3}Mn_{0.8}Ti_{0.2}O_3$, J. Korean Phys. Soc. **52**, 1518 (2008).

36. L. Chen, J. H. He, Y. Mei, Y. Z. Cao, W. W. Xia, H. F. Xu, Z. W. Zhu and Z. A. Xu, *Critical behavior of Mo-doping* $La_{0.67}Sr_{0.33}Mn_{1-x}Mo_xO_3$ *perovskite system*, Physica B **404**, 1879 (2009).

37. T. L. Phan, S. G. Min, S. C. Yu and S. K. Oh, *Critical exponents of* $La_{0.9}Pb_{0.1}MnO_3$ *perovskite*, J. Magn. Magn. Mater. **304**, e778 (2006).

38. A. K. Heilman, Y. Y. Xue, B. Lorenz, M. Gospodinov, S. G. Dobreva and C. W. Chu, *Field-induced crossover in* $La_{0.7}Pb_{0.3}MnO_3$, Physica C **341 – 348**, 707 (2004).

39. A. Peles, H. P. Kunkel, X. Z. Zhou and Gwyn Williams, *Field-dependent magnetic and transport properties and anisotropic magnetoresistance in ceramic* $La_{0.67}Pb_{0.33}MnO_3$, J. Phys.:Condens. Matter **11**, 8111 (1999).

40. J. C. Le Guillou and J. Zinn-Justin, *Critical exponents from field theory*, Phys. Rev. B **21**, 3976 (1980).

41. S. N. Kaul and M. Sambasiva Rao, *Asymptotic critical behaviour of quenched random-exchange Heisenberg ferromagnets*, J.Phys.: Condens. Matter **6**, 7403 (1994);
Asymptotic and leading correction-to-scaling specific-heat critical exponents and amplitudes for quench-disordered ferromagnets from resistivity measurements, Phys. Rev. B **43**, 11240 (1991).

42. S. N. Kaul, *Asymptotic and leading "correction-to-scaling" susceptibility critical exponents and amplitudes for ferromagnets with quenched disorder*, Phys. Rev. B **38**, 9178 (1988).

43. S. Srinath, S. N. Kaul and H. Kronmüller, *Observation of isotropic dipolar to uniaxial dipolar crossover in gadolinium*, Phys. Rev. B **59**, 1145 (1999).

44. S. Srinath, S. N. Kaul and M. -K. Sostarich, *Isotropic-Heisenberg to isotropic-dipolar crossover in amorphous ferromagnets with composition near the percolation threshold*, Phys. Rev. B **62**, 11649 (2000).

45. S. N. Kaul, *Static critical phenomena in ferromagnets with quenched disorder*, J. Magn. Magn. Mater. **53**, 5 (1985).

46. A. Aharony and M. E. Fisher, *Critical Behavior of Magnets with Dipolar Interactions. I. Renormalization Group near Four Dimensions*, Phys. Rev. B **8**, 3323 (1973).

47. A. D. Bruce and A. Aharony, *Critical exponents of ferromagnets with dipolar interactions: Second-order ε expansion*, Phys. Rev. B **10**, 2078 (1974).

48. T. Nattermann and S. Trimper, *Influence of dipolar interaction on critical behaviour*, J.Phys. C: Solid State Phys. **9**, 2589 (1976).

49. A. D. Bruce, J. M. Kosterlitz and D. R. Nelson, *Crossover phenomena in isotropic dipolar ferromagnets*, J.Phys. C: Solid State Phys. **9**, 825 (1976).

50. A. D. Bruce, *Susceptibility crossover in dipolar ferromagnets*, J.Phys. C: Solid State Phys. **10**, 419 (1977).

51. E. Frey and F. Schwabl, *Renormalized field theory for the static crossover in isotropic dipolar ferromagnets*, Phys. Rev. B **43**, 833 (1991).

52. E. K. Riedel and F. J. Wegner, *Effective critical and tricritical exponents*, Phys. Rev. B **9**, 294 (1974).

53. H. S. Kogon and A. D. Bruce, *Transition temperature shifts and correction-to-scaling amplitudes in systems exhibiting crossover behaviour*, J. Phys. C **15**, 5729 (1982).

54. J. B. Goodenough and J.-S. Zhou, *Localized to Itinerant Electronic Transition in Perovskite Oxides*, Structure and Bonding Vol. 98, edited by J. B. Goodenough (Springer, Berlin, 2001).

Chapter 5

Nature of magnetic order in Fe doped LPMO manganites

In this chapter, a conclusive evidence is provided for the occurrence of a cluster spin glass state in the random Fe-substituted optimally hole-doped manganite $La_{0.7}Pb_{0.3}(Mn_{1-y}Fe_y)O_3$ *(*$y = 0.2, 0.3$*) based on the results of an exhaustive study of nonlinear magnetic susceptibilities. . As expected for a spin glass (SG), the nonlinear ac magnetic susceptibilities* $\chi_3(T, \omega)$ *and* $\chi_5(T, \omega)$ *(odd harmonics) diverge at the SG freezing temperature* $T_g = 80.00(3)K$ *(*$T_g = 56.25(5)K$*) in the static limit and, like the imaginary part of linear susceptibility, follow the dynamic scaling with the critical exponents* $\beta = 0.56(3)$ *(*$\beta = 0.63(3)$*),* $\gamma = 1.80(5)$ *(*$\gamma = 2.0(1)$*) and* $z\nu = 10.1(1)$ *(*$z\nu = 8.0(5)$*) in the sample with composition* $y = 0.2$ *(*$y = 0.3$*). The nonlinear susceptibility* χ_{nl}*, which has contributions from both* χ_3 *and* χ_5*, satisfies the static scaling with the same choice of* T_g*,* β *and* γ*. Irrespective of the Fe concentration, the values of the critical exponents* γ*,* ν *and* η *are in much better agreement with those theoretically predicted for a three-dimensional (d = 3) Heisenberg chiral SG than for a d = 3 Ising SG. True thermodynamic*

nature of the 'zero-field' spin glass transition is preserved even in finite magnetic fields. Unlike odd harmonics, even harmonics $\chi_2(T,\omega)$ and $\chi_4(T,\omega)$ make it evident that, apart from the macroscopic length scale of the spin glass order in the static limit, there exists a length scale that corresponds to the short-range ferromagnetic order. Thus, a combined investigation of both odd and even harmonics of the ac magnetic response not only permits an unambiguous distinction between the canonical and cluster spin glasses but also probes the magnetic order existing within the clusters.

5.1 Introduction

Hole-doped mixed-valent Manganites of the type $La^{3+}_{1-x}A^{2+}_{x}Mn^{3+}_{1-x}Mn^{4+}_{x}O^{2-}_{3}$ (A = Ca,Sr, Ba, Pb, Cd) have been at the forefront of condensed matter research since they provide a rare opportunity to study a unique combination, and a rich variety, of physical phenomena brought about by a complex interplay between the energy scales associated with the charge, spin, orbital and lattice degrees of freedom. This interplay enables these systems to be driven to various states (charge/spin/orbital or a combination thereof) of order by tuning the chemical-pressure (with doping at La and/or Mn sites) or oxygen off-stoichiometry or by applying pressure. One such system is the double-exchange metallic ferromagnet, $La_{0.7}Pb_{0.3}MnO_3$ (LPMO), in which Mn is partially substituted by the 3d transition metal Fe, Co, Ni. Compared to Ni or Co substitution [1] at the Mn site in LPMO, Fe substitution causes more drastic changes in the magnetic and electronic properties of the host and gives rise to different states of magnetic order of varying complexity in different Fe concentration regimes. The nature of magnetism in

$La_{0.7}Pb_{0.3}Mn_{1-y}Fe_yO_3$ for Fe concentrations $y > 0.1$, in particular, is a subject of intense debate [2–8] in the recent years.

It is generally agreed that, in $La_{0.7}Pb_{0.3}Mn_{1-y}Fe_yO_3$, Fe^{3+} (high-spin (HS), $S = 5/2$, $\mu = 5\mu_B$) ions substitute for the Mn^{3+} (HS, $S = 2$, $\mu = 4\mu_B$) ions at random. Therefore, as y increases, the number of Mn^{3+} ions available for the $Mn^{3+} - O^{2-} - Mn^{4+}$ double-exchange (DE) mechanism (responsible for metallic ferromagnetism) reduces while the $Fe^{3+} - O^{2-} - Mn^{3+}$ super-exchange (SE) bonds (leading to an antiferromagnetic (AFM) coupling between the magnetic moments of the neighboring Fe^{3+} and Mn^{3+} ions) increase in number, with the result that a precipitous drop [2–8] in the Curie temperature, T_C, and the low-temperature magnetic moment occurs. A random substitution of Mn^{3+} ions by Fe^{3+} ions thus gives rise to both the random site- and (exchange) bond-disorder (and hence to the quenched random-exchange disorder).

However, the opinions on issues such as the threshold Fe concentration y_c, beyond which the long-range FM order ceases to exist, and the nature of magnetic order for $y \geq y_c$, are sharply divided, as elucidated below. On the one hand, spin-polarized neutron diffraction (SPND) [5,6,8] and small-angle neutron scattering (SANS) experiments [6] strongly indicate that, as y increases, the AFM SE interactions grow at the expense of the ferromagnetic (FM) DE interactions so that the FM correlated regions shrink in size to the extent that the long-range FM order breaks down for $y \geq 0.2$. Consistent with this inference, a semiconducting/insulating state (without a transition to a metallic state) is found to persist down to $2K$ for $y > 0.15$ [2, 5]. The muon spin relaxation (μSR) [5] and neutron spin-echo (NSE) [7] investigations of spin dynamics in $La_{0.7}Pb_{0.3}Mn_{1-y}Fe_yO_3$ reveal the presence of the

fast and slow relaxation components, that are attributed to overdamped spin waves and collective reorientation of nanoscale ferromagnetic domains, respectively. On the other hand, based on bulk magnetization measurements [3,4] mainly, it is claimed [4] that the long-range FM order is present even up to Fe concentrations as high as $y = 0.4$ and beyond this concentration, a long-range AFM order sets in. Since the samples with $y \geq 0.2$ are electrically insulating/semiconducting [2,3,5] down to the lowest temperatures, long-range FM order is sustained in the insulating state over the Fe concentration regime $0.2 \leq y \leq 0.4$. Obviously, the DE mechanism fails to explain the existence of ferromagnetism in the insulating state.

In this chapter, a conclusive evidence is provided for a cluster spin glass state in the compositions $y = 0.2$ and $y = 0.3$ based on the static and dynamic scaling of the nonlinear (NL) magnetic susceptibilities.

5.2 Experimental details

The $La_{0.7}Pb_{0.3}(Mn_{1-y}Fe_y)O_3$ samples with $y = 0.2$ and $y = 0.3$ were prepared in the nanocrystalline (average grain size $\simeq 100nm$) form by the sol gel method and are the same as those used previously for the SPND, SANS, μSR and NSE experiments [5–8]. Magnetic susceptibility at a static magnetic field of $H \equiv H_{dc} = 10Oe$, $\chi_{dc}(H = 10Oe)$, was recorded over the temperature range $2K \leq T \leq 300K$ in both the ZFC and FC modes. The bifurcation, marking the onset of magnetic irreversibility, in the ZFC and FC $\chi_{dc}(T, H = 10Oe)$ curves opens up at $T < T_{irr} = 80K$. The first five harmonics of the ac magnetic response, $\chi_n(\omega, T, H) = \chi'_n(\omega, T, H) + i\chi''_n(\omega, T, H)$ with $n = 1, 2, 3, 4, 5$, were mea-

sured at 0.5 K, 0.2 K, 0.1 K, 0.2 K and 0.5 K steps in the temperature ranges 2 K - 10 K, 10 K - 60 K, 60 K - 100 K, 100 K - 120 K and 120 K - 150 K, respectively, at the rms amplitudes $h = 0.1, 1, 5, 10Oe$ and frequencies $10Hz \leq \omega \leq 10kHz$ of the ac driving field in the absence or presence of static fields in the range $30Oe \leq H \leq 1kOe$. In these measurements, dc and/or ac fields were applied after a fixed waiting time, t_w, of 5 minutes. After identifying the spin glass transition temperature, T_g, with the *frequency-independent* temperature where the nonlinear susceptibilities $\chi_3(T)$ and $\chi_5(T)$ peak, i.e., $T_g = 80K$, in the next experimental run, the dependence of $\chi_n(\omega, T, H)$ on the waiting time was recorded up to $t_w = 30\ min.$ ($t_w = 15\ min.$) at fixed temperatures in the steps of <100 mK (0.2 K) over the temperature range $78K \leq T \leq 82K$ (down to 60 K and up to 100 K, outside this range). We could not carry out experiments at frequencies lower than $10Hz$ for very long times since the accessible frequency window for high-precision measurements on the Quantum design PPMS-ACMS magnetometer is limited to the frequency range $10Hz - 10kHz$. Since the samples with Fe concentrations $y = 0.2$ and $y = 0.3$ yield essentially similar results, the χ_n $(n = 1 - 5)$ data for $y = 0.2$ only are presented here and the final results for $y = 0.3$ are quoted at the end. Unless specified otherwise, $\chi_n = \chi_n'$ since $\chi_n' \gg \chi_n''$.

5.3 Data analysis, Results and discussion

Figure 5.1 shows that, as a function of temperature, the linear susceptibility χ_1 goes through a broad peak, centred at $T_p \simeq 80K$, which reduces slightly in height and shifts to *higher* temperatures with increasing

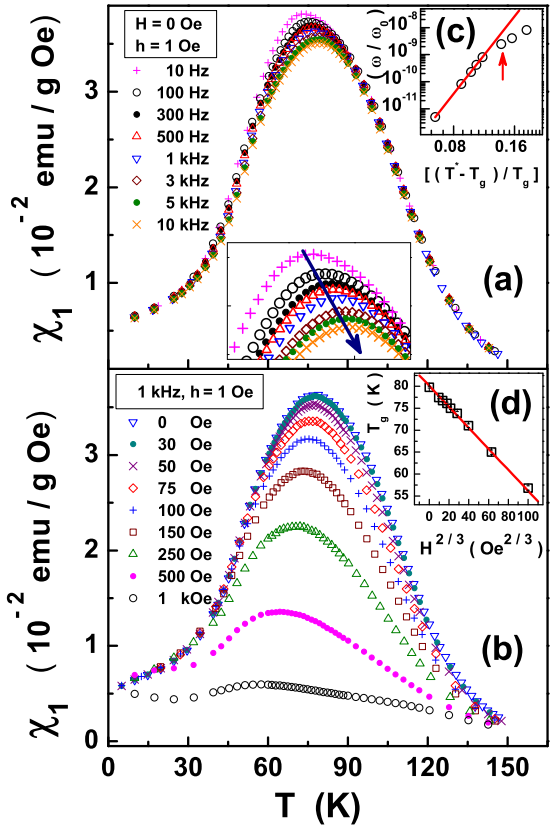

Figure 5.1: *The variations of the linear susceptibility, χ_1, with temperature (a) at different frequencies when $H = 0$ Oe and $h = 1$ Oe (the enlarged view of the peak in $\chi_1(T)$ serves to highlight the shift in the peak with frequency), and (b) at different static fields, H, when $h = 1Oe$ and $\omega = 1kHz$. The inset (c) of Fig.5.1(a) testifies to the validity of the critical slowing down model, Eq.(5.1), in the static limit, by demonstrating that the plot of $log(\omega/\omega_0)$ versus $log[(T^*(\omega) - T_g)/T_g]$ is linear for frequencies $\omega \leq 1$ kHz (the upward arrow marks the onset of strong deviations from Eq.(5.1) at $\omega = 3$ kHz) while the inset (d) of Fig.5.1(b) shows that the spin glass temperature T_g has the same dependence on the static field, H, as the AT irreversibility line in the (T, H) plane of a $d = 3$ Ising spin glass or as the spin-glass phase transition line at low fields within the chiral scenario of a $d = 3$ Heisenberg spin glass with weak random magnetic anisotropy.*

ac driving-field frequency, ω. By contrast, this peak gets drastically suppressed, smeared out and displaced to *lower* temperatures as the superposed dc magnetic field, H, increases in strength. The observation that T_p depends on *frequency* precludes the possibility of a true thermodynamic FM-to-PM (paramagnetic) phase transition at T_p but instead reflects the non-ergodic behaviour normally associated with spin glasses. If the peak temperature T_p is identified with the spin-glass (SG) freezing temperature T_g, the relative variation in T_g per decade of frequency $\Delta T_g/T_g\Delta(log\omega)$ is $3.1(2) \times 10^{-2}$ $(2.0(2) \times 10^{-2})$ for $y = 0.2$ $(y = 0.3)$. These values compare favourably with $\simeq 6 \times 10^{-2}$ or $\simeq 2 \times 10^{-2}$ reported previously for the insulating $(Eu, Sr)S$ [9] or semiconducting $Cd_{0.6}Mn_{0.4}Te$ [10] and $Zn_{0.1}Mn_{0.9}In_2Te_4$ [11] spin glasses but are an order of magnitude greater than $\simeq 5 \times 10^{-3}$ observed [9] in $CuMn$ and $AuMn$ metallic canonical spin glasses. This finding is consistent with the insulating/semiconducting behaviour [2,5] of the samples with $y = 0.2$ and $y = 0.3$ down to 2 K. Another important observation is that the peak at T_p is *much broader* and $\chi_1(T)$ is *two orders of magnitude larger* than that in the canonical spin glasses [12]. A broad peak at T_p and a huge enhancement in $\chi_1(T)$ are indicative of the presence of FM clusters.

5.3.1 Critical slowing down

In the case of a continuous second-order phase transition, the spin-spin correlation length (ξ) diverges as $\xi \sim \epsilon^{-\nu}$ (where the reduced temperature $\epsilon = (T-T_g)/T_g$ and ν is static critical exponent) when T_g is approached from above. Assuming the conventional critical slowing down on approaching T_g from high temperatures, the relaxation time ($\tau = 2\pi/\omega$) due to the

correlated dynamics is related to ξ as $\tau \propto \xi^z$, where z is the dynamic critical exponent. This relation for τ, when recast in terms of the measuring frequency ω, yields

$$\omega = \omega_0 \left[\frac{T^*(\omega) - T_g}{T_g} \right]^{z\nu} \tag{5.1}$$

If $T^*(\omega) = T_p(\omega)$, Eq.(5.1) is approximately followed over the entire frequency range with the values $\tau_0 = 2\pi/\omega_0 = 1.25(50) \times 10^{-12} s$, $z\nu = 10.0(10)$ and $T_g = 70.0(10) K$. This approach yields a much lower value of T_g than that obtained from the scaling analysis of the nonlinear susceptibilities in sub-section 5.3.2. This is so because such an assignment defines a set of $T^*(\omega)$ values for which τ is not necessarily constant, as should be the case for Eq.(5.1) to be applicable. To remedy this, we use the criterion [13] that $T^*(\omega)$ is the temperature at which the quantity $tan\theta = \chi''/\chi' = \omega\tau_{av}$ is a constant. This is true only when the phase angle θ is so small (e.g., $\lesssim 0.1^\circ$) that $tan\theta \approx \theta = const.$ At a given frequency, T^* thus marks the temperature at which $\theta(T)$ goes through a minimum ($\sim 0.05^\circ$). In accordance with Eq.(5.1), the plot of $log(\omega/\omega_0)$ versus $log[(T^*(\omega) - T_g)/T_g]$, shown in the inset (c) of figure 5.1(a), is linear for frequencies $\omega \leq 1 kHz$ with the choice of parameters $\tau_0 = 5.2(6) \times 10^{-12} s$, $z\nu = 9.5(8)$ and $T_g = 79.9(4) K$. The values of $z\nu$ and T_g, so obtained, agree quite well with those determined from the static (dynamic) scaling of χ_{nl} (χ_3 and χ_5) in sub-section 5.3.2. However, the deviations from Eq.(5.1) progressively grow as the driving field frequency increases beyond $3 kHz$. The source of these deviations is addressed in sub-section 5.3.5.

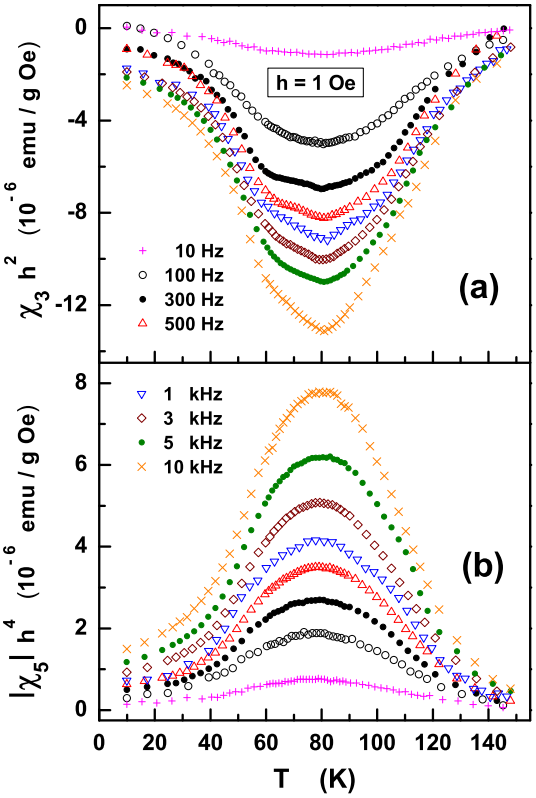

Figure 5.2: *Temperature variations of the nonlinear susceptibilities (a) χ_3 and (b) χ_5 at various fixed frequencies when $H = 0$ Oe and $h = 1$ Oe.*

5.3.2 Static and dynamic scaling of nonlinear susceptibilities

In the static limit ($\omega \to 0$), magnetization of a spin glass system, at temperatures below or above T_g, can be expressed in the powers of the applied dc magnetic field, H, as

$$M = \chi_1 H + \chi_3 H^3 + \chi_5 H^5 + \cdots \tag{5.2}$$

The terms with even powers of H do not appear in the above expression for the following reason. The even harmonics in the magnetic response, i.e., the NL susceptibilities χ_2, χ_4, ..., are zero [14] for an ideal SG at temperatures $T \gtrless T_g$ because they are proportional to spontaneous magnetization, M_0, or its powers, and $M_0 = 0$ in both SG and PM phases. By contrast, for a ferromagnet, χ_2, χ_4 are (finite) *negative*, *diverge* as T_c is approached from below and, in the mean-field description [15], abruptly jump to zero at $T = T_c$ and stay at zero for $T > T_c$. If the SG-PM phase transition occurs at a finite temperature T_g, χ_1 is *non-singular* but the NL susceptibilities χ_3, χ_5, ... diverge [14, 16] at $T = T_g$. Again in sharp contrast with this behaviour, in a ferromagnet, χ_1 and χ_5 are positive and diverge at $T = T_c$ whereas χ_3 is positive, changes sign at $T = T_c$ and diverges on both sides of T_c [15]. Thus, based on the temperature variations of χ_n $(n = 1 - 5)$, a spin glass can be unambiguously distinguished from a ferromagnet, or even from an antiferromagnet [14].

The NL susceptibility, χ_{nl}, at a static field H defined as, $\chi_{nl} = (M/H) - \chi_1 = \chi_3 H^2 + \chi_5 H^4 + \cdots$, can, in the vicinity of $T = T_g$, be expressed as a function of a single variable $H^2/\epsilon^{\beta+\gamma}$ as [12]

$$\chi_{nl} = \epsilon^{\beta}\ G\left(H^2/\epsilon^{\beta+\gamma}\right) \tag{5.3}$$

where $G(x)$ is the static scaling function while β and γ are the critical exponents for the SG order parameter and χ_3, respectively. The critical exponents γ and $\beta + 2\gamma$ characterize the divergence [12] of χ_3 and χ_5, respectively, as T_g is approached from above. When instead of a static field, a time-varying field, $H(t) = H + h\ sin\omega t$ with $h/H \ll 1$, is applied, the NL susceptibility is given by the expression [12, 17] $\chi'_{nl} = (\partial m/\partial h) - \chi_1 = 3\chi_3 H^2 + 5\chi_5 H^4 + \cdots$, where m is the ac component of magnetization. The

frequency-dependent NL susceptibilities $\chi_3(\epsilon,\omega)$ and $\chi_5(\epsilon,\omega)$, in the above expression for χ'_{nl}, follow the dynamic scaling equations of state [12]

$$\chi_n(\epsilon,\omega)/\epsilon^{-\gamma_n} = g_n\left(\omega/\epsilon^{z\nu}\right) \tag{5.4}$$

with $n = 3, 5, \cdots$, $g_n(x)$ the corresponding dynamic scaling function, $\gamma_3 = \gamma$ and $\gamma_5 = \beta + 2\gamma$.

While the divergence of χ_3 at $T = T_g$ together with the static scaling, Eq.(5.3), and dynamic scaling, Eq.(5.4), of NL susceptibility constitute a stringent test for ascertaining whether or not a spin glass state exists and a phase transition to the PM state occurs at a finite temperature $T = T_g$, the critical exponents β, γ and $z\nu$ decide the universality class ($d = 3$ Ising or Heisenberg SG) to which a given system belongs.

Unlike T_p in $\chi_1(T)$, the temperature $T_p^{NL} = 80K$, at which the $|\chi_3(T)|$ and $|\chi_5(T)|$ curves (taken at fixed frequencies) peak, *does not depend on the frequency* of the ac driving field, as should be the case for a true thermodynamic phase transition. This conclusion rests on the observation that no shift in T_p^{NL} with ω over three decades of frequency (figure 5.2(a) and 5.2(b)) could be discerned within the measurement temperature interval of $\simeq 30mK$ around T_p^{NL}. To determine the true asymptotic value of the exponent γ, we make use of the 'range-of-fit' (ROF) data analysis, detailed in reference 23, and the following expression for $\chi_3(T)$

$$\begin{aligned} \chi_3^{-1}(T) &= [\chi_3^{int}(T)]^{-1} + const. \\ &= A_{eff}(T)\ \epsilon^{\,\gamma_{eff}(T)} + const. \quad (\epsilon > 0) \end{aligned} \tag{5.5}$$

where χ_3^{int} is the intrinsic nonlinear (third harmonic) susceptibility that diverges at T_g, the effective critical exponent for χ_3, γ_{eff}, depends on tem-

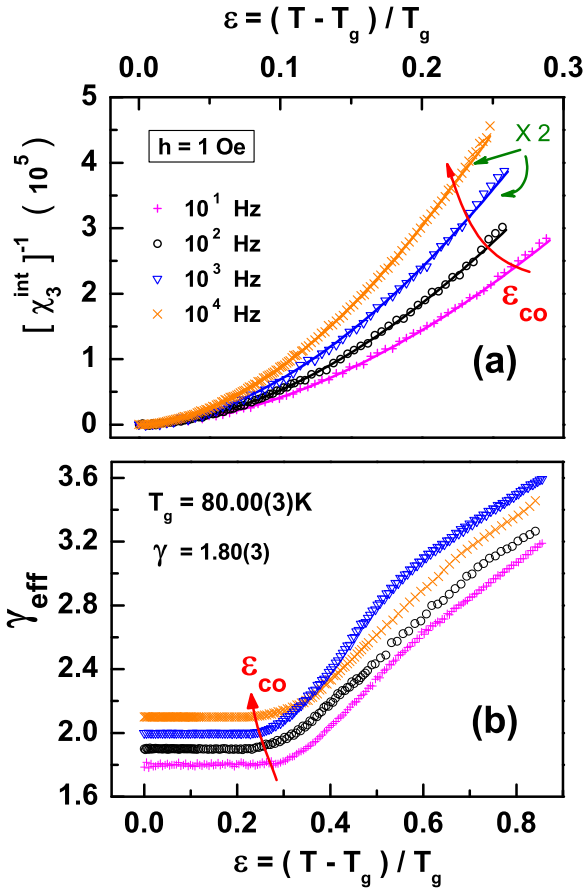

Figure 5.3: *(a) $[\chi_3^{int}]^{-1}(\epsilon)$ (symbols), in a temperature range wider than the asymptotic critical region, ACR, ($\epsilon \leq \epsilon_{co}$), at the ac driving field frequencies $\omega = 10^1, 10^2, 10^3, 10^4 Hz$ and amplitude $h = 1Oe$, along with the theoretical fits (continuous curves), based on Eq.(5.5) of the text, obtained in the ACR. Note that the $[\chi_3^{int}]^{-1}(\epsilon)$ data corresponding to $\omega = 10^3$ and $10^4 Hz$ are multiplied by a factor of 2, in Fig.3(a). (b) The temperature variations of the effective critical exponent for χ_3 yielded by the range-of-fit analysis based on Eq.(5.5). For the sake of clarity, the $\gamma_{eff}(\epsilon)$ data for $\omega = 10^2, 10^3$ and $10^4 Hz$ are shifted up by 0.1, 0.2 and 0.3, respectively, with respect to that for $\omega = 10^1 Hz$.*

perature and attains the constant limiting value γ in the asymptotic critical region (ACR), i.e., $\gamma_{eff}(\epsilon) \rightarrow \gamma$ as $\epsilon \rightarrow 0$. The constant in Eq.(5.5) accounts for the fact that the finite size of the system limits the divergence of χ_3 at $\epsilon = 0$ (i.e., at $T = T_g$). As an illustration, figure 5.3(a) shows the theoretical fits to $[\chi_3^{int}(T)]^{-1}$ $(= \chi_3^{-1}(T) - \chi_3^{-1}(T = T_g))$ at $\omega = 10^1 Hz, 10^2 Hz, 10^3 Hz, 10^4 Hz$, $h = 1Oe$ and $H = 0$, based on Eq.(5.5) with $\gamma_{eff} = 1.80$, obtained in the ACR. The $[\chi_3^{int}(T)]^{-1}$ data deviate from such fits (continuous curves) when the temperature exceeds the crossover temperature, ϵ_{co}, which marks the upper bound of the ACR. The width of the ACR shrinks with increasing frequency as ϵ_{co} reduces from 0.27 at $\omega = 10^1 Hz$ to 0.23 at $\omega = 10^4 Hz$. The ROF analysis yields $T_g = 80.00(3)K$, $\gamma_{eff}(\epsilon)$ (as depicted in figure 5.3(b)) and the *frequency-independent* value, $\gamma = 1.80(3)$ in the ACR, $1.0 \times 10^{-3} \leq \epsilon \lesssim 2.5 \times 10^{-1}$ for $10^1 Hz \leq \omega \leq 10^4 Hz$. By following the same procedure as above for analyzing the $\chi_5(T)$ data, we arrive at the value 4.16(6) for the exponent $\beta + 2\gamma$, implying thereby that the exponent $\beta = 0.56(2)$. Note that the $\chi_3(T)$ and $\chi_5(T)$ data taken at $h = 0.1Oe$ over the frequency range $10^1 Hz \leq \omega \leq 10^4 Hz$ yield exactly the same values for the critical exponents β and γ as those for $h = 1Oe$. The *frequency-independent* values for the critical exponents strongly indicate that the *static* critical exponents have been determined in this work.

That the *true thermodynamic nature* of the 'zero-field' spin glass transition is *preserved even in finite magnetic fields* is corroborated by the observation that well-defined $T_g(H)$, marking the temperature at which the $|\chi_3(T)|_{\omega,H}$ or $|\chi_5(T)|_{\omega,H}$ curves peak, is *independent of* ω *over three decades of frequency* and decreases with increasing H, as shown in the inset (d) of Fig.5.1(b) at a representative frequency of $10^3 Hz$.

In order to verify if the static scaling, Eq.(5.3), holds in the present case,

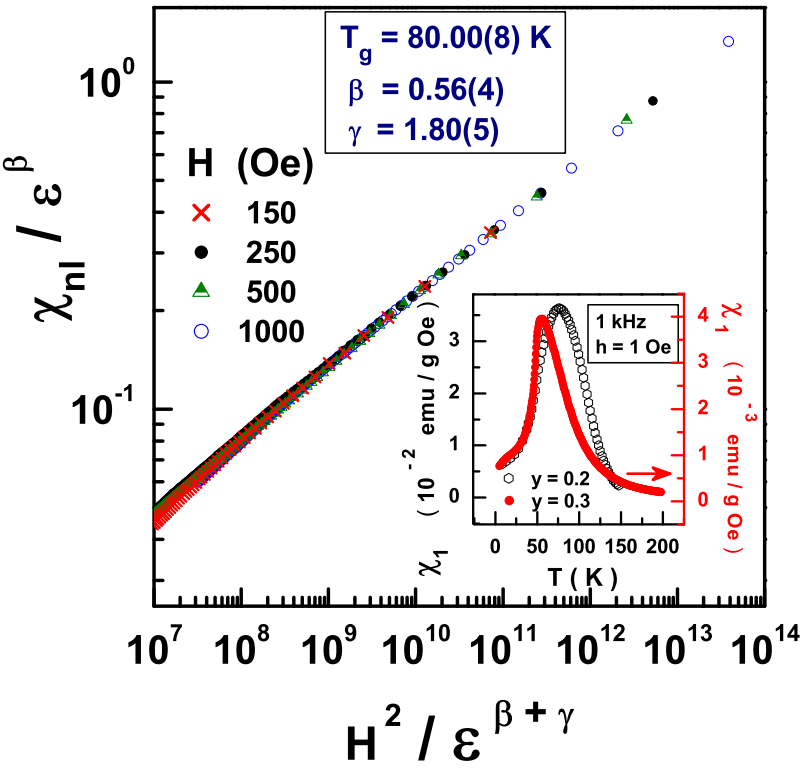

Figure 5.4: *The reduced nonlinear susceptibility $\chi_{nl}/\epsilon^{\beta}$ plotted against the reduced conjugate static field $H^2/\epsilon^{\beta+\gamma}$ for the composition $y = 0.2$. The validity of the static scaling, Eq.(5.3), is demonstrated by an optimum collapse of the data, taken at different static fields, onto a single universal scaling curve for the choice $T_g = 80.00(8)K$, $\beta = 0.56(4)$ and $\gamma = 1.80(5)$. The inset compares the linear susceptibilities of the samples $y = 0.2$ and $y = 0.3$, measured, in the absence of static field, at the ac field amplitude of $h = 1Oe$ and frequency $\omega = 1kHz$.*

T_g and γ are kept fixed at the values $T_g = 80.00K$ and $\gamma = 1.80$, obtained from the ROF analysis, and the exponent β is varied so that the χ_{nl} data at different but fixed static fields collapse onto a single universal $\chi_{nl}/\epsilon^{\beta}$ versus $H^2/\epsilon^{\beta+\gamma}$ scaling plot. The residual freedom, if any, in T_g, β and γ is then

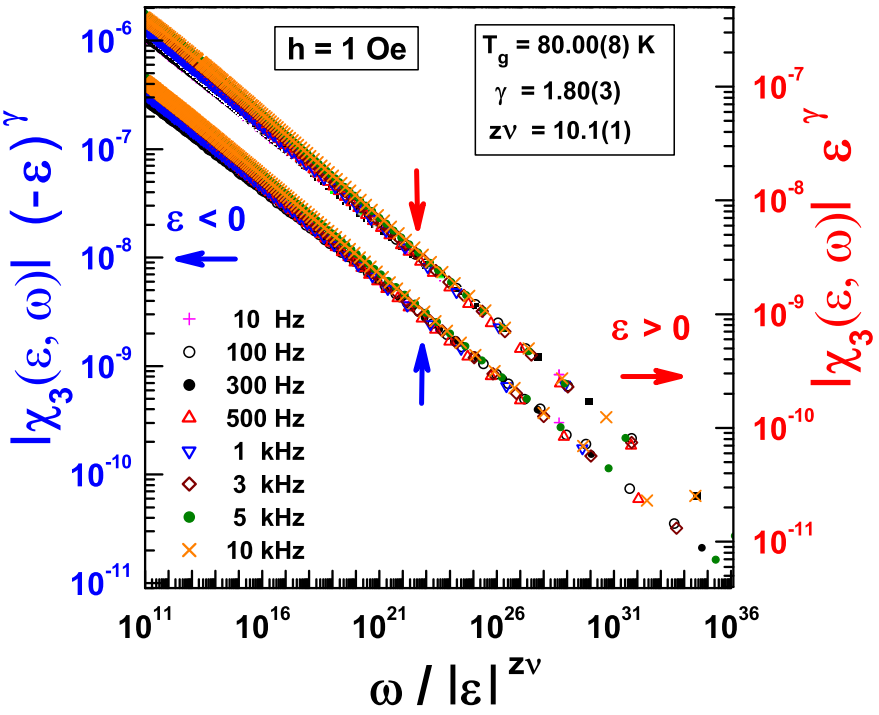

Figure 5.5: *Dynamic scaling of the nonlinear susceptibility χ_3, based on equation (5.4) of the text, for temperatures below ($\epsilon < 0$) and above ($\epsilon > 0$) T_g. Vertical arrows mark the bifurcation temperatures (see text).*

used to obtain the best data collapse over the largest possible range of the scaling argument, which corresponds to the ϵ range $1.1 \times 10^{-3} - 1.3 \times 10^{-1}$. Figure 5.4 demonstrates that a very good data collapse is achieved for the choice $T_g = 80.00(8)K$, $\beta = 0.56(4)$ and $\gamma = 1.80(5)$. Note that the χ_{nl} data used to construct the scaling plot are obtained by subtracting $\chi_1(T, h = 1Oe, \omega = 100Hz)$, for fixed H, from FC $\chi_{dc}(T, H = 10Oe)$. But for a slight increase in the scatter in the scaling plot, results similar to those presented in Fig.5.4 are obtained when $\chi_1(T, h = 1Oe, \omega = 10Hz)$ data are

used.

Similarly, at first, we set $T_g = 80.00K$, $\gamma = 1.80$ and $\beta = 0.56$ and vary the

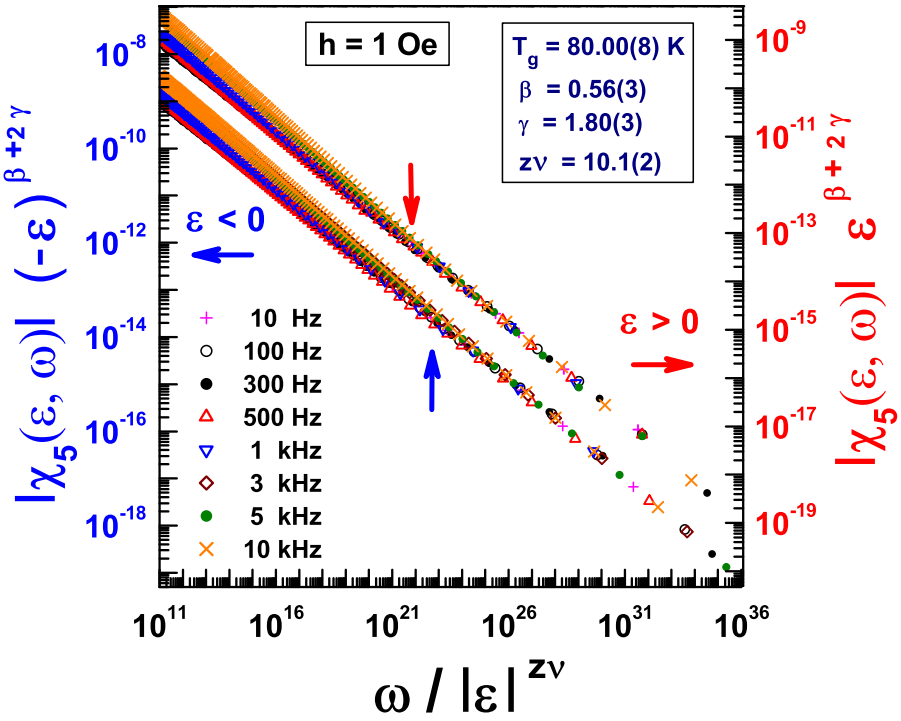

Figure 5.6: *Dynamic scaling of the nonlinear susceptibility χ_5, based on equation (5.4) of the text, for temperatures below ($\epsilon < 0$) and above ($\epsilon > 0$) T_g. Vertical arrows mark the bifurcation temperatures (see text).*

exponent $z\nu$ in the dynamic scaling plots for $\chi_3(\epsilon, \omega)$ and $\chi_5(\epsilon, \omega)$, based on Eq.(5.4), to accomplish a good data collapse separately for temperatures below ($\epsilon < 0$) and above ($\epsilon > 0$) T_g. In the next step, the parameters T_g, β, γ and $z\nu$ are fine-tuned to optimize the data collapse over as large a range of $\omega/|\epsilon|^{z\nu}$ as possible while aiming at achieving the best data collapse in the vicinity of $\epsilon = 0$. Since the quality of data collapse cannot

be directly assessed from the scaling plots, presented in figures 5.5 and 5.6, because of the insensitive nature of logarithmic scales, a blow-up of these scaling plots over every decade of the scaling argument $\omega/|\epsilon|^{z\nu}$ reveals that, for the choice $T_g = 80.00(8)K$, $\gamma = 1.80(3)$, $\beta = 0.56(3)$ and $z\nu = 10.1(2)$, the SG dynamic scaling, Eq.(5.4), holds (scatter $< 5\%$) in the range $10^8 \leq \omega/|\epsilon|^{z\nu} \leq 3.7 \times 10^{33}$ for $\epsilon > 0$ and $10^{10} \leq \omega/|\epsilon|^{z\nu} \leq 3.7 \times 10^{33}$ for $\epsilon < 0$ over three decades of frequency $10^1 Hz \leq \omega \leq 10^4 Hz$. These ranges of the scaling argument correspond to the reduced temperature ranges $1.0 \times 10^{-3} \leq \epsilon \leq 2.3 \times 10^{-1}$ and $1.0 \times 10^{-3} \leq (-\epsilon) \leq 1.3 \times 10^{-1}$), respectively. While the $\chi_3(\epsilon, \omega)$ and $\chi_5(\epsilon, \omega)$ data for the frequencies 3, 5 and 10 kHz, like those taken at frequencies $\omega \leq 1\ kHz$, obey dynamic scaling in the above temperature ranges below and above T_g, the former set of data starts deviating from the latter set at $\epsilon = -1.05 \times 10^{-2}$ for $\epsilon < 0$ and $\epsilon = 1.25 \times 10^{-2}$ for $\epsilon > 0$. The bifurcation in the two sets of data is all the more pronounced in the scaling plots for $\chi_5(\epsilon, \omega)$ in figure 5.6. Though higher values of $z\nu$, β and/or γ get rid of this bifurcation, they spoil the agreement between the two sets of data at temperatures close to T_g where the dynamic scaling should be valid at all frequencies if the SG transition at T_g is a thermodynamic phase transition. Since the dynamic spin-spin correlation length is related to the frequency as $\omega \propto \xi^{-z}$, the contribution to $\chi_3(\epsilon, \omega)$, and more so to $\chi_5(\epsilon, \omega)$, from the FM clusters becomes important when the frequency exceeds a threshold value because at such frequencies, ξ becomes comparable to the sizes of such clusters. Another important point to note is that the deviations from the dynamic scaling are observed when the temperature approaches T_g closer than $\epsilon = 1.0 \times 10^{-3}$ or when the temperature falls outside the ACR on either side of T_g. While the deviations as $\epsilon \to 0$ could be a consequence of the well-known fact

that the waiting time of 30 minutes is not sufficient for the spin system to attain complete thermodynamic equilibrium, those outside the ACR may either reflect the increasing importance of the 'correction-to-scaling' terms or magnetic ageing particularly for $T \ll T_g$ (the SG ageing effects become apparent at temperatures below $T \simeq 0.8T_g$). At this stage, it should be emphasized that the present manganite system marks the only spin glass system for which the dynamic scaling of $\chi_5(\epsilon, \omega)$ has been demonstrated so far and T_g could be approached as closely as $\epsilon = 1.0 \times 10^{-3}$.

5.3.3 Dynamic scaling of $\chi_1''(\omega, T)$

For an independent determination of the exponents $z\nu$ and β, we use the dynamic scaling equation for $\chi_1''(\omega, T)$, proposed by Geschwind et al. [18],

$$T\chi_1''(\omega, T)/\epsilon^{\beta} = g_1\left(\omega/\epsilon^{z\nu}\right) \tag{5.6}$$

Setting $T_g = 80.0K$ and varying β and $z\nu$, a nearly perfect data collapse (scatter $< 4\%$), as witnessed in figure 5.7, is obtained for the $\chi_1''(\omega, T)$ data taken over three decades of frequency in the reduced temperature range $-0.13 \leq \epsilon \leq \epsilon_{co}(\omega)$ (where $\epsilon_{co}(\omega)$ reduces from 0.27 at $\omega = 10^1 Hz$ to 0.23 at $\omega = 10^4 Hz$) for the choice $\beta = 0.56(2)$ and $z\nu = 9.9(5)$. These values for β and $z\nu$ as well as the temperature ranges over which the dynamic scaling of $\chi_1''(\omega, T)$ holds are in excellent agreement with those determined earlier from the static and dynamic scaling of NL susceptibilities. Consistent with the observations made based on the dynamic scaling of $\chi_3(\epsilon, \omega)$ and $\chi_5(\epsilon, \omega)$, the quality of data collapse deteriorates drastically when $\epsilon > \epsilon_{co}(\omega)$. In order to ensure that departures from perfect scaling, Eq.(5.6), that are considerably

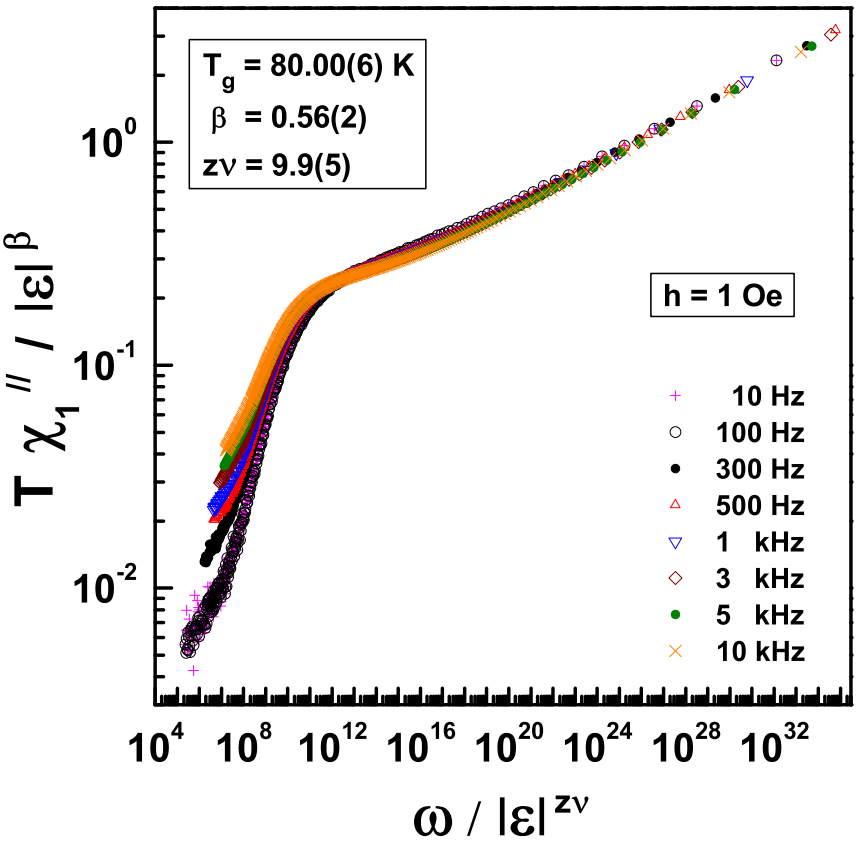

Figure 5.7: *Dynamic scaling of the imaginary part of linear susceptibility, $\chi_1''(T)$, based on equation (5.6).*

larger than the experimental error, are not concealed by the log-log plot in Fig.5.7, the data used in Fig.5.7, with exactly the same parameter values $T_g = 80.00(6)K$, $\beta = 0.56(2)$ and $z\nu = 9.9(5)$ as those obtained using Eq.(5.6), are re-plotted according to the alternative form of the dynamic scaling equation [18]

$$T\chi_1''(\omega, T)/\omega^{\beta/z\nu} = f_1\left(\epsilon/\omega^{1/z\nu}\right) \tag{5.7}$$

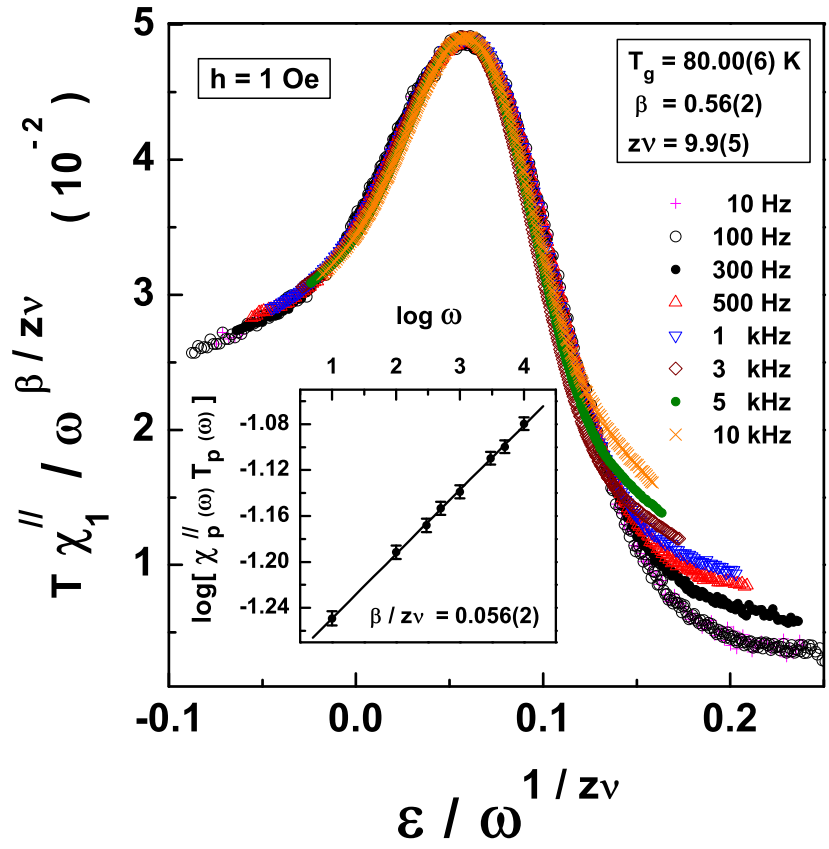

Figure 5.8: *Dynamic scaling of the imaginary part of linear susceptibility, $\chi_1''(T)$, based on equation (5.7). Linear plot of $log[\chi_p''(\omega)\ T_p(\omega)]$ against log ω with slope $\beta/z\nu = 0.056(2)$ in the inset demonstrates the validity of the scaling relation $\chi_p''(\omega)\ T_p(\omega) \sim \omega^{\beta/z\nu}$.*

that is expected to bring out clearly any such departures due to the high sensitivity of the ordinate and abscissa scales. With the parameter values stated above, the same observations about the validity or otherwise of the dynamic scaling of $\chi_1''(\omega, T)$ are made regardless of whether the scaling equation (5.6)

or (5.7) is used, as is evident from figure 5.8. However, the use of Eq.(5.7) clearly demonstrates that the overall scatter in the scaling plots within the temperature ranges where the $\chi_1''(\omega, T)$ data follow dynamic scaling over three decades of frequency does not exceed 3%, which is comparable to the typical scatter in the low-frequency ($\omega \leq 300Hz$) data. The main advantage in employing Eq.(5.7) instead of Eq.(5.6) is that it provides an independent estimate of the ratio $\beta/z\nu$ as follows. According to Eq.(5.7), the peaks in $T\chi_1''(\omega, T)$ at $T_p(\omega)$, where $\chi_1''(\omega) = (\chi_1'')_p(\omega) \equiv \chi_p''(\omega)$, must collapse onto a single point on the scaling plot with the result that $\chi_p''(\omega)\ T_p(\omega) \sim \omega^{\beta/z\nu}$. Inset of Fig.5.8 demonstrates that the plot of $log[\chi_p''(\omega)\ T_p(\omega)]$ against $log\omega$ is indeed a straight line with slope $\beta/z\nu = 0.056(2)$. This ratio conforms well with the values determined for β and $z\nu$ individually throughout this work from different forms of scaling, static or dynamic, and from the critical slowing down. Considering that a t_w of 15 min (30 min) amounts to $\sim 10^4\tau_{\chi''}$ ($\sim 2 \times 10^4\tau_{\chi''}$), where $\tau_{\chi''}$ is the characteristic time for χ_1'' at $\omega = 10\ Hz$ ($\tau_{\chi''} \sim 1/\omega$) for temperatures not very far from T_g (in the immediate vicinity of T_g), the spin system presumably attains equilibrium even for the lowest frequency $\omega = 10\ Hz$.

5.3.4 Comparison with theory

The above self-consistent method of data analysis yields $T_g = 56.25(5)K$, $\beta = 0.63(3)$, $\gamma = 2.0(1)$ and $z\nu = 8.0(5)$ for the composition $y = 0.3$. These values of β, γ and $z\nu$, like those for $y = 0.2$, fall within the ranges $0.5 \leq \beta \leq 0.9$, $2 \leq \gamma \leq 4$ and $7 \leq z\nu \leq 11$, reported for a wide variety of spin glass systems [9–12, 17, 19–22]. For a recent compilation of the experimental values of critical exponents for d = 3 Heisenberg spin glass

Table 5.1: *Comparison of the critical exponents determined in this work for the manganite system $La_{0.7}Pb_{0.3}(Mn_{1-y}Fe_y)O_3$ $(y = 0.2, 0.3)$ with those reported for the canonical spin glass $AgMn$ and with the best theoretical estimates (currently available) for bimodal $(\pm J)$ Heisenberg chiral spin glass (HCSG), Gaussian (G) HCSG, $\pm J$ Ising spin glass (ISG) and G ISG.*

Exponent	$AgMn$ [12]	$y = 0.2$	$y = 0.3$	$\pm JHCSG$ [26]	$GHCSG$ [24,25]	$\pm JISG$ [27]	$GISG$ [28]
β	0.9(2)	0.56(3)	0.63(3)	1.2(7)	1.1(3)	0.77(5)	0.77(5)
γ	2.3(2)	1.80(5)	2.0(1)	1.5(4)	2.0(5)	5.8(4)	5.8(3)
δ	3.3(3)	4.2(3)	4.2(3)	2.3(4)	2.75(4)	8.6(1)	8.5(8)
η	0.23(32)	0.14(13)	0.2(2)	0.8(2)	0.6(2)	-0.375(10)	-0.37(5)
ν	1.30(15)	0.97(4)	1.1(1)	1.2(2)	1.4(2)	2.45(15)	2.44(9)
z	5.3(8)	10.4(10)	7.3(12)	-	-	-	-

materials with weak anisotropy, we refer the reader to the recent review by Campbell and Petit [23]. In Table I, the presently determined values for the critical exponents are compared with the best theoretical estimates, yielded hitherto by the Monte Carlo simulations, for d = 3 bimodal $(\pm J)$ or Gaussian Heisenberg chiral spin glasses (HCSG) with weak random magnetic anisotropy [24–26] and d = 3 bimodal/Gaussian Ising spin glass (ISG) systems [27,28]. To put such a comparison between theory and experiment in a proper perspective, one has to recognize that the theory calculates the critical exponents ν and η and uses the scaling and hyperscaling relations $\beta = \nu\ (1+\eta)/2$, $\gamma = (2-\eta)\ \nu$ and $\delta = (d+2-\eta)/(d-2+\eta)$ to obtain the exponents β, γ and δ whereas the experiments determine β, γ and occasionally, δ, and deduce ν and η via the hyperscaling relations $d\ \nu = 2\beta + \gamma$ and $\eta = 2 - d\ (\delta - 1)/(\delta + 1)$. We have used the scaling and hyperscaling relations $\delta = 1 + (\gamma/\beta)$, $d\ \nu = 2\beta + \gamma$ with $d = 3$ and $\eta = 2 - (\gamma/\nu)$ to arrive at the values of δ, ν and η displayed in Table I. With the exception of the

exponent β, all the exponents for the samples $y = 0.2$ and $y = 0.3$ possess values that are *closer* to those predicted by the HCSG model. Apart from the widely different exponent values for the HCSG and ISG models, the main distinguishing feature is the opposite sign of the exponent η. In the present case, η has the same magnitude (within the uncertainty limits) and sign as that predicted by the HCSG model. Consistent with this observation, the SG transition temperature T_g follows the $H^{2/3}$ (inset (d) of figure 5.1(b)) variation with the static field that the HCSG model (which considers a weak coupling between the chiral and spin degrees of freedom induced by magnetic anisotropy) yields for the CG transition at low fields in a $d = 3$ Heisenberg spin glass with weak random anisotropy [25]. Incidentally, the Edwards-Anderson mean-field model also predicts the $H^{2/3}$ power law dependence of T_g [29] along the Almeida-Thouless *irreversibility line* in the (T, H) plane for $d = 3$ ISG but *no thermodynamic* spin-glass *phase transition in finite fields* occurs in ISGs [30]. In contradiction with the above agreement between our results and the predictions of the HCSG model, the SG order parameter critical exponent β turns out to be a factor of two smaller in magnitude. Instead, the numerical estimate given by the ISG model for β is closer to the observed value. The coexistence of ferromagnetic short-range order with SG order for $T \leq T_g$ (sub-section: 5.3.5) may have a direct bearing on this discrepancy in the value of β. Note that in view of the scaling identity $\delta = 1 + (\gamma/\beta)$, the lower value of β is basically responsible for the value of δ higher than that predicted by the HCSG model. The present results thus favour the thesis that the random Fe-substituted optimally hole-doped manganite $La_{0.7}Pb_{0.3}(Mn_{1-y}Fe_y)O_3$ $(y = 0.2, 0.3)$ behaves as a $d = 3$ (localized-spin) Heisenberg spin glass with weak random magnetic anisotropy in the critical region and that the observed phase transition at

T_g basically reflects the chiral-glass transition of the isotropic Heisenberg SG [25].

5.3.5 Ferromagnetic short-range order

Had it not been for the presence of the characteristic experimental signatures of the FM short-range order in the temperature variations of the NL susceptibilities χ_2 and χ_4, displayed in figure 5.9 for $y = 0.2$, the results presented so far would have strongly indicated that the manganite system in question is, at best, a spin glass. At this stage, it should be recalled that $\chi_2(T)$ and $\chi_4(T)$ are better suited for a clear-cut distinction between a SG and a ferromagnet than $\chi_3(T)$ and $\chi_5(T)$. This is so because the divergences in $\chi_3(T)$ and $\chi_5(T)$ at T_g in a SG and at T_c in a ferromagnet are not radically different unless the long-range FM order is fully developed. In comparison, $\chi_2(T)$ and $\chi_4(T)$ are *zero* at all temperatures including those close to T_g in an ideal/canonical SG whereas they are *negative* and *diverge* at T_c in a ferromagnet. Based on these considerations, the $\chi_2(T)$ and $\chi_4(T)$ data, presented in Fig.5.9, provide direct evidence for the existence of two different time (and hence length) scales for the SG and FM order: the long-range (global) SG order and the short-range FM order observed at the experimental time scales $\tau_{ex} \gtrsim 1ms$ (in the static limit) and $\tau_{ex} \lesssim 10^{-4}s$, respectively. The short-range nature of FM order is inferred from the considerably broad negative peaks centred at $T_c \simeq 80K$ that result when the spin-spin correlation length, ξ, does not diverge, but remains finite, at T_c. Obviously, at a shorter time scale (high frequencies), smaller FM clusters (regions with ferromagnetically-ordered spins) essentially dictate the magnetic response whereas in the static limit $t \to \infty$, global cluster SG order at $T \leq T_g$

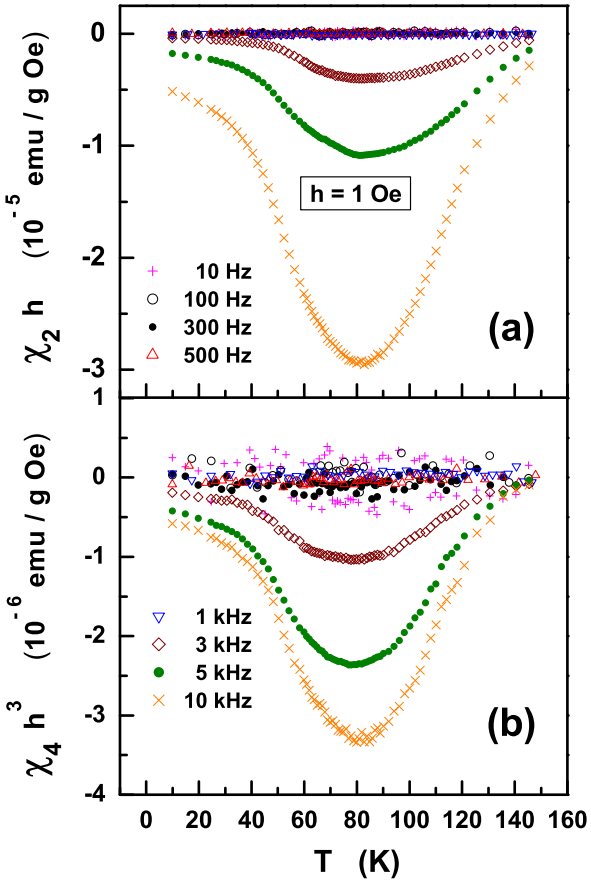

Figure 5.9: *Temperature variations of the nonlinear susceptibilities* χ_2 *and* χ_4 *at different frequencies when* $H = 0Oe$ *and* $h = 1Oe$*, revealing that the magnetic response is dominated by the long-range spin glass order (short-range ferromagnetic order) at frequencies* $\omega \leq 1kHz$ *(*$\omega \geq 3kHz$*).*

(brought about by the competing interactions between the finite FM clusters) governs the thermal behaviour of NL susceptibilities. The existence of two distinct time (or length) scales for SG and short-range FM order

(Fig.5.9) also explains the strong departures observed from the SG critical slowing down in the inset (c) of Fig.5.1(a) and from the SG dynamic scaling of nonlinear susceptibilities and linear susceptibility in figures 5.5-5.8 at frequencies $\omega \geq 3\ kHz$. For the sample with $y = 0.3$, a broad negative peak centred at $T_c \simeq 56K$ in $\chi_2(T)$ and $\chi_4(T)$ first appears at $\omega = 10kHz$, implying thereby that the FM order is prevalent over much shorter length scales than that in $y = 0.2$. This inference is also supported by the observation that $\chi_1(T)$ is *lower by an order of magnitude* and exhibits a *much sharper* peak at $T_g \simeq 56K$ in $y = 0.3$ than in $y = 0.2$ (inset of Fig.5.4). In conformity with this observation, the SANS data [6] corroborate that the FM correlated regions shrink in size as the Fe concentration increases such that the FM correlations do not grow beyond $\simeq 3\ nm$ in $y = 0.2$ even at $T = T_c \simeq 80K$, where $\xi(T)$ peaks. Note that for both $y = 0.2$ and $y = 0.3$, T_g practically coincides with T_c whereas the samples with lower Fe concentration (e.g., $y = 0.1$) exhibit two transitions: the high-temperature FM - PM transition followed, at much lower temperatures, by a re-entrant transition.

5.4 Summary and Conclusion

The final picture that emerges from our results in the Fe concentration regime $0.2 \leq y \leq 0.3$ is the one in which completely isolated finite metallic FM clusters coexist with an infinite insulating SG (PM) matrix for $T \leq T_g$ ($T > T_g$). The double-exchange interactions between the spins of Mn^{3+} and Mn^{4+} nearest neighbours give rise to finite metallic FM clusters whereas the insulating matrix is a consequence of the localiza-

tion of e_g electrons on both Fe^{3+} and Mn^{3+} ions because the high-spin states of Fe^{3+} and Mn^{3+} ions block the e_g-electron hopping [2] between them and also between Fe^{3+} - Fe^{3+} and Mn^{3+} - Mn^{3+}). Random substitution of Mn^{3+} ions by Fe^{3+} ions and the competing FM and AFM interactions respectively cause the quenched random-exchange disorder and spin-frustration, that constitute the necessary ingredients for the cluster spin glass state. The FM coupling between the magnetic moments of FM clusters is presumably due to the inter-cluster dipole-dipole interactions whereas the AFM coupling arises from the $TM_1^{3+} - O^{2-} - TM_2^{3+}$ super-exchange interactions, where TM_1, TM_2 stand for either Fe or Mn. As elucidated in reference [1], the above percolation picture, applicable to all those hole-doped manganites with quenched random-exchange disorder that are below, but close to, the threshold for long-range FM or AFM order, is strikingly similar to the percolation model proposed earlier [31] for amorphous ferromagnets. According to this picture [1, 31], the crossover temperature, ϵ_{co}, above which $\gamma_{eff}(\epsilon)$ in Fig.5.3(b) starts increasing from the asymptotic value of $\gamma = 1.8$, corresponds to the temperature at which the SG spin-spin correlation length ξ equals the caliper dimension, D_c, of the largest FM spin cluster. Thus, an estimate of the size of FM clusters can be made from the relation $\xi(\epsilon = \epsilon_{co}) = D_c = r_{av}\ \epsilon_{co}^{-\nu}$, where r_{av} is the average nearest-neighbour distance between TM_1^{3+} and TM_2^{3+} ions. Inserting $r_{av} = 0.3925\ nm$ $(0.3928\ nm)$ [2], $\epsilon_{co} = 0.25(2)$ $(\epsilon_{co} = 0.45(5))$ and $\nu = 0.97(4)$ $(\nu = 1.1(1))$ in the above relation yields an average FM spin cluster size of $2.0(5)\ nm$ $(1.0(2)\ nm)$ for $y = 0.2$ $(y = 0.3)$. The average FM cluster size for $y = 0.2$, so determined, compares well with that deduced from the SANS data [6]. Furthermore, considerably smaller value of the exponent β compared to that theoretically predicted for a $d = 3$

Heisenberg chiral spin glass with weak random magnetic anisotropy asserts that a meaningful comparison between theory and experiment is possible only when the probability of finding magnetic impurity atoms as nearest neighbours, in a non-magnetic host, is extremely low or when the theory takes into account the influence of magnetic short-range order on the critical behaviour of spin glass systems. The existence of magnetic short-range order could also be a root cause for a wide dispersion in the exponent values reported for spin glass systems.

To summarize, a combined investigation of both odd and even harmonics of the ac magnetic response enables one to unambiguously distinguish between a canonical and a cluster spin glass. While the odd harmonics yield true asymptotic values of the critical exponents (that characterize the universality class of the spin glass system in question), the even harmonics not only confirm the presence or absence of correlated-spin regions (spin clusters) but also reveal the nature of the intra-cluster magnetic order.

References

1. Y. Bitla, S. N. Kaul, L. Fernández Barquín, J. Gutiérrez, J. M. Barandiarán and A. Peña, *Observation of isotropic-dipolar to isotropic-Heisenberg crossover in Co- and Ni-substituted manganites*, New J. Phys. **12**, 093039 (2010) and references cited therein.

2. J. Gutiérrez, A. Peña, J. M. Barandiarán, J. L. Pizarro, T. Hernandez, L. Lezama, M. Insausti and T. Rojo, *Structural and magnetic properties of* $La_{0.7}Pb_{0.3}(Mn_{1-x}Fe_x)O_3$ $(0 \leq x \leq 0.3)$ *giant magnetoresistance perovskites*, Phys. Rev. B **61**, 9028 (2000).

3. G. Gritzner, M. Koppe, K. Kellner, J. Przewoznik, J. Chmist, A. Kolodziejczyk and K. Krop, *Preparation and properties of* $La_{0.67}Pb_{0.33}(Mn_{1-x}Fe_x)O_3$ *compounds*, Appl. Phys. A - Mater. Sci. Proc. **81**, 1491 (2005).

4. S. L. Young, H. Z. Chen, M. C. Kao, L. Horng and Y. T. Shih, *Magnetization processes of polycrystalline* $La_{0.7}Pb_{0.3}Mn_{1-x}Fe_xO_3$, J. Magn. Magn. Mater. **303**, e351 (2006).

5. J. Gutiérrez, F. J. Bermejo, J. M. Barandiarán, S. P. Cottrell, P. P. Romano, C. Mondelli, J. R. Stewart, L. Fernández Barquín, and A. Peña, *Role of disorder and competing ferromagnetic and antiferromagnetic interactions in the magnetic, electrical, and dynamic properties of* $La_{0.7}Pb_{0.3}(Mn_{1-x}Fe_x)O_3$, $0 \leq x \leq 0.2$ *manganites*, Phys. Rev. B **73**, 054433 (2006).

6. J. Gutiérrez, F. J. Bermejo, N. Veglio, J. M. Barandiarán, P. Romano, C. Mondelli, M. A. González and A. P. Murani, *Structural cor-*

relations in $La_{0.7}Pb_{0.3}(Mn_{1-x}Fe_x)O_3$ manganites as probed by small-angle and polarized neutron diffraction, J.Phys.: Condens. Matter **18**, 9951 (2006).

7. J. Gutiérrez, J. M. Barandiarán, F. J. Bermejo, C. Mondelli, P. Romano, P. Fouquet and M. Monkenbusch, *Evidence for two disparate spin dynamic regimes within Fe-substituted $La_{0.7}Pb_{0.3}(Mn_{1-x}Fe_x)O_3$ ($0 \leq x \leq 0.2$) colossal magnetoresistive manganites: Neutron spin-echo measurements*, Phys. Rev. B **76**, 184401 (2007).

8. J. M. Barandiarán, F. J. Bermejo, J. Gutiérrez and L. Fernández Barquín, *Spin disorder in Fe-doped manganites*, J. Non-Cryst. Solids **353**, 757 (2007).

9. J.A. Mydosh, *Spin Glasses: An Experimental Introduction*, (Taylor and Francis, London, 1993).

10. A. Mauger, J. Ferré, M. Ayadi, and P. Nordblad, *Dynamics of the spin-glass freezing in $Cd_{0.6}Mn_{0.4}Te$*, Phys. Rev. B **37**, 9022 (1988).

11. G. F. Goya and V. Sagredo, *Spin-glass ordering in $Zn_{1-x}Mn_xIn_2Te_4$ diluted magnetic semiconductor*, Phys. Rev. B **64**, 235208 (2001).

12. L. P. Lévy and A. T. Ogielski, *Nonlinear dynamic susceptibilities at the spin-glass transition of Ag:Mn*, Phys. Rev. Lett. **57**, 3288 (1986); L. P. Lévy, *Critical dynamics of metallic spin glasses*, Phys. Rev. B **38**, 4963 (1988).

13. N. Bontemps, J. Rajchenbach, R. V. Chamberlin and R. Orbach, *Dynamic scaling in the $Eu_{0.4}Sr_{0.6}S$ spin-glass*, Phys. Rev. B **30**, 6514 (1984).

14. M. Suzuki, *Phenomenological Theory of Spin-Glasses and Some Rigorous Results*, Prog. Theor. Phys. **58**, 1151 (1977); K. Wada and H. Takayama, *Nonlinear Susceptibilities of the Sherrington-Kirkpatrick Model and the Spherical Model*, Prog. Theor. Phys. **64**, 327 (1980); S. Fujiki and S. Katsura, *Nonlinear Susceptibility in the Spin Glass*, Prog. Theor. Phys. **65**, 1130 (1981).

15. Y. Bitla and S. N. Kaul, *Mean-field treatment of nonlinear susceptibilities for a ferromagnet of arbitrary spin*, EuroPhys. Lett. **96**, 37012 (2011).

16. J. Chalupa, *Scaling at the critical temperature of a spin glass*, Solid State Commun. **24**, 429 (1977).

17. K. Gunnarsson, P. Svedlindh, P. Nordblad, L. Lundgren, H. Aruga, and A. Ito, *Static scaling in a short-range Ising spin glass*, Phys. Rev. B **43**, 8199 (1991).

18. S. Geschwind, D. A. Huse and E. Devlin, *New approach to critical dynamic scaling in random magnets*, Phys. Rev. B **41**, 4854 (1990).

19. A. Labarta, X. Batlle, B. Martínez, and X. Obradors, *Magnetic study of spin freezing in the spin glass* $BaCo_6Ti_60_{19}$*: Static and dynamic analysis*, Phys. Rev. B **46**, 8994 (1992).

20. B. Leclercq, C. Rigaux, A. Mycielski, and M. Menant, *Critical dynamics in* $Cd_{1-x}Mn_xTe$ *spin glasses*, Phys. Rev. B **47**, 6169 (1993).

21. R. Mathieu, A. Asamitsu, Y. Kaneko, J. P. He, and Y. Tokura, $Eu_{0.5}Sr_{1.5}MnO_4$*: A three-dimensional XY spin glass*, Phys. Rev. B **72**, 014436 (2005).

22. S. Nair and A. K. Nigam, *Critical exponents and the correlation length in the manganite spin glass* $Eu_{0.5}Ba_{0.5}MnO_3$, Phys. Rev. B **75**, 214415 (2007).

23. I. A. Campbell and D. C. M. C. Petit, *Heisenberg Spin Glass Experiments and the Chiral Ordering Scenario*, J. Phys. Soc. Jpn. **79**, 011006 (2010).

24. D. X. Viet and H. Kawamura, *Monte Carlo studies of chiral and spin ordering of the three-dimensional Heisenberg spin glass*, Phys. Rev. B **80**, 064418 (2009).

25. H. Kawamura, *Chirality Scenario of the Spin-Glass Ordering*, J. Phys. Soc. Jpn. **79**, 011007 (2010).

26. K. Hukushima and H. Kawamura, *Monte Carlo simulations of the phase transition of the three-dimensional isotropic Heisenberg spin glass*, Phys. Rev. B **72**, 144416 (2005).

27. M. Hasenbusch, A. Pelissetto and E. Vicari, *Critical behavior of three-dimensional Ising spin glass models*, Phys. Rev. B **78**, 214205 (2008).

28. H. G. Katzgraber, M. Koerner and A. P. Young, *Universality in three-dimensional Ising spin glasses: A Monte Carlo study*, Phys. Rev. B **73**, 224432 (2006).

29. J. R. L. de Almeida and D. J. Thouless, *Stability of the Sherrington-Kirkpatrick solution of a spin glass model*, J. Phys. A **11**, 983 (1978).

30. J. Mattsson, T. Jonsson, P. Nordblad, H. Aruga Katori and A. Ito, *No Phase Transition in a Magnetic Field in the Ising Spin Glass*

$Fe_{0.5}Mn_{0.5}Ti0_3$, Phys. Rev. Lett. **74**, 4305 (1995).

31. S. N. Kaul, *Static critical phenomena in ferromagnets with quenched disorder*, J. Magn. Magn. Mater. **53**, 5 (1985).

Chapter 6

Critical Phenomena

The current chapter demonstrates the importance of dipolar interactions in $La_{1-x}Ca_xMnO_3$ in 'zero-field' across the ferromagnetic(FM)-insulating to paramagnetic(PM)-insulating transition from an elaborate analysis of the ac susceptibility data. The strength of uniaxial anisotropy weakens with increasing x. Magnetic field stabilizes a three-dimensional Ising FM behaviour in the critical region in $x = 1/8$ and $x = 3/8$ while $x = 5/8$ do not belong to any universality class. The isothermal magnetic entropy change is well described by the magnetic scaling equation of state with mean field exponents over a wide temperature range.

6.1 Introduction

A phase is a region in the parameter space of thermodynamic variables in which the free energy is analytic. As long as the free energy is analytic, all the thermodynamic properties (such as entropy, heat capacity, magnetization, etc.,) will be well-behaved as they can be expressed in terms of free

energy and its derivatives. When the system undergoes a transition from one phase to the other, at one point the free energy becomes non-analytic. This is the critical point. Due to this non-analyticity (which stems from the interactions of an extremely large number of particles in the system), the free energies on either side of transition are different, so one or more thermodynamic properties behaves very differently after the transition. Examples of phase transitions are ice-water, ferromagnetic (antiferromagnetic) - paramagnetic, ferroelectric - paraelectric, superfluid - normal, superconducting - normal phase transitions, to name a few. According to the Ehrenfest classification [1], a phase transition is of first-order (discontinuous phase transition) if the Gibbs free energy, $G(X \equiv T, P \text{ or } H)$, is a continuous function of its arguments but the first-order derivative of the Gibbs free energy with respect to each of its arguments X, i.e., $\frac{\partial G}{\partial X}$, is discontinuous. By contrast, if the Gibbs free energy and its first-order derivatives with respect to T, P or H are continuous whereas the second-order derivative $\frac{\partial^2 G}{\partial X^2}$ is discontinuous, it is called a second-order (continuous) phase transition and so on. According to Fisher [2], a second-order phase transition is marked by either a discontinuity or a singularity (divergence) in the second order derivative of the Gibbs free energy. The region around critical point is called the critical region and the associated phenomena are called critical phenomena.

The reason for phase transitions to occur can be understood in terms of free energy $F = U - TS$ which when minimized, corresponds to state of thermodynamic equilibrium. The internal energy U (favouring order) competes with entropy S (favouring disorder) so that a raise in system temperature tilts the balance in favour of entropy and disorder. In other words, real systems exhibiting different phases contain thermodynamic fluctuations. When

a system is far from a phase transition, these fluctuations are unimportant, but as it approaches a critical point, the fluctuations of the order parameter begin to grow in amplitude and get correlated over larger distances. At the ideal critical point, they are expected to get correlated over infinite distance (i.e., the fluctuation-fluctuation correlation length diverges), but before that can happen, the range of correlated fluctuations becomes as large as the system itself. In this regime, "finite-size" effects come into play and one is unable to accurately predict the behaviour of the system. Thus, phases in a real system are only well-defined away from phase transitions, and how far away it needs to be is dependent on the size of the system. The two phases can be distinguished from each other by an order parameter [1–3] which is non-zero in the ordered phase and zero in the disordered phase. For instance, order parameter for a magnetic (fluid) system is the spontaneous magnetization (difference in the liquid and gaseous densities). For a second-order phase transition, order parameter goes to zero continuously and is not uniquely specified below the critical point by external conditions. Phase transitions often take place between phases with different symmetry. In general, non-zero value of the order parameter corresponds to the breaking of symmetry. In the magnetic case, the broken symmetry is the symmetry of the spin system under rotations. Typically, the phase on the high-temperature side of a phase transition is more symmetrical than on the low-temperature side. This is certainly the case for the fluid and ferromagnetic transitions. This happens because the Hamiltonian of a system usually exhibits all the possible symmetries of the system, whereas the low-energy states lack some of these symmetries (this phenomenon is known as spontaneous symmetry breaking). At low temperatures, the system tends to be confined to the low-energy states. At higher temperatures, thermal

fluctuations allow the system to access states in a broader range of energy, and thus more of the symmetries of the Hamiltonian.

6.2 Magnetic phase transitions

The critical region, whose extent depends on the type of material, is typically of the order of $|\epsilon| = |(T - T_C)/T_C| \leq 0.01$, where T_C is the critical temperature. As the critical temperature is approached, the thermally-excited critical fluctuations of the local spin-density (order parameter) rapidly pick up in amplitude and get correlated in space over larger and larger distances with the result that they destroy the long-range magnetic order at T_C, where the spin-density-fluctuation-spin-density-fluctuation correlation length, $\xi(T = T_C)$, (henceforth referred to as the spin-spin correlation length) diverges and the magnetic order-disorder phase transition occurs. Note that the thermally-driven classical phase transitions are distinctly different from the quantum phase transitions which occur only at the temperature of absolute zero where the quantum (zero-point) fluctuations, demanded by the Heisenberg uncertainty principle, destroy cooperative ordering in the system. Experimental investigations in the critical region near a thermally-driven phase transition provide a unique and direct means of probing the type of interactions present and the interplay between them, which finally decides the nature of magnetic order prevailing in the systems under study for temperatures below the transition temperature. This is so because the critical behavior of a system is solely governed by the nature of the underlying interactions. For instance, an interplay between interactions, such as crystal-field (leading to uniaxial anisotropy), isotropic

short-range Heisenberg, and long-range dipole-dipole interactions, in a localized spin system gives rise to a series of crossovers from uniaxial dipolar (UD) critical regime (where both uniaxial anisotropy and dipolar interactions dominate) to isotropic dipolar critical regime (where anisotropy is negligibly small and isotropic dipolar interactions take over) to isotropic Heisenberg critical regime (where short-range isotropic Heisenberg interactions become prominent) to Gaussian regime, as the temperature is raised above T_C in the critical region. To facilitate understanding of the magnetic phase transitions, the prerequisites such as the definition of the asymptotic critical exponents and amplitudes, which quantify the static critical behaviour near a magnetic order-disorder phase transition, and the physical concepts relating to the critical phenomena such as the scaling hypothesis, universality, renormalization group (RG) approach, and crossover between different critical regimes, are covered in the following subsections.

6.2.1 Critical amplitudes and exponents

In the critical regime, the behaviour of a magnetic system undergoing a continuous transition at the critical point T_C is characterized by a set of critical exponents and amplitudes [1–4] . Critical exponents (the exponents in the power laws that define the deviations of various thermodynamic quantities from their values at T_C) and the corresponding critical amplitudes (coefficients in the power laws), characterizing FM-PM transition, are defined in terms of reduced temperature $\epsilon = (T - T_C)/T_C$ (a dimensionless variable measuring the deviation of temperature from the critical point) as follows:

Spontaneous magnetization (B, β)

In the asymptotic critical region, the order parameter, i.e., the spontaneous magnetization, M_S, in the case of a ferromagnet, varies with ϵ as

$$M_s(\epsilon) = \lim_{H\to 0} M(H,T) = B\ (-\epsilon)^{\beta}\quad ,\quad \epsilon < 0, \tag{6.1}$$

Initial susceptibility $(\Gamma', \Gamma; \gamma', \gamma)$

Initial susceptibility, defined as $\chi_0 = \lim_{H\to 0}[\frac{\partial M}{\partial H}]_T$, diverges at T_C as

$$\chi_0(\epsilon) \quad = \Gamma'\ (-\epsilon)^{-\gamma'},\quad \epsilon < 0\quad , \tag{6.2}$$

$$\chi_0(\epsilon) \qquad = \Gamma\ \epsilon^{-\gamma},\quad \epsilon > 0\quad . \tag{6.3}$$

Critical isotherm $(D; \delta)$

At $T = T_C$, magnetization M varies with field H as

$$H \quad = D\ M^{\delta},\qquad \epsilon = 0 \tag{6.4}$$

or

$$M \quad = A_0\ H^{1/\delta},\qquad \epsilon = 0 \tag{6.5}$$

δ quantifies the rate at which critical fluctuations in the orderder parameter get suppressed with H.

Specific heat $(A', A; \alpha', \alpha)$

Zero-field specific heat, $C_{H=0} = T[\partial^2 G(H,T)/\partial T^2]_{H=0}$, diverges at T_C as

$$C_M(\epsilon) \quad = C_{H=0}(\epsilon) = \tfrac{A'}{\alpha'}[(-\epsilon)^{-\alpha'} - 1] + B',\quad \epsilon < 0, \tag{6.6}$$

$$C_M(\epsilon) \qquad = C_{H=0}(\epsilon) = \tfrac{A}{\alpha}[\ \epsilon^{-\alpha} - 1] + B,\quad \epsilon > 0. \tag{6.7}$$

Specific heat exhibits a cusp at T_C when $\alpha < 0$ whereas for $\alpha = 0$ the singularity is logarithmic. B' and B represent the non-singular background for $\epsilon < 0$ and $\epsilon > 0$, respectively.

Spin-fluctuation-spin-fluctuation correlation function $(N; \eta)$

At T_C, the spin-fluctuation-spin-fluctuation correlation function, $g(r) = \langle [s(\mathbf{r}) - < s >][s(\mathbf{0}) - < s >] \rangle$, decays with distance, r, as

$$g(r) = N|r|^{-(d-2+\eta)} \text{ [large}|r|\text{]}, \quad \epsilon = H = 0, \tag{6.8}$$

d is the lattice dimensionality and η is a measure of deviation from the mean-field behaviour.

Spin-spin correlation length $(\xi_0', \xi_0; \nu', \nu)$

Correlation length, ξ, is the distance over which the order parameter fluctuations are correlated and is defined through the relation $g(r) \sim |r|^{-1} e^{-|r|/\xi}$ for $|r| \longrightarrow \infty$ and $d = 3$. In the critical region, ξ depends on temperature as

$$\xi(\epsilon) \ = \xi_0' \ (-\epsilon)^{-\nu'}, \quad \epsilon < 0, \quad H = 0, \tag{6.9}$$

$$\xi(\epsilon) \ = \xi_0 \ (\epsilon)^{-\nu}, \quad \epsilon > 0, \quad H = 0. \tag{6.10}$$

In Eqs. (6.1)-(6.10), β, γ', γ, δ, α', α, η, ν' and ν are the critical exponents and B, Γ', Γ, D, A', A, N, ξ_0' and ξ_0 are the corresponding amplitudes. Due to the fact that scaling gives (Table 6.2) rise to relations between critical exponents only two out of nine aforementioned critical exponents are independent.

As is evident from the above definitions, the critical exponents and amplitudes characterize the way in which various physical quantities diverge to infinity or go to zero as the temperature, or other thermodynamic variable, approaches its critical point value. Strictly speaking, the single power laws are valid *only* at $T = T_C$. In practice, however, the power laws are fitted to the experimental data over a wide temperature range. This approach yields average exponent values since, in general, the amplitudes as well as the exponents are temperature-dependent and they assume temperature-independent values only in the asymptotic critical region [4]. In order to tackle this problem effectively, the concept of effective critical exponent was introduced by Riedel and Wegner [5]. The effective critical exponents provide a local measure for the degree of singularity of physical quantities in the critical region. Near the critical point all thermodynamic functions can be written in the form

$$f(\epsilon) = A\epsilon^{\lambda}(1 + B\epsilon^{y} + \cdots) \tag{6.11}$$

where $y > 0$. The effective critical exponent of a function $f(\epsilon)$ is defined by the logarithmic derivative as $\lambda_{eff} = \dfrac{d\ \ln[f(\epsilon)]}{d\ \ln[\epsilon]}$ and $\lambda_{eff}(\epsilon \to 0) = \lambda$. The following cases arise depending on the sign of λ. (a) If $\lambda < 0$, $f(\epsilon)$ diverges at the critical point, (b) If $\lambda > 0$, $f(\epsilon)$ goes to zero at transition temperature, and (c) If $\lambda = 0$, it may correspond to a logarithmic divergence $f(\epsilon) = A|\ln\epsilon| + B$ or to a dependence on ϵ of the form $f(\epsilon) = A + B\epsilon^{1/2}$. For such cases modified exponent of the form $\lambda' = j + \lim\limits_{\epsilon\to 0} \dfrac{\ln|f^{(j)}(\epsilon)|}{\ln\epsilon}$, is introduced with $f^{(j)}(\epsilon) = \dfrac{d^j f(\epsilon)}{d\epsilon^j}$ and j is the smallest integer.

Table 6.1: *Scaling relations between various critical exponents [1, 3]*

Sl. no	Name	Relation
1		$\alpha' = \alpha$
2		$\gamma' = \gamma$
3		$\nu' = \nu$
4	Widom	$\beta\delta = \beta + \gamma(= \Delta)$ or $\gamma = \beta(\delta - 1)$
5	Rushbrooke	$\alpha + 2\beta + \gamma = 2$
6	Griffiths	$\alpha + \beta(\delta + 1) = 2$ $\gamma(\delta + 1) = (2 - \alpha)(\delta - 1)$
7		$(2 - \alpha - \gamma)\delta = (2 - \alpha + \gamma)$ $(d - 2 + \eta)\delta = (d + 2 - \eta)$
8	Fisher	$(2 - \eta)\nu = \gamma$
9	Josephson	$d\nu = 2 - \alpha$

6.2.2 Scaling and universality

Historically, the observation that a huge body of experimental data on a variety of systems could be represented in the form of a scaled equation of state led to the scaling hypothesis, which asserts that in the asymptotic critical region the singular part of the Gibbs free energy, $G_s(\epsilon, H)$, is a generalized homogeneous function [1] of its arguments ϵ and H. Scaling hypothesis or,

equivalently, the homogeneity postulate makes two specific predictions: (i) it relates various critical exponents through the scaling equalities, and (ii) makes specific predictions concerning the form of the equation of state. For magnetic systems, the scaling hypothesis predicts that all the magnetization, $M(\epsilon, H)$, curves (either magnetization isotherms at different temperatures or $M(\epsilon)$ at different fields) taken in the critical region collapse onto two universal curves, one for $\epsilon < 0$ and the other for $\epsilon > 0$, if scaled magnetization, $M/|\epsilon|^{\beta}$, is plotted against scaled field, $H/|\epsilon|^{\Delta}$, where $\Delta = \beta\delta$ is the gap exponent.

The Hamiltonians describing systems which undergo phase transitions are usually quite complicated and involve many parameters. The basic idea of Universality is that the critical behaviour of these systems, when the correlation length becomes very large depends only on a small number of general features of these Hamiltonians, and not on the actual values of the various parameters involved. *Universality*, basically amounts to cataloging, under a single category (class), all types of systems that possess the same values for critical exponents and critical amplitude ratios and for which the equation of state and the correlation functions become *identical* near criticality, provided the order parameter, the ordering field, and the correlation length (time) are scaled properly by material-dependent factors. Thus, the critical exponents and the ratios between critical amplitudes (but not the amplitudes themselves) are universal [1,3,6] in the sense that they possesses exactly the same numerical values for a number of widely different systems, irrespective of the type and range of the underlying interactions, so long as the range of interaction in question is much smaller than the correlation length, which diverges at T_C. The universality class, in turn, is decided by (i) the space dimensionality d, (ii) the number of order parameter com-

ponents, or equivalently, the order parameter dimensionality n, (iii) the symmetry of the Hamiltonian, and (iv) the range of interactions. For $d = 1$, $n = 1$ corresponds to one-dimensional Ising system in which the spins are constrained to point either in +z (up) or -z (down) directions. However, symmetry properties of the systems do make some difference in the exponent values, e.g., the exponents for uniaxial ferromagnets differ from those for isotropic ferromagnets. Other factors that affect the critical exponents are long-range interactions [1, 3, 6–8], such as dipolar interactions, whose range is comparable to the correlation length, ξ, in some ferromagnets. It should be noted that critical exponents as well as critical amplitudes are very sensitive to the choice of transition temperature. Hence, extremely high accuracy in the determination of T_C is a must.

6.2.3 Crossover phenomena

Crossover theory explores the possibility for, and the consequences of, switching over between different critical behaviours upon variation of temperature when, in addition to temperature and field, one or more of the scaling variables becomes relevant. In any real ferromagnet, apart from the dominant short-range exchange interactions, which are responsible for the existence of spontaneous magnetization below T_C, there exist other physical interactions that differ in strength, range of action and spatial symmetry. The presence of dominant short-range exchange interactions along with the long-range dipolar interactions (covariant under spatial symmetry) between the localized magnetic moments and the crystal field interactions (inducing magnetocrystalline anisotropy) that are one/two order smaller in magnitude, in a magnetic system leads to a variety of interesting but complicated physi-

cal phenomena in the critical region. Considerable effort has been devoted to study how the critical behaviour near the paramagnetic-ferromagnetic phase transition gets modified when the dipolar interactions between magnetic moments as well as the uniaxial anisotropy are included along with the dominant exchange interaction. In the above examples, isotropic dipolar interactions and the uniaxial anisotropy act as relevant scaling fields. For instance, dipolar interactions modify the critical behaviour of $d = 3, n = 1$ system (i.e., three-dimentional spin system with infinite *uniaxial* anisotropy) so much so that, instead of behaving as a three-dimentional Ising ferromagnet in the asymptotic critical region, it exhibits *mean-field* behaviour with *logarithmic* corrections [9–12]. Elaborate RG study [11, 12] of the second-order phase transition in a Heisenberg ferromagnet in which, in addition to the dominant short-range exchange interactions, dipole-dipole interactions and a uniaxial anisotropy are present, reveals that, due to the competition between the three types of interactions that differ in symmetry and range, the critical region encompasses a series of crossovers between four nontrivial fixed points: Gaussian $\longrightarrow$ isotropic short-range Heisenberg $\longrightarrow$ isotropic dipolar $\longrightarrow$ uniaxial dipolar, as the critical point is approached from high temperatures.

Isotropic Heisenberg to isotropic dipolar crossover

According to the general theory [13–16] of crossover, 'zero-field' susceptibility of a $d = 3$ isotropic short-range Heisenberg ferromagnet with weak isotropic dipolar interactions of normalized strength g, for temperatures close to criticality, behaves as [13, 14]

$$\chi(\epsilon_H, g_D) \backsim \epsilon_H^{-\gamma_H} \; X(\tau) \tag{6.12}$$

where $\epsilon_H = [T - T_C(0)]/T_C(0)$, $T_C(0) = T_C(g_D = 0)$ and γ_H, respectively, are the reduced temperature, transition temperature and susceptibility critical exponent of *pure* ($g_D = 0$) isotropic short-range Heisenberg ($d = 3, n = 3$) spin system, $\tau = x/x_g, x \equiv g_D/\epsilon_H^{\phi}, x_g \equiv g_D/\epsilon_g^{\phi}, \epsilon_g = [T_C(g_D) - T_C(0)]/T_C(0)$ is the shift in the transition temperature caused by long-range interactions, ϕ is the crossover exponent which equals [17] γ_H, and $X(\tau)$ is the crossover scaling function. The asymptotic critical behavior is determined by the singularity in $X(\tau)$ occurring at $\tau = 1$ (or equivalently, at $\epsilon = (T - T_C(g))/T_C(g) = 0$):

$$X(\tau \approx 1) \sim (1 - \tau)^{-\gamma_D} \tag{6.13}$$

where γ_D is the susceptibility critical exponent and $T_C \equiv T_C(g)$ is the true transition temperature of isotropic dipolar ferromagnet. According to Eqs. (6.12) and (6.13), dipole - dipole interactions are expected to manifest themselves in the vicinity of a crossover temperature $\epsilon_{CO} \equiv g_D^{1/\phi}$ such that for $\epsilon >> \epsilon_{CO}$ the spin system behaves as a pure d = 3, n = 3 system whereas for $\epsilon << \epsilon_{CO}$ the asymptotic critical behavior is that of a d = 3 isotropic dipolar ferromagnet. A detailed RG calculation [13, 14] of the crossover scaling function yields the final expression for susceptibility and its effective critical exponent, defined as $\gamma_{eff}(\epsilon) = \partial[ln\chi^{-1}(\epsilon)]/\partial(ln\epsilon)$, as

$$\chi(\tau) = \Gamma \ \ \tau^{\gamma_H/\phi} \ \ (1 - \tau)^{-\gamma_D} \ \ p(\tau) \tag{6.14}$$

$$\gamma_{eff}(\tau) = (1 - \tau^{1/\phi}) \left[\gamma_H + \phi \ \gamma_D \left(\frac{\tau}{1 - \tau}\right) + \phi \ \left(\frac{\tau \ p\,'(\tau)}{p(\tau)}\right)\right] \tag{6.15}$$

where Γ is a non-universal critical amplitude, $\tau = (\epsilon_g/\epsilon_H)^{\phi}$, $\epsilon_H = [T - T_C(0)]/T_C(0)$, $T_C(0) \equiv T_C(g = 0)$ is the transition temperature and γ_H the susceptibility critical exponent of the pure ($g = 0$) IH $d = 3, n = 3$

spin system, $\epsilon_g = [T_C(g) - T_C(0)]/T_C(0)$ is the shift in T_C caused by ID interactions of relative strength (i.e., the ratio of the ID energy to isotropic exchange energy), g, γ_D is the susceptibility critical exponent of the $d = 3$ ID fixed point, $\phi = \gamma_H$ is the crossover exponent, $p(\tau)$ is the 'correction-to-scaling' function, $\tau^{-1/\phi} - 1 = \widehat{\epsilon} = [(1+\epsilon_g)/\epsilon_g]\ \epsilon$ and $\epsilon = (T - T_C(g))/T_C(g)$. The explicit forms of $p(\tau)$ and its derivative with respect to τ, $p\,'(\tau)$, are given in [14]. Equations (6.14) and (6.15) assert the following. (a) The ID interactions become important below a crossover temperature $\epsilon_{co} \approx \epsilon_{dip} \equiv g^{1/\phi}$ such that for $\epsilon \ll \epsilon_{co}$, the asymptotic critical behavior is that of a $d = 3$ ID ferromagnet whereas for $\epsilon \gg \epsilon_{co}$ the spin system behaves as a *pure* $d = 3, n = 3$ system. (b) $\gamma_{eff}(\epsilon)$ goes through a minimum in the crossover region such that at $\epsilon = \epsilon_{dip}$, γ_{eff} has the universal (*independent* of the RG coupling parameter [15]) value [14] $\gamma_{dip} = 1.28(1)$, for weak dipolar system with $g \leq 10^{-4}$. (c) $\gamma_{eff} \to \gamma_D$ and γ_H in the ID ($\tau \to 1$) and IH ($\tau \ll 1$) limits. In the ACR ($0 < \epsilon \leq \epsilon^* \ll \epsilon_{co}$), the expansion of the scaling function $p(\tau)$ in Eqs.(6.14) and (6.15) yields the result [18, 20]

$$\chi(\epsilon) = A_\chi\ \epsilon^{-\gamma_D}[1 + a_\chi\ \epsilon^{\Delta_D}] \tag{6.16}$$

$$\gamma_{eff}(\epsilon) = \gamma_D - a_\chi\ \Delta_D\ \epsilon^{\Delta_D} \tag{6.17}$$

$$a_\chi \simeq 0.099\ \epsilon_g^{-\Delta_D} \tag{6.18}$$

and

$$\epsilon_g \cong 0.349\ \dot{\epsilon}, \tag{6.19}$$

where a_χ and Δ_D are the leading 'correction-to-scaling' amplitude and exponent, and $\chi^{-1}(\epsilon = \dot{\epsilon}) = 4\pi$. This type of crossover has been observed for the *first time* in $La_{0.7}Pb_{0.3}Mn_{0.8}(Ni, Co)_{0.2}O_3$ manganites, emphasizing the importance of dipolar interactions in stabilizing FM order and is elaborated in chapter 4.

Isotropic dipolar to uniaxial dipolar crossover

The RG calculations [11, 12] show that the crossover scenario in the critical region gets quite complicated when both dipolar interaction and magnetic anisotropy are present in an otherwise isotropic short-range ($d = 3, n = 3$) Heisenberg spin system. This is so because the dipolar interaction and magnetic anisotropy act as relevant scaling fields in the RG sense and make the Heisenberg fixed point unstable. In this case, zero-field susceptibility at temperatures above T_C takes the scaling form [19]

$$\chi(\epsilon_H, g_D, g_A) \propto \epsilon_H^{-\gamma_H} \; X\left(\frac{g_D}{\epsilon_H^{\phi_D}}, \frac{g_A}{\epsilon_H^{\phi_A}}\right) \tag{6.20}$$

where $\epsilon_H = [T - T_C(0)]/T_C(0)$, $T_C(0) = T_C(g_D = g_A = 0)$ and γ_H, respectively, are the reduced temperature, transition temperature and susceptibility critical exponent of pure ($g_D = g_A = 0$) isotropic short-range Heisenberg ($d = 3, n = 3$) spin system. The crossover exponents ϕ_D and ϕ_A are *positive* while g_D (g_A) is the dimensionless ratio of dipolar energy (anisotropy energy) and isotropic short-range exchange energy. Alternatively, g_D and g_A are a direct measure of the dipolar and anisotropy (relevant) perturbations. For sufficiently high temperatures, i.e., $\epsilon_H >> g_D^{1/\phi_D}, g_A^{1/\phi_A}$, the critical behaviour is that of an isotropic Heisenberg ferromagnet. As the temperature is lowered towards the critical point, a series of crossovers occur depending on the initial values of g_A and g_D and their relative strengths. In the temperature ranges $g_D^{1/\phi_D} << \epsilon_H << g_A^{1/\phi_A}$ and $g_A^{1/\phi_A} << \epsilon_H << g_D^{1/\phi_D}$, the spin system exhibits anisotropic short-range (e.g., $d = 3, n = 1$) and isotropic dipolar critical behaviour, respectively. The behaviour of the system in the asymptotic critical region, i.e., at temperatures $\epsilon_H << g_D^{1/\phi_D}, g_A^{1/\phi_A}$ or equivalently, in the limit $\epsilon \to 0$, is determined by both anisotropy and dipolar interac-

tions; the reduced temperature ϵ measures the temperature deviation from the critical temperature $T_C(g_D \neq 0, g_A \neq 0)$ of the anisotropic dipolar fixed point. The RG calculations [11,12] have addressed three distinctly different cases. Based on the calculated temperature dependence of the effective critical exponent for susceptibility, $\gamma_{eff}(\epsilon) = dln\chi^{-1}(\epsilon)/dln\epsilon$, at temperatures spanning the asymptotic critical region and crossover regimes, these RG theories predict the following sequences of crossovers as the temperature is lowered from high temperatures to the critical point, T_C. Case I: When both g_D and uniaxial anisotropy (g_U) are extremely large [11], Gaussian regime→short-range Ising (I) → uniaxial dipolar (UD) fixed point (characterized by mean-field critical exponents with logarithmic corrections [9–12]). Case II: When $g_U >> g_D$ [12], Gaussian → Isotropic short-range Heisenberg (IH) → I → UD. Case III: when $g_U << g_D$ [12], Gaussian → IH → isotropic long-range dipolar (ID) → UD. Theoretical investigations of the cases I, II, and III were basically motivated by the expectation that the materials such as $LiTbF_4$ or $GdCl_3$, $Fe_{14}Nd_2B$ or $Fe_{14}Y_2B$, and Gd could be their respective experimental realizations.

6.3 Magnetocaloric effect

The magnetocaloric effect (MCE) is intrinsic to all magnetic materials and is caused by changes of the magnetic entropy of the material. The MCE, initially called *adiabatic demagnetization*, discovered in 1881 by Warburg, was used to achieve temperature less than 1 K using paramagnetic salts. As expected, the maximum field-induced change in magnetic entropy occurs around the ferromagnetic-to-paramagnetic transition temperature, T_C.

Realizing this fact, the application of MCE for magnetic cooling in a wide temperature range including room temperature, and even higher, was investigated in the pioneer experimental work by *Brown* in 1976 [21]. He suggested the use of ferromagnetic rare-earths or rare-earth based compounds with a Curie temperature around room temperature for magnetic refrigeration. In general, the magnetocaloric effect manifests itself as either absorption or emission of heat when a magnetic material is placed in a magnetic field [22]. This is caused by the coupling between the magnetic spin system and the lattice. MCE is also used as a complimentary tool to understand the thermodynamics in magnetic materials. The MCE is most easily observed as the adiabatic temperature change, ΔT_{ad}, but can also be measured indirectly as the isothermal entropy change, ΔS_M. The relationship between the two properties can be illustrated using a schematic $S-T$ diagram (Fig.6.1). In general, the total entropy of a magnetic material can be expressed as $S_{Tot}(T,H) = S_L(T) + S_E(T) + S_M(T,H)$, where the lattice entropy $S_L(T)$ and the electronic entropy $S_E(T)$ depend only on temperature while the magnetic entropy, $S_M(T,H)$, strongly depends on both the magnetic field and temperature. When an external magnetic field is applied under *isothermal conditions*, the magnetic moments tend to get aligned in the field direction, resulting in the increase in the magnetic ordering with consequent decrease in the magnetic entropy, ΔS_M. If the magnetic field is applied under *adiabatic conditions*, the total entropy remains constant during the magnetization process. Thus, when the magnetic entropy is decreased, the lattice and electronic entropy must increase concomitant with the increase in temperature, ΔT_{ad}. When the external field is removed, the magnetic spin system reverts to its original alignment, which decreases the thermal entropy and returns the sample to its original temperature. This

way of changing the temperature of a material by a magnetic field is the principle behind magnetic refrigeration. Heating and cooling caused by a changing magnetic field are used analogous to the heating and cooling of a refrigerant gas in response to compression and expansion.

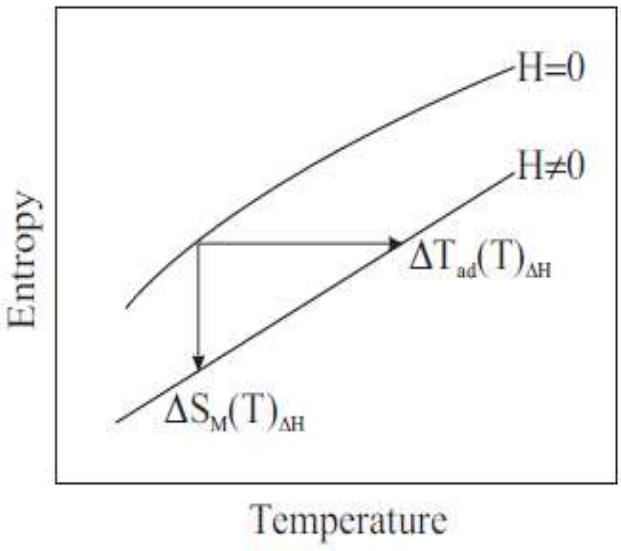

Figure 6.1: *Thermodynamic T-S diagram demonstrating the magnetocaloric effect by the adiabatic temperature change, $\Delta T_{ad}(T, \Delta H)$, and the isothermal mag- netic entropy change, $\Delta S_M(\Delta H, T)$.*

Different methods to determine the MCE have been categorized into [22]: 1. Direct method. Measuring the adiabatic temperature change, ΔT_{ad}, either by subjecting a stationary sample to a pulsed field or by rapidly moving

the sample in and out of a uniform magnetic field region. However, the accuracy of this method is limited to $5-10\%$ due errors in thermometry, field setting and the degree of the thermal isolation of the sample.
2. Indirect method (i) Magnetization method: By determining the magnetization curves at various temperatures, the magnetic contribution to the entropy change, ΔS_M, can be extracted.
(ii) Calorimetric method: By measuring specific heat capacity as a function of temperature at various magnetic fields.

$$\mid \triangle S_M \mid = \sum_i \frac{M_i - M_{i+1}}{T_{i+1} - T_i} \triangle H_i \tag{6.21}$$

The mixed-valent manganites show simultaneous occurrence of structural and magnetic transitions that can strongly influence the magnetic entropy change. The Curie temperature of these materials covers the entire temperature range from very low temperatures to near 300 K and some show sufficient MCE to be used as magnetic refrigerants.

The effect of size reduction on the nature of the FM-PM phase transition for $x = 0.33$ [23] system has revealed that the first-order transition seen in bulk [24–27] changes over to a continuous (second order) transition on reducing the size, and the exponents approach a value close to that predicted by the mean-field theory. A similar result has been obtained in the present study. This change in the order of transition was attributed to the truncation of the coherence length by the finite sample size. In nanocrystalline $x3$, the critical exponent for the order parameter has the value [3] $\beta = 0.33$. This estimate for β is at variance with presently obtained value $\beta = 0.5$. It has been pointed [29] out that the composition $x = 0.4$ is at the boundary of first-order and second-order phase transition line and exhibits a tricritical

behaviour. This tricritical point separates the first-order ($x < 0.4$) from the second-order ($x > 0.4$) in $La_{1-x}Ca_xMnO3$ manganites.

6.4 Experimental details

Extensive ac magnetic susceptibility measurements have been carried out on $x1$ ($La_{0.875}Ca_{0.125}MnO_3$), $x2$ ($La_{0.875}Ca_{0.125}MnO_{3.06}$), $x3$ ($La_{0.625}Ca_{0.375}MnO_3$) and $x5$ ($La_{0.375}Ca_{0.625}MnO_3$) at an ac driving field of rms amplitude, ranging from 0.1 Oe to 10 Oe, and frequency, from 87 Hz to 10 kHz, over a wide temperature range $2\ K \leq T \leq 310\ K$ that embraces the critical region. However, only representative data sets are presented in the following sections. Magnetization as a function of magnetic field was measured at several fixed temperatures in the above mentioned temperature range on $x1$, $x2$, $x3$ and $x5$ in fields up to 90 kOe, using Quantum Design PPMS-VSM and SQUID-VSM systems.

6.5 Data analysis, results and discussion

6.5.1 'Zero-field' critical behaviour

The real component of linear ac susceptibility, $\chi'(T)$, of the sample $x1$ ($x2$) measured as a function of temperature at an ac driving field of rms amplitudes $h_{ac} = 0.1, 1, 5, 10\ Oe$ and frequency $\nu = 111(333)\ Hz$, peaks at $113K$ ($108K$), is depicted in Fig. 6.2 (6.3)(a). The observed temperature variation resembles that in the bulk counterpart, annealed under helium gas atmosphere [30]. By contrast, the imaginary component, χ'', exhibits

two peaks : a *frequency-dependent* peak at $T_{p1} = 102\ K$ $(104\ K)$ and a *frequency-independent* peak at $T_{p2} = 124.0(5)\ K$ $(\simeq 124\ K)$ in the sample $x1$ $(x2)$. T_{p1} is very close to the onset of JT distortion (Q2 mode) in the bulk counterpart [31].

The inverse *intrinsic* susceptibility, $\chi^{-1}(T)$, is related to $\chi'^{-1}(T)$ as $\chi^{-1}(T) = \chi'^{-1}(T) - 4\pi N$, where N is the demagnetizing factor. We first analyse $\chi^{-1}(T)$ at $T \geq T_C$ in terms of the single power law (SPL)

$$\chi^{-1}(T) = A_{eff}(T)\ \ \epsilon^{\gamma_{eff}(T)}, \qquad \epsilon > 0 \tag{6.22}$$

where $\epsilon = (T - T_C)/T_C$, T_C is the Curie temperature, and γ_{eff} (A_{eff}) is the effective critical exponent (amplitude). N, T_C $(T_C = 143.13(3)K$ for $x1$ and $T_C = 134.10(2)K$ for $x2)$, $A_{eff}(T)$ and $\gamma_{eff}(T)$ were determined by the "range-of-fit" (ROF) method, detailed in chapter 4. γ_{eff} has values close to the mean-field (MF) value of $\gamma = 1$ for temperatures below a well-defined *crossover* temperature $\epsilon_{co} = 1.90(6) \times 10^{-2}$ $(1.50(5) \times 10^{-2})$ for $x2$ $(x1)$ above which γ_{eff} rises steeply. $A_{eff}(T)$ and $\gamma_{eff}(T)$ in $x1$ $(x2)$ for $\epsilon \leq \epsilon_{co}$ are displayed (open circles) in the right-middle and bottom panels of Fig.6.2 (6.3). The MF behaviour is normally expected at a lattice dimensionality of $d \geq 4$ unless the dipole-dipole interaction, concomitant with the uniaxial anisotropy, lowers the upper critical dimensionality from 4 to 3. Since we are dealing with a $d = 3$ system, the observation $\gamma_{eff} \to 1$ as $\epsilon \to 0$ strongly indicates a uniaxial dipolar behaviour in the ACR, $\epsilon \leq \epsilon_{co}$. Thus, the expression [33]

$$\chi^{-1}(T) = A\ \ \epsilon^{\gamma}\ \ |ln\epsilon|^{-1/3}, \qquad \epsilon > 0 \tag{6.23}$$

with $\gamma = 1$, predicted by the renormalization group (RG) calculations for uniaxial dipolar (UD) ferromagnets, is used to analyze $\chi^{-1}(T)$ in the ACR.

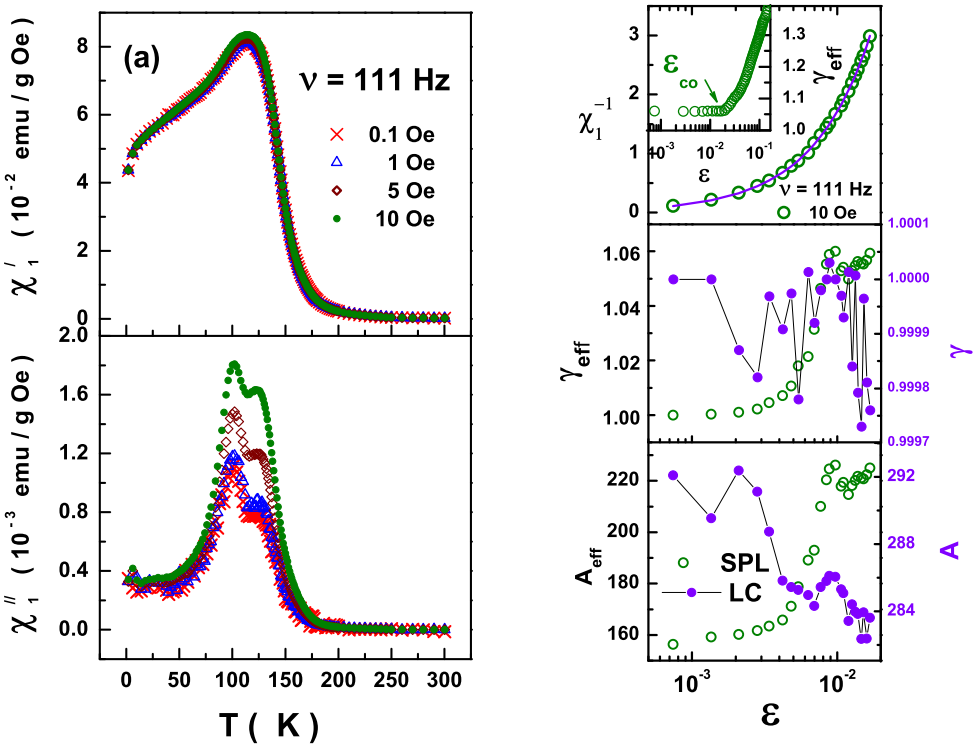

Figure 6.2: *Temperature dependence of the (a) real and imaginary components of ac susceptibility, measured at fixed frequency, $\nu = 111\ Hz$ and different driving field amplitudes, for the sample $x1$. The top right panel displays inverse susceptibility data (open circles) along with the LC fit (continuous curve), based on Eq.(6.23), in the asymptotic critical region (ACR) and its inset shows the temperature variation of the effective susceptibility critical exponent, γ_{eff}. The temperature variations of the SPL and LC fit parameters in the ACR are displayed in middle and bottom panels.*

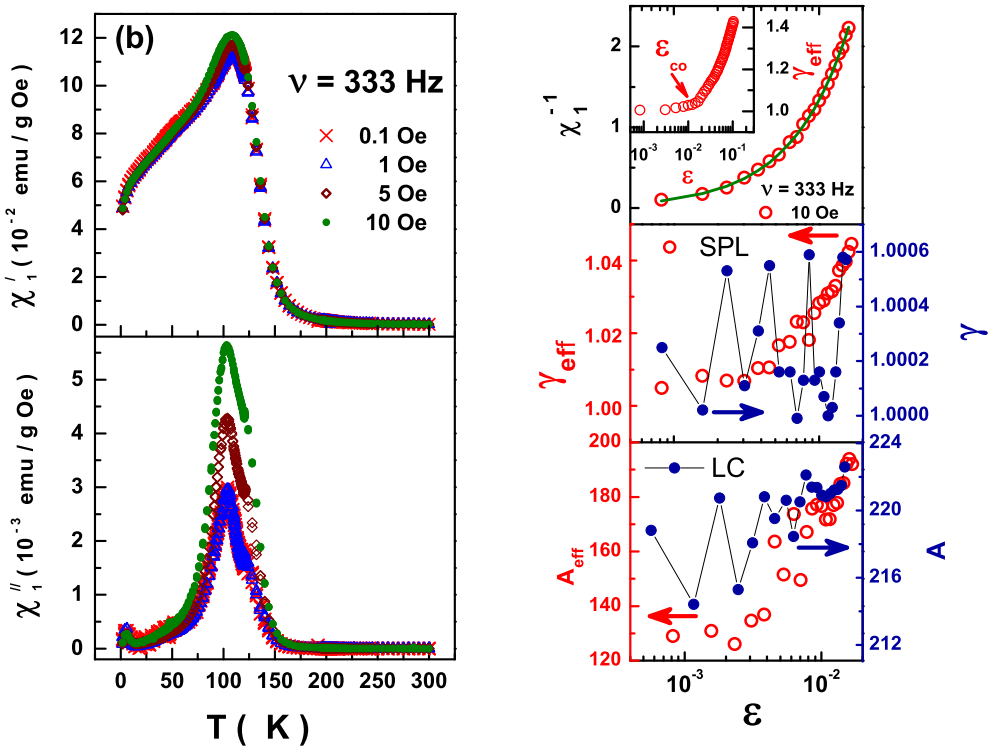

Figure 6.3: *Temperature dependence of the (a) real and imaginary components of ac susceptibility, measured at fixed frequency, $\nu = 333\ Hz$ and different driving field amplitudes, for the sample $x2$. The top right panel displays inverse susceptibility data (open circles) along with the LC fit (continuous curve), based on Eq.(6.23), in the ACR and its inset shows the temperature variation of the effective susceptibility critical exponent, γ_{eff}. The temperature variations of the SPL and LC fit parameters in the ACR are displayed in middle and bottom panels.*

The ROF analysis [33] (see chapter 4) of $\chi^{-1}(T)$ in the ACR (open circles), based on Eq.(6.23), which, besides SPL, includes the leading multi-

plicative *logarithmic correction* (LC), yields the optimum LC fit (continuous curve), shown in the top right panel of Fig.6.2(6.3). A and γ (solid circles) at different $\epsilon = (T - T_C^{UD})/T_C^{UD}$ (with $T_C^{UD} = T_C^{SPL}$), are displayed in right-middle and bottom panels of Fig.6.2 (6.3). Unlike A_{eff}

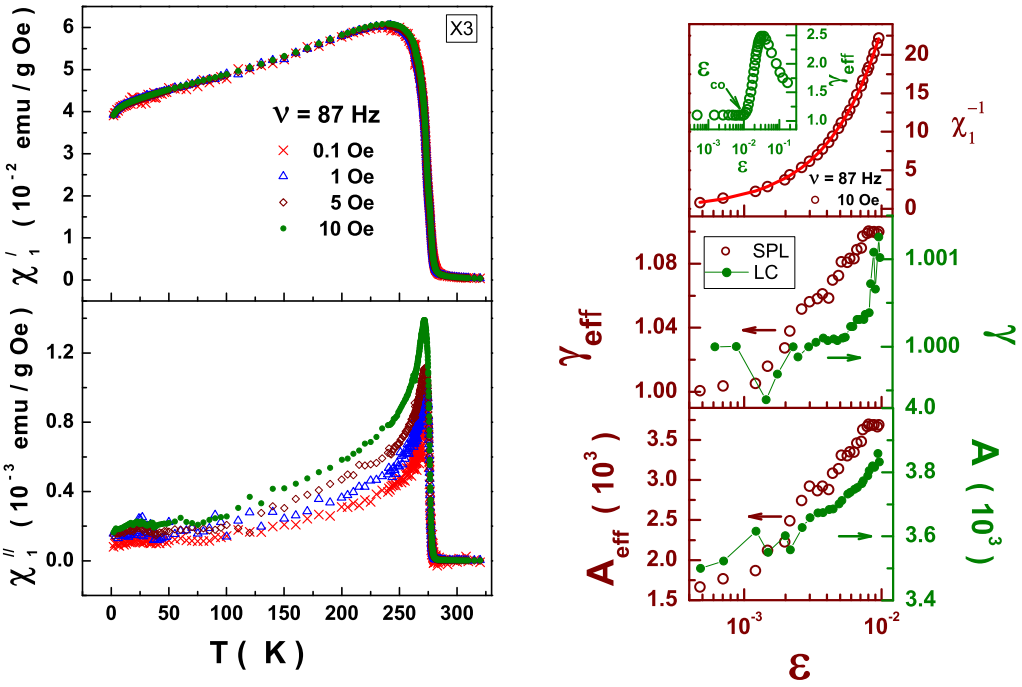

Figure 6.4: *Temperature dependence of the (b) real and imaginary components of ac susceptibility, measured at fixed frequency, $\nu = 87\ Hz$ and different driving field amplitudes, for the sample $x3$. The top right panel displays inverse susceptibility data (open circles) along with the LC fit (continuous curve), based on Eq.(6.23), in the ACR and its inset shows the temperature variation of the effective susceptibility critical exponent, γ_{eff}. The temperature variations of the SPL and LC fit parameters in the ACR are displayed in middle and bottom panels.*

and γ_{eff} that constantly increase with ϵ, A is a *non-universal* constant and γ ($\gamma = 0.9999(2)$ for $x1$ and $\gamma = 1.0003(3)$ for $x2$) has the value

$\gamma = 1$ predicted by the RG calculations. This result asserts that the asymptotic critical behaviour of $x1$ and $x2$ is that of a $d = 3$ UD ferromagnet. Narrower ACR ($7.45 \times 10^{-4} \leq \epsilon \leq \epsilon_{co} = 1.5 \times 10^{-2}$ in $x1$ and $7.0 \times 10^{-4} \leq \epsilon \leq \epsilon_{co} = 2.0 \times 10^{-2}$ in $x2$) in $x1$ indicates that the uniaxial anisotropy is stronger in $x2$ and persists to higher temperatures. Similar results obtained for $x3$ and $x5$ systems are displayed in figures 6.4 and 6.5, respectively. Various parameters obtained from the above analysis, presented in table 6.2, reveal that the width of ACR decreases with the hole doping in LCMO manganites. This observation signals the weakening of dipolar interactions due to the reduced dipole moments on hole doping. Considering that the FM-PM transition occurs in the insulating state (as revealed by the resistivity data in chapter 8), the dipolar interactions operate between the *localized* e_g-electron spins (due to polaron effects) and/or the *localized* t_{2g}-electron spins and thereby sustain FM order in the insulating state. Another important point to note is that, in conformity with RG prediction for the case when $g_U << g_D$ (case III under subsection 6.2.3), a crossover from the uniaxial dipolar to isotropic dipolar critical behaviour occurs when $\epsilon > \epsilon_{co}$.

6.5.2 'in-field' critical behaviour

Several methods of analysis have been used in the literature [4] to extract the critical exponents from bulk magnetization data. The critical exponents that some of these methods yield are the effective ones which depend on the temperature range used in the analysis (even within the ACR) and can be significantly different in magnitude from the 'true' asymptotic exponents that are of interest in the theory. The values of these effective exponents ap-

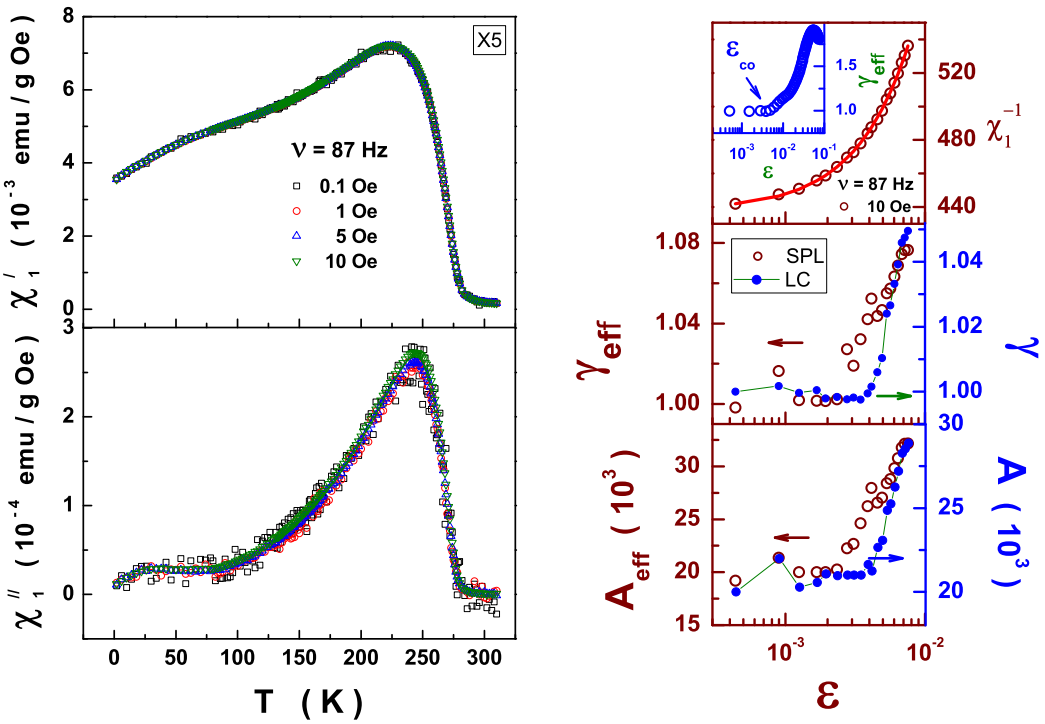

Figure 6.5: *Temperature dependence of the real and imaginary components of ac susceptibility, measured at fixed frequency, $\nu = 87\ Hz$, and different driving field amplitudes, for the sample $x5$. The top right panel displays inverse susceptibility data (open circles) along with the LC fit (continuous curve), based on Eq.(6.23), in the ACR and its inset shows the temperature variation of the effective susceptibility critical exponent, γ_{eff}. The temperature variations of the SPL and LC fit parameters in the ACR are displayed in middle and bottom panels.*

proach those of the asymptotic exponents only in the immediate vicinity of T_C (i.e., in the limit $T \to T_C$). On the other hand, the method that includes the 'correction-to-scaling' terms in the analysis yields the true asymptotic values of the exponents. It is customary to determine the critical exponents β and γ from bulk magnetization data taken in external magnetic fields

Table 6.2: *Various parameters extracted from acs data*

	$x1$	$x2$	$x3$	$x5$
T_C (K)	143.13(3)	134.10(2)	273.50(2)	270.00(5)
γ	0.9999(2)	1.0003(3)	1.000(1)	1.00(1)
ϵ_{co} (10^{-2})	1.50(5)	1.90(6)	1.00(4)	0.80(5)
ACR (10^{-3})	0.75-15	0.7-20	0.5-10	0.5-7.5

by using a specialized form of the general scaling-equation-of state (SES), proposed by Arrott and Noakes [36], given by

$$(H/M)^{1/\gamma} = a'\ \epsilon + b'\ M^{1/\beta} \tag{6.24}$$

where β and γ are the spontaneous magnetization and initial susceptibility critical exponents, respectively, and the *temperature-independent* coefficients a' and b' are related to the critical amplitudes Γ, D and B of Eqs.(6.3), (6.4) and (6.1) as [4]

$$a' = \Gamma^{-1/\gamma}, \quad b' = D^{1/\gamma} \quad \text{and} \quad a'/b' = B^{1/\beta} \tag{6.25}$$

According to this method, the raw M vs. H isotherms taken at different temperatures in the critical region are used to construct the $M^{1/\beta}$ vs. $(H_i/M)^{1/\gamma}$ plot, popularly known as the modified Arrott plot (MAP). Note that $H_i = H_{ext} - 4\pi N\ M(T, H_{ext})$, where N is the demagnetization factor. As a first step, the measured magnetic isotherms, $M(H)$, at various temperatures are converted in to $M(H_i)$ isotherms (Figs. 6.6 and 6.7)

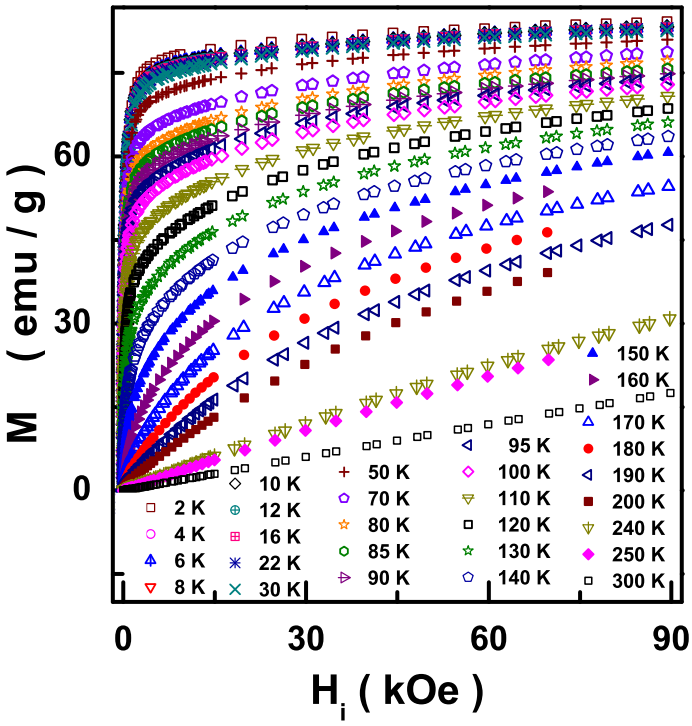

Figure 6.6: *Magnetization as a function of intrinsic field at various temperatures for* $x1$.

by taking slope in linear $M(H)$ region (very low-field region) to calculate $H_i = H - (M/slope)$. The values of critical exponents β and γ are varied so as to make the $M^{1/\beta}$ vs. $(H_i/M)^{1/\gamma}$ isotherms in a narrow temperature range around T_C a set of parallel straight lines, especially in the high-field region, (with the critical isotherm at T_C passing through the origin) over as wide a range of H/M values as possible. The critical exponents obtained in this way are still effective exponents and exponent values very close to the asymptotic ones can be obtained if the temperature range around T_C is narrowed down to such an extent as to approach T_C as closely as possible.

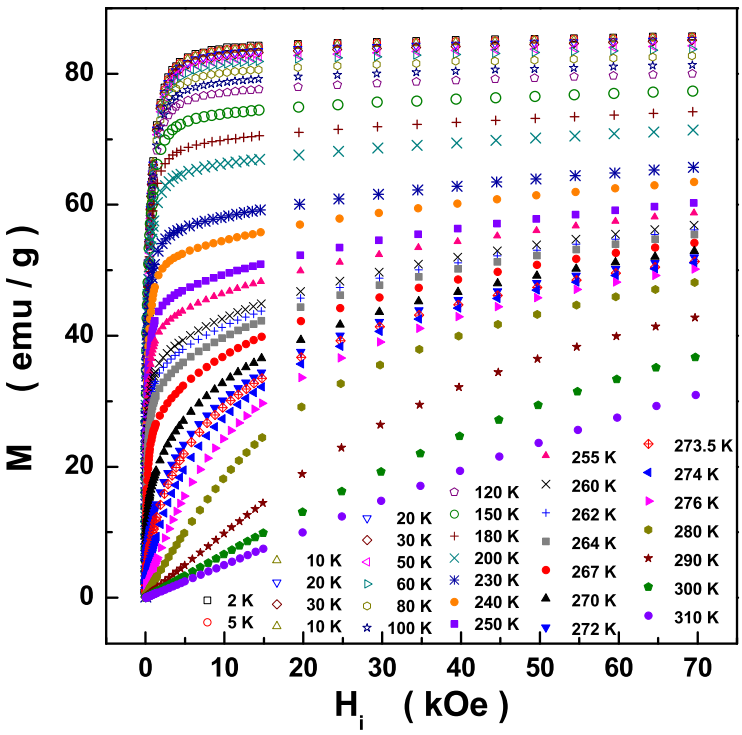

Figure 6.7: *Magnetization as a function of intrinsic field at various temperatures for $x3$.*

Note that Eq. (6.24) with mean exponent values ($\beta = 0.5$ and $\gamma = 1.0$) yields the well-known Arrott-Kouvel plots.

The modified Arrott plots constructed in this way for $x1$ and $x3$ are well described by the $3D$ Ising ($\beta = 0.325$ and $\gamma = 1.241$) and tricritical ($\beta = 0.25$ and $\gamma = 1.0$) exponent values as can be seen in figure 6.8. In contrast to $x1$, modified Arrott plot isotherms for $x2$ could not be made straight in the high field range by choice of any known universality class critical exponents. This clearly suggests that oxygen off-stiochiometry brings in unconventional magnetic order in the presence of magnetic field. It is

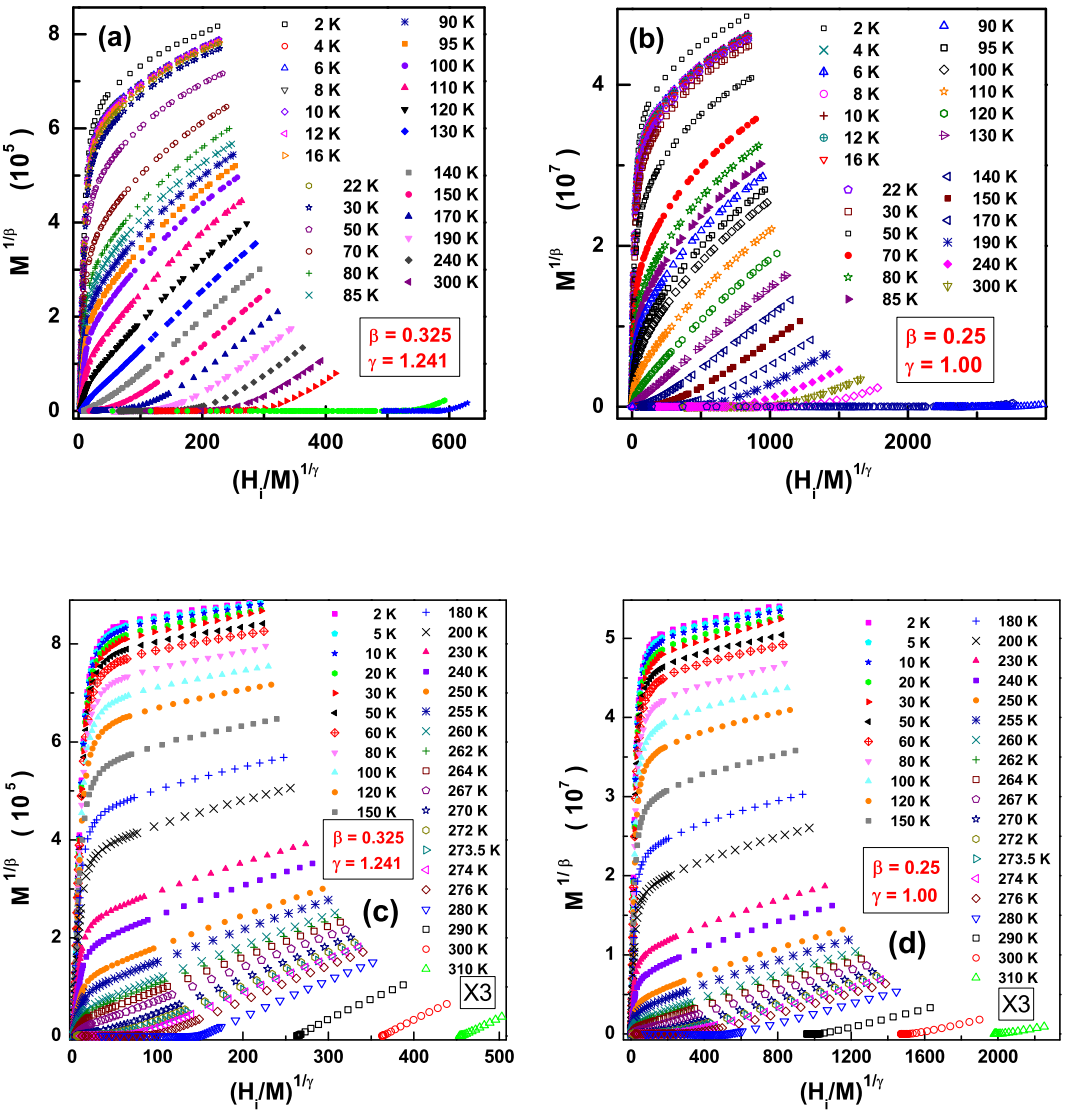

Figure 6.8: *The modified Arrott plots (MAP) for x1 (a,b) and x3 (c,d) using 3D Ising and tricritical critical exponent values.*

evident from the figure 6.8 that the $M(T,H)$ data significantly deviate from the linear MAP isotherms at low fields for temperatures away from T_C and such deviations become more pronounced as, $|T - T_C|$ increases. In order to determine the 'zero-field' quantities such as spontaneous magnetization, $M_S(T,0)$, and initial susceptibility, $\chi(T)$, the high-field linear portions of the MAP isotherms are extrapolated to $H/M = 0$ to yield intercepts $[M(T,0)]^{1/\beta}$ and $[\chi^{-1}(T)]^{1/\gamma}$ on the ordinate ($T < T_C$) and abscissa ($T > T_C$), respectively, as shown in figure 6.9. The $M_S(T,0)$ and $\chi^{-1}(T)$ data, computed from these intercepts, are plotted against $\epsilon = (T - T_C)/T_C$ in Figs. 6.10 and 6.11, respectively. The $M_S(T,0)$ and $\chi^{-1}(T)$ data, so obtained, are analyzed in terms of the single power laws

$$M_S(\epsilon) = B\ (-\epsilon)^{\beta}, \qquad T < T_C^- \tag{6.26}$$

and

$$\chi^{-1}(\epsilon) = \Gamma^{-1}\ \epsilon^{\gamma}, \qquad T > T_C^+ \tag{6.27}$$

In order to arrive at accurate estimates of T_C, β and γ the following steps (i) and (ii) are used self-consistently/iteratively till the trial and final parameter values are identical and $T_C^- = T_C^+$. (i) Construct Modified Arrott plots with initial/trial β and γ values and obtain $M_S(T)$ and $\chi^{-1}(T)$ through linear extrapolation of the MAP isotherms. (ii) Fit the single power laws, Eqs.(6.26) and (6.27) to the $M_S(T)$ and $\chi^{-1}(T)$ data to obtain T_C, β and γ.

From figures 6.10 and 6.11, it is evident that the critical exponents obtained from $M_S(T)$ and $\chi^{-1}(T)$ are in better agreement, within the uncertainty limits, with the critical exponents characterizing the $3D$ Ising (I) than those corresponding to the tricritical (tr) universality class. To reinforce this finding further, the critical isotherm (the $M - H$ isotherm at a

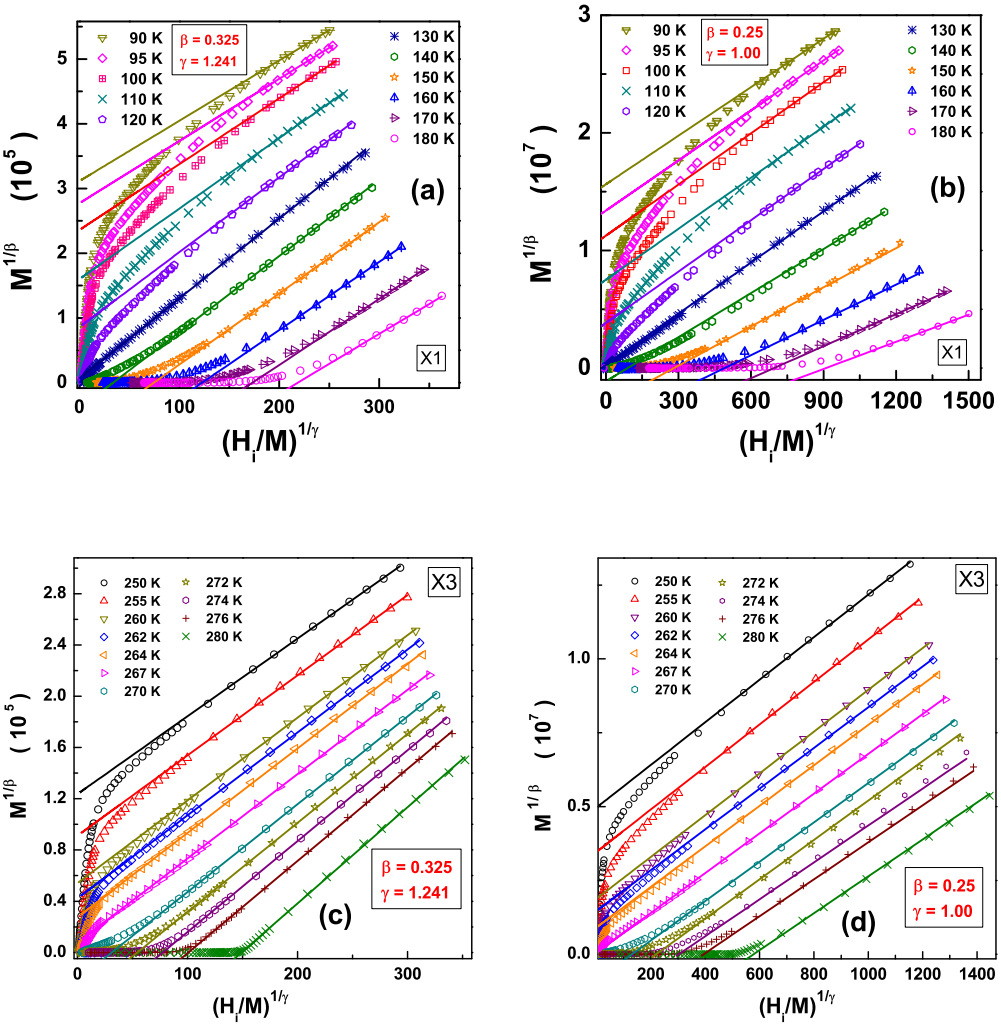

Figure 6.9: *MAP for $x1$ and $x3$ using 3D Ising (a,c) and tricritical (b,d) critical exponent values with linear extrapolation resulting in intercepts on ordinate and abscissa that yield $M_S(T)$ and $\chi^{-1}(T)$, respectively.*

temperature closest to the T_C obtained from the above analysis) depicted in figures 6.12 (a) and 6.12 (b) for $x1$ at 130 K ($T_C(I)$ = 130.60(5) K

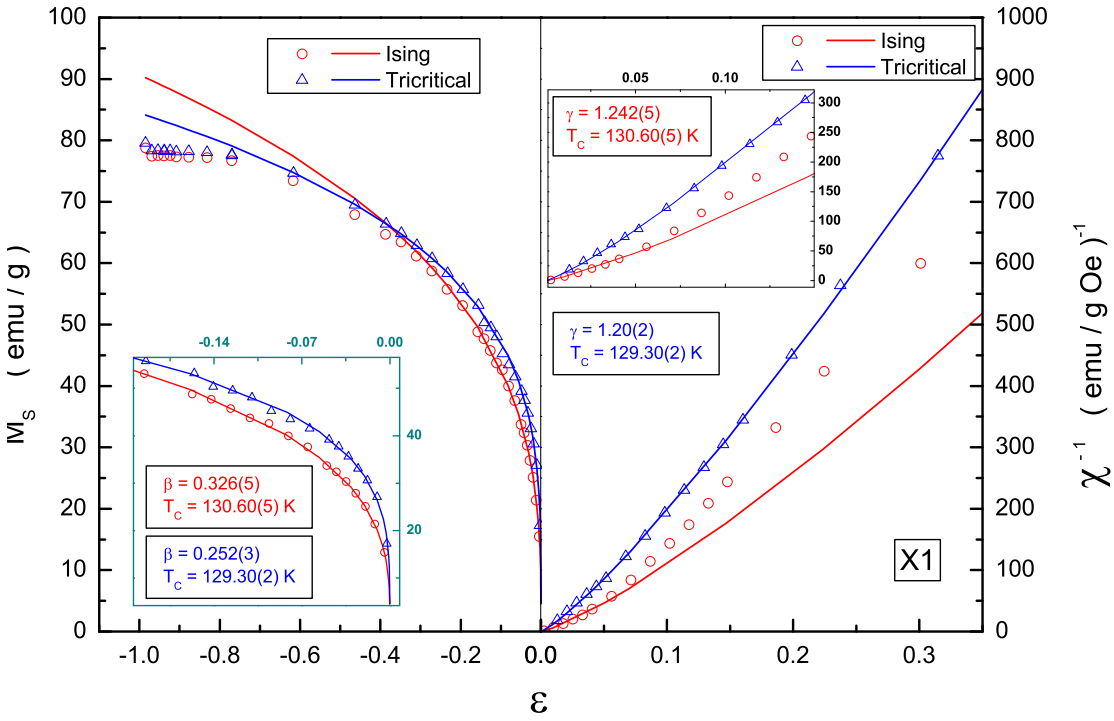

Figure 6.10: *The temperature variation of spontaneous magnetization and intrinsic inverse susceptibility for $x1$, obtained from the linear extrapolation method demonstrated in Figs. 6.9(a,b), and the continuous curves are the fits based on Eqs.(6.26) and (6.27), respectively. The insets depict $M_S(\epsilon)$ and $\chi^{-1}(\epsilon)$ in the ACR.*

and $T_C(tr) = 129.30(2)\ K$) and for $x3$ at 267 K ($T_C(I) = 268.16(2)\ K$ and $T_C(tr) = 267.35(15)\ K$), respectively. The single power law fit to the isotherm at $T = 130\ K$ and $T = 267\ K$, insets of Fig. 6.12, based on Eq.(6.5), yielded the critical exponent $\delta(T = 130\ K) = 4.92(1)$ for $x1$ and $\delta(T = 267\ K) = 5.06(2)$ for $x3$. The values for $\delta(T)$ over the temperature

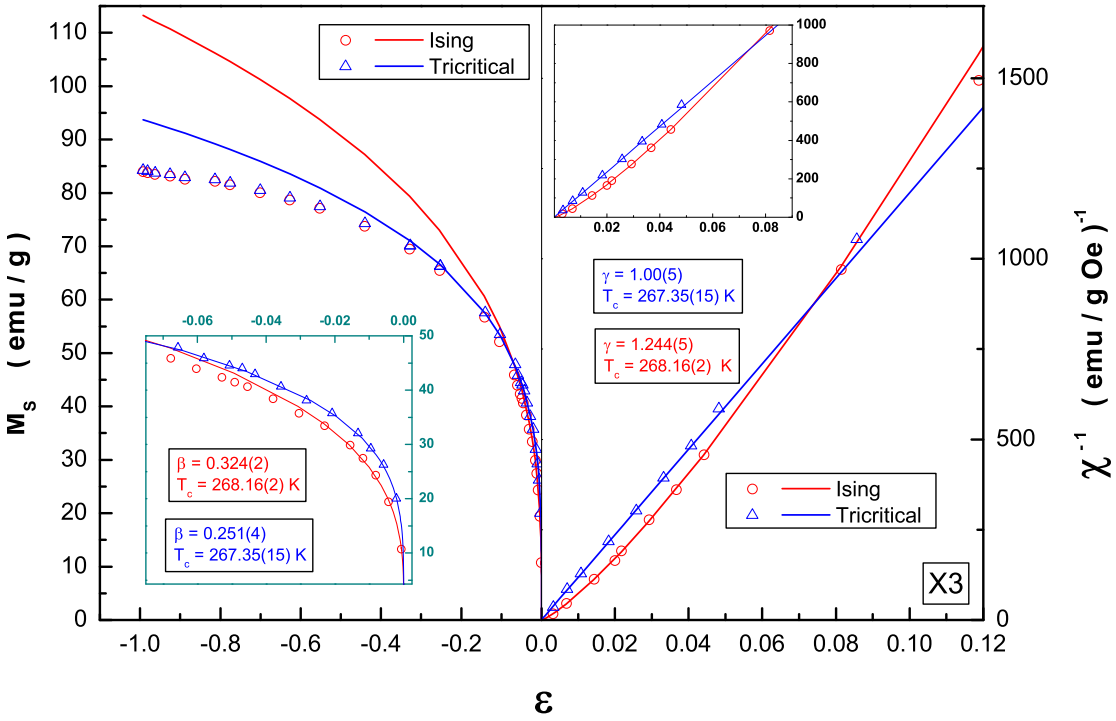

Figure 6.11: *$M_S(\epsilon)$ and $\chi^{-1}(\epsilon)$ for $x3$, obtained from the linear extrapolation method shown in Figs. 6.9(c,d), and the continuous curves are the fits based on Eqs.(6.26) and (6.27), respectively. The insets depict $M_S(\epsilon)$ and $\chi^{-1}(\epsilon)$ in the ACR.*

range $T_C \pm 1\ K$ are obtained the same way from the $logM - logH$ plots. $\delta(T)$, so obtained, is found to obey the relation [4]

$$T_C = T - A\ [\delta(T_C) - \delta(T)] \tag{6.28}$$

with $A = 9(1)$ for $x1$ and $A = 4.6(12)$ for $x3$. The values for the critical exponent δ for the critical isotherm deduced from this relation corresponding

to $d = 3$ Ising (Tricritical point) $\delta(T_C^I = 130.6\ K) = 4.85(1)$ ($\delta(T_C^{tr} = 129.3\ K) = 5.01(1)$) and $\delta(T_C^I = 268.16\ K) = 4.85(2)$ ($\delta(T_C^{tr} = 267.35\ K) = 5.04(4)$) for $x1$ and $x3$, respectively.

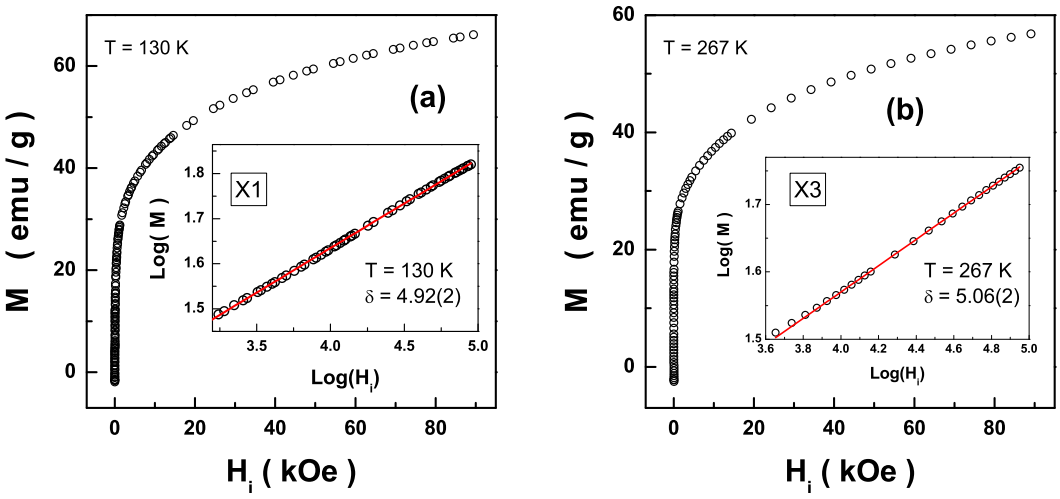

Figure 6.12: *The $M - H_i$ isotherms closest to the critical isotherms for (a) $x1$ and (b) $x3$. The insets show $logM$ vs. $logH$ plots with the linear fits based on Eq.(6.5)*

As a further check, the magnetic scaling equation of the state (SES) of the form [4]

$$M(\epsilon, H)/\epsilon^{\beta} = f_{\pm}(H/\epsilon^{\beta+\gamma}), \tag{6.29}$$

that predicts that $M(\epsilon, H)$ is a universal function of reduced conjugate field, $H/\epsilon^{\beta+\gamma}$, is employed. Here f_+ (f_-) is the scaling function above (below) T_C. By plotting M/ϵ^{β} against $H/\epsilon^{\beta+\gamma}$, all the $M - H$ isotherms taken at temperatures below (above) T_C are expected to fall on a single universal curve f_- (f_+). Figure 6.13 shows such a scaling plot for $x1$ and $x3$ with $3D$ Ising and tricritical critical exponents. It is observed that the $3D$

Ising rather than the tricritical choice of critical exponents yields a better collapse of the data onto two universal curves. As a final test, the best least-squares straight fit to the modified Arrott plot (MAP) for the isotherms at $T = 130\ K$ and $T = 267\ K$ (the temperatures closest to the corresponding T_C) using $3D$ Ising and tricritical universality class exponents values along with the corresponding deviation plots are shown in figure 6.14 (a)-(d). Important observations are that the MAP isotherm is linear over a much wider field range and deviations from linearity are much weaker in the $3D$ Ising case. Hence, $3D$ Ising critical exponents describe the 'in-field' behaviour of $x1$ and $x3$ better than tricritical critical exponents. This result clearly demonstrates that the three-dimensional Ising fixed point is *stabilized* in $x1$ and $x3$ in the presence of magnetic field. Note that the modified Arrott plots, $M^{1/\beta}$ vs. $(H_i/M)^{1/\gamma}$, at fixed temperatures, from which $M_S(T)$ and $\chi_0(T)$ are obtained by extrapolating from *high fields* (typically $\gtrsim 1.5\ kOe$). This extrapolation procedure only yields the expected 'zero-field' behaviour of the high-field stabilized state, which is completely different from the *true zero-field* state. The completely different 'zero-field' ($d = 3$ Uniaxial dipolar) and 'in-field' ($d = 3$ Ising) critical behaviours can be understood as follows. Application of a magnetic field at temperatures near T_C polarizes the t_{2g} spins and thereby aids the uniaxial anisotropy and promotes the e_g electron mobility via double exchange. Thus, the e_g electrons, localized by the polaronic mechanism in zero-field, get delocalized by the field. In the process, the dipole-dipole interations operating between the localized e_g electrons get progressively suppressed as the field increases in strength. Hence, it can be concluded that the magnetic field makes the uniaxial dipolar fixed point unstable and instead stabilizes the $3D$ Ising fixed point in $x1$ and $x3$.

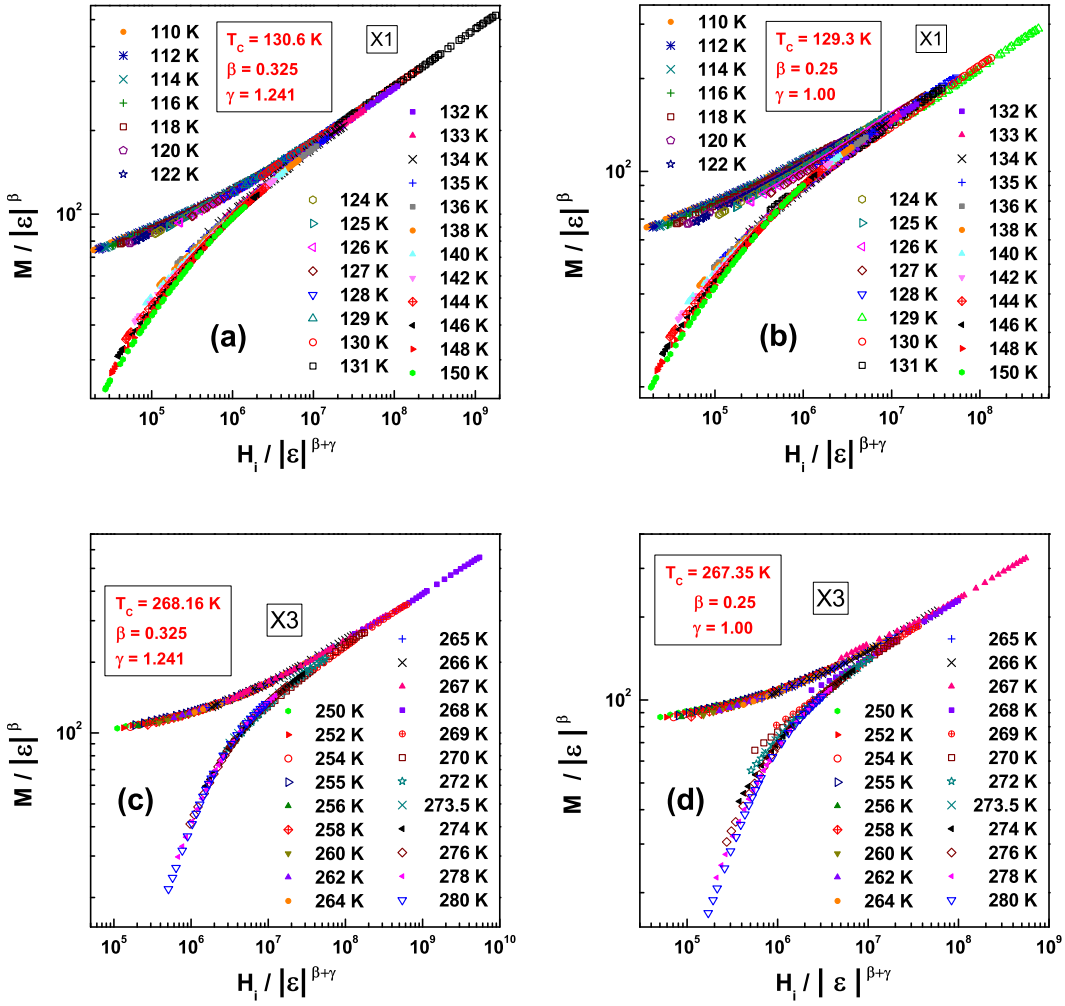

Figure 6.13: *Magnetic scaling equation of state (SES) for $x1$ and $x3$ using (a,c) 3D Ising and (b,d) tricritical critical exponent values.*

By contrast, modified Arrott plot isotherms for $x5$ could not be made straight over any field range by any choice of the critical exponents that corresponds to a known universality class. For this reason, $M(H)$ isotherms

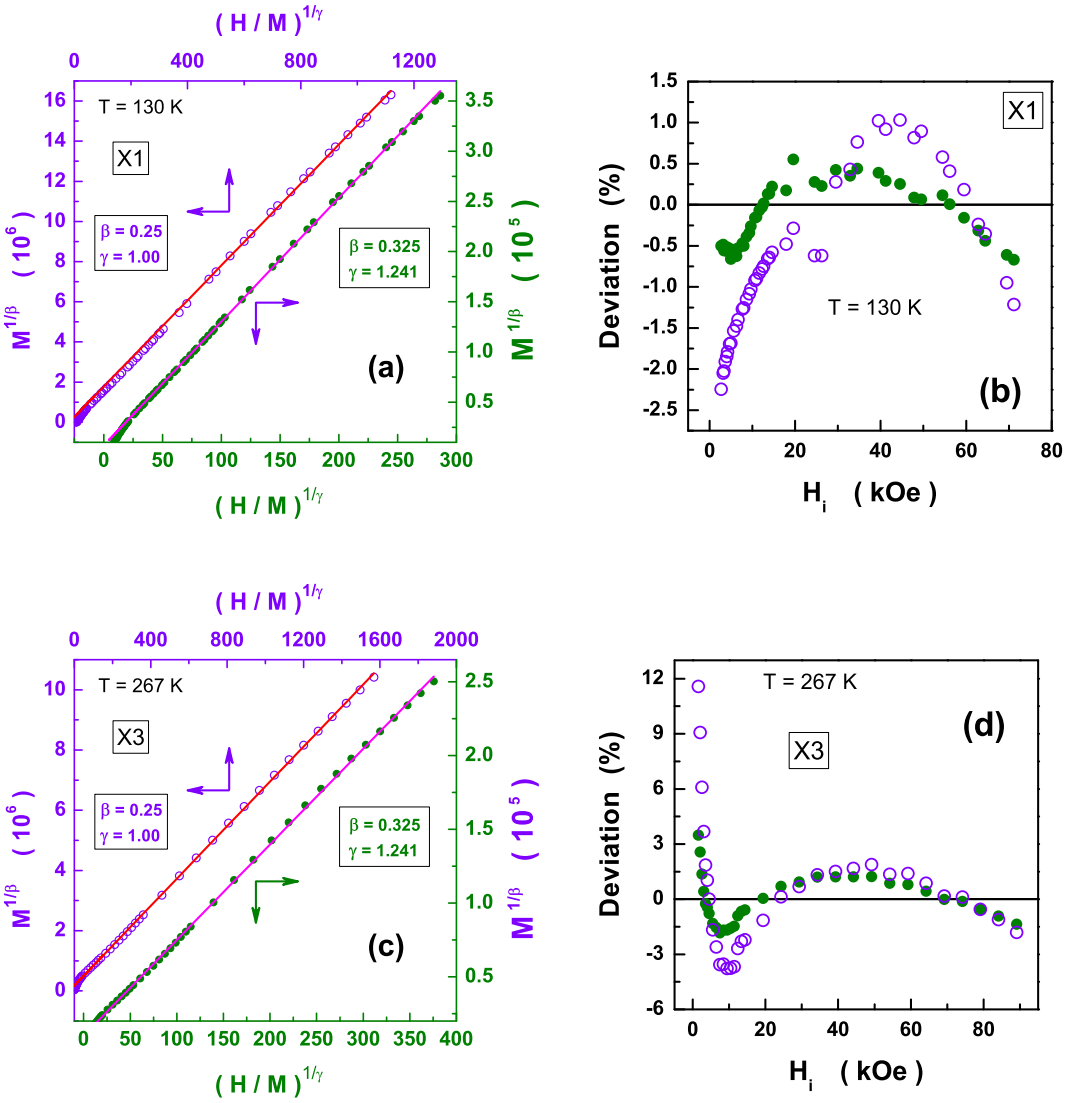

Figure 6.14: *(a) Linear fit to the modified Arrott plot isotherm at $T = 130$ K and $T = 267$ K based on 3D Ising and tricritical critical exponents, for (a) $x1$ and (c) $x3$. The corresponding deviation plot for 3D Ising (closed circle) and tricritical (open circle) exponents are shown in (b) and (d).*

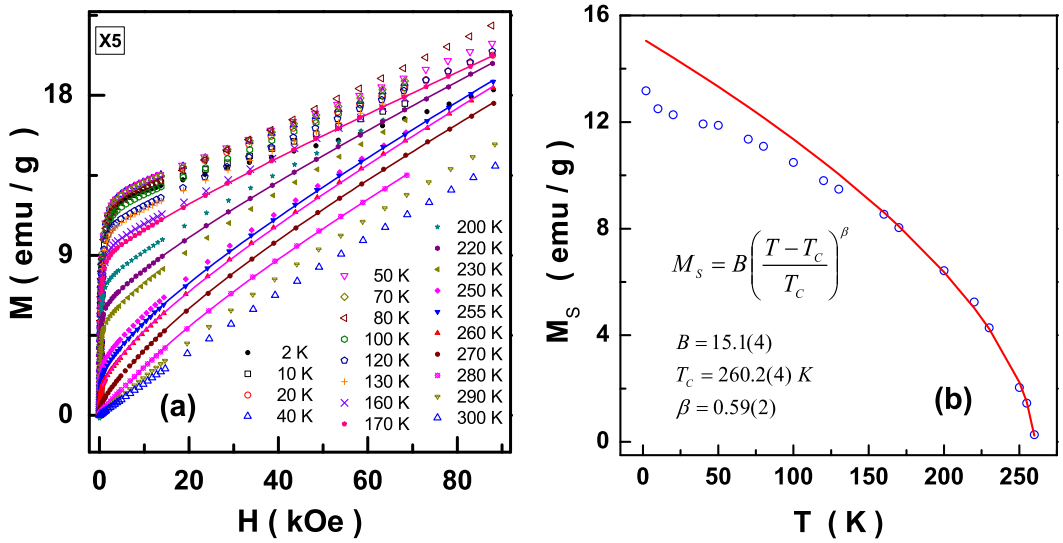

Figure 6.15: *(a) Magnetization as a function of field for $x5$ at various fixed temperatures with fits (solid lines), at a few representative temperatures, based on Eq. (6.30). (b) Temperature variation of M_S corresponding to the fits shown in (a), described by the power law, Eq. (6.1), with the critical exponent $\beta = 0.59(2)$.*

were analyzed in terms of the following expression

$$M(T,H) = M_S(T,0) + b\ H^{1/2} + \chi_{hf}\ H \tag{6.30}$$

where M_S is the spontaneous magnetization, the term $b\ H^{1/2}$ gives the contribution to $M(T,H)$ arising from the suppression of spin waves by the external field, H, and χ_{hf} is the high-field susceptibility. Figure 6.15 displays the $M(H)$ isotherms along with the fits based on Eq.(6.30); for the sake of clarity, the fits for only a few representative isotherms are shown. The spontaneous magnetization, so obtained from the use of Eq. (6.30), when analyzed in terms of Eq.(6.26) yields $B = 15.1(4)\ emu/g$, $260.2(4)\ K$ and $\beta = 0.59(2)$. This value for the critical exponent β does not conform to any known universality class, consistent with our earlier observation.

6.5.3 Magnetocaloric effect

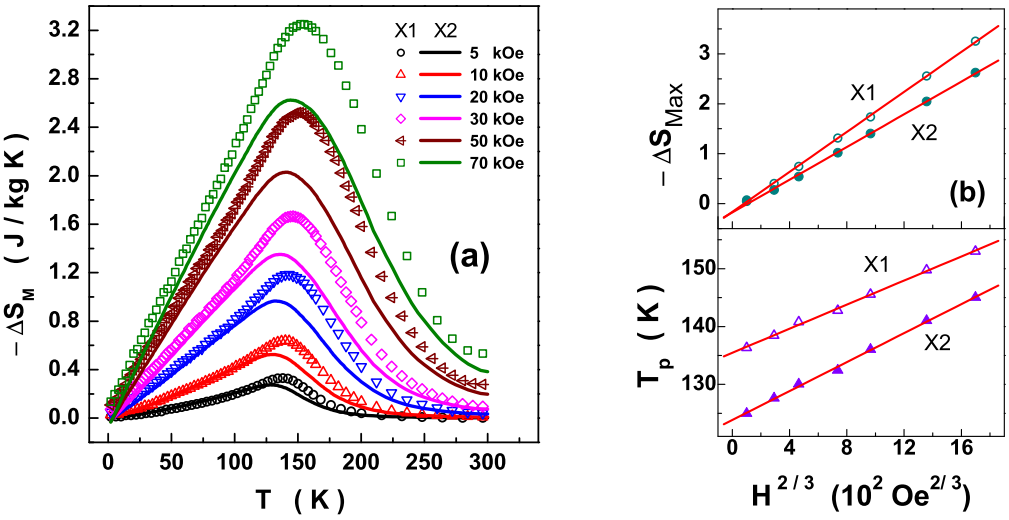

Figure 6.16: *(a) Temperature variation of the isothermal negative magnetic entropy change, $-\Delta S_M(T)$, at various applied fields for $x1$ (symbols) and $x2$ (lines). (b) The $H^{2/3}$ variations of the peak value, $-\Delta S_{max}$, and the temperature T_p at which $-\Delta S_M(T)$ peaks, for $x1$ (open symbols) and $x2$ (closed symbols).*

The temperature variations of the isothermal magnetic entropy change, $-\Delta S_M(T)$, at fixed H, calculated using the Maxwell thermodynamic relation

$$\Delta S_M(T,H) = \int_0^H \left(\frac{dM(T,H)}{dT}\right)_H dH, \tag{6.31}$$

are depicted in Figs. 6.16(a) and 6.17 for the samples $x1$ (symbols), $x2$ (lines), $x3$ and $x5$, respectively. Fig.6.16(b) displays the variations of the peak value, $-\Delta S_{max}$, and the temperature T_p at which $-\Delta S_M(T)$ peaks, with H for $x1$ (open symbols) and $x2$ (closed symbols). The reduced magnitude of $-\Delta S_M(T,H)$ in $x2$ is a consequence of the lower rate of thermal decline of magnetization (higher spin-wave stiffness, see chapter 7). By contrast, lower T_C is responsible for lower T_p in $x2$. $-\Delta S_{max}$ in $x3$ and $x5$ also

follows $H^{2/3}$ variation as shown in figure 6.18. Furthermore, the $H^{2/3}$ power law behaviour of $-\Delta S_{max}$ is consistent with the predictions of the scaling theory [34] when the MF values $\beta = 0.5$ and $\gamma = 1$ are used.

The customary approach of using mean-field (MF) theory to describe $\triangle S_{mag}(T, H)$ and $\triangle T_{ad}(T, H)$ of magnetocaloric materials over a temperature range that embraces the critical region near T_C has met with limited success [35]. Apart from failing to address certain material-specific issues [35], MF theory cannot describe the suppression of critical magnetization fluctuations by H because it neglects spin fluctuations completely. As a step forward, the Arrott-Noakes magnetic equation of state [36] has been used to arrive at the magnetic field dependence of $\triangle S_{mag}$ at $T = T_C$ [37], i.e., $\triangle S_{mag}|_{T=T_C} \sim H^{[(\beta-1)/\Delta]+1}$, where $\Delta = \beta + \gamma$ is the gap exponent while β and γ are the critical exponents for spontaneous magnetization and initial susceptibility, respectively. For the MF values $\beta = 0.5$ and $\gamma = 1$, this relation predicts $\triangle S_{mag}|_{T=T_C} \sim H^{2/3}$, in agreement with the earlier MF result [38]. To obtain a correct theoretical description of $\triangle S_{mag}(T, H)$ within and outside the critical region, we make use of the form of the magnetic equation of state [39]

$$M(\widetilde{\varepsilon}, \widetilde{h}) = |\widetilde{h}|^{\beta/\Delta} \;\; \widetilde{f}_{\pm}\left(\frac{|\widetilde{\varepsilon}|}{|\widetilde{h}|^{1/\Delta}}\right) \tag{6.32}$$

in nonlinear scaling variables $\widetilde{\varepsilon} = (T - T_C)/T = \varepsilon/t$; $\varepsilon = (T - T_C)/T_c$ and $\widetilde{h} = H/t$; $t = T/T_C$, that holds [40–42] over a very wide temperature range around T_C. In Eq.(6.32), $\widetilde{f}_{\pm}$ are the scaling functions for temperatures above (plus) and below (minus) T_C, and these functions approach $\widetilde{f}_0$ (which is analytic at $|\widetilde{\varepsilon}| = 0$) as $\widetilde{\varepsilon} \to 0$. In the limit $|\widetilde{\varepsilon}|/|\widetilde{h}|^{1/\Delta} \ll 1$, the scaling functions $\widetilde{f}_{\pm}(z)$ can be expanded in Taylor series [39] around $z = 0$, i.e.,

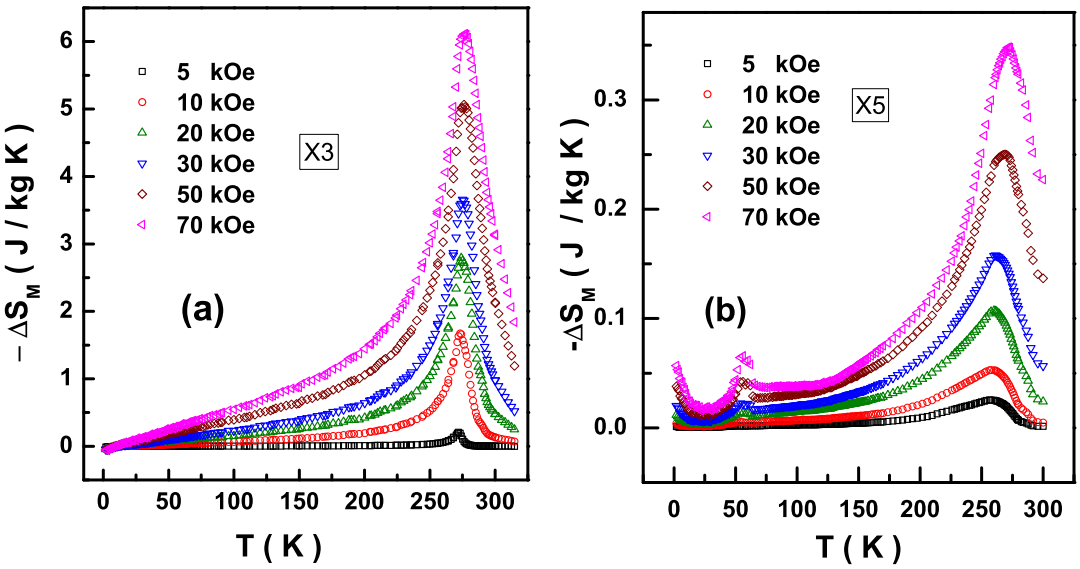

Figure 6.17: *$-\Delta S_M(T)$ at various applied fields for (a) $x3$ and (b) $x5$.*

$\widetilde{f}_0(0)$, as

$$M(\widetilde{\varepsilon},\widetilde{h}) = |\widetilde{h}|^{\frac{\beta}{\Delta}}\left[\widetilde{f}_0(0) + \frac{|\widetilde{\varepsilon}|}{|\widetilde{h}|^{\frac{1}{\Delta}}}\widetilde{f}_0'(0) + \frac{|\widetilde{\varepsilon}|^2}{2|\widetilde{h}|^{\frac{2}{\Delta}}}\widetilde{f}_0''(0) + \frac{|\widetilde{\varepsilon}|^3}{6|\widetilde{h}|^{\frac{3}{\Delta}}}\widetilde{f}_0'''(0) + \cdots\right]$$
$$= \widetilde{f}_0(0)|\widetilde{h}|^{\frac{\beta}{\Delta}} + \widetilde{f}_0'(0)|\widetilde{\varepsilon}||\widetilde{h}|^{\frac{(\beta-1)}{\Delta}} + \frac{1}{2}\widetilde{f}_0''(0)|\widetilde{\varepsilon}|^2|\widetilde{h}|^{\frac{(\beta-2)}{\Delta}}$$
$$+\frac{1}{6}\widetilde{f}_0'''(0)|\widetilde{\varepsilon}|^3|\widetilde{h}|^{\frac{(\beta-3)}{\Delta}} + \cdots \qquad (6.33)$$

Retaining only the first four terms in the expansion and using in Eq.(6.31), one obtains the final result [34]

$$\triangle S_{mag}(T,H) = a_0\ |\widetilde{h}|^{n_0+1} + a_1\ |\widetilde{h}|^{n_1+1}(t^{-1} - n_1\ |\widetilde{\varepsilon}|)$$
$$+a_2\ |\widetilde{h}|^{n_2+1}\ |\widetilde{\varepsilon}|(t^{-1} - (n_2/2)\ |\widetilde{\varepsilon}|)$$
$$+a_3\ |\widetilde{h}|^{n_3+1}\ |\widetilde{\varepsilon}|^2(t^{-1} - (n_3/3)\ |\widetilde{\varepsilon}|) \qquad (6.34)$$

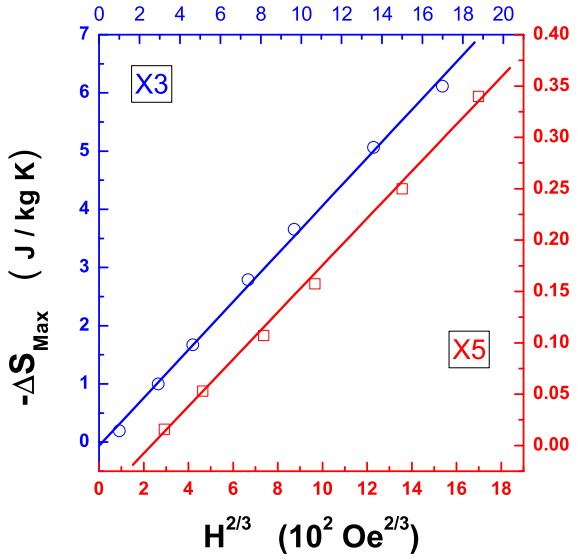

Figure 6.18: *Field dependence of* $-\Delta S_{max}$ *for* $x3$ *and* $x5$.

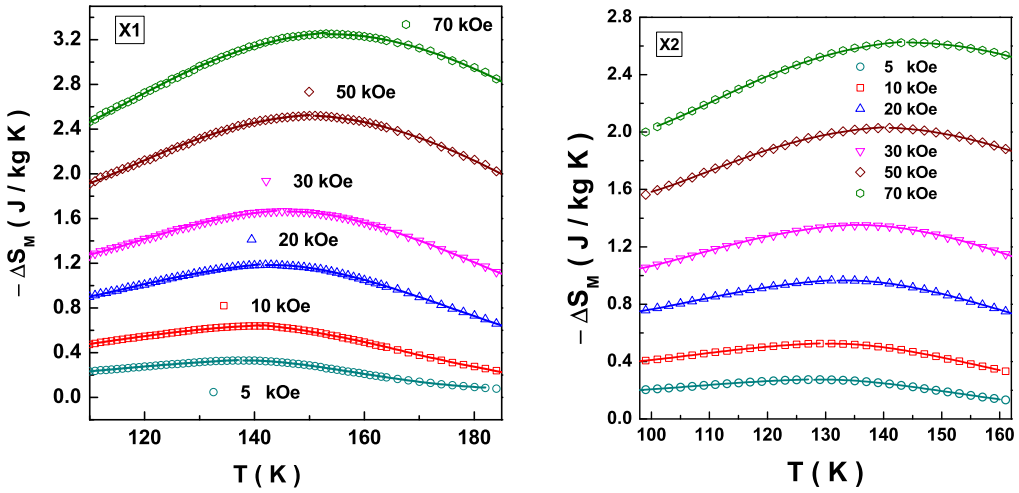

Figure 6.19: $-\Delta S_M(T)$ *at various applied fields for* $x1$ *and* $x2$ *along with the fits (continuous lines) based on Eq. (6.34).*

with

$$
\begin{aligned}
a_0 &= -(\widetilde{f}_0(0)/T_C)\ [n_0/(n_0+1)] \ ; \qquad n_0 = \beta/\Delta \\
a_1 &= (\widetilde{f}_0'(0)/T_C)\ [1/(n_1+1)] \qquad ; \qquad n_1 = (\beta-1)/\Delta \\
a_2 &= (\widetilde{f}_0''(0)/T_C)\ [1/(n_2+1)] \qquad ; \qquad n_2 = (\beta-2)/\Delta \\
a_3 &= (\widetilde{f}_0'''(0)/T_C)\ [1/(n_3+1)] \qquad ; \qquad n_3 = (\beta-3)/\Delta
\end{aligned}
$$

and the derivative functions $\widetilde{f}_0'(0)$, $\widetilde{f}_0''(0)$ and $\widetilde{f}_0'''(0)$, like $\widetilde{f}_0(0)$, treated as constants. The continuous curves through the data in figures 6.19 and 6.20 are obtained, independently below and above the peak temperature, T_p (taking $T_C(H) = T_p(H)$), by using the MF values $\beta = 0.5$ and $\gamma = 1$ and optimizing the parameters a_0, a_1, a_2 and a_3. Eq.(6.34), with the MF choice of critical exponents, adequately describes $\triangle S_{mag}$ over wide ranges of temperature and field. Consistent with the above finding that Eq.(6.34) with mean-field exponent values closely reproduces the observed $\Delta S_{mag}(T,H)$ particularly near T_C, at $T = T_C$, $\Delta S_{mag}(T,H)$ does obey the MF prediction $\Delta S_{mag}|_{T=T_C} \sim H^{2/3}$ (Fig.6.16(b))) and in $x3/x5$ (Fig.6.18). $3D$ Ising exponents also give reasonably good description of $\Delta S_{mag}(T,H)$ in $x1$ and $x3$.

6.6 Summary and Conclusion

A detailed study of the '*zero-field*' FM-PM phase transition occuring in the insulating state has revealed that the systems $x1$, $x2$, $x3$ and $x5$ behave as a three-dimensional ($d = 3$) *uniaxial dipolar* (UD) ferromagnet in the asymptotic critical region (ACR) and exhibit a *crossover* to the $d = 3$ *isotropic dipolar* (ID) critical behaviour outside ACR. The width of the ACR *narrows*

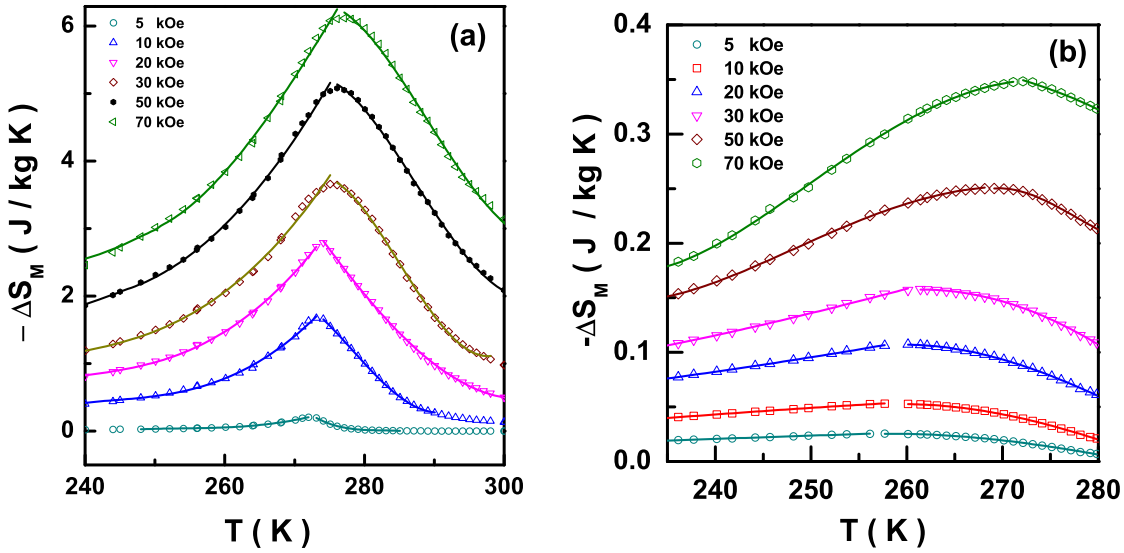

Figure 6.20: *$-\Delta S_M(T)$ at various applied fields for (a) $x3$ and (b) $x5$ along with the fits (continuous lines) based on Eq.(6.34).*

down with increasing Ca concentration indicating weakening of the uniaxial anisotropy. Reducing the average grain size to nano metre regime brings in an additional constraint of confining the long-range ordered ferromagnetic-insulating/ferromagnetic-metallic/charge-ordered-insulating regions to a few nm so that these regions compete with other inhomogeneities of similar length scales and the physics of these systems is governed by a complex interplay of these phase separated entities of similar dimensions. Irrespective of the Ca concentration, the dipolar interactions operate between the localized e_g-electron spins. The magnetic field stabilizes the three-dimensional Ising FM fixed point in the asymptotic critical region and reduces $T_C(H = 0)$ by $5\ K - 13\ K$ in $x = 1/8$ and $x = 3/8$ while $x = 5/8$ does not belong to any known universality class. The magnetic scaling equation of state with mean

field exponents describes the magnetic entropy change well over a wide temperature range embracing the critical region. Ample experimental evidence is provided for a continuous second-order $FM - PM$ phase transition in $x3$ and for simultaneous $FM - PM$ and $CO - PM$ second-order phase transitions in $x5$ at $T_C/T_{CO} = 270\ K$ in the absence of external magnetic field. The question whether or not the distinctly different 'in-field' critical behaviour compared to the one observed in 'zero-field' in the presently studied systems are characteristic of only the nano systems, forms an interesting topic which needs to be investigated further.

References

1. H. E. Stanley, *Introduction to Phase transitions and critical phenomena* (Clarendon press, Oxford, 1971).

2. M. E. Fisher, in the Proceedings of the International School of Physics, Enrico Fermi, *Critical Phenomena* (Academic press, New York, 1971).

3. S. K. Ma, *Modern theory of Critical Phenomena* (Benjamin, Inc., 1976).

4. S. N. Kaul, *Static critical phenomena in ferromagnets with quenched disorder*, J. Magn. Magn. Mater. **53**, 5 (1985).

5. E. K. Riedel and F. J. Wegner, *Effective critical and tricritical exponents*, Phys. Rev. B **9**, 294 (1974).

6. L. P. Kandonoff, in the Proceedings of the International School of Physics, Enrico Fermi, *Critical Phenomena* (Academic press, New York, 1971).

7. M. E. Fisher, *The renormalization group in the theory of critical behavior*, Rev. Mod. Phys. **46**, 597 (1974).

8. E. Ising, *Beitrag zur Theorie des Ferromagnetismus*, Z. Phys. **31**, 253 (1925).

9. A. I. Larkin and D. E. Khmel'Nitskii, *Phase Transition in Uniaxial Ferroelectrics*, Sov. Phys. JETP **29**, 1123 (1969); F. J. Wegner and E. K. Riedel, *Logarithmic corrections to the molecular-field behavior of critical and tricritical systems*, Phys. Rev. B **7**, 248 (1973).

10. E. Brézin and J. Zinn-Justin, *Critical behavior of uniaxial systems with strong dipolar interactions*, Phys. Rev. B **13**, 251 (1976).

11. E. Frey and F. Schwabl, *Renormalized field theory for the static crossover in uniaxial dipolar ferromagnets*, Phys. Rev. B **42**, 8261 (1990).

12. K. Ried, Y. Millev, M. Fähnle and H. Kronmüller, *Phase transitions in ferromagnets with dipolar interactions and uniaxial anisotropy*, Phys. Rev. B **51**, 15229 (1995)

13. A. D. Bruce, J. M. Kosterlitz and D. R. Nelson, *Crossover phenomena in isotropic dipolar ferromagnets*, J.Phys. C: Solid State Phys. **9**, 825 (1976).

14. A. D. Bruce, *Susceptibility crossover in dipolar ferromagnets*, J.Phys. C: Solid State Phys. **10**, 419 (1977).

15. E. Frey and F. Schwabl, *Renormalized field theory for the static crossover in isotropic dipolar ferromagnets*, Phys. Rev. B **43**, 833 (1991).

16. P. Pfeuty, D. Jasnow and M. E. Fisher, *Crossover scaling functions for exchange anisotropy*, Phys. Rev. B **10**, 2088 (1974).

17. A. Aharony and M. E. Fisher, *Critical Behavior of Magnets with Dipolar Interactions. I. Renormalization Group near Four Dimensions*, Phys. Rev. B **8**, 3323 (1973); M.E. Fisher and A. Aharony, *Dipolar Interactions at Ferromagnetic Critical Points*, Phys. Rev. Lett. **30**, 559 (1973).

18. H. S. Kogon and A. D. Bruce, *Transition temperature shifts and correction-to-scaling amplitudes in systems exhibiting crossover behaviour*, J.

Phys. C **15**, 5729 (1982).

19. S. N. Kaul, *Phase Transitions and Finite Temperature Magnetism: Experiment and Analysis*, in Handbook of Magnetism and Advanced Magnetic Materials, Eds: H. Kronmüller and S. Parkin (John Wiley & Sons, 2007) and S. N. Kaul, *Critical Behaviour of Heisenberg Ferromagnets with Dipolar Interactions and Uniaxial Anisotropy* in Lect. Notes Phys. **678**, *Local-Moment Ferromagnets: Unique Properties for Modern Applications.* Eds.: Markus Donath and Wolfgang Nolting, (Springer, Berlin Heidelberg, 2005).

20. S. N. Kaul, *Asymptotic and leading "correction-to-scaling" susceptibility critical exponents and amplitudes for ferromagnets with quenched disorder*, Phys. Rev. B **38**, 9178 (1988).

21. G. V. Brown, *Magnetic heat pumping near room temperature* , J. Appl. Phys. **47**, 3673 (1976).

22. A. Tishin and Y. Spichkin, *The Magnetocaloric Effect and its Applications*, Institute of Physics Publishing (2003).

23. T. Sarkar, A. K. Raychaudhuri, A. K. Bera and S. M. Yusuf, *Effect of size reduction on the ferromagnetism of the manganite* $La_{1-x}Ca_xMnO_3$ *(*$x = 0.33$*)*, New J. Phys. **12**, 123026 (2010).

24. J. Mira, J. Rivas, F. Rivadulla, C. Vázquez-Vázquez and M. A. López-Quintela, *Change from first- to second-order magnetic phase transition in* $La_{2/3}(Ca, Sr)_{1/3}MnO_3$ *perovskites*, Phys. Rev. B **60**, 2998 (1999).

25. C. P. Adams, J. W. Lynn, V. N. Smolyaninova, A. Biswas, R. L. Greene, W. Ratcliff II, S. -W. Cheong, Y. M. Mukovskii, and D. A.

Shulyatev, *First-order nature of the ferromagnetic phase transition in* $(La - Ca)MnO_3$ *near optimal doping*, Phys. Rev. B **70**, 134414 (2004).

26. N. Moutis, I. Panagiotopoulos, M. Pissas and D. Niarchos, *Structural and magnetic properties of* $La_{0.67}(Ba_xCa_{1-x})_{0.33}MnO_3$ *perovskites* $(0 < x < 1)$, Phys. Rev. B **59**, 1129 (1999).

27. S. Rößler, U. K. Rößler, K. Nenkov, D. Eckert, S. M. Yusuf, K. Dörr and K.-H. Müller, *Rounding of a first-order magnetic phase transition in Ga-doped* $La_{0.67}Ca_{0.33}MnO_3$, Phys. Rev. B **70**, 104417 (2004).

28. Chetan Dhital, Clarina de la Cruz, C. Opeil, A. Treat, K. F. Wang, J.-M. Liu, Z. F. Ren and Stephen D. Wilson, *Neutron scattering study of magnetic phase separation in nanocrystalline* $La_{5/8}Ca_{3/8}MnO_3$, Phys. Rev. B **84**, 1444401 (2011).

29. D. Kim, B. Revaz, B. L. Zink, F. Hellman, J. J. Rhyne and J. F. Mitchell, *Tricritical Point and the Doping Dependence of the Order of the Ferromagnetic Phase Transition of* $La_{1-x}Ca_xMnO_3$, Phys. Rev. Lett. **89**, 227202 (2002).

30. M Pissas and G Papavassiliou, *The phase diagram and magnetic properties of* $La_{1-x}Ca_xMnO_3$ *compounds for* $0 \leq x \leq 0.23$, J. Phys.: Condens. Matter **16**, 6527 (2004).

31. S. Begum, Y. Ono, Y. Tomika, Y. Tokura, Y. Ishii, Y. Morii and T. Kajitani, *Jahn-Teller distortion and cluster-glass like behavior in* $La_{0.875}Ca_{0.125}MnO_3$, J. Phys. Chem. Sol. **63**, 939 (2002).

32. Yugandhar Bitla, S. N. Kaul, L. Fernández Barquín, J. Gutiérrez, J. M. Barandiarán and A. Peña, *Observation of isotropic-dipolar to isotropic-Heisenberg crossover in Co- and Ni-substituted manganites*, New J. Phys. **12**, 093039 (2010).

33. S. Srinath, S. N. Kaul and H. Kronmüller, *Observation of isotropic dipolar to uniaxial dipolar crossover in gadolinium*, Phys. Rev. B **59**, 1145 (1999) and references cited therein.

34. S. P. Mathew and S. N. Kaul, *Tuning magnetocaloric effect with nanocrystallite size*, Appl. Phys. Lett. **98**, 172505 (2011).

35. M. -H. Phan and S. -C. Yu, *Review of the magnetocaloric effect in manganite materials*, J. Magn. Magn. Mater. **308**, 325 (2007).

36. A. Arrott and J. E. Noakes, *Approximate Equation of State For Nickel Near its Critical Temperature*, Phys. Rev. Lett. **19**, 786 (1967).

37. V. Franco, J. S. Blázquez and A. Conde, *Field dependence of the magnetocaloric effect in materials with a second order phase transition: A master curve for the magnetic entropy change*, Appl. Phys. Lett. **89**, 222512 (2006).

38. H. Oesterreicher and F. T. Parker, *Magnetic cooling near Curie temperatures above 300 K*, J. Appl. Phys. **55**, 4334 (1984).

39. S. N. Kaul, *Nonlinear scaling and its application to ferromagnetic systems*, Phase Transitions **47**, 23 (1994).

40. M. Seeger, S. N. Kaul, H. Kronmüller and R. Reisser, *Asymptotic critical behavior of Ni*, Phys. Rev. B **51**, 12585 (1995).

41. M. Sambasiva Rao and S. N. Kaul, *Validity of the generalized Curie-Weiss law in ferromagnetic systems with 'frozen' disorder*, J. Magn. Magn. Mater. **171**, 341 (1997).

42. P. D. Babu and S. N. Kaul, *Scaling behaviour of magnetization for temperatures in the vicinity of, and far from, the ferromagnetic-paramagnetic phase transition in amorphous* $Fe_{90-x}Co_xZr_{10}$ *and* $Fe_{90+y}Zr_{10-y}$ *alloys*, J. Phys.: Condens. Matter **9**, 7189 (1997).

Chapter 7

Low-lying magnetic excitations and magnetic irreversibility

The present chapter deals with the study of magnetic irreversibility and low-lying magnetic excitations in the nanocrystalline $La_{1-x}Ca_xMnO_3$ manganites. The low-temperature magnetic moments are lower than those expected based on the nominal Mn^{3+}/Mn^{4+} concentration, suggesting thereby a canted spin structure. The effective magnetic moments, calculated from the Curie constant, obtained from the Curie-Weiss fits in paramagnetic (PM) region, are higher than the expected values. This observation is indicative of the presence of small ferromagnetic clusters in the PM state. At low temperatures, the temperature dependence of magnetization in $x1$, $x2$ and $x3$, is adequately described by the conventional spin-wave relation. The spin-wave stiffness, so obtained, has values comparable to those for the bulk counterparts. Irreversibility in magnetization, observed at low fields, presents several anomalous features which are absent in the bulk.

7.1 Introduction

In a crystalline ferromagnet, the local deviation from the perfect alignment at a finite temperature does not remain confined to a microscopic region of space but propagates like a wave due to exchange coupling between the spins. These low-lying magnetic excitations are called spin-waves. A spin wave can be thought of as one spin reversal coherently spread over the entire crystal. The conventional spin-wave theories are based on localized-electron picture, in which the magnetic electrons are localized on atomic orbitals. However, in metallic systems, the magnetic electrons have itinerant character. Thus, localized-electron and itinerant-electron models form two exactly opposite descriptions of the low-lying magnetic excitations. The domains, the domain wall structure and the non-uniform internal field distribution play a fundamental role in spin wave generation, propagation and magnon-magnon interactions.

Hysteresis and coercivity are two consequences of the various metastable energy states in the domain structure distribution. The coercivity mechanism has roots in domain wall pinning via defects, inhomogeneities and nonuniform distribution of magnetic properties. The strong dependence on temperature, crystalline and shape anisotropies determines the relaxation rate (and hence the time-scale during which no change of magnetization occurs and ferromagnetic state remains stable) exists. Metastability is governed by local energy minima. The remanence is the remaining magnetization after the applied magnetic field has been removed. The coercivity is the magnetic field needed to reduce the remanent magnetization of the sample to zero. It is a measure of the pinning of magnetic domain walls in

the sample. The coercivity depends on the microstructure of the sample, and therefore depends on the type of processing.

The thermomagnetic irreversibility, a bifurcation in the 'field-cooled' (FC) and 'zero-field-cooled' (ZFC) magnetizations, $M_{FC}(T)$ and $M_{ZFC}(T)$, is observed at low temperatures. The $M_{FC}(T)$ and $M_{ZFC}(T)$ curves coincide beyond a certain temperature, T_{bf}, which lies between the temperature at which $M_{ZFC}(T)$ peaks, T_p^{ZFC}, and the Curie temperature, T_C. Thermomagnetic irreversibility $(M_{FC}(T) - M_{ZFC}(T)) > 0$ and a peak in $M_{ZFC}(T)$ are more often considered as the characteristic features of spin-glass or superparamagnetic systems. However, such a behaviour is also observed in many long-range ordered systems, like ferrimagnetic systems, due to domain wall pinning effects. For ferromagnetic systems, it reflects the temperature variation of magnetocrystalline anisotropy energy barriers. A peak is observed at a temperature below which the anisotropy field overcomes the applied magnetic field. Magnetic irreversibility is observed below a certain temperature at magnetic fields lower than a threshold field. The bifurcation between ZFC and FC magnetizations reflects the presence of magnetic irreversibilities that could result from the anisotropy barriers and/or magnetic inhomogeneities. Generally, irreversibilities in magnetization at low fields and temperatures well below T_C are attributed to progressive stiffening of domain walls with increasing temperatures.

Magnetic hysteresis is negligible at $T = 10\ K$ for $x1$ in the bulk [1] which is the limiting case of A-type antiferromagnetic structure and exhibits a low- and high-energy spin-wave branch and has an energy gap of $\sim 0.25\ meV$ between these two spin wave branches in the canted state. It is reasoned that the magnetic percolation does not coincide with the electronic percolation

and the spin wave dispersion is anisotropic. The presence of AFM and FM clusters of sizes 20 $\mathring{A}$ and $3-4$ $\mathring{A}$ at 8 K and 293 K in bulk $x1$ was inferred from small angle neutron scattering experiments [2]. Neutron scattering study on nanocrystalline $x3$ [3] has shown intriguing features: a FM transition at $T_C = 233$ K followed by an antiferromagnetic transition at $T_N = 140$ K (generally, not expected for optimally hole-doped LCMO). At 10 K, FM and AFM clusters of 59 nm and 30 nm sizes were found. A peculiar type of magnetic irreversibility has been observed in $x3$ at T_C in the present study. This anomalous form of irreversibility finds a straight forward explanation in terms of the competition between the high-temperature AFM insulating and low-temperature FM metallic phases.

7.2 Experimental details

Magnetic hysteresis loops were measured on the nanocrystalline samples $x1$ ($La_{0.875}Ca_{0.125}MnO_3$), $x2$ ($La_{0.875}Ca_{0.125}MnO_{3.06}$), $x3$ ($La_{0.625}Ca_{0.375}MnO_{2.99}$) and $x5$ ($La_{0.375}Ca_{0.625}MnO_{2.94}$) with average grain sizes of $d = 27(5)$ nm, $d = 18(3)$ nm and $d = 13(5)$ nm, respectively, in fields up to ± 90 kOe at various temperatures. The low-field magnetization at $25\ Oe \leq H \leq\ 1\ kOe$ in the 'zero-field-cooled'(ZFC) and 'field-cooled'(FC) modes and magnetization as a function of temperature at fields in the range $5\ kOe \leq H \leq 90\ kOe$ were measured over the temperature range, $2\ K \leq T \leq 310\ K$, that embraces the critical region. All these measurements were carried on the PPMS-VSM and SQUID-VSM systems of Quantum Design make.

7.3 Data analysis, results and discussion

7.3.1 Magnetic hysteresis, remanence and coercivity

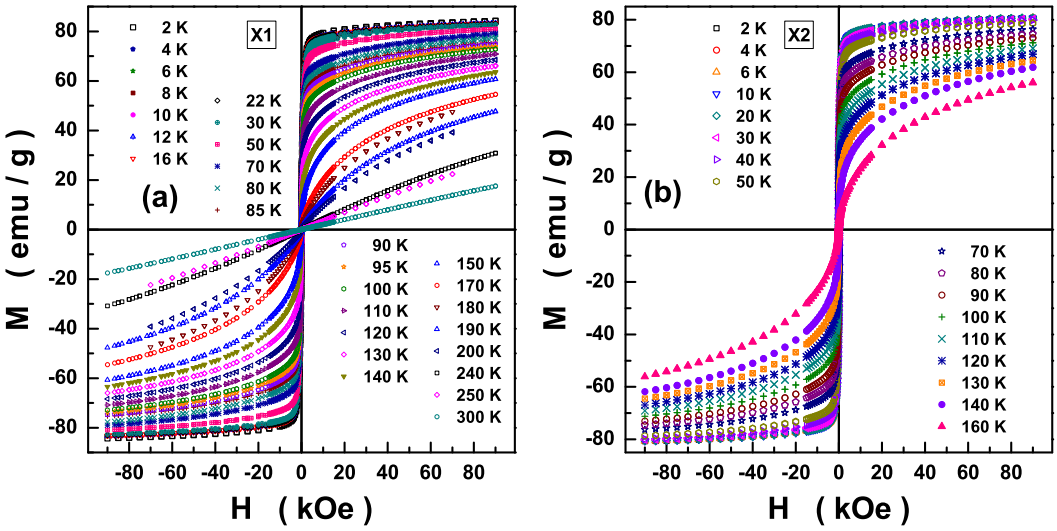

Figure 7.1: *M-H hysteresis loops measured for the samples (a) x1 and (b) x2 at different temperatures.*

A direct comparison between the $M - H$ loops for the samples $x1$ and $x2$, made in figure 7.1, reveals that, in $x2$, (i) at any given temperature, magnetization is consistently lower in magnitude at all fields, and (ii) it is more difficult to saturate magnetization even at magnetic fields as high as 90 kOe. While the observation (i) reflects a higher concentration of Mn^{4+} ions in $x2$ due to the oxygen off-stoichiometry, (ii) is a manifestation of stronger magnetocrystalline anisotropy (MCA) in $x2$ as is also indicated by higher coercivity (figure 7.3).

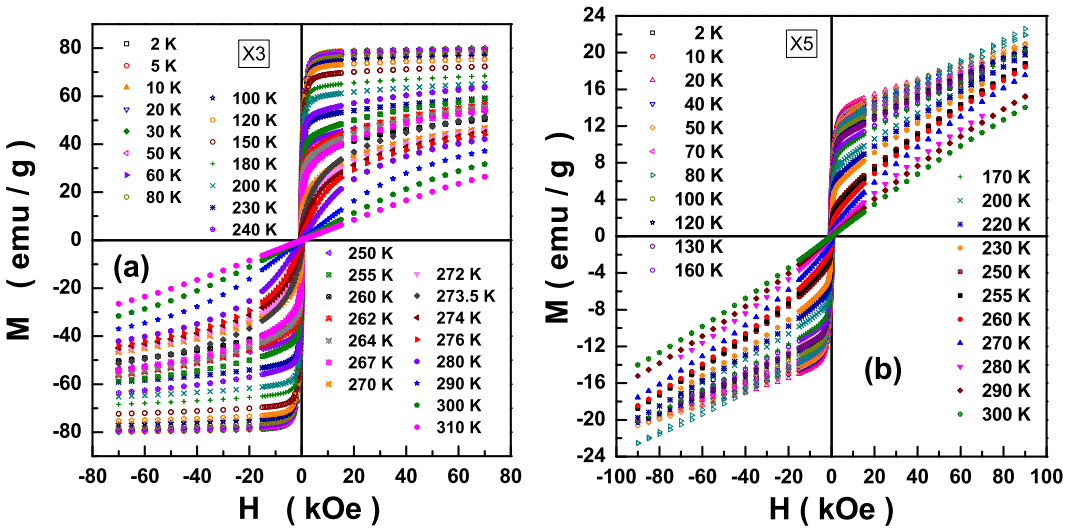

Figure 7.2: *M-H hysteresis loops measured for the samples (a) x3 and (b) x5 at different temperatures.*

The $M-H$ hysteresis loops for the samples $x3$ and $x5$, as shown in Fig. 7.2, present the following obvious features. (i) Saturation in magnetization at 2 K in $x3$ is essentially achieved in fields as low as 10 kOe. (ii) By contrast, the magnetization at 2 K in $x5$ shows no signs of saturation even at fields as strong as 90 kOe although the technical saturation is reached at fields $\simeq$ 5 kOe. Unusually large high-field susceptibility in the latter case is a clear indication of strong canted antiferromagnetic-correlated spin regions coexisting with the regions of ferromagnetically coupled spins.

The temperature variations of remanence, M_r, and coercivity, H_c, for $x1$-$x5$, obtained from the hysteresis loops, presented in Figs. 7.1 and 7.2, are displayed in figures 7.3 and 7.4. Out of these systems, only $x3$ displays features that are expected in an archetypal ferromagnet. The $M_r(T)$ and

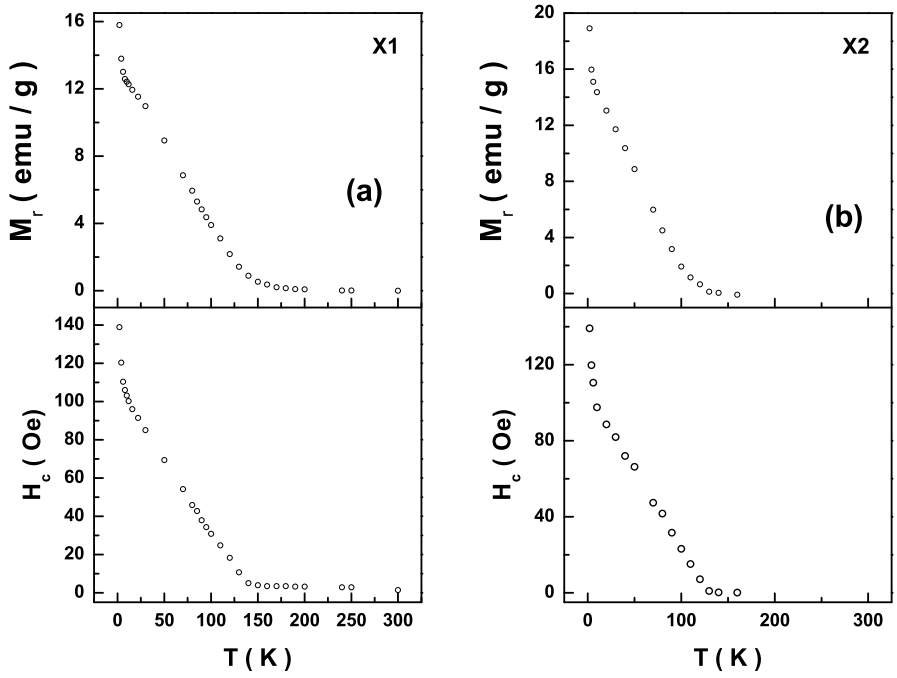

Figure 7.3: *The temperature dependence of remanent magnetization, M_r, and coercive field, H_c, for the samples (a) x1 and (b) x2, obtained from M-H loops presented in Fig. 7.1.*

$H_c(T)$ in $x1$ and $x2$ decrease at a faster rate till 6 K and then the rate slows down, and is roughly linear till $M_r = H_c = 0$ at T_C. This behaviour is similar to the thermal decline of magnetocrsytalline anisotropy constant [4]. Higher coercivity in $x2$ than in $x1$ signals the presence of stronger magnetocrystalline anisotropy in $x2$.

The temperature variation of M_r, that mimics the thermal dependence of spontaneous magnetization, M_S, is analyzed in terms of the power law

$$M_r(T) = B \left(\frac{T - T_C}{T_C}\right)^{\beta} \tag{7.1}$$

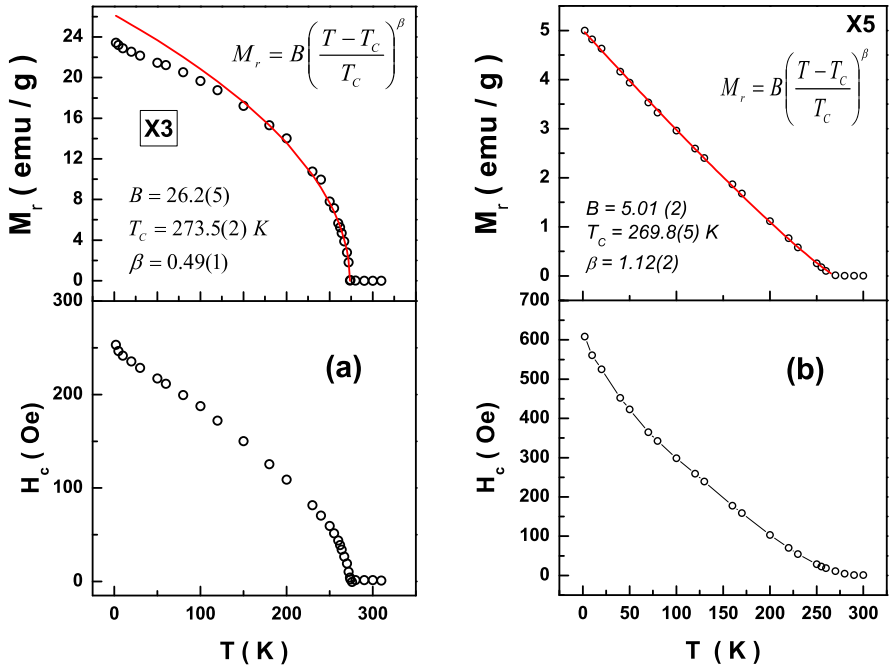

Figure 7.4: *The temperature dependence of remanent magnetization, M_r, and coercive field, H_c, for the samples (a) x3 and (b) x5, obtained from M-H loops presented in Fig. 7.2. The top panel show the fits based on Eq. (7.1)*

In Eq. (7.1), which holds for $M_S(T)$ in the asymptotic critical region, T_C is the critical temperature and β is the critical exponent of the order parameter. The fits to the $M_r(T)$ for $x3$ and $x5$, based on Eq. (7.1), and displayed in the top panels of Fig.7.4 yield $B = 26.2(5)$ emu/g, $T_C = 273.50(2)$ K and $\beta = 0.49(1)$ for $x3$ and $B = 5.01(2)$ emu/g, $T_C = 269.8(5)$ K and $\beta = 1.12(2)$ for $x5$. These values for T_C are in excellent agreement with those obtained from the analysis of 'zero-field' ac susceptibility in chapter 6. The value of $\simeq 0.5$ for the critical exponent β for $x3$ is also consistent with the results obtained in chapter 6 wherein an elaborate analysis of the

ac susceptibility clearly demonstrates that the sample $x3$ behaves as a three-dimensional uniaxial dipolar ferromagnet in the asymptotic critical region. In contrast, β in $x5$ possesses a value that does not belong to any universality class. This result is consistent with in-field magnetization analysis discussed in chapter 6.

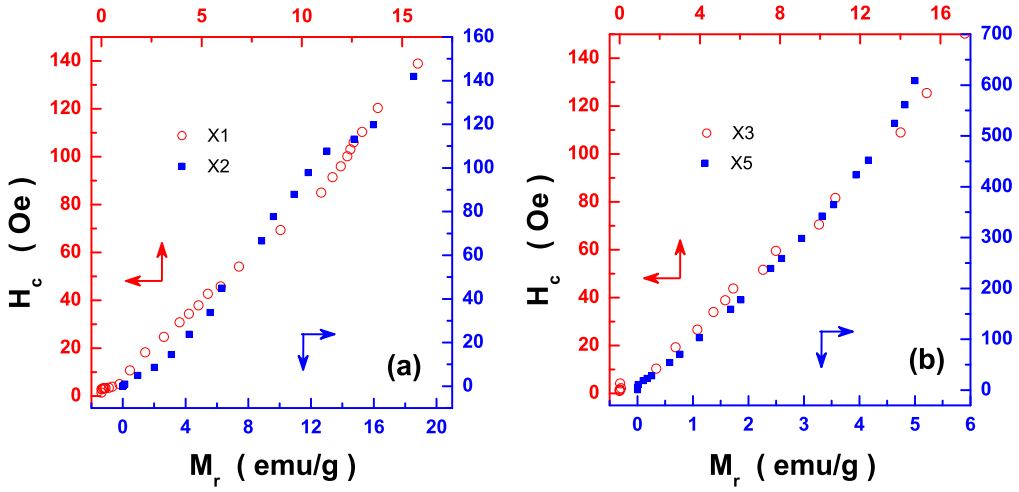

Figure 7.5: *The scaling of the coercive field, $H_c(T)$, with remanent magnetization, $M_r(T)$, for the samples (a) x1 and x2 and (b) x3 and x5.*

Figure 7.5 displays that $H_c(T)$ scales with $M_r(T)$ for $x1$, $x2$, $x3$ and $x5$. This observation strongly indicates that the anisotropy energy barriers play a crucial role in the magnetization reversal process.

7.3.2 Magnetic irrevesibility

In order to quantify the effect of size reduction on the magnetic properties in $x1$, a comparison with the bulk counterpart [5] is displayed in Fig.7.6.

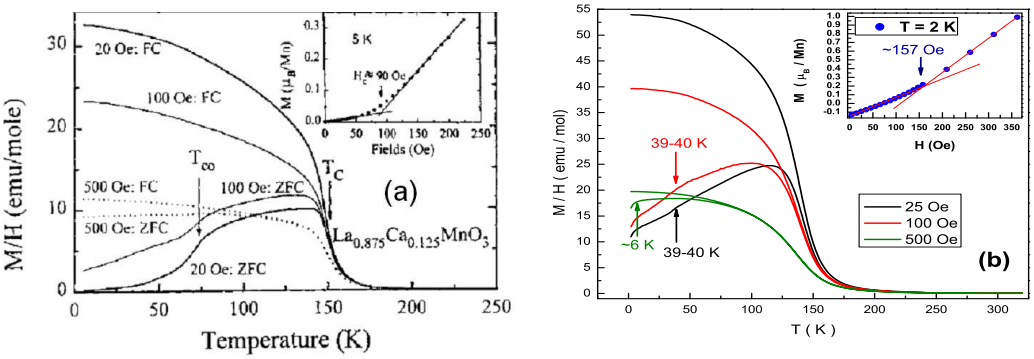

Figure 7.6: *The temperature variations of susceptibility, $\chi = M/H$, for x1 in the (a) bulk [5] (b) nanocrystalline state.*

The following observations are noteworthy. The charge order temperature, T_{CO}, and the ferromagnetic-paramagnetic phase transition temperature, T_C, reduces from 80 K to 40 K and 150 K to 143 K, respectively. The CO features are suppressed and transition becomes broader in the nanocrystalline system. An anomaly at 6 K is observed in $x1$ that is absent in the bulk. The critical field, H_{cr}, beyond which the irreversible domain wall motion governs the functional dependence of magnetization on field increases from 90 Oe (at 5 K) to 157 Oe (at 2 K) and magnetization at 2 K and 100 Oe is ~ 1.7 higher than in the bulk [5]. Although the shape of the $M(T)$ curves recorded at 100 Oe on $x1$ and its bulk counterpart [6] is similar, magnetization at 2 K is higher by a factor of $\simeq 3.8$ and the magnetic irreversibility is stronger in the former case.

$M(T)$ for $x3$ is similar to that in bulk at $H = 2$ kOe [7] while it is higher than the one reported in [25] at $H = 1$ kOe. The magnetic irreversibility in $x3$ depicted in Fig.7.8 shows an unusual feature around T_C. Contrary

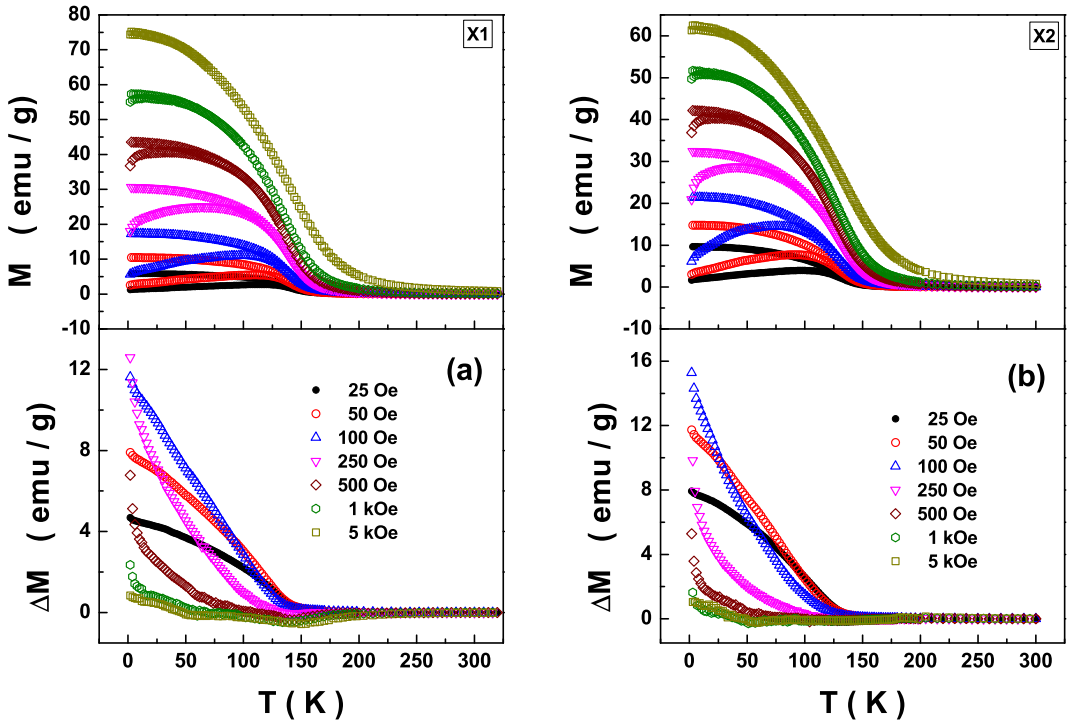

Figure 7.7: *The temperature variations of 'zero-field-cooled' (ZFC) and 'field-cooled' (FC) magnetizations, and magnetic irreversibility* $\Delta M(T)$=$M_{FC}(T) - M_{ZFC}(T)$ *for the samples (a)* $x1$ *and (b)* $x2$*, at low static fields.*

to the usual observation that the irreversibility in magnetization, $\Delta M(T) = [M_{FC}(T) - M_{ZFC}(T)] > 0$ at all H where ΔM is finite, $\Delta M(T) < 0$ and exhibits a (negative) dip at $T \simeq T_C$ whose magnitude increases with H. This observation asserts the coexistence of randomly-oriented insulating antiferromagnetic t_{2g}-spin clusters with the insulating e_g-spin ferromagnetic matrix for $T < T_C$, in the FC state and the coexistence of FM insulating clusters with the paramagnetic matrix that consists of randomly-oriented insulating antiferromagnetic clusters, in the ZFC state. This observation

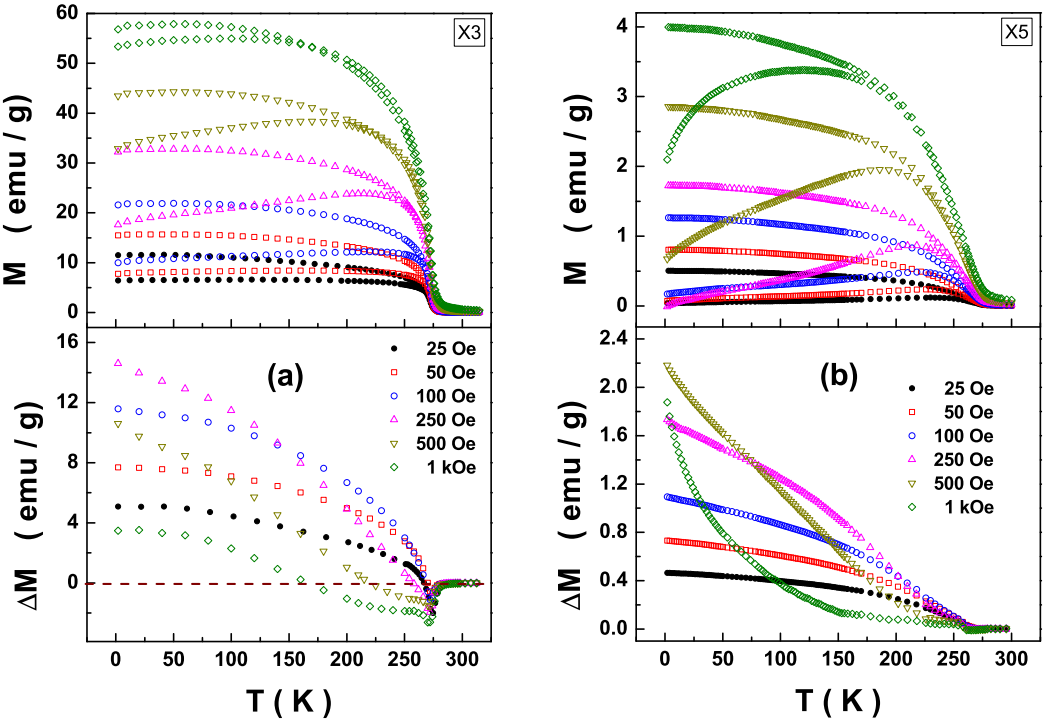

Figure 7.8: *M(T) in ZFC and FC modes and magnetic irreversibility, ΔM, at different static fields for the samples (a) x3 and (b) x5.*

is consistent with the presence of short-range/dynamic CE-type charge-ordered phase (consisting of FM zigzag chains that couple antiferromagnetically with each other) in the high temperature region reported [7, 9] earlier. At high temperatures, the spatial or temporal fluctuation of CO is such that the short-range CO state may contain only one short FM 'zigzag' $Mn^{3+} - Mn^{4+} - Mn^{3+} - Mn^{4+} - Mn^{3+}$ with 11 $\mathring{A}$ in length or one short FM 'zig or zag' ($Mn^{3+} - Mn^{4+} - Mn^{3+}$) with 5.5 $\mathring{A}$ in length. These extended objects enhance the overall FM correlation. The short FM zigzag can be considered as correlated FM polarons which could exhibit dynamic

nature [9]. The $M(T)$ curves in $x5$ resemble that of a conventional ferromagnet in contrast to the bulk that exhibits a CO transition at 270 K and an antiferromagnetic transition of CE-type at 150 K, characterized by a drop and a kink in the magnetic susceptibility, respectively [10]. In $x5$, $M(T)$ is larger by at least an order than that in the bulk at $H = 1\ kOe$ [10] and at $H = 1\ kOe$ for $x = 0.63$, suggesting that the grain size reduction results in the enhancement of FM behaviour at the expense of CO. Another important observation is that $\Delta M(T)$ at 250 Oe/250 Oe in $x1/x2$, 100 Oe in $x3$ and 500 Oe in $x5$ mimics the corresponding $H_c(T)$. That $\Delta M(T) \sim H_c(T)$ underscores the common origin of the irreversibility in magnetization and coercivity in the competition between the external field and anisotropy field.

Magnetic susceptibility, in the paramagnetic state, obeys the Curie-Weiss law,

$$\chi(T) = \frac{C}{T - \theta} \tag{7.2}$$

where $C = N\mu_{eff}^2/3k_B$ is the Curie constant with N, the number of magnetic ions per unit volume, μ_{eff}, the high-temperature magnetic moment and k_B, the Boltzmann constant. The paramagnetic Curie temperature, θ, is positive for ferromagnets. The theoretical high-temperature moment has been estimated using the formula $(\mu_{HT}^{th})^2 = [(1-x)g^2 S_{Mn^{3+}}(S_{Mn^{3+}}+1) + xg^2 S_{Mn^{4+}}(S_{Mn^{4+}}+1)]\ \mu_B^2$ with Landé factor $g = 2$, $S_{Mn^{3+}} = 2$, $S_{Mn^{4+}} = 3/2$ and x, the doping concentration. It follows that $\mu_{HT}^{th} = \sqrt{(24 - 9x)}$ in units of μ_B. The low-temperature moment is calculated from the magnetization value at 2 K and 90 kOe on the virgin curve. The corresponding theoretical estimate is given by $\mu_{LT}^{th} = [(1-x)gS_{Mn^{3+}} + xgS_{Mn^{4+}}]\ \mu_B$ resulting in $\mu_{LT}^{th} = (4-x)\ \mu_B$ with doping concentration x. The Griffith's temperature,

T_G, below which χ^{-1} shows a downturn when approaching T_C from above is also displayed in table 7.1. It is noticed that $M(2\ K, 90\ kOe)$ in $x1$, $x2$, $x3$

Table 7.1: *Comparison between the parameters, extracted from the magnetization data, and the corresponding values expected from the theoretical considerations based on the concentration of Mn^{3+}/Mn^{4+} ions*

	$x1$	$x2$	$x3$	$x5$
μ_{LT}^{th} (μ_B)	3.875	3.875	3.625	3.375
μ_{LT}^{obs} (μ_B)	3.46	3.30	3.165	0.59
μ_{HT}^{th} (μ_B)	4.783	4.783	4.542	4.287
μ_{HT}^{obs} (μ_B)	6.48	5.72	6.07	2.71
C $(10^{-2}$) (emu K/g Oe)	2.29	1.79	2.25(5)	0.51(1)
θ (K)	187(1)	194(2)	270(1)	270(4)
T_C (K)	143.13(3)	134.10(2)	273.50(2)	270.00(5)
$T_G^{H=0}$ (K)	270(2)	275(1)	285(2)	298(2)

and $x5$ reaches only 89%, 85%, 87% and $\sim$ 18% of the values theoretically predicted for a collinear ferromagnet. This observation indicates a much weaker spin canting at low temperatures in $x1 - x3$ compared to that in $x5$. However, the observed high-temperature magnetic moments in $x1$, $x2$, $x3$ and $x5$ are 1.36, 1.20, 1.34 and 0.63 times larger than those theoretically expected. This result underscores the presence of FM correlations/magnetic

polarons in $x1$, $x2$, $x3$ as opposed to the AFM/CO correlations in $x5$ in the paramagnetic insulating state. The low-temperature moments in $x1$ and $x2$ are higher than in the bulk [2, 19] and so also the Curie constants [12, 19]. $M(T)$ in $x1$ at $H = 5\ kOe$ is comparable in magnitude to that reported in bulk [16]. $T_C = \theta$ for $x1$ in the bulk [1]. The low-temperature moment in $x3$ is slightly smaller than that in the bulk [14] but definitely higher than the nanocrstalline sample [3], reported recently. The order parameter critical exponent of 0.33 in contrast to the present case of 0.5. For $x5$, $\mu_{LT}^{obs} << \mu_{LT}^{th}$ indicates large canting in the spin structure or presence of an antiferromagnetic ordering at low temperatures while $\mu_{HT}^{obs} < \mu_{HT}^{th}$ implies the presence of non-interacting (randomly oriented) antiferromagnetic clusters in the paramagnetic insulating state. Moreover, $\theta \lesssim T_C$ indicates that the first-order nature of the magnetic phase transition. The inflection point of M_{FC} stays constant at 260 K for magnetic fields 50 $Oe - 500\ Oe$ while that in M_{ZFC} starts at 268 K for 25 Oe and decreases to 260 K at 1 kOe. The temperature at which a dip in the temperature derivative of M_{FC} occurs, T_{dip}, has a field dependence that yields upon extrapolation to $H = 0$ the value of T_{dip} $(H = 0)$ that matches with the one obtained from the $M_S(T)$ analysis presented in chapter 6. This clearly demonstrates that the in-field magnetic phase transition in $x5$ is unconventional/first-order-like. In contrast, T_{dip} $(H = 0)$ equals the Curie temperature obtained from the ac susceptibility analysis (chapter 6). This observation asserts that the FM-PM phase transition in $x1 - x5$ is a continuous second-order phase transition in zero-field and, as shown in chapter 6, these samples behave as an uniaxial dipolar ferromagnet in the critical region.

7.3.3 Low-lying magnetic excitations: spin waves

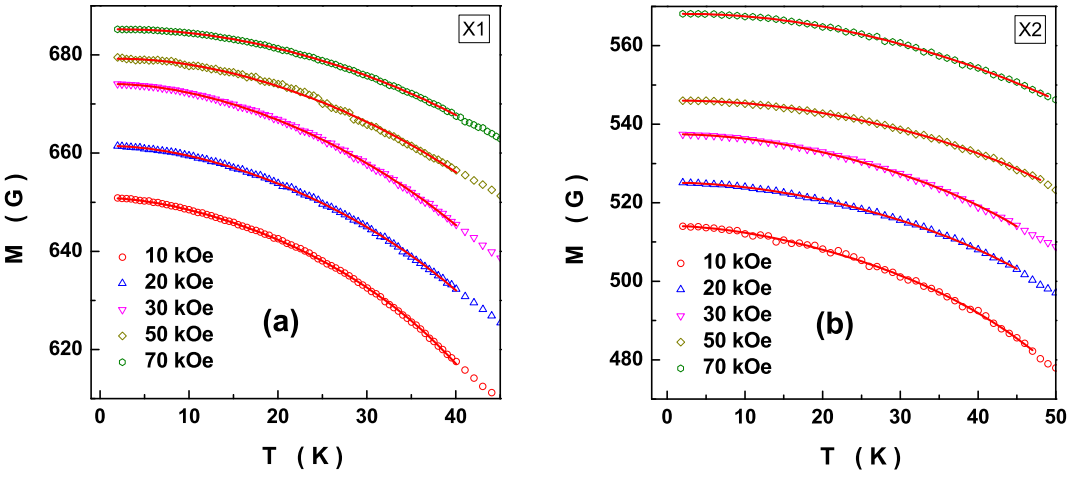

Figure 7.9: *Thermal decline in magnetization at high fields along with the corresponding spin-wave fits (continuous curves), based on Eq.(7.3), at low temperatures for (a) x1 and (b) x2.*

The thermal decline in magnetization up to $T = 50K$ at magnetic fields in the range $10kOe \leq H \leq 70kOe$, shown in figure 7.9(a), demonstrates that, regardless of H, M is higher at all the temperatures for $x1$. The magnetization at low temperatures is fitted to the conventional spin-wave (SW) relation for magnetization in a three-dimensional Heisenberg ferromagnet

$$M(T,H) = M(0,H) - g\mu_B \; Z\left(\frac{3}{2}, t_H\right) \left[\frac{k_B T}{4\pi D(T)}\right]^{3/2} \tag{7.3}$$

where the Bose-Einstein integral function

$$Z(\frac{3}{2}, t_H) = \xi(3/2)F(3/2, t_H) = \sum\nolimits_{n=1}^{\infty} n^{-\frac{3}{2}} exp(-nt_H) \tag{7.4}$$

with $\xi(3/2)$, the Riemann zeta function, $t_H = g\mu_B H/k_B T$ allows for the energy gap in the spin-wave spectrum. The thermal renormalization of

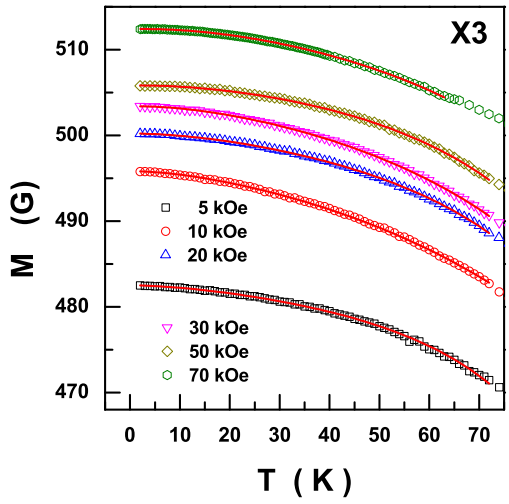

Figure 7.10: *Spin-wave description (continuous curves) of the observed low-temperature and high-magnetic field magnetization of x3.*

spin-wave stiffness in conventional localized/itinerant-electron ferromagnets occurs in accordance with the relation

$$D(T) = D(0)\ [1 - D_2 T^2 - D_{5/2} T^{5/2}] \tag{7.5}$$

where $D(0)$ is the spin-wave stiffness at $T = 0\ K$ and the $T^{5/2}$ (T^2) term arises from the *direct* (*indirect*) magnon-magnon interactions (mediated by conduction-electron spins). That Eq.(7.3) along with the $T^{5/2}$ term in Eq.(7.5) adequately describes the observed $M(T, H)$ variation is obvious from the quality of the SW fits (continuous curves) to the data (symbols) shown in figures 7.9 and 7.10. Excitation of spin waves costs much higher thermal energy in $x2$ since $D(0)$ is larger ($D(0) = 45(3)\ meV\mathring{A}^2$) in $x2$ than ($D(0) = 35(2)\ meV\mathring{A}^2$) in $x1$. The spin-wave stiffness $D(0) = 145(5)\ meV\mathring{A}^2$ in $x3$. These values of spin-wave stiffness are comparable

to their corresponding values in the bulk counterparts determined from the inelastic neutron scattering experiments [1, 15]. $M\ (T, H)$ for $x5$ could not be analyzed using the spin-wave expression, Eq.(7.3), as it shows an upturn in magnetization at temperatures below $T_N = 50\ K$. However, the magnetization at $T < 50\ K$ could be described well by the expression $M(T, H) = M(0, H)\ (1 - a\ T^{1/2})$.

7.4 Conclusion

The estimated low-temperature magnetic moments suggest a canted spin structure at low temperatures while high-temperature moments confirm the presence of small ferromagnetic clusters in the paramagnetic state. For $x1$, $x2$ and $x3$, spin wave stiffness has values comparable to those for the bulk counterparts. In all the samples studied, the temperature dependence of the (uniaxial) magnetocrystalline anisotropy energy barriers is basically responsible for the observed temperature variations of the remanence, coercive field and irreversibility in magnetization. Reducing the average crystallite size to nanometer regime brings about the following changes. (i) Larger spin wave stiffness in $x2$ than in $x1$ indicates the strengthening of magnetocrystalline anisotropy caused by oxygen off-stoichiometry. (ii) Presence of randomly oriented antiferromagnetic t_{2g}-spin clusters within the insulating ferromagnetic matrix at $T \lesssim T_C$ in $x3$. (iii) Charge ordered phase gets suppressed and ferromagnetic order appears in $x5$.

References

1. G. Biotteau, M. Hennion, F. Moussa, J. Rodríguez-Carvajal, L. Pinsard, A. Revcolevschi, Y. M. Mukovskii and D. Shulyatev, *Approach to the metal-insulator transition in* $La_{1-x}Ca_xMnO_3$ $(0 \leq x \leq 0.2)$*: Magnetic inhomogeneity and spin-wave anomaly*, Phys. Rev. B **64**, 104421 (2001).

2. S. Begum, Y. Ono, Y. Tomika, Y. Tokura, Y. Ishii, Y. Morii and T. Kajitani, *Jahn-Teller distortion and cluster-glass like behavior in* $La_{0.875}Ca_{0.125}MnO_3$, J. Phys. Chem. Sol. **63**, 939 (2002).

3. Chetan Dhital, Clarina de la Cruz, C. Opeil, A. Treat, K. F. Wang, J.-M. Liu, Z. F. Ren and Stephen D. Wilson, *Neutron scattering study of magnetic phase separation in nanocrystalline* $La_{5/8}Ca_{3/8}MnO_3$, Phys. Rev. B **84**, 1444401 (2011).

4. V. Likodimos and M. Pissas, *Phase coexistence and magnetic anisotropy in* $La_{1-x}Ca_xMnO_3$ *(*$0 \leq x \leq 0.23$*) studied via electron spin resonance*, Phys. Rev. B **76**, 024422 (2007).

5. S. -W. Cheong and H. Y. Hwang, *Ferromagnetism vs. Charge/Orbital Ordering* in Ch. 7 *Colossal Magnetoresistive Oxides*, (ed. Y. Tokura, Gordon and Breach, 2000.)

6. M. Pissas and G. Papavassiliou, *The phase diagram and magnetic properties of* $La_{1-x}Ca_xMnO_3$ *compounds for* $0 \leq x \leq 0.23$, J. Phys.: Condens. Matter **16**, 6527 (2004).

7. K. H. Kim, M. Uehara, C. Hess, P. A. Sharma and S. -W. Cheong, *Thermal and Electronic Transport Properties and Two-Phase Mixtures in* $La_{5/8-x}Pr_xCa_{3/8}MnO_3$, Phys. Rev. Lett. **84**, 2961 (2000).

8. J. A. Collado, C. Frontera, J. L. García-Muñoz and M. A. G. Aranda, *Effect of cation site-disorder on the structure and magneto-transport properties of* $Ln_{5/8}M_{3/8}MnO_3$ *manganites*, J. Solid State Chem. **178**, 1949 (2005).

9. K. H. Kim, M. Uehara and S. -W. Cheong, *High-temperature charge-ordering fluctuation in manganites*, Phys. Rev. B **62**, 11945 (2000).

10. T. Katsufuji, S. -W. Cheong, S. Mori and C. -H. Chen, *Impurity Effects on the Electronic/Magnetic Ground States of Perovskite Manganites*, J. Phys. Soc. Jpn. **68**, 1090 (1999).

11. E. Bose, S. Karmakar, B. K. Chaudhuri, S. Pal, C. Martin, S. Hébert and A. Maignan, *Anomalous thermal properties and local lattice effects in low doped manganites* $La_{0.875}Ca_{0.125}MnO_3$ *and* $La_{0.875}Ca_{0.0625}Sr_{0.0625}MnO_3$, J. Phys. D: Appl. Phys. **40**, 3728 (2007).

12. M. Castro, R. Burriel and S. -W. Cheong, *Magnetic and heat-capacity anomalies of* $La_{7/8}Ca_{1/8}MnO_3$, J. Magn. Magn. Mater. **196-197**, 512 (1999).

13. H. Fujishiro, T. Fukase, M. Ikebe and T. Kikuchi, *Sound Velocity Anomaly at around* $X \approx 1/8$ *in* $La_{1-X}Ca_XMnO_3$, J. Phys. Soc. Jpn. **68**, 1469 (1999).

14. M. Uehara, S. Mori, C. H. Chen and S. -W. Cheong, *Percolative phase separation underlies colossal magnetoresistance in mixed-valent manganites*, Nature **399**, 560 (1999).

15. J. J. Rhyne, H. Kaiser, L. Stumpe, J. F. Mitchell, T. McCloskey and A. R. Chourasia, *Composition dependence of the spin wave stiffness parameter in $La_{1-x}Ca_xMnO_3$ CMR materials*, J. Magn. Magn. Mater. **226 – 230**, 775 (2001).

Chapter 8

Electrical and magneto-transport properties

The transport and magneto-transport properties of the nanomanganite $La_{1-x}Ca_xMnO_{3\pm\delta}$ ($x = 1/8, 3/8, 5/8$) system have been studied treating the bulk counterpart as the reference system. Resistivity data have been analyzed in the light of existing theoretical models. It is shown that these properties get drastically affected upon crystallite size reduction.

8.1 Introduction

The electronic properties of manganites are governed by competing $Mn^{3+} - O - Mn^{3+}$ superexchange and $Mn^{3+} - O - Mn^{4+}$ double-exchange interactions, local Jahn-Teller distortions, charge ordering and phase separation effects. In various CMR compounds, adiabatic nearest-neighbhour hopping (NNH) conductivity of small polarons that obey the Arrhenius law, is observed above room temperature [1, 2]. In $La_{1-x}Ca_xMnO_3$ (LCMO), this

behaviour persists up to $T \sim 700\ K$ [3] or even up to temperatures as high as 1200 K [4]. Below room temperature, the hopping conductivity is strongly influenced by features of the density of the localized states (DOS), $g(\epsilon)$, near the Fermi level, ϵ_F [5].

The soft gap is attributed to Coulomb interactions (and referred to as the Coulomb gap [6]) between localized charge carriers while the rigid gap is associated with the Jahn-Teller effect [7]. Generally, when temperature is decreased it is energetically favorable for charge carriers to hop beyond the nearest-neighbor sites, leading to the variable-range hopping (VRH) conductivity [8]. The Mott VRH conductivity sets in when the DOS around ϵ_F is finite and constant [8], whereas the soft Coulomb gap leads to another type of deviation from the Arrhenius law, i.e., the Shklovskii-Efros (SE) VRH conductivity [6]. In turn, the rigid gap modifies the SE-VRH conductivity law [5].

In the high temperature regime, i.e., at $T > T_C$, LCMO is usually a paramagnetic insulator (PMI). In this regime, electric conductivity is governed by electrons hopping through a dielectric insulator. There are three possible mechanisms for conduction in this regime, each supported by some experimental evidence: 1) the thermally-activated hopping model [9], 2) the nearest-neighbour hopping model [3] and 3) the variable range hopping (VRH) model [10]. Since the experimental observations are carried out in a narrow temperature range just above T_C it is sometimes very difficult to distinguish between the three mechanisms. Consequently, there is no agreement regarding the mechanism actually prevalent in these systems.

8.2 Insulating/semiconducting regime

8.2.1 Thermally activated carriers

In this model, the carriers are thermally excited across the band gap from the valence band to a conduction band. The resistivity ρ follows the Boltzmann law, i.e., (8.1), where E is the energy gap and ρ_∞ is the resistivity at infinite temperature.

$$\rho = \rho_\infty \; exp(E/k_B T) \tag{8.1}$$

This simple model is based on the resistivity given by $\rho = (ne\mu)^{-1}$, where n is the carrier density in the conduction band, e is the charge of an electron and μ is the carrier mobility. The dominant factor is normally the thermally activated form of n, and μ is assumed to be independent of temperature. In general, the mobility can have some temperature dependence, which would introduce additional factors into equation (8.1). If the conduction mechanism in the insulating paramagnetic and charge-ordered phases is due to thermally-activated carriers, the activation energy should be different for different phases. A transition from the paramagnetic to charge-ordered states thus shows up via a sudden change of gradient in the logarithm of resistance versus temperature curve.

8.2.2 Nearest-neighbour hopping

In this model, electrical conduction proceeds via polaron motion. A localized electron distorts its surrounding lattice relative to an unoccupied site because of the Coulombic interaction of the electron and the surrounding ions on the lattice and thus producing a potential well that acts as a trapping

center for the self-trapped carrier. Thus, a self-trapped electronic carrier together with the pattern of atomic displacements constitutes a polaron and when this quasi-particle moves as a whole, the electron propagates along with the lattice distortion. Long-range electron-lattice interactions produce large polarons with a finite radius, that decreases with the strength of electron-lattice interaction. The self-trapped electronic carrier extends over multiple sites and this multi-site extension of the large polaron results in its itinerant motion with large mobility (metallic-like). In contrast, small polarons are confined to a single lattice position due to strong short-range electron-lattice interaction. The extreme confinement of the small polaron typically leads to its motion by thermally-assisted hopping. One of these two different types of polarons is stable when both long-range and short-range electron-lattice interactions coexist [11]. The presence of long-range interactions eases the requirements for forming a small-polaron, but only once the interactions are sufficiently strong does the polaron change from large to small. In the paramagnetic-insulating state, e_g, electrons are thought to be associated with lattice distortions (i.e., they form polarons). In this model, the lattice distortions are of a size similar to unit cell and the polarons move between the nearest neighbour sites. The resistivity in this case is given by:

$$\rho = A\ T\ exp(E/k_B T) \tag{8.2}$$

where A is a constant and E is the energy required to move a polaron. However, the strong electron-polaron coupling in the $La_{1-x}Ca_xMnO_3$ permits a motion of the charge-carriers slower than the lattice vibration. The motion of the electrons and lattice cannot be separated so that in the non-adiabatic limit, the resistivity is given by [12]:

$$\rho = A\ T^{3/2}\ exp(E/k_B T) \tag{8.3}$$

8.2.3 Variable range hopping

If the activated energies for hopping to neighbouring atoms are not the same, hopping to a non-nearest neighbour may require a smaller activation energy. Mott variable range hopping (VRH) assumes a finite density of states at the Fermi energy level $N(E_F) \neq 0$ and localized electronic states near the Fermi energy, E_F. Resistivity due to Mott VRH is given by [8, 12, 13]

$$\rho = \rho_\infty \; exp(T_0/T)^{1/4} \tag{8.4}$$

where T_0 is a characteristic temperature. This mechanism is observed for doped smiconductors and non-crystalline insulating solids at low temperatures. The localization length, l_{VRH}, can be computed from T_0 by using the following expression

$$l_{VRH} = (\frac{171 U_m V}{k_B T_0})^{1/3}$$

As the distance of hopping grows $l > l_{VRH}$, direct tunneling becomes a dominant conduction process. Smaller localization length implies that the electron wavefunction is localized at Mn ions. Larger localization length implies that the electron wave function is more spread out. The localization length must be greater than the $Mn - O - Mn$ bond length, so that the electrons are not localized and can participate in conduction. T_0 is usually of the order of $10^7 K$ [14]. As T_0 decreases, the localization length (l_{VRH}) increases. As a result, the resistivity at peak temperature, T_p, and resistivity for the regime $T > T_p$ is reduced. Shklovskii-Efros (SE) variable range hopping [6] has the form

$$\rho = \rho_\infty \; exp(T_0/T)^{1/2} \tag{8.5}$$

which assumes a gap in the density of states brought in by the Coulomb interactions. The prefactors in Eqs.(8.4)-(8.5) can also have temperature

dependence. Eqs.(8.1)-(8.5) can be written in a more generalized form as

$$\rho(T) = \rho_0 \; T^p exp(T_0/T)^q.$$

The above expression reduces to thermal activation law (Eq.(8.1)) for $p = 0$ and $q = 1$, adiabatic small polaron hopping (Eq.(8.2)) for $p = 1$ and $q = 1$, non-adiabatic polaron (Eq.(8.3)) for $p = 3/2$ and $q = 1$, SE VRH (Eq.(8.5)) for $p = q = 1/2$ and Mott VRH (Eq.(8.4)) for $p = 0$ and $q = 1/4$, respectively.

8.3 Conducting/metallic regime

Electron transport (electrical resistivity) in the conducting regime is generally described by the expression [2]

$$\rho = \rho_0 + \rho_2 \; T^2 + \rho_n \; T^n \tag{8.6}$$

where ρ_0 is the residual resistivity, the second term denotes the contribution to resistivity due to electron-electron/coherent electron-magnon scattering while the third term with $n = 9/2$ and $n = 5$ represents contributions from the two-magnon and electron-phonon scattering.

8.4 Experimental details

Electrical resistivity was measured in both 'zero-field-cooled' (ρ^{ZFC}) and 'field-cooled' (ρ^{FC}) modes, analogous to earlier magnetization measurements, in zero and finite magnetic fields of $H = 10, 20, 30, 50, 70$ and $90kOe$, over the temperature range $2K \leq T \leq 310K$ on Quantum Design PPMS using the four-probe method.

8.5 Data analysis, results and discussion

8.5.1 Under hole-doped LCMO- $La_{0.875}Ca_{0.125}MnO_3$

The bulk sample is an insulator right up to the lowest temperature. The thermal dependence of sound velocity, sensitive to phase transitions, if any, exhibited two anomalies at 145 K and 170 K, where the resistivity versus temperature curve exhibited an upturn and a change of slope, corresponding to charge ordering (CO) and ferromagnetic (FM)-paramagnetic (PM) transition temperatures, respectively [16]. Resistivity as a function of temperature indicates a small decrease just below $T_C = 155\ K$, with an upturn below 110 K (signalling the occurrence of a small antiferromagnetic (AFM) component or residual canting) and it becomes more insulating at low temperatures with a structural transition at $T_{O'O''} = 80\ K$ [17]. It was concluded that the ordering of $d_{3x^2-r^2}$ and $d_{3z^2-r^2}$ orbitals below $T_{JT} = 100\ K$ results in a long-range AFM order. The presence of small FM clusters was revealed by the neutron diffraction study on bulk and single crystal samples [18]. For bulk samples, prepared by the solid-state reaction method, electrical resistivity continues to increase as temperature is lowered from room temperature, except for a small slope change at $T_C = 168\ K$ [19–21].

The effect of particle size reduction to nanometric dimensions on magnetic and transport properties of $La_{0.875}Ca_{0.125}MnO_{3.00}$ ($x1$) revealed that the 29 nm ($T_C = 147\ K$) and 55 nm samples ($T_C = 174\ K$) have resistivities higher than the bulk counterpart, at least, by two orders of magnitude at low temperatures. By contrast, the 45 nm sample ($T_C = 160\ K$), with metal(M)-insulator(I) transition at $T_{MI} = 153\ K$, has lower resistivity [22].

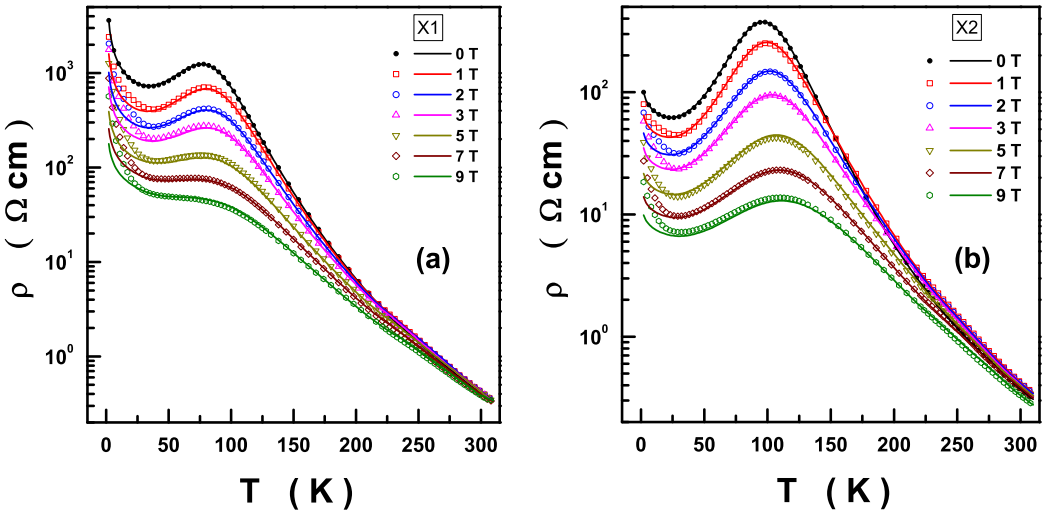

Figure 8.1: *'Zero-field-cooled' (symbols) and 'field-cooled' (lines) resistivity as functions of temperature at fixed magnetic fields for (a)* $La_{0.875}Ca_{0.125}MnO_{3.00}$ $(x1)$ *and (b)* $La_{0.875}Ca_{0.125}MnO_{3.06}$ $(x2)$.

The occurrence of the M-I transition was attributed to the breakdown of long-range AFM order and enhanced FM interactions via grain boundaries at the critical size of 45 nm. However, the oxygen off-stoichiometry of this sample is not known. That oxygen off-stoichiometry has profound effect on the electrical transport will be demonstrated in the present section.

As the temperature is lowered from 300 K, 'zero-field' electrical resistivity, $\rho(T)$, undergoes an insulator $(d\rho/dT < 0)$ to metal $(d\rho/dT > 0)$ transition at $T_{MI} = 97K$ $(77K)$ and exhibits a minimum (less prominent in $x1$) at $T_{min} \simeq 30K$ $(T_{min} \simeq 35K)$ in $x2$ $(x1)$ below which the system enters a 're-entrant semiconducting/insulating regime' (Fig.8.1). Such a resistivity upturn is absent in the bulk counterpart [21], that shows an insulating behaviour in the entire temperature range. The magnetic field tends to sup-

press these features and create a bifurcation in the 'zero-field-cooled' (ZFC, higher magnitude) and 'field-cooled' (FC, lower magnitude) $\rho(T)$ curves below the minimum that grows with H (Fig.8.1). T_{MI} and T_{min} shift to higher temperatures with increasing H. The $T_{min}(H = 0)$ has a value closer to the T_{CO}, obtained from $M(T)$ data at low static fields, in chapter 7. That at $T < T_{min}$, $\rho_H^{ZFC} > \rho_H^{FC}$ implies that, in the FC mode, H suppresses the magnon scattering contribution to $\rho(T)$ more effectively as H does not have to work against magnetocrystalline anisotropy. The most striking feature of the $\rho(T, H)$ curves in Fig.8.1 is that, regardless of the field, the oxygen off-stoichiometry reduces $\rho(T)$ at $T \leq T_{MI}$ by an order of magnitude. This is so because an increase in the concentration of Mn^{4+} ions due to oxygen off-stoichiometry promotes the metallic ferromagnetic double-exchange interaction at the expense of insulating antiferromagnetic super-exchange interaction and thus makes $x2$ more metallic in over a wider temperature range.

The resistivity data have been analyzed, independently, in two different temperature ranges, namely, $T < T_{MI}$ and $T > T_C$. The resistivity minima in both $\rho^{ZFC}(T)$ and $\rho^{FC}(T)$ around T_{min} are described well by the following expression

$$\rho = \rho_0 \; exp[(T_0/T)^{1/4}] - a_{1/2} \; T^{1/2} + a_2 \; T^2 + a_{9/2} \; T^{9/2} \qquad (8.7)$$

where the first term is the conventional Mott-VRH mechanism with T_0 reflecting the localization length of charge carriers, the second term represents the enhanced electron-electron interaction due to inherent disorder (leading to short mean free path) while the terms with the coefficients a_2 and $a_{9/2}$ denote the contributions from the electron-electron/electron-magnon scattering and two-magnon scattering, respectively [23]. The high-temperature

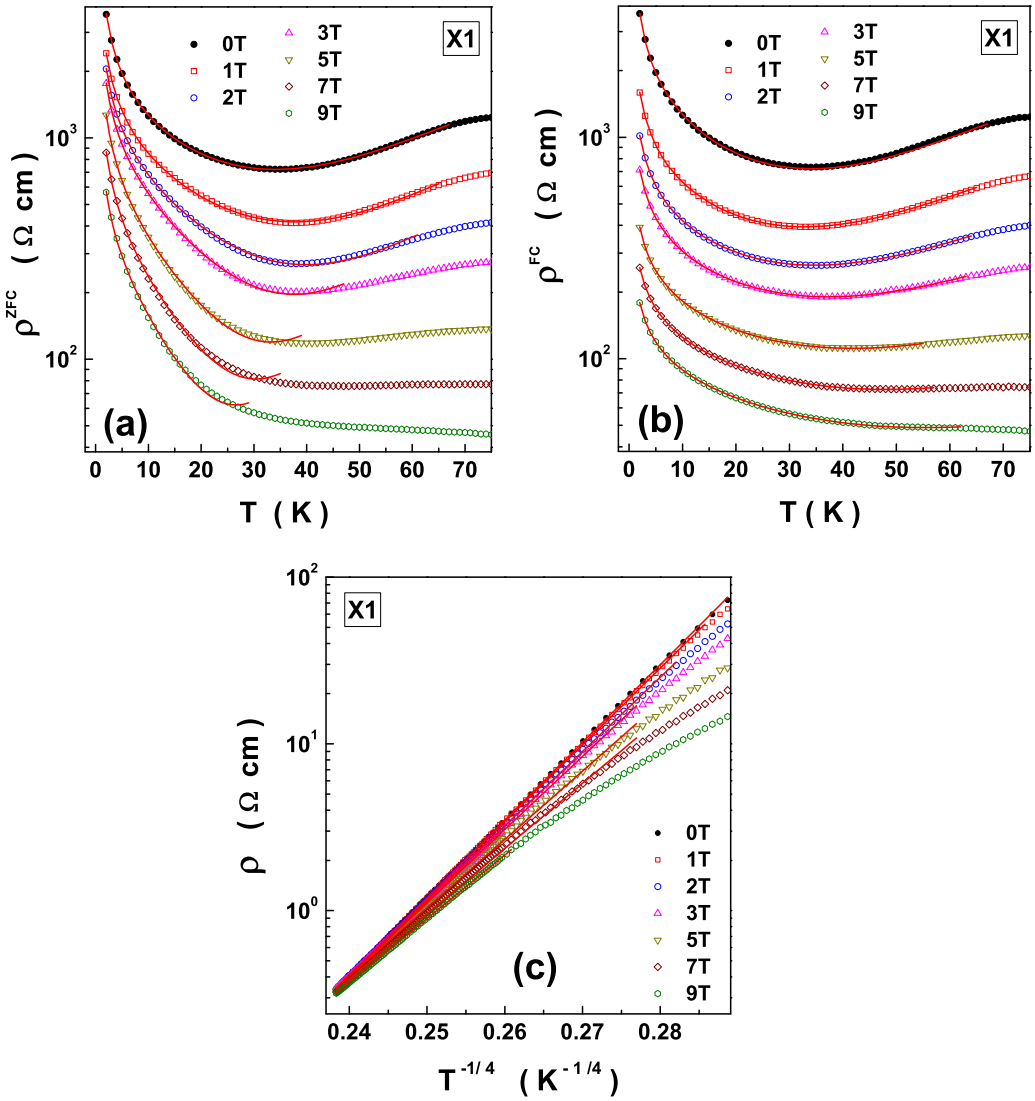

Figure 8.2: *Fits (continuous lines) to the low-temperature (a) 'zero-field-cooled' resistivity, ρ^{ZFC} and (b) 'field-cooled' resistivity, ρ^{FC}, of $x1$ around T_{min}, based on Eq.*(8.7)*. (c) For $T > T_C$, resistivity is adequately described by the conventional Mott VRH model, i.e., the first term in Eq.*(8.7)*.*

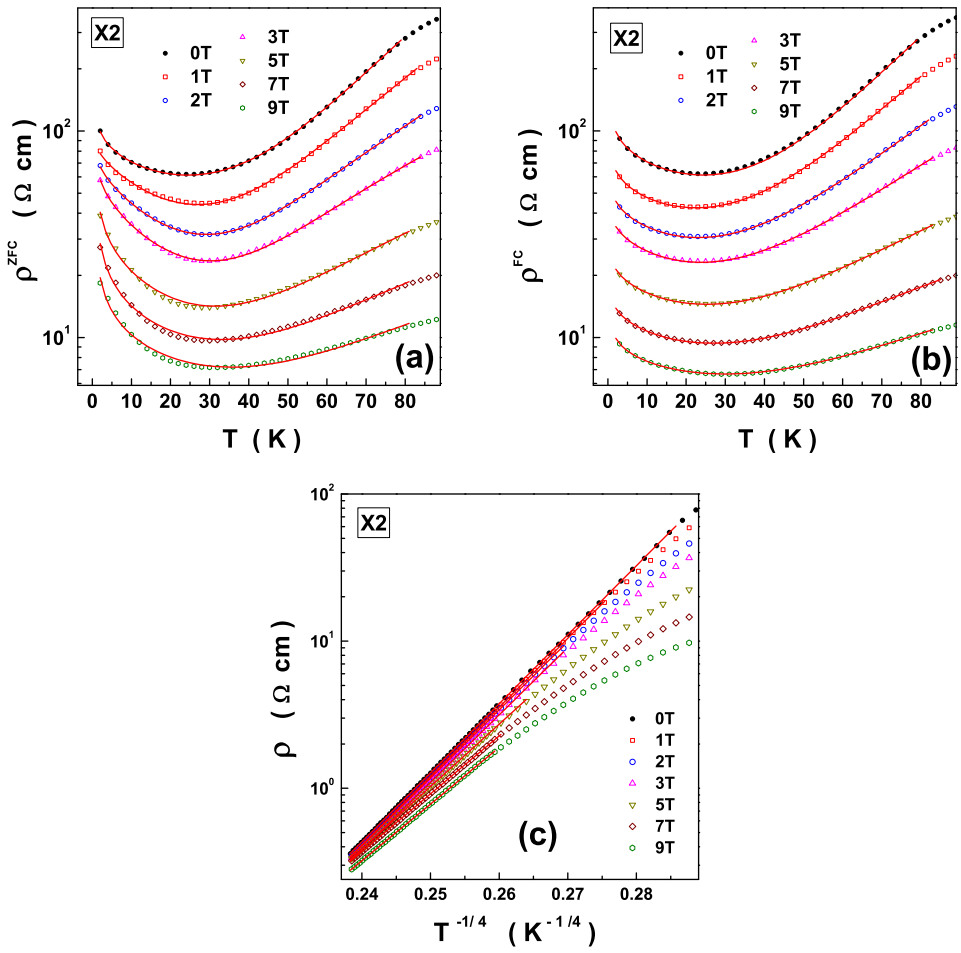

Figure 8.3: *Fits (continuous lines) to the low-temperature (a) 'zero-field-cooled' resistivity, ρ^{ZFC} and (b) 'field-cooled' resistivity, ρ^{FC}, of $x2$ around T_{min}, based on Eq.(8.7). (c) For $T > T_C$, resistivity is adequately described by the conventional Mott VRH model, i.e., the first term in Eq.(8.7).*

resistivity for both the samples $x1$ and $x2$ is well described by Mott-VRH model, i.e., by the relation

$$\rho = \rho_0 \; exp[(T_0/T)^{1/4}] \tag{8.8}$$

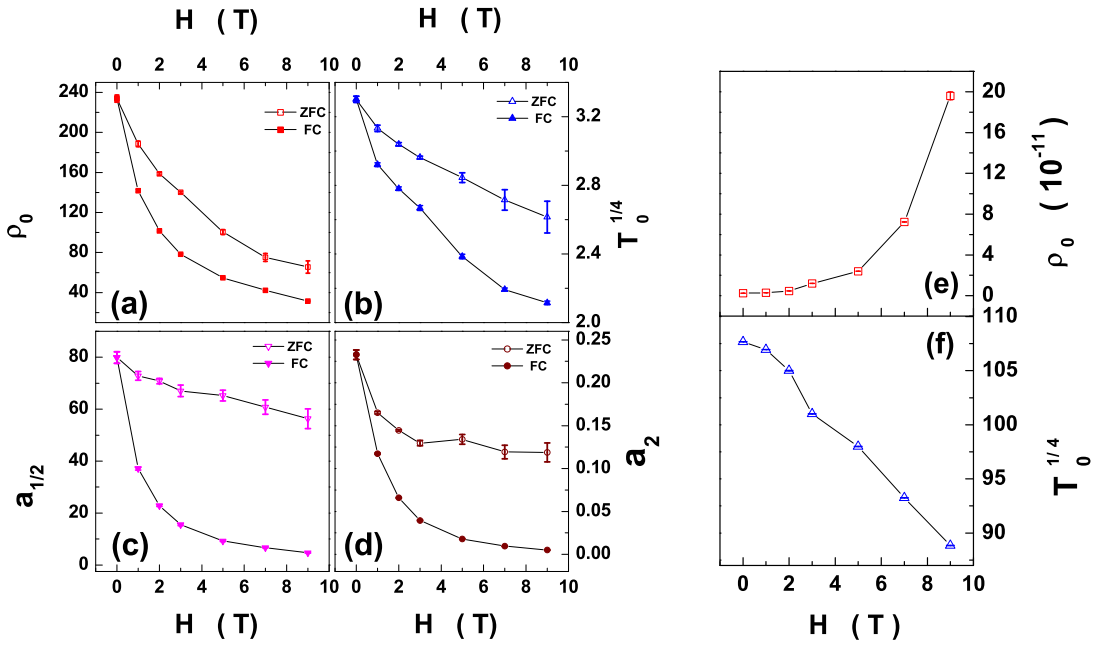

Figure 8.4: *(a)-(d) Fit parameters for ρ^{ZFC} and ρ^{FC}, below T_{min}. (e)-(f) The field variation of parameters, ρ_0 and $T_0^{1/4}$ in Eq.(8.8) for resistivity, of $x1$ at temperatures above T_C.*

The fits to the resistivity data at low temperatures around the minimum for both $x1$ and $x2$, based on equations (8.7)-(8.8), are presented in Figs.8.2 and 8.3, respectively, while the field variations of the corresponding fit parameters are shown in Figs.8.4 and 8.5. Based on the data presented in figures 8.1-8.5, the following observations can be made. The parameters ρ_0, $T_0^{1/4}$, $a_{1/2}$ and a_2 decrease with H more rapidly in the FC mode than in the ZFC mode, as shown in panels (a)-(d). This is so because the field overcomes the contribution to the resistivity resulting from the magnetocrystalline anisotropy more effectively in FC mode. Inclusion of the $a_{9/2}\, T^{9/2}$ term in the fits based on Eq.(8.7) led to only a marginal improve-

ment in the quality of fits and hence this term was dropped altogether. Parameter values for $x1$ are higher than those for $x2$ due to the fact that the former has an order of magnitude higher resistivity in the temperature ranges of interest. The reduction of parameters with applied field implies that the ferromagnetic-metallic clusters present in the insulating phase get polarized and percolate depending on field strength leading to the reduced in-field resistivity. The field variation of the parameters for $T > T_C$, shown in panels (e)-(f), are obtained by considering different temperature ranges. The variation of $T_0^{1/4}$, in both temperature regimes (FMI and PMI), with H implies that the localization length decreases as the field strength increases. The observed nature of resistivity mechanism in $x1$ and $x2$ is completely different from that in the bulk system where it follows the SE-VRH mechanism in a narrow temperature range above $T_C \approx 168\ K$ [20] with localization length $\sim 5.48\ \mathring{A}$ and $T_0 \approx 2.12 \times 10^4\ K$.

The irreversibility in resistivity due to magnetic field

$$\Delta\rho_{irr}(T)/H = (\rho^{ZFC}(T) - \rho^{FC}(T))/H \tag{8.9}$$

calculated below T_{min}, at various static fields, is displayed in figure 8.6. At 2 K, $\Delta\rho_{irr}(T, H)$ increases with H while it decreases with temperature at a fixed field. It reflects the degree of spin polarization at the grain boundaries leading to its reduced contribution to the total resistivity. Higher the value of $\Delta\rho_{irr}$, the weaker is the contribution of $T^{1/2}$ term. As localization increases, the influence of $T^{1/2}$ increases but the field tends to suppress this tendency. As expected, $\Delta\rho_{irr}$ is higher in sample $x1$.

As a result of the M-I transition, the negative magnetoresistance (MR), $\Delta\rho = (\rho(H) - \rho(0))/\rho(0)$, reaches a value of 96% for both $x1$ and $x2$ at

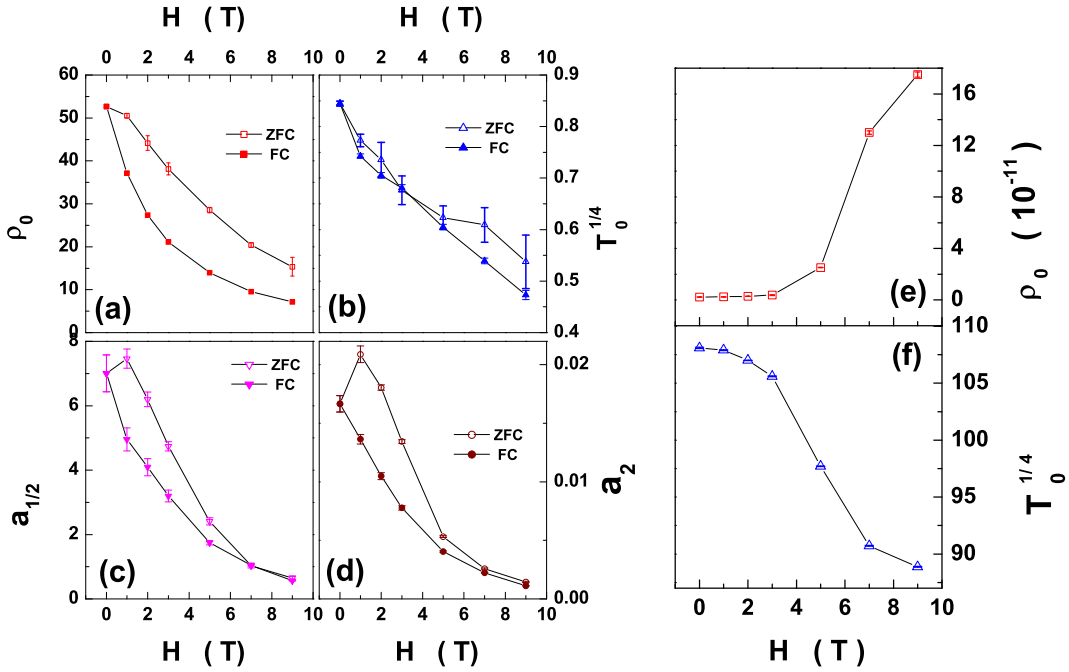

Figure 8.5: *(a)-(d) Fit parameters for ρ^{ZFC} and ρ^{FC}, below T_{min}. (e)-(f) The field variation of parameters, ρ_0 and $T_0^{1/4}$ in Eq.(8.8) for resistivity, of $x2$ at temperatures above T_C.*

$H = 90\ kOe$. MR is much higher than that in the bulk at a field of 70 kOe. In sharp contrast with the observations made on the nanocrystalline samples $x1$ and $x2$, as temperature is lowered, MR goes through a maximum at T_C with a value of 75% at a field of 70 kOe, shows an upturn at 115 K and decreases further below 50 K in the bulk counterpart [21]. This temperature variation of MR in bulk resembles that in the FC mode of the present samples but here upturn occurs at $T = 50\ K$ and MR attains its maximum value at a temperature which lies well below T_C. In ZFC mode, MR exhibits a continuous increase for temperatures below 50 K. Thus, the reduction in

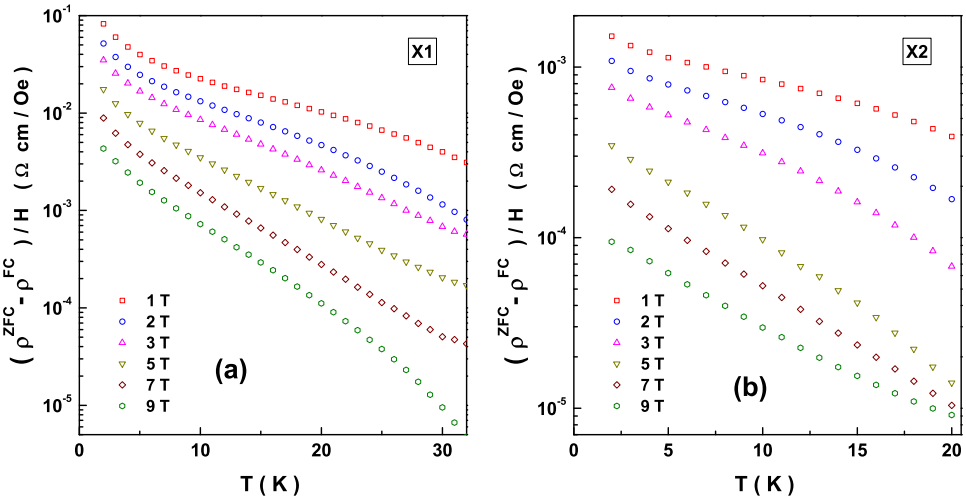

Figure 8.6: *The irreversibility in 'in-field' resistivity as a function of temperature below T_{min} for (a) $x1$ and (b) $x2$.*

the grain size to nanometre regime (i) induces the M-I transition with the re-entrant insulating behaviour at $T < T_{min}$, (ii) shifts the CO temperature to a lower value and (iii) changes the nature of the conductivity mechanism.

8.5.2 Optimally hole-doped LCMO - $La_{0.625}Ca_{0.375}MnO_3$

The bulk counterpart of the optimally hole-doped $LCMO$ (i.e., $La_{1-x}Ca_xMnO_3$ with $x = 3/8$) exhibits highest CMR effect at $T_C \sim T_{MI}$ where it undergoes ferromagnetic-metallic (FMM) to paramagnetic-insulating (PMI) phase transition [24–26]. It is also inferred that the PMI region consists of small FM correlated clusters, often termed as magnetic polarons. The effective medium approach was used to compute the total resistivity due to coexisting T- and H-dependent polaronic and band-electron fractions in

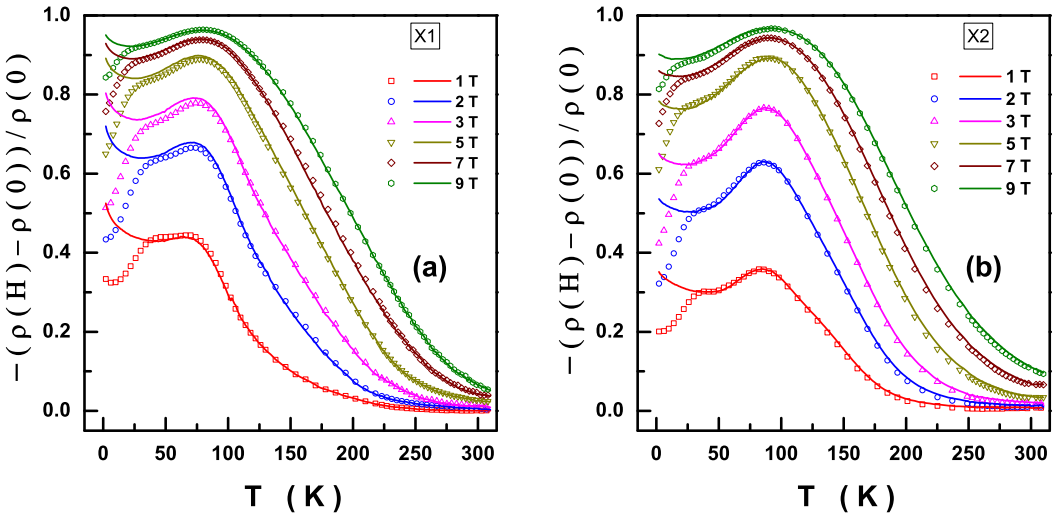

Figure 8.7: *The magnetoresistance in 'zero-field-cooled' (symbols) and 'field-cooled' (lines) modes as functions of temperature at various magnetic fields for (a) $x1$ and (b) $x2$.*

$x = 0.33$ [27] and $x = 3/8$ [28]. The activation energy associated with adiabatic small polaron hopping in PMI state for $x = 3/8$ is 125 meV.

From figure 8.8, it is clear that, as the temperature is decreased from $300K$, $\rho(T, H = 0)$ exhibits an abrupt slope change at T_C, undergoes an insulator-to-metal transition at $T_{MI} = 238.5\ K$ and goes through a shallow minimum at $T_{min} \simeq 30\ K$ in $x3$. The magnitude of resistivity in $x3$ is comparable to that in the bulk samples [29]. External magnetic field smears out the kink at T_C and creates a bifurcation between ρ_H^{ZFC} and ρ_H^{FC} below the T_{min} that grows with H. T_{MI} shifts to higher temperature with H while T_{min} differs within 1 K for ZFC and FC modes and shifts to lower temperatures. That at $T < T_{min}$, $\rho_H^{ZFC} > \rho_H^{FC}$ implies that, in the FC mode, H suppresses the electron-magnon scattering contribution to $\rho(T)$

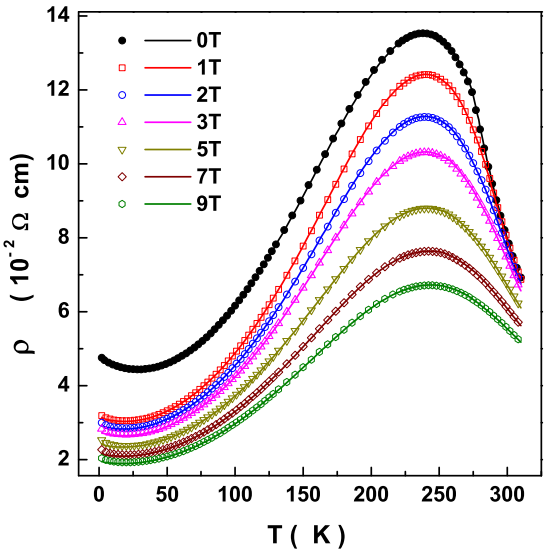

Figure 8.8: *'Zero-field-cooled' (symbols) and 'field-cooled' (lines) resistivities as functions of temperature at fixed magnetic fields for the composition* $La_{0.625}Ca_{0.375}MnO_3$ *(referred to as* $x3$*).*

more effectively.

The resistivity data have been analyzed in two different temperature ranges, namely, $T < T_{MI}$ and $T \geq T_C$. The low-temperature resistivity data are fitted over a temperature range $2\ K - 140\ K$ (that embraces the temperature region where the resistivity minima in both $\rho^{ZFC}(T)$ and $\rho^{FC}(T)$ are observed) by employing the following expression

$$\rho = \rho_0 - a_{1/2}\ T^{1/2} + a_2\ T^2 \tag{8.10}$$

In the high-temperature region ($T \geq T_C$), resistivity is well described by Eq. (8.8).

The fits to the resistivity data for $x3$ based on equations (8.10) and

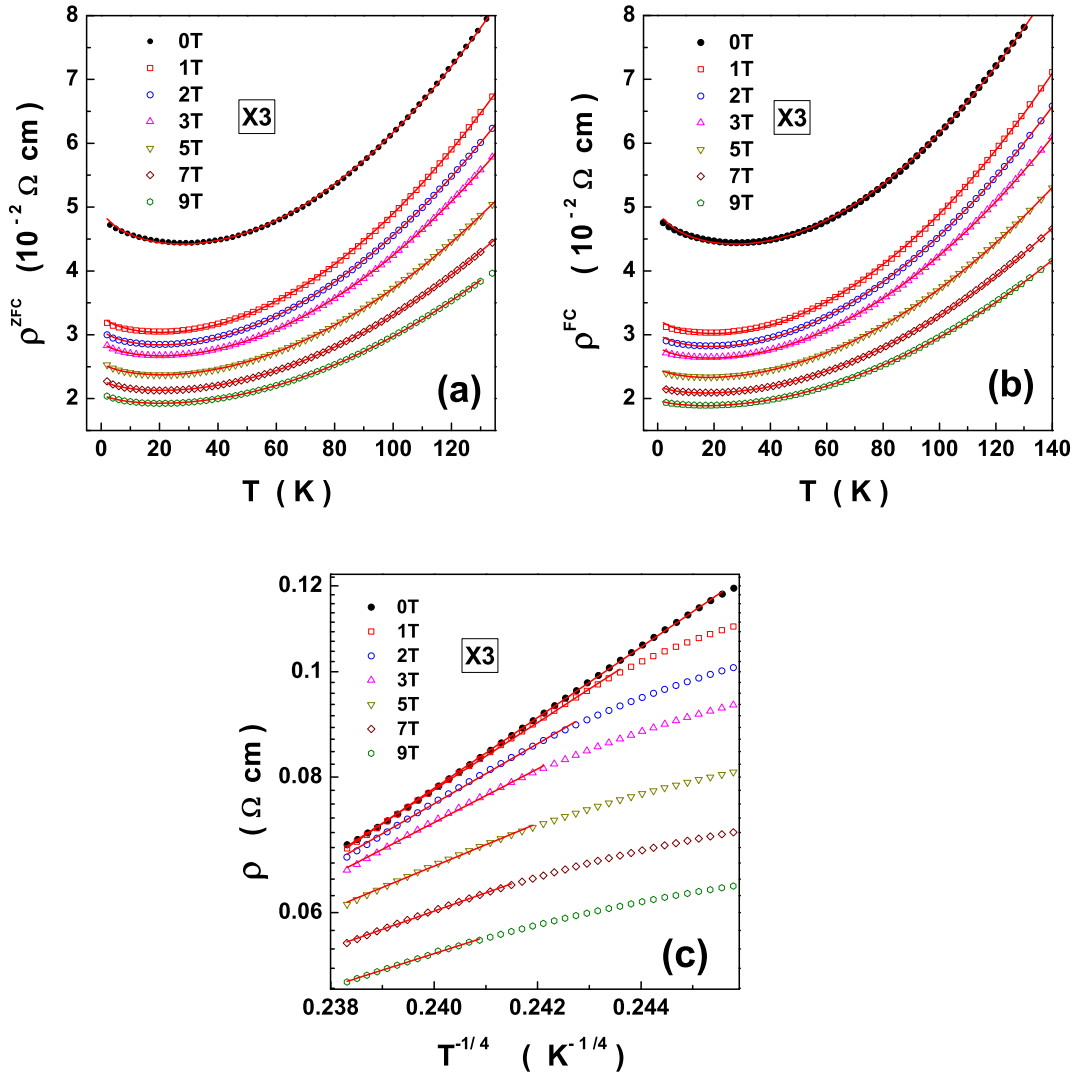

Figure 8.9: *Fits (continuous lines) to the low-temperature (a) 'zero-field-cooled' resistivity, ρ^{ZFC} and (b) 'field-cooled' resistivity, ρ^{FC}, of $x3$ around T_{min}, based on Eq.*(8.10)*. (c) For $T > T_C$, resistivity is adequately described by the conventional Mott VRH model, Eq.*(8.8)*.*

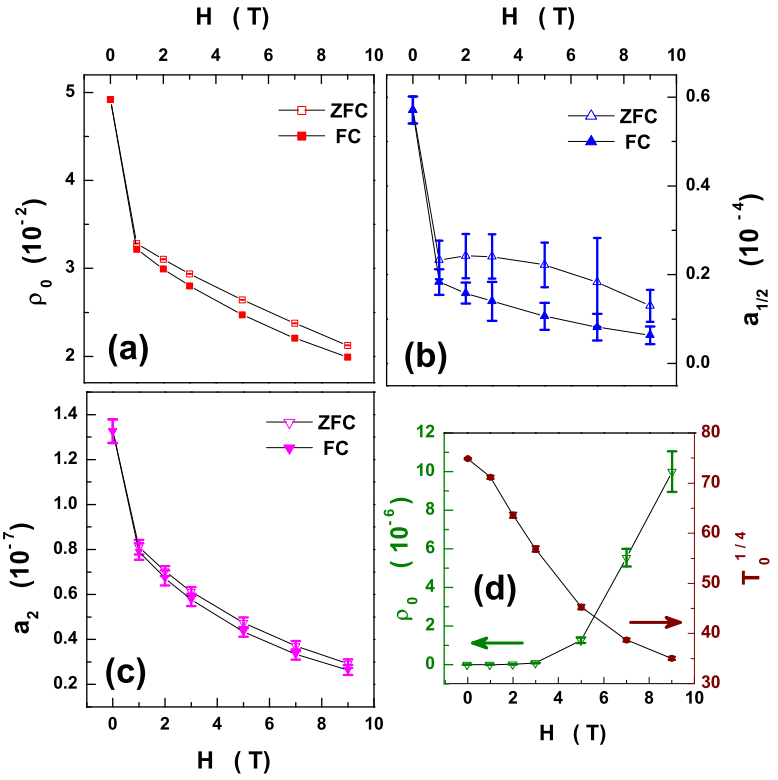

Figure 8.10: *(a)-(c) Fit parameters for ρ^{ZFC} and ρ^{FC}, below T_{min}. (d) The field variation of parameters ρ_0 and $T_0^{1/4}$ in Eq.(8.8) for resistivity in $x3$ at temperatures above T_C.*

(8.8) are presented in Fig.8.9 while the field variations of the corresponding fit parameters are shown in Fig.8.10. The parameters ρ_0, $a_{1/2}$ and a_2 decrease gradually with H, as shown in figure 8.10(a)-(c). The reduction of parameters with applied field is due to the fact that the non-collinear spins at the grain boundaries get polarized, spin waves get progressively suppressed and so also the electron-magnon scattering, while e_g (conduction) electrons get delocalized with the result electron-electron interactions

weaken. Consequently, the resistivity exhibits an overall suppression with increasing field. The field variation of parameters for $T > T_C$, shown in panel (d), are obtained from fits based on Eq.(8.8) in different temperature ranges. The variation of $T_0^{1/4}$ with H implies that the localization length decreases as the field strength increases.

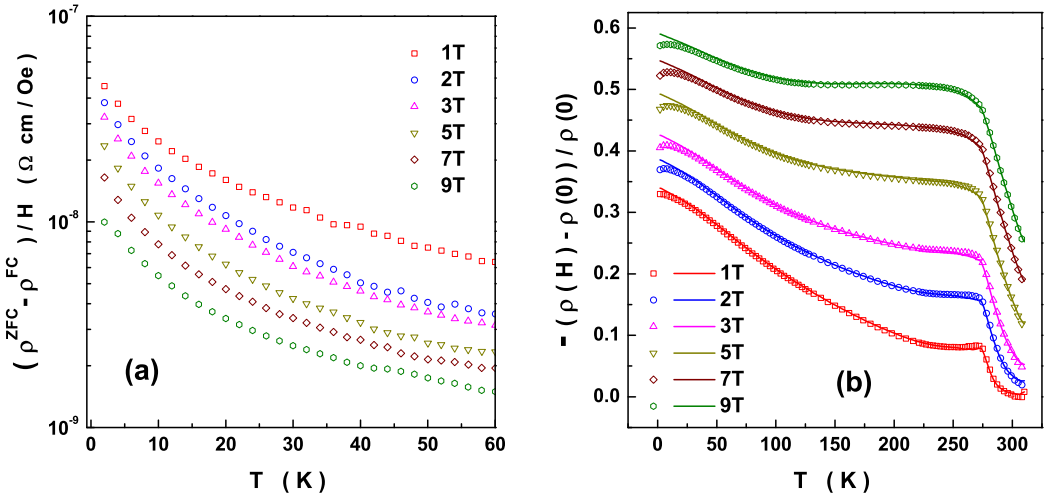

Figure 8.11: *(a) Irreversibility in resistivity due magnetic field below T_{min} and (b) magnetoresistance in 'zero-field-cooled' (symbols) and 'field-cooled' (lines) mode as a function of temperature at various magnetic fields for $x3$.*

The irreversibility in resistivity calculated using Eq.(8.9) for temperatures $T < 60\ K$ at various static fields, displayed in figure 8.11(a), has a very small value and decreases with temperature. MR, depicted in Fig.8.11(b), increases as the temperatures falls below T_C reaching values as high as $\simeq$ 58% at $\simeq$ 30 K and 90 kOe and MR measured in the ZFC and FC modes shows a slight bifurcation below T_{min}. MR in a close by composition $x = 0.33$ in nanocrystalline form has shown a similar trend with respect

to the bulk [30]. The large percentage magnetoresistance at low temperatures was attributed to spin-polarized tunnelling at grain boundaries. Thus, the M-I transition smears out and shifts to lower temperatures while the T_C remains more or less robust when the average particle size is reduced to nanometer range. However, the reduced particle size results in a low-temperature resistivity minimum.

8.5.3 Over hole-doped LCMO - $La_{0.375}Ca_{0.625}MnO_3$

The optimally electron-doped $LCMO$ system is an insulator which undergoes a PMI-charge ordering (CO) transition at $T_{CO} \sim 270\ K$, where a sudden upturn in resistivity occurs, followed by a transition to an antiferromagnetic state at $T_N = 150\ K$. The resistivity of a similar system with $x = 0.65$ is described in terms of adiabatic hopping of polarons in different temperature ranges with three different activation energies: 45 meV for $T > T_{CO}$, 220 meV for $T_N < T < T_{CO}$ and 220 meV for $T < T_N$ [31]. Electron diffraction studies on compounds with $x > 0.5$ have shown intriguing charge localization patterns below T_{CO} that take the form of a extremely stable pairs of $Mn^{3+}O_6$ octahedra stripes (with lattice contraction due to the JT effect). These $Mn^{3+}O_6$ stripes are separated with a period of commensurate carrier concentration $(1/2, 2/3, 3/4, 4/5)$ times the orthorhombic unit cell lattice parameter by stripes of $Mn^{4+}O_6$ octahedra. In other words, the charge segregate preferentially between different sites with nominally Mn^{3+} or Mn^{4+} valence producing an insulating CO state [32]. It is shown that the CO state of $x = 5/8$ consists of a fine mixture of 25% $2a_0$ and 75% $3a_0$ paired JT distorted diagonal $Mn^{3+}O_6$ stripes [33]. It is believed that the manganite consists of a competing charge (orbital) ordered and

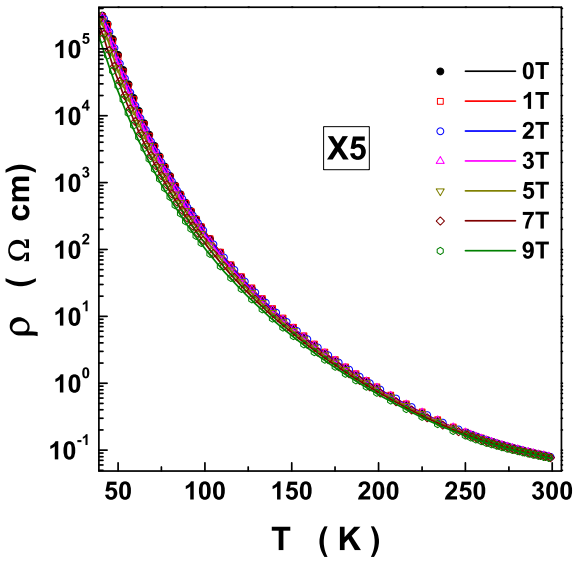

Figure 8.12: *'Zero-field-cooled' (symbols) and 'field-cooled' (lines) resistivities as functions of temperature at fixed magnetic fields for $x5$.*

ferromagnetic phases that have large strain mismatch [32]. The electrical resistivity reveals a metallic or an insulating nature depending on whether or not the FMM grains form a percolating network through the sample. External perturbation such as temperature, magnetic field, radiation, stress, doping, pressure, etc., change the relative proportions of these phases.

The thermal variation of resistivity at various static fields for $x5$, shown in figure 8.12, indicates that the system is an insulator in the measured temperature range $(42 - 305\ K)$. There is no sudden upturn in resistivity at the so-called T_{CO}, as normally expected and observed in bulk over-doped $LCMO$. The fits to the resistivity data for $x5$, based on equation (8.8), are presented in Fig.8.13 in two different temperature ranges and the variations

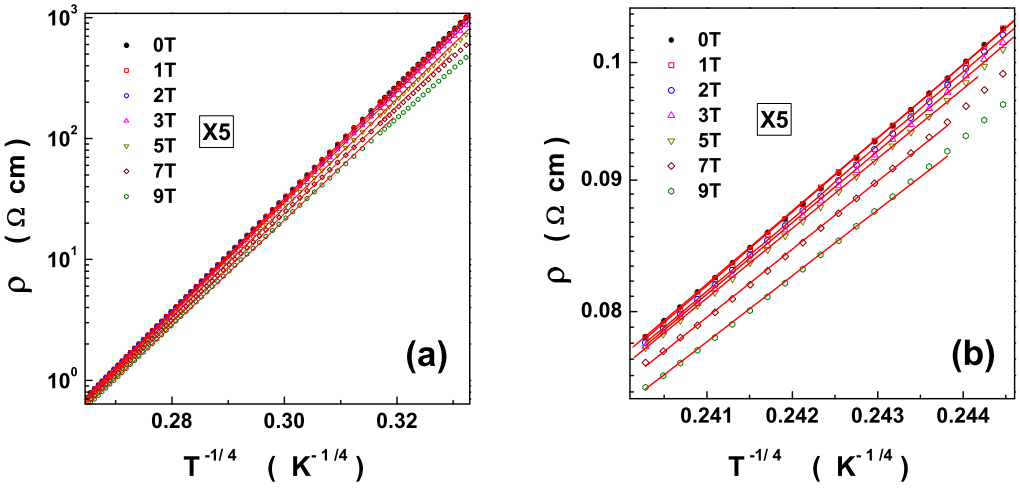

Figure 8.13: *Fits (continuous lines) for resistivity data (a) below and (b) above* $T_C(H = 0)$ *as a function of temperature at various magnetic fields for* $x5$ *based on Eq.(8.8).*

of the corresponding fitting parameters with field are shown in Fig.8.14. The parameters ρ_0 and $T_0^{1/4}$ show a smooth variation with H.

The irreversibility in resistivity, $\Delta\rho_{irr}(T)$, in the temperature range 2 K-100 K, shown in figure 8.15(a), decreases with temperature at various fields. The MR, depicted in Fig.8.15(b), has higher magnitude in the low temperature region than at T_C. The MR in ZFC and FC modes shows a bifurcation below T_C. It exhibits a peak with the highest value of 74% at 90 kOe at 44 K, that shifts to higher temperatures with increasing field, and a small shoulder around T_C. The peak temperature in MR is close to one of the characteristic peak temperatures in $-\Delta S_M$ and can be identified with T_N. A plausible explanation for the intriguing behaviour in magneto-transport in $x5$ can be understood in terms of a picture where the system is composed

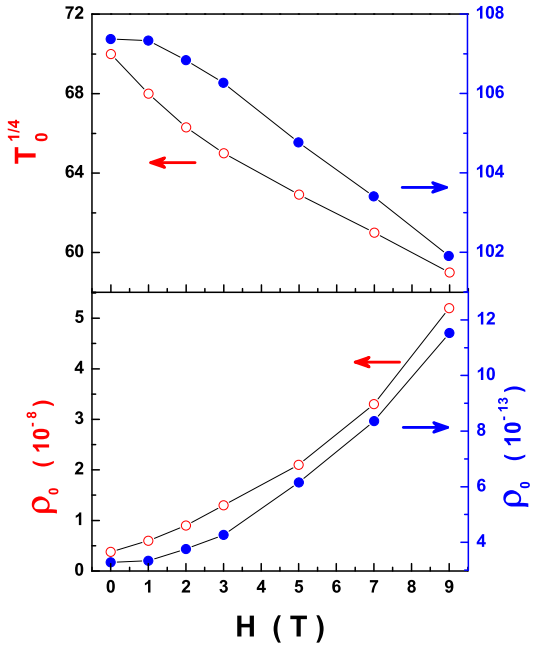

Figure 8.14: *Variations of the fit parameters with field corresponding to the fits (continuous lines) to the resistivity data above and below T_C, based on Eq.(8.8) for $x5$.*

of CO ordered grains with disordered spins at grain boundaries at low temperature while both grain and grain boundaries have disordered spins in the PMI state. Thus, reducing the grain size to nanometer regime shifts the T_N to lower value and suppresses the CO features.

8.6 Conclusion

From the detailed analysis of resistivity data of $x1$, $x2$, $x3$ and $x5$ systems outlined in preceding sections, it is clear that the transport properties of

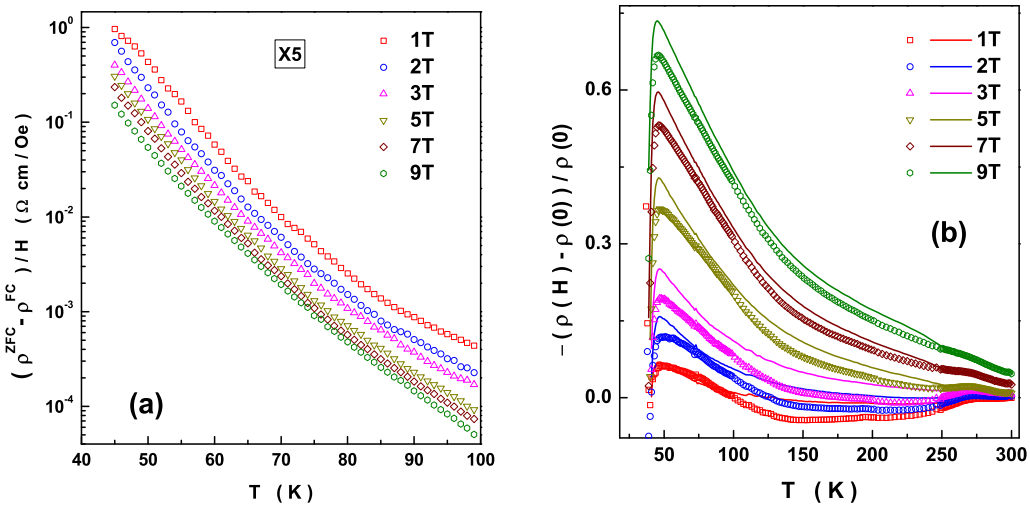

Figure 8.15: *(a) Irreversibility in resistivity due magnetic field below* 100 *K and (b) magnetoresistance in 'zero-field-cooled' (symbols) and 'field-cooled' (lines) mode as a function of temperature at various magnetic fields for* $x5$.

these systems are strongly affected by the reduction in the average grain size to nanometer regime. The nature of electronic transport that was believed to be of small polaron hopping type in PMI state in the bulk changes over to Mott VRH type in the nanocrystalline counterparts. Interesting behaviour is seen at low temperatures that completely differs from that of the bulk. The dispersion in $\rho_H^{ZFC}(T) - \rho_H^{FC}(T)$ absent in zero field builds up with field indicating the percolating behaviour. The thermal hysteresis in $\rho(T)$ arises from the competition between the carrier-localizing JT effect and the delocalizing tendency of the DE interaction. The aforementioned features can be qualitatively explained on the basis of a picture where nanometric grains, having certain type of order (FMI for $x1$ and $x2$, FMM for $x3$ and CO for $x5$), are separated by grain boundaries with uncompensated spins

at low temperatures and in the PM state the spin/charge order within the grains also gets disordered.

References

1. J. M. D. Coey, M. Viret and S. von Molnar, *Mixed-Valence Manganites*, Adv. Phys. **48**, 167 (1999).

2. A. P. Ramirez, *Colossal magnetoresistance*, J. Phys.: Condens. Matter **9**, 8171 (1997).

3. G. J. Snyder, R. Hiskes, S. Di Carolis, M. R. Beasley and T. H. Geballe, *Intrinsic electrical transport and magnetic properties of* $La_{0.67}Ca_{0.33}MnO_3$ *and* $La_{0.67}Sr_{0.33}MnO_3$ *MOCVD thin films and bulk material*, Phys. Rev. B **53**, 14434 (1996).

4. D. C. Worledge, G. J. Snyder, M. R. Beasley and T. H. Geballe, *Anneal-tunable Curie temperature and transport of* $La_{0.67}Ca_{0.33}MnO3$, J. Appl. Phys. **80**, 5158 (1996).

5. R. Laiho, K. G. Lisunov, E. Lähderanta, P. A. Petrenko, J. Salminen, M. A. Shakhov, M. O. Safontchik, N. V. Stamov, M. L. Shubnikov and V. S. Zakhvalinskii, *Variable-range hopping conductivity in* $La_{1-x}Ca_xMn_{1-y}Fe_yO_3$*: evidence of a complex gap in density of states near the Fermi level*, J. Phys.: Condens. Matter **14**, 8043 (2002).

6. B. I. Shklovskii and A. L. Efros, *Electronic Properties of Doped Semiconductors* (Berlin: Springer, 1984).

7. V. N. Smolyaninova, X. C. Xie, F. C. Zhang, M. Rajeswari, R. L. Greene and S. Das Sarma, *Anomalous field-dependent specific heat in charge-ordered* $Pr_{1-x}Ca_xMnO_3$ *and* $La_{0.5}Ca_{0.5}MnO_3$, Phys. Rev. B **62**, R6093(2000).

8. N. F. Mott and E. A. Davies, *Electron Processes in Non-Crystalline Materials* (Oxford: Clarendon, 1979).
N. F. Mott, *MetalInsulator Transitions* (London: Taylor and Francis, 1990).

9. R. M. Kusters, J. Singleton, D. A. Keen, R. McGreevy and W. Hayes, *Magnetoresistance Measurements on the Magnetic Semiconductor* $Nd_{0.5}Pb_{0.5}MnO_3$, Physica B **155**, 362 (1989).

10. M. Viret, L. Ranno and J. M. D. Coey, *Magnetic Localization in Mixed-Valence Manganites*, Phys. Rev. B **55**, 8067 (1997).

11. G. Jeffrey Snyder, *Magnetism and electron transport in magnetoresistive lanthanum calcium manganite*, Ph.D. Thesis, Stanford University (1997).

12. N. F. Mott, *Conduction in Non-Crystalline Materials* (Clarendon Press, Oxford, 1993).

13. N. F. Mott, *Conduction in Glasses Containing Transition Metal Ions*, J. Non-Cryst. Solids **1**, 1 (1968).

14. P. K. Siwach, H. K. Singh and O. N. Srivastava, *Influence of strain relaxation on the magneto-transport properties of the epitaxial LCMO films*, J. Phys.: Condes. Matter **18**, 9783 (2006).

15. M. B. Salamon and M. Jaime, *The physics of manganites: Structure and transport*, Rev. Mod. Phys. **73**, 583 (2001).

16. H. Fujishiro, T. Fukase, M. Ikebe and T. Kikuchi, *Sound Velocity Anomaly at around* $X \approx 1/8$ *in* $La_{1-X}Ca_XMnO_3$, J. Phys. Soc. Jpn.

68, 1469 (1999).

17. G. Biotteau, M. Hennion, F. Moussa, J. Rodrguez-Carvajal, L. Pinsard, A. Revcolevschi, Y. M. Mukovskii and D. Shulyatev, *Approach to the metal-insulator transition in* $La_{1-x}Ca_xMnO_3$ *(*$0 \leq x \leq 0.2$*): Magnetic inhomogeneity and spin-wave anomaly*, Phys. Rev. B **64**, 104421 (2001).

18. S. Begum, Y. Ono, Y. Tomioka, Y. Tokura, Y. Ishii, Y. Morii and T. Kajitani, *Jahn-Teller distortion and cluster-glass like behavior in* $La_{0.875}Ca_{0.125}MnO_3$, J. Phys. Chem. Solids **63**, 939 (2002).

19. E. Bose, S. Karmakar, B. K. Chaudhuri, S. Pal, C. Martin, S. Hébert and A. Maignan, *Anomalous thermal properties and local lattice effects in low doped manganites* $La_{0.875}Ca_{0.125}MnO_3$ *and* $La_{0.875}Ca_{0.0625}Sr_{0.0625}MnO_3$, J. Phys. D: Appl. Phys. **40**, 3728 (2007).

20. E. Bose, S. Karmakar, B. K. Chaudhuri, S. Pal, C. Martin, S. Hébert and A. Maignan, *Correlation of structural, magnetic and transport properties with the tolerance factor in a low-doped* $La_{0.875}Sr_{0.125-x}Ca_xMnO_3$ *(*$0 \leq x \leq 0.125$*) system: cross-over from Mott to Shklovskii-Efros variable range hopping conduction*, J. Phys.: Condens. Matter. **19**, 266218 (2007).

21. E. Bose, S. Karmakar, B. K. Chaudhuri and S. Pal, *Importance of double-exchange interaction in low-doped ferromagnetic insulator* $La_{0.875}Ca_{0.125}MnO_3$, Solid State Commun. **145**, 149 (2008).

22. A. Banerjee, N. Gayathri and R. Ranganathan, *Magnetism and transport in $La_{0.875}Ca_{0.125}MnO_3$ nanocrystalline particles*, Sol. Stat. Phys. (India) **46**, 227 (2003).

23. K. Kubo and N Ohata, *A Quantum Theory of Double Exchange*, J. Phys. Soc. Japn. **33**, 21 (1972).

24. J. A. Collado, C. Frontera, J. L. García-Muñoz, C. Ritter, M. Brunelli and M. A. G. Aranda, *Room Temperature Structural and Microstructural Study for the Magneto-Conducting $La_{5/8-x}Pr_xCa_{3/8}MnO_3$ ($0 \leq x \leq 5/8$) Series*, Chem. Mater. **15**, 167 (2003).

25. J. A. Collado, C. Frontera, J. L. García-Muñoz and M. A. G. Aranda, *Effect of cation site-disorder on the structure and magneto-transport properties of $Ln_{5/8}M_{3/8}MnO_3$ manganites*, J. Solid State Chem. **178**, 1949 (2005).

26. S. H. Masunaga and R. F. Jardim, *Competition between coexisting phases in $(La, Pr)CaMnO_3$ manganites*, J. Appl. Phys. **102**, 073903 (2007).

27. M. Jaime, P. Lin, S. H. Chun, M. B. Salamon, P. Dorsey and M. Rubinstein, *Coexistence of localized and itinerant carriers near T_C in calcium-doped manganites*, Phys. Rev. B **60**, 1028 (1999).

28. K. H. Kim, M. Uehara, C. Hess, P. A. Sharma and S. -W. Cheong, *Thermal and Electronic Transport Properties and Two-Phase Mixtures in $La_{5/8-x}Pr_xCa_{3/8}MnO_3$*, Phys. Rev. Lett. **84**, 2961 (2000).

29. G. Li, T. Qian, S. -J. Feng, F. Liu, H. -D. Zhou and X. -G. Li, *Magnetoresistance in $La_{1-x}Ca_xMnO_3$ ($0 \leq x < 4$)*, Solid State Commun.

128, 171 (2003).

30. L.E. Hueso, F. Rivadulla, R.D. Sánchez, D. Caeiro, C. Jardón, C. Vázquez-Vázquez, J. Rivas and M.A. López-Quintela, *Influence of the grain-size and oxygen stoichiometry on magnetic and transport properties of polycrystalline* $La_{0.67}Ca_{0.33}MnO_{3\pm\delta}$ *perovskites*, J. Magn. Magn. Mater. **189**, 321 (1998).

31. M. R. Ibarra, J. M. De Teresa, J. Blasco, P. A. Algarabel, C. Marquina, J. García, J. Stankiewicz and C. Ritter, *Lattice effects, stability under a high magnetic field, and magnetotransport properties of the charge-ordered mixed-valence* $La_{0.35}Ca_{0.65}MnO_3$ *perovskite*, Phys. Rev. B **56**, 8252 (1997).

32. Peter Littlewood, *Phases of resistance*, Nature **399**, 529 (1999).

33. S. Mori, C. H. Chen and S. -W. Cheong, *Pairing of charge-ordered stripes in* $(La, Ca)MnO_3$, Nature **392**, 473 (1998).

Chapter 9

Concluding remarks

The present chapter summarizes the results obtained in the preceeding chapters on Mn-site doped LPMO and on the under, optimal and over hole-doped LCMO series and outlines the future scope for work in this area.

With a view to arrive at a final picture about the nature of magnetic order present in both LPMO and LCMO, the main results presented in the preceding chapters are summarized in table 9.1.

$TM = Fe, Co, Ni$ ions exist in TM^{3+} valence state in Mn-site doped LPMO. The partial substitution of Mn by Co or Ni stabilizes the long-range isotropic dipolar (ID) fixed point at the cost of the short-range isotropic Heisenberg (IH) critical behaviour prevalent in the parent compound. The presence of TM^{3+} ions gives rise to the localization of e_g electrons, promotes long-range dipolar interactions between e_g-electron spins and drives the system towards an insulating regime. Increase in the Co or Ni concentration progressively enhances antiferromanetic (AFM) super-exchange

Table 9.1: *Nature of magnetic order in the asymptotic critical region for the systems studied in the present work.*

Sl. no	System	T_C (K)	T_{MI} (K)	ACR
1	$La_{0.7}Pb_{0.3}MnO_3$	345	270	IH
2	$La_{0.7}Pb_{0.3}Mn_{0.8}Ni_{0.2}O_3$	247.43	-	ID
3	$La_{0.7}Pb_{0.3}Mn_{0.8}Co_{0.2}O_3$	234.3	-	ID
4	$La_{0.7}Pb_{0.3}Mn_{0.8}Fe_{0.2}O_3$	80.0	-	CSG
5	$La_{0.875}Ca_{0.125}MnO_{3.00}$	143.13	97	UD
6	$La_{0.875}Ca_{0.125}MnO_{3.06}$	134.10	77	UD
7	$La_{0.625}Ca_{0.375}MnO_{2.99}$	273.5	234	UD
8	$La_{0.375}Ca_{0.625}MnO_{2.94}$	270.0	-	UD

(SE) interactions at the expense of the ferromagnetic (FM) double-exchange (DE) interactions and the dipolar interactions tilt the balance in favour of long-range ferromagnetic order when the competing DE and SE interactions become comparable in magnitude. Random substitution of Mn^{3+} ions by Fe^{3+} ions and the competing FM and AFM interactions respectively cause the quenched random-exchange disorder and spin-frustration, that constitute the necessary ingredients for the cluster spin glass state. The FM coupling between the magnetic moments of FM clusters is presumably due to the inter-cluster dipole-dipole interactions whereas the AFM coupling arises from the $TM_1^{3+} - O^{2-} - TM_2^{3+}$ super-exchange interactions, where TM_1,

TM_2 stand for either Fe or Mn. The above results support the percolation picture (applicable to all those hole-doped manganites with quenched random-exchange disorder that are below, but close to, the threshold for long-range FM or AFM order). Furthermore, considerably smaller value of the exponent β compared to that theoretically predicted for a $d = 3$ Heisenberg chiral spin glass with weak random magnetic anisotropy asserts that a meaningful comparison between theory and experiment is possible only when the probability of finding magnetic impurity atoms as nearest neighbours, in a non-magnetic host, is extremely low or when the theory takes into account the influence of magnetic short-range order on the critical behaviour of spin glass systems. The existence of magnetic short-range order could also be a root cause for a wide dispersion in the exponent values reported for spin glass systems. Non-linear ac susceptibility is a powerful experimental tool to study the phenomena of phase separation. Regardless of the degree of hole doping in LCMO, uniaxial anisotropy accompanies the dipole-dipole interactions in stabilizing the uniaxial dipolar (UD) behaviour in the asymptotic critical region throughout the concentration range studied. The observations made on CMR compounds in the thesis, particularly in the critical region, underscores the importance of dipolar interactions (which have been completely left out of theoretical considerations so far) in establishing FM order in the insulating state.

$T - H$ phase diagrams for $x1$, $x2$, $x3$ and $x5$, as depicted in Figs. 9.1 and 9.2, are arrived at based on the field-dependent characteristic temperatures corresponding to the peak in the isothermal magnetic entropy change, $T_p^{-\Delta S}$, Curie temperature, T_C, as deduced from the temperature derivative of FC (open symbols) and ZFC (filled symbols) magnetization, maximum in

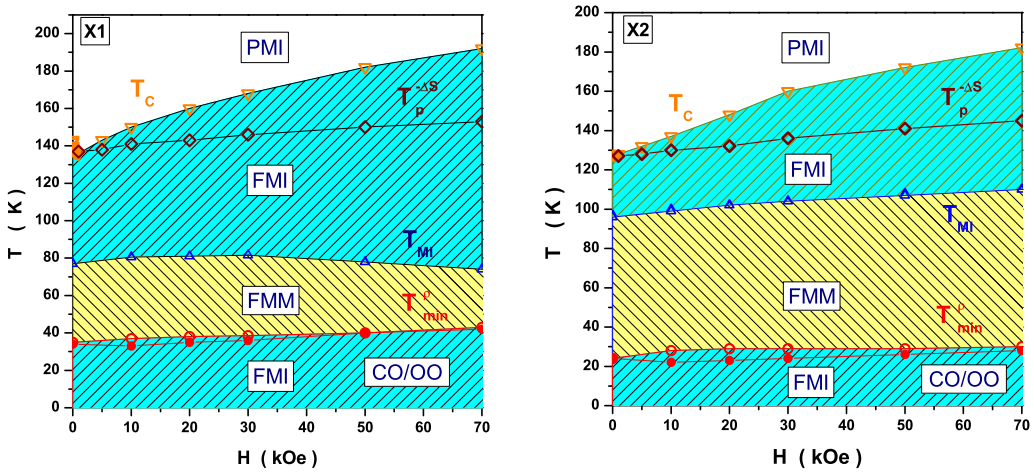

Figure 9.1: *T-H phase diagram for (a) $x1$ ($La_{0.875}Ca_{0.125}MnO_3$) and (b) $x2$ ($La_{0.875}Ca_{0.125}MnO_{3.06}$) based on the field variation of various characteristic temperatures obtained in the chapters 6-8.*

resistivity, T_{MI}, resistivity minimum, T^{ρ}_{min}, obtained in the previous chapters. As is evident from figure 9.1, the oxygen off-stoichiometry increases the ferromagnetic-metallic (FMM) region at the expense of ferromagnetic-insulating (FMI) region for $x = 1/8$ due to the increase in the concentration of Mn^{4+} ions, which promotes DE interactions at the cost of SE interactions. The reduction of magnetization and resistivity in $x2$, compared to that in $x1$, is also brought about by the oxygen off-stoichiometry for the same reason. Bringing the crystallite size down to nanometre range induces an insulating-to-metal transition and a re-entrant insulating (ferromagnetic) phase at temperatures $T < 30\ K$ in the samples $x1$ and $x2$. The low-temperature FMI state could be accompanied by the charge/orbital ordered state, as is indicated by the up turn in resistivity at low temperatures. The sample $x3$ has the largest extent of the FMM temperature region, as

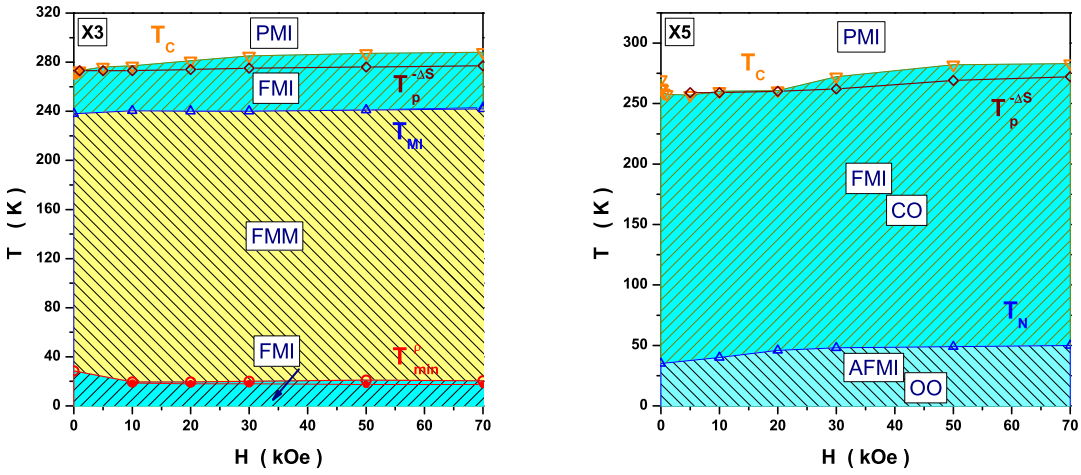

Figure 9.2: *$T-H$ phase diagram for $x3$ and $x5$ based on various characteristic temperatures as a function of applied magnetic field.*

seen from figure 9.2. That $T_C \neq T_{MI}$ and the re-entrance of the FMI state at low temperatures in $x1$, $x2$ and $x3$ are specific to the nanocrystalline state, as they are not observed in the bulk. Thus, the crystallite size reduction is at the root of these physical phenomena. The reduction of crystallite size down to 13 nm promotes FMI order in the sample $x5$ and the transitions from the PMI state to the FMI and CO states occur simultaneously in 'zero-field' at $T_{C/CO} = 270\ K$. $x5$ remains insulating throughout the temperature range $2K \leqslant T \leqslant 320\ K$ and undergoes a transition to the antiferromagnetic state below T_N which is, most likely, an orbitally ordered state.

Reducing the average grain size to nano metre regime in $x1$ $(x2)/x3/x5$ brings into play additional complications due to the comparable length scales of the inherent phase-separated Ferromagnetic-Insulating/Ferromagnetic-

Metallic/Charge Ordered-Insulating regions with those set by the grain/ crystallite sizes. Spin alignment in the grain boundaries also has an important role to play as the number of atoms at the grain-surface increases at the expense of the number of atoms within the core of grains as the grain/crystallite size reduces. Thus, smaller the grain size, the larger the contribution from grain surfaces, grain boundaries and interfaces. The observed glassy like features can be understood in terms of the interaction of spins within the grain core, grain boundaries and between the grains. The magnetic field stabilizes the three-dimensional Ising FM fixed point in $x = 1/8$ and $x = 3/8$ while $x = 5/8$ does not belong to any known universality class. The question whether or not the distinctly different 'zero-field' and 'in-field' critical behaviours in the presently studied $x1$, $x2$, $x3$ systems is specific to only the nanocrystalline systems forms an interesting topic which needs to be investigated further. Neutron scattering experiments and transmission electron microscopy at different temperatures promises further insights into the nature and evolution of magnetic (charge) order in these systems. The nature of magnetic anisotropy can be probed via the ferromagnetic resonance technique.

List of Publications

1. Isotropic-dipolar to isotropic-Heisenberg crossover in Co- and Ni- substituted manganites
   Yugandhar Bitla, S. N. Kaul, L. Fernández Barquín, J. Gutiérrez, J. M. Barandiarán and A. Peña, New J. Phys. **12**, 093039 (2010).

2. Nature of magnetic order in under- and optimally- doped LCMO manganite
   Yugandhar Bitla and S. N. Kaul
   AIP Conf. Proc. **1347**, 285 (2011).

3. Spin glass behaviour in Fe-substituted LPMO manganite
   Yugandhar Bitla, S. N. Kaul and L. Fernández Barquín
   AIP Conf. Proc. **1349**, 125 (2011).

4. Mean field treatment of nonlinear susceptibilities for a ferromagnet of arbitrary spin
   Yugandhar Bitla and S. N. Kaul,
   EuroPhys. Lett. **96**, 37012 (2011).

5. Effect of oxygen off-stoichiometry on magnetic and magneto-transport properties of nanocrystalline under-doped LCMO
   Yugandhar Bitla and S. N. Kaul,
   J. Appl. Phys. **111**, 07D717(2012).

6. Nonlinear susceptibilities as a probe to unambiguously distinguish between canonical and cluster spin glasses
   Yugandhar Bitla, S. N. Kaul and L. Fernández Barquín
   (communicated to *Phys. Rev. B*)

Manuscripts under preparation

1. Nonlinear susceptibility as a probe for magnetic inhomogeneities in transition metal doped manganites
   Yugandhar Bitla, S. N. Kaul and L. Fernández Barquín
   (Manuscript under preparation)

Papers presented at national/international conferences

1. *Effect of magnetic impurities in double-exchange ferromagnets* at Indian National Science Academy (INSA) - Hungarian Academy of Sciences (HAS) joint Workshop on Condensed Matter Research: Magnetic Materials organized by School of Physics, University of Hyderabad, on 4 December, 2006.

2. *Crossover from Isotropic dipolar to Isotropic Heisenberg Critical regime in Double-exchange Ferromagnets* at the 51^{st} DAE Solid State Physics symposium, during 26-31 December, 2006, held at Bhopal and it was published in the proceedings of the DAE Solid Sate Physics (India) 51, 137-138 (2006).

3. *Nonlinear susceptibility of Co- and Ni-substituted manganites* at the 54^{th} DAE Solid State Physics symposium, during 14-18 December, 2009, held at the Maharaja Sayajirao University of Baroda, Vadodara.

4. *Critical phenomena in partially Mn-site doped manganites* at the India-Singapore Joint Physics Symposium (ISJPS 2010), during 19-21 February, 2010, held at School of Physics, University of Hyderabad, Hyderabad.

5. *Effect of Fe substitution in optimally hole-doped LPMO manganite* at the Conference on Advances in Magnetism: Phenomena and Materials (AMPM 2010) during 3-5 June, 2010 at Manali, Himachal Pradesh, INDIA.

6. *Nature of magnetic order in under- and optimally- doped LCMO manganite* at the International Conference on Magnetic Materials (ICMM-2010), during 25-29 October, 2010, held at Saha Institute of Nuclear Physics, Kolkata.

7. *Spin glass behaviour in Fe-substituted LPMO manganite* at the 55^{th} DAE - SSPS 2010, during 26-30 Dec., 2010, held at the Manipal University, Manipal.

8. *Effect of oxygen off-stoichiometry on magnetic and magneto-transport properties of nanocrystalline under-doped LCMO* at 56^{th} Magnetism and Magnetic Materials (MMM-2011) Conference held at Scottsdale, Arizona, U.SA., during Oct 30-Nov 3, 2011.